TTI: 0-6613

Texas A&M Transportation Institute

Evaluation of Binder Aging and Its Influence in Aging of Hot Mix Asphalt Concrete: Technical Report

Technical Report 0-6613-1

Cooperative Research Program

TEXAS A&M TRANSPORTATION INSTITUTE
COLLEGE STATION, TEXAS

in cooperation with the
Federal Highway Administration and the
Texas Department of Transportation
http://tti.tamu.edu/documents/0-6613-1.pdf

Technical Report Documentation Page

1. Report No.	2. Government Accession No.	3. Recipient's Catalog No.
FHWA/TX-14/0-6613-1		

4. Title and Subtitle	5. Report Date
EVALUATION BINDER AND MIXTURE AGING FOR WARM MIX ASPHALT: TECHNICAL REPORT	Published: April 2014
	6. Performing Organization Code
7. Author(s) Charles J. Glover, Guanlan Liu, Avery A. Rose, Yunwei Tong, Fan Gu, Meng Ling, Edith Arambula, Cindy Estakhri, and Robert Lytton	8. Performing Organization Report No. Report 0-6613-1
9. Performing Organization Name and Address Texas A&M Transportation Institute College Station, Texas 77843-3135	10. Work Unit No. (TRAIS)
	11. Contract or Grant No. Project 0-6613
12. Sponsoring Agency Name and Address Texas Department of Transportation Research and Technology Implementation Office 125 East 11th St. Austin, Texas 78701-2483	13. Type of Report and Period Covered Technical Report: September 2011–August 2013
	14. Sponsoring Agency Code

15. Supplementary Notes

Project performed in cooperation with the Texas Department of Transportation and the Federal Highway Administration.
Project Title: Evaluate Binder and Mixture Aging for Warm Mix Asphalt.
URL: http://tti.tamu.edu/documents/0-6613-1.pdf

16. Abstract

Warm mix asphalt (WMA) technologies, through reduced mixing and placement temperatures, have reduced fuel consumption, enhanced compaction, increased haul distances and an extended paving season. Issues of concern in WMA are binder oxidation and absorption and their impact on pavement durability. *Key future work* should combine results from this project with other recent TxDOT projects to develop a *comprehensive and fundamentals based mixture design and pavement performance prediction methodology* that accounts for climate, traffic loading, pavement structural properties, life-cycle cost analysis, and that is applicable to HMA, WMA, polymer-modified binders, and mixtures that incorporate RAP and RAS. Such an effort would be a major contribution to pavement design and is a realistic goal.

Some other key findings are: 1) absorption is directly related to aggregate void fraction, 2) WMA absorption is somewhat less than HMA absorption, 3) the DGC provides a reliable and relatively easy measure of absorption for an aggregate/binder pair, 4) standard (ASTM) methods for measuring absorption can be problematic, depending on the level of absorption, 5) binders modified using warm mix technologies were found to have similar oxidation kinetics to their base binders, 6) the overlay tester and VEC measurements were successfully used to characterize mixture fatigue, 7) mixture fatigue resistance declines with binder oxidation, a result that is omitted entirely from typical pavement design guides (e.g., the MEPDG), and 8) during the first summer of its service life, oxidative aging, curing, and absorption have a significant beneficial effect on the performance of warm mixes.

17. Key Words	18. Distribution Statement
Asphalt Oxidation Kinetics, DSR Function, Carbonyl Area, Density Gradient Column, Warm Mix Asphalt, Mixture Stiffness Gradient, Asphalt Absorption, Dynamic Mechanical Analyzer, Asphalt Specification	No restrictions. This document is available to the public through NTIS: National Technical Information Service Alexandria, Virginia 22312 http://www.ntis.gov

19. Security Classif. (of this report)	20. Security Classif. (of this page)	21. No. of Pages	22. Price
Unclassified	Unclassified	216	

Form DOT F 1700.7 (8-72) **Reproduction of completed page authorized**

EVALUATE BINDER AND MIXTURE AGING FOR WARM MIX ASPHALT: TECHNICAL REPORT

by

Charles J. Glover, Ph.D., P.E.
Professor/Research Engineer
Texas A&M Transportation Institute

Guanlan Liu, Avery A. Rose
Graduate Research Assistants
Texas A&M Transportation Institute

Yunwei Tong, Fan Gu, Meng Ling
Graduate Research Assistants
Texas A&M Transportation Institute

Edith Arambula, Ph.D., P.E.
Associate Research Engineer
Texas A&M Transportation Institute

Cindy Estakhri, P.E.
Research Engineer/Program Manager
Texas A&M Transportation Institute

and
Robert Lytton, PhD, P.E.
Research Engineer
Texas A&M Transportation Institute

Report 0-6613-1
Project 0-6613
Project Title: Evaluate Binder and Mixture Aging for Warm Mix Asphalt

Performed in cooperation with the
Texas Department of Transportation
and the
Federal Highway Administration

Published: April 2014

TEXAS A&M TRANSPORTATION INSTITUTE
College Station, Texas 77843-3135

DISCLAIMER

This research was performed in cooperation with the Texas Department of Transportation (TxDOT) and the Federal Highway Administration (FHWA). The contents of this report reflect the views of the authors, who are responsible for the facts and the accuracy of the data presented herein. The contents do not necessarily reflect the official view or policies of the FHWA or TxDOT. This report does not constitute a standard, specification, or regulation.

This report is not intended for construction, bidding, or permit purposes. The engineer in charge of the project was Charles J. Glover, P.E. #48732, TX. The United States Government and the State of Texas do not endorse products or manufacturers. Trade or manufacturers' names appear herein solely because they are considered essential to the object of this report.

ACKNOWLEDGMENTS

This project was conducted in cooperation with TxDOT and FHWA and the authors are indebted to them for their support and funding of this research project. The authors also thank Mr. Gerald Peterson, for providing valuable leadership, support, and technical assistance as the TxDOT project director, and members of the project monitoring committee. We thank Wade Odell for his excellent service as the project manager. We thank Rick Canatella, and David Zeig, of the Texas A&M Transportation Institute for their laboratory and field contributions. Finally, the authors also thank the various TxDOT district offices that provided assistance in material and pavement core procurement.

TABLE OF CONTENTS

LIST OF FIGURES ..... **xii**

LIST OF TABLES ..... **xv**

LIST OF ABBREVIATIONS ..... **xvii**

LIST OF SYMBOLS ..... **xxi**

CHAPTER 1. INTRODUCTION **1**
Background and Significance of Work 1
Description of Warm Mix Asphalt Technologies 1
Evotherm and Akzo Nobel Redi-Set Wmx *1*
Sasobit *2*
Advera *3*
Foaming Processes *3*
Research Project 0-5597 Evaluation of Warm Mix Asphalt Technologies 4
Research Project 0-6009 Evaluation of Binder Aging and Its Influence in Aging of Hot Mix Asphalt Concrete 5

CHAPTER 2. WMA FIELD TEST SECTIONS **9**
Lufkin FM 324 9
Mixture Production Properties *12*
Summary of Mixture Properties *12*
Field Performance Evaluation *14*
FM 973 16
Field Sampling and Testing *18*
Field Performance *18*

CHAPTER 3. MEASURE WARM MIX BINDER OXIDATION AND HARDENING KINETICS **21**
Abstract 21
Objective 21
Materials and Methods 21
Results and discussion 22
Analysis of Carbonyl Area Data *22*
Correlation between Oxidation Kinetic Parameters *23*
Analysis of Rheological Data *25*
Conclusions 29

CHAPTER 4. ESTIMATE WMA BINDER OXIDATIVE AGING BY A TRANSPORT MODEL **31**
Abstract 31
Introduction 31
Model Background and Parameter Determination 31

Results and Discussion 32
Conclusions 34

CHAPTER 5. CHARACTERIZATION OF LAB MIXED LAB COMPACTED (LMLC) WARM MIX SPECIMENS AND RECOVERED BINDERS 35
Mixture Stiffness Evaluation (Resilient Modulus) 35
Rutting and Moisture Susceptibility Testing (Hamburg Wheel Tracking) TRA 38
Results *39*
Compressive Permanent Deformation Properties of Lab Compacted Mixes 44
Tensile Properties of Lab Compacted Mixes 46

CHAPTER 6. CHARACTERIZE FIELD CORE DURABILITY AND CHARACTERIZE BINDER OXIDATION AND HARDENING IN TEST SECTIONS 51
Characterize Field Core Durability 51
Introduction *51*
Methodology *51*
Stiffness Gradient Calculation Module *52*
Development of FGM Numerical Model *53*
Estimation of the Fracture Properties for Field Samples *53*
Experiment *55*
Result and Discussion *58*
Conclusion *68*
Characterize Binder Oxidation and Hardening in Test Sections 69
Introduction *69*

CHAPTER 7. INTRODUCTION TO THE STANDARD METHOD FOR MEASURING ABSORPTION WITH STATISTICAL DISCUSSION 73
Abstract 73
Introduction 73
Objectives 73
Background 73
Concepts of Mixture Properties *73*
Background and Literature *74*
Water Absorption *75*
Previous Research on Water Absorption *76*
Asphalt Absorption *77*
Previous Research on Asphalt Absorption *79*
Previous Research on Selective Asphalt Absorption *84*
Result and Discussion 85
Statistical Analysis of Standard Method on Water Absorption and Binder Absorption *85*
AMRL Statistics on Water Absorption *86*
Asphalt Absorption Error Calculation in ASTM D4469 ..... *89*
Error Propagation for Asphalt Absorption *90*
Summary 94

CHAPTER 8. INTRODUCTION TO USING THE DENSITY GRADIENT COLUMN (DGC) FOR AGGREGATE AND ABSORPTION MEASUREMENTS 95
Abstract 95
Materials and Methods 95
The Density Gradient Column Method and Procedure 95
Binder Absorption Calculation 96
Bulk Density from the Wax Coating Method 96
Apparent Density and Vacuum Water Saturation 97
Result and Discussion 97
DGC Calibration 97
Aggregate and Absorption Characteristics 98
Conclusion 100

CHAPTER 9. AGGREGATE CHARACTERISTICS 103
Abstract 103
Materials and Methods 103
Density Gradient Column 103
Aggregate Image Measurement System (AIMS) 103
Aggregates 103
Results and Discussion 103
Aggregate Volumetric Measurement by Density Gradient Column 103
Aims Test and Surface Energy of Aggregates 109
Surface Pore Size Distribution with Mercury Porosimeter 109
Aggregate Imaging System (AIMS) Measurements of the Cumulative Spectra of the Shape, Angularity, and Texture of Each Aggregate 109
Surface Energy Components with the Universal Sorption Device (USD) in Our Advanced Characterization of Infrastructure Materials Laboratory 114
Summary 116

CHAPTER 10. MEASUREMENT OF BINDER ABSORPTION 119
Introduction 119
Materials and Methods 120
Asphalt 120
Aggregate 120
Density Gradient Column 120
Result and Discussion 121
Asphalt Absorption in Each Aggregate Piece 121
Aggregate Void Volume per Mass of Aggregate 123
Importance of Void Volume in Asphalt Absorption 126
Effect of Time and Temperature on Asphalt Absorption 129
Mixing Time 130
Curing Time 131
Temperature and Asphalt Absorption 133
Conclusion 134

CHAPTER 11. ASPHALT ABSORPTION MEASUREMENT OF LOOSE MIX SAMPLES USING THE DENSITY GRADIENT COLUMN 135
Abstract 135
Objective 135
Materials and Methods 135
Materials Characterization *136*
Density Gradient Column *136*
Result and Discussion 136
Asphalt Absorption Calculated by ASTM Method *136*
Asphalt Absorption Calculated by Density Gradient Column Method *138*
Characteristics of Recovered Lufkin Binder *141*
Summary 143

CHAPTER 12. ABSORPTION SPECTRUM TESTS 145
Introduction 145
Visualization of Aggregates in Asphalt Mixtures 146
Lab-Mixed-Lab-Compacted Mixtures *146*
Field Cores of Asphalt Pavements *149*
Verification of Aggregate Absorption Using Mass Spectrometer 151
Sample Preparation *151*
LDI-IM-MS Testing *156*
Quantification of Absorption Effect *159*
Conclusions 161

CHAPTER 13. DYNAMIC MECHANICAL ANALYZER TESTS ON FINE AGGREGATE MIXTURES 163
Experimental Testing Plan 163
Materials and Mix Design *163*
Laboratory Aging and Moisture Conditioning 165
Test Procedure 167
Modeling and Analysis 168
Conclusion 170

CHAPTER 14. SUMMARY AND RECOMMENDATIONS 171
Summary of Significant Findings 171
Absorption *171*
Oxidation Kinetics *171*
Mixture Fatigue *171*
WMA Curing at Early Pavement Lives *171*
Recommendation for a New Binder Specification for WMA Pavement Durability 172
Two Approaches to a Binder Durability Specification 172
Procedure 1 ..... *172*
Procedure 2 ..... *173*
Recommendation for Determining Binder Absorption 175
Suggested Implementation 175
Suggestion for Future Work 175

REFERENCES **177**

APPENDIX A: FM 973 FIELD CORE AIR VOID DATA **181**

APPENDIX B: ASPHALT CHARACTERIZATION TESTS **183**

LIST OF FIGURES

Figure 1. Wirtgen Laboratory Scale Foamed Bitumen Equipment in TTI's Laboratory. 4
Figure 2. Oxidation of Alon 64-22 at Five Temperatures. 6
Figure 3. Binder Hardening in Pavements with Oxidation (CA Increase). 7
Figure 4. Construction of Lufkin WMA Field Trials. 9
Figure 5. Hamburg Wheel Tracking Test Results for Lab Molded Warm Mix and Hot Mix Compared to Roadway Cores for FM 324. 13
Figure 6. Overlay Test Results for Plant Mix-Lab Compacted HMA and WMA and Roadway Cores for FM 324. 13
Figure 7. Indirect Tensile Strength Results for HMA and WMA Roadway Coresm FM 324. 14
Figure 8. Alligator Cracking at South End of Project. 15
Figure 9. Test Section Layout on FM 973. 18
Figure 10. Types of Distress Being Exhibited on FM 973. 19
Figure 11. Sampling Times for Asphalt at Different Aging Temperature. 22
Figure 12. CA Growth of Valero PG70-22 with/without Evotherm Additives at Five Temperatures in Air. 22
Figure 13. Empirical Linear Correlation between the Fast-Rate and Constant-Rate Activation Energies. 24
Figure 14. The Correlation between Constant-Rate Kinetics Parameters. 24
Figure 15. The Correlation between Fast-Rate Kinetics Parameters. 25
Figure 16. HS of Limiting Viscosity of Valero PG70-22. 26
Figure 17. HS of Limiting Viscosity of Valero PG70-22 with Evotherm Additives. 26
Figure 18. HS of Limiting Viscosity of Foamed Valero PG70-22. 27
Figure 19. HS of DSR Function of Valero PG70-22. 27
Figure 20. HS of DSR Function of Valero PG70-22 with Evotherm Additives. 28
Figure 21. HS of DSR Function of Foamed Valero PG70-22. 28
Figure 22. Comparison of the Increase in Binder Carbonyl Content with Time for Both Valero PG 70-22 Binder and Valero PG 70-22 Binder with Evotherm Additive. 32
Figure 23. Comparison of the Increase in DSR Function with Time for Both Valero PG 70-22 Binder and Valero PG 70-22 Binder with Evotherm Additive. 34
Figure 24. Schmidt Device for Measuring Resilient Modulus (ASTM D 4123). 35
Figure 25. Evolution of MR Stiffness with Laboratory Aging for the Texas Field Project. 36
Figure 26. MR Results of PMFC Cores and LMLC Specimens with Different Aging for the Texas Field Project. 37
Figure 27. HWTT Machine with Cylindrical SGC Specimens. 38
Figure 28. HWTT Load Cycles versus Rut Depth by Mixture Type for the Texas Mixtures. 39
Figure 29. HWTT Test Parameter of LC_{SN} for Texas Mixtures (log scale). 41
Figure 30. HWTT Test Parameter of Remaining Life for Texas Mixtures (log scale). 41
Figure 31. HWTT Test Parameter $\Delta\varepsilon p$ for Texas Mixtures. 42
Figure 32. Rut Depth Slope at the Stripping Number for Texas Mixtures (Three Parameter MEPDG Fitting Model). 42
Figure 33. Permanent Strain Slope at the Stripping Number for Texas Mixtures (FHWA-VESYS Power Model). 43
Figure 34. HWTT Test Parameter of Crack Speed Index for Texas Mixtures (Larger Positive Number Means Better Performance in Terms of Crack Speed Index). 44
Figure 35. Schematic Plot of the Loading Sequences Used in the Tests (Not Scaled). 45

Figure 36. Testing Configurations of the Compressive Tests 46
Figure 37. Different Material States of an Asphalt Mixture. 47
Figure 38. Test Results n' for HMA and WMA. 49
Figure 39. Test Results of A' for HMA and WMA. 49
Figure 40. Plot of log A′ vs. n′. 50
Figure 41. Procedures of the Test Protocol of Field Samples 52
Figure 42. Sample Preparation for VEC Test. 56
Figure 43. Configuration of VEC Test. 56
Figure 44. Sample Preparation for OT Test. 57
Figure 45. Loading Pattern for Field Specimen in OT Test. 57
Figure 46. Stiffness Gradient Curves of 1 Month Aged Top Layers from Each Section. 61
Figure 47. Stiffness Gradient Curves of Field Core 1-26-1 at Different Temperatures. 62
Figure 48. Stiffness Gradient Curves of 8 Months Aged Top Layers from Each Section. 63
Figure 49. Stiffness Gradient Curves of Top and Underlying Layers from HMA Section. 64
Figure 50. Pavement Performance Information of the Experimental Section. 65
Figure 51. Average Stiffness Values of Top and Bottom Layers for Each Section. 65
Figure 52. Variation of Fracture Properties of Field Samples with Aging Time. 67
Figure 53. Correlation between n and –log(A). 68
Figure 54. Component Diagram of Compacted Sample. 74
Figure 55. Example DGC Density versus Height Calibration. 98
Figure 56. Correlation between Absorbed Binder Volume and Void Volume 100
Figure 57. Aggregate Characteristics Statistics, Mass, and Density, Results Plot as Mean ± 1SD (n for Each Aggregate Type Is Given in Table 32). 108
Figure 58. Aggregate Characteristics Statistics, Volume, and Void Fraction, Results Plot as Mean ± 1SD (n for Each Aggregate Type Is Given in Table 32). 108
Figure 59. AIMS Angularity Chart (3/8"). 110
Figure 60. AIMS Angularity Chart (#4). 110
Figure 61. AIMS Angularity Chart (#8). 111
Figure 62. AIMS Angularity Chart (#16). 111
Figure 63. AIMS 3D Shape Ratio Chart (3/8"). 112
Figure 64. AIMS 3D Shape Ratio Chart (#4). 112
Figure 65. AIMS 3D Shape Ratio Chart (#8). 113
Figure 66. AIMS 3D Shape Ratio Chart (#16). 113
Figure 67. AIMS Texture Chart (3/8"). 114
Figure 68. AIMS Texture Chart (#4). 114
Figure 69. Asphalt Absorption versus Aggregate Mass, Hanson Limestone. 122
Figure 70. Asphalt Absorption versus Aggregate Mass, Jones Mill Quartzite 123
Figure 71. Air Void Distribution in Hanson Limestone Aggregates. 124
Figure 72. Air Void Distribution in Jones Mill Aggregates. 124
Figure 73. Relationship of Void Volume and Volume of Absorbed Binder, Hanson Limestone. 125
Figure 74. Relationship of Void Volume and Volume of Absorbed Binder, Jones Mill. 126
Figure 75. Correlation of Void Volume and Absorbed Binder Volume for Six Types of Aggregate. 127
Figure 76. Linear Correlation of Water Absorption and Asphalt Absorption from Literature Data, Traditional Method. 128

Figure 77. Statistical Analysis on the Ratio of Occupied Void Volume, DGC Method, and Traditional Methods. 129
Figure 78. Linear Correlations of Void Volume and Absorbed Asphalt Volume at Different Mixing Times. 130
Figure 79. Statistical Analysis of Asphalt Absorption and Mixing Time. 131
Figure 80. Linear Correlations of Absorbed Asphalt and Volume of Air Voids on Different Curing Time at 121°C. 132
Figure 81. Statistical Analysis of the Volume Fraction of Air Voids Occupied by Asphalt. 132
Figure 82. Hyperbolic Trendline of Curing Time and Asphalt Binder Absorption 121°C Curing, after 15 Seconds Mixing. 133
Figure 83. Binder Absorption of Lufkin Samples, Calculated Using ASTM Method. 138
Figure 84. Linear Correlations of Asphalt Absorption and Air Void, Volumetric View. 140
Figure 85. Mean Slope and 95 Percent Confidence Interval of the Mean. 141
Figure 86. Exponential Correlation of Absorption Fraction and 60°C Limiting Viscosity. 142
Figure 87. Linear Correlation of Absorption Fraction and DSR Function. 142
Figure 88. Linear Correlation of Absorption Fraction and Carbonyl Area Value. 143
Figure 89. Limestone Aggregate Particle after Laboratory Mixing. 147
Figure 90. LMLC HMA Specimen with AAD Binder and Limestone Aggregates. 148
Figure 91. HMA Field Core Taken from Loop 368, San Antonio, Texas. 150
Figure 92. WMA Field Core Taken from Loop 368, San Antonio, Texas. 151
Figure 93. Limestone Rocks Collected from San Marcos, Texas. 152
Figure 94. Cylindrical Limestone Specimens. 153
Figure 95. Round Aggregate with Absorbed Asphalt Binder. 154
Figure 96. Cross Section of Limestone Specimen after Soaking in AAD Binder for 32 Hours. 156
Figure 97. Schematic Illustration of LDI-IM-MS. 157
Figure 98. IM-MS Spectrums of Selected Points on Limestone Sample. 158
Figure 99. Detailed IM-MS Spectrums. 159
Figure 100. Configuration of Creep Test on Limestone Samples. 160
Figure 101. Measured Axial Strain of Limestone Samples in Creep Tests. 161
Figure 102. SGC Compactor and DMA Cylindrical Specimen. 165
Figure 103. Moisture-Conditioned DMA Specimens in Desiccators. 166
Figure 104. DMA Specimens Conditioning in Desiccators. 166
Figure 105. DMA Test Configuration. 167
Figure 106. Stress And Strain Curve Measured From Controlled-Stress RDT Test. 168
Figure 107. Damage Density vs. Loading Cycles. 169
Figure 108. Test Results for HMA and WMA. 169
Figure 109. Climate/Soils Zones in Texas. 174

LIST OF TABLES

Table 1. WMA Technologies Evaluated in Field Projects. 9
Table 2. Lufkin WMA Field Trial Project Details. 10
Table 3. Lufkin Mix Design Report. 11
Table 4. Project Production Data for Lufkin Field Trials. 12
Table 5. Summary of Distress on US 71 WMA and HMA Test Sections. 15
Table 6. FM 973 Project Details. 16
Table 7. Mix Design Used for the HMA and WMA Sections on FM 973. 17
Table 8. Summary of Pavement Performance Distress on FM 973. 19
Table 9. Calculation of Oxidation Kinetic Parameters. 23
Table 10. Summary of Construction Information of Experimental Sections in FM 973. 55
Table 11. Number of Field Cores for Each Section. 55
Table 12. Results of the Stiffness Gradient Analysis for Field Cores (First Set: F; Second Set: S; Third Set: T). 58
Table 13. Viscoelastic Properties of Field Samples. 66
Table 14. Selection of Core Material for Binder Extraction and Recovery. 69
Table 15. FTIR and DSR Results for Extracted and Recovered Binder. 70
Table 16. AMRL Compilation of Statistics: Coarse Aggregate Water Absorption. 87
Table 17. AMRL Compilation of Statistics: Fine Aggregate Water Absorption. 88
Table 18. Effect of Measurement Errors on Calculated Percent Asphalt Absorption in ASTM D4469 (adapted from Table XX, ASTM D4469, 2011). 90
Table 19. Error Propagation on Water Absorption, Based on AMRL Coarse Aggregate Sample 165, Multilaboratory. 92
Table 20. Error of Variables Related to ASTM D4469. 93
Table 21. Error Propagation Calculation on Asphalt Absorption, ASTM D4469. 93
Table 22. Estimated Error Statistics for Binder Absorption in ASTM D4469. 93
Table 23. Aggregate and Absorption Characteristics for Delta Sandstone (9 Pieces). 99
Table 24. Aggregate and Absorption Characteristics for MM Granite (7 Pieces). 99
Table 25. Aggregate and Absorption Characteristics for Hanson Limestone (10 Pieces). 99
Table 26. Aggregate Characteristics, Delta Sandstone (n=9). 104
Table 27. Aggregate Characteristics, Granite (n=7). 104
Table 28. Aggregate Characteristics, Hanson Limestone (n=10). 105
Table 29. Aggregate Characteristics, Gravel (n=14). 105
Table 30. Aggregate Characteristics, Jones Mill Quartzite (n=7). 106
Table 31. Aggregate Characteristics, Lightweight (n=7). 106
Table 32. Statistical Analysis on Aggregate Characteristics. 107
Table 33. Aggregate Specific Gravity. 109
Table 34. Quartzite Full Mix Design Gradation. 109
Table 35. Surface Energy Component for Different Aggregates. 115
Table 36. Surface Energy Components for Different Aggregates Used in Texas. 116
Table 37. Absorption Data for Hanson Limestone. 121
Table 38. Absorption Data for Jones Mill Quartzite. 122
Table 39. Effect of Mixing and Curing Temperature on Asphalt Absorption. 133
Table 40. Aggregate Properties of Lufkin Aggregates. 136
Table 41. Aggregate Properties for the Lufkin Project. 137
Table 42. Binder and Water Absorption, Lufkin Samples. 137

Table 43. Lufkin Loose Mix Asphalt Absorption by Density Gradient Column Method..... 139
Table 44. Characteristics of Recovered Lufkin Binder. 141
Table 45. Aggregate Gradation for Lab Mix. 164
Table 46. Corresponding Gradation for FAM Specimens. 164
Table 47. Relation between the DSR Function and Pavement Fatigue Life. 174

LIST OF ABBREVIATIONS

AIMS	Aggregate Image Measurement System
AMRL	AASHTO Materials Reference Laboratory
ANOVA	Analysis of Variance
AO	Linear Viscoelastic State Unloading Path
BISG	Bulk Impregnated Specific Gravity
CA	Carbonyl Area
CKE	Centrifuge Kerosene Equivalent
CO	Nonlinear Viscoelastic State Unloading Path
d2s%	Difference Two-Sigma Limit in Percent
DGC	Density Gradient Column
DSR	Dynamic Shear Rate
DT	Direct Tension
EDTA	Ethylene Diamine Tetraacetic Acid
EF	Damaged State Unloading Path
fcf	Field Calibration Factor
FGM	Functionally Graded Material
FGM-FE	Functionally Graded Material-Finite Element
FGM-UMAT	Functionally Graded Material User Defined Material Subroutine
FTIR	Fourier Transform Infrared Spectroscopy
HMA	Hot Mix Asphalt
HS	Hardening Susceptibility
HWTT	Hamburg Wheel Tracking Test
IDT	Indirect Tension Test
LDI	Laser Desorption Ionization
LDI-IM-MS	Laser Desorption Ionization-Ion Mobility–Mass Spectrometer
LMLC	Laboratory Mixed-Laboratory Compacted
LMT	Lithium Metatungstate
LTOA	Long-Term Oven Aged
LVDTs	Vertical Linear Variable Differential Transformers
MEPDG	Mechanistic Empirical Pavement Design Guide

M_R	Resilient Modulus
M_{RTFOT}	Maximum Increase in CA Due to Fast-rate Reaction after Rolling Thin Film Oven Test
MTS	Material Test System
OA	Linear Viscoelastic State Loading Path
OBC	Nonlinear Viscoelastic State Loading Path
OCE	Damaged State Loading Path
OT	Overlay Tester
PMFC	Plant Mixed-Field Compacted
PMLC	Plant Mixed-Laboratory Compacted
POVs	Pressure Oxidation Vessels
QA	Quality Acceptance
QC	Quality Control
RDC	Repeated Direct Compression
RDT	Repeated Direct Tension
SBS	Styrene Butadiene Styrene
SGC	Superpave Gyratory Compacted
SSD	Saturated Surface Dry
TOF	Time-Of-Flight
Tukey's HSD	Tukey-Kramer Honestly Significant Difference
UMAT	User Defined Material Subroutine
USD	Universal Sorption Device
UTM	Universal Testing Machine
UV	Ultraviolet
VEC	Viscoelastic Characterization
VEC	Viscoelastic Characterization
VFA	Voids Filled With Asphalt
VMA	Voids In Mineral Aggregate
WMA	Warm Mix Asphalt
$\overline{\Delta\varepsilon_p}$	Rutting Susceptibility Parameter
AIMS	Aggregate Image Measurement System
AMRL	AASHTO Materials Reference Laboratory

ANOVA	Analysis of Variance
AO	Linear Viscoelastic State Unloading Path
BISG	Bulk Impregnated Specific Gravity
CA	Carbonyl Area
CKE	Centrifuge Kerosene Equivalent
CO	Nonlinear Viscoelastic State Unloading Path
d2s%	Difference Two-Sigma Limit in Percent
DGC	Density Gradient Column
DSR	Dynamic Shear Rate
DT	Direct Tension
EDTA	Ethylene Diamine Tetraacetic Acid
EF	Damaged State Unloading Path
fcf	Field Calibration Factor
FGM	Functionally Graded Material
FGM-FE	Functionally Graded Material-Finite Element
FGM-UMAT	Functionally Graded Material User Defined Material Subroutine
FTIR	Fourier Transform Infrared Spectroscopy
HMA	Hot Mix Asphalt
HS	Hardening Susceptibility
HWTT	Hamburg Wheel Tracking Test
IDT	Indirect Tension Test
LDI	Laser Desorption Ionization
LDI-IM-MS	Laser Desorption Ionization-Ion Mobility–Mass Spectrometer
LMLC	Laboratory Mixed-Laboratory Compacted
LMT	Lithium Metatungstate
LTOA	Long-Term Oven Aged
LVDTs	Vertical Linear Variable Differential Transformers
MEPDG	Mechanistic Empirical Pavement Design Guide
M_R	Resilient Modulus
M_{RTFOT}	Maximum Increase in CA Due to Fast-rate Reaction after Rolling Thin Film Oven Test
MTS	Material Test System

OA	Linear Viscoelastic State Loading Path
OBC	Nonlinear Viscoelastic State Loading Path
OCE	Damaged State Loading Path
OT	Overlay Tester
PMFC	Plant Mixed-Field Compacted
PMLC	Plant Mixed-Laboratory Compacted
POVs	Pressure Oxidation Vessels
QA	Quality Acceptance
QC	Quality Control
RDC	Repeated Direct Compression
RDT	Repeated Direct Tension
SBS	Styrene Butadiene Styrene
SGC	Superpave Gyratory Compacted
SSD	Saturated Surface Dry
TOF	Time-Of-Flight
Tukey's HSD	Tukey-Kramer Honestly Significant Difference
UMAT	User Defined Material Subroutine
USD	Universal Sorption Device
UTM	Universal Testing Machine
UV	Ultraviolet
VEC	Viscoelastic Characterization
VEC	Viscoelastic Characterization
VFA	Voids Filled With Asphalt
VMA	Voids In Mineral Aggregate
WMA	Warm Mix Asphalt

LIST OF SYMBOLS

A	Asphalt Absorption at any Given Time
A_0	Asphalt Absorption at Time Zero
A_c	Pre-Exponential Factor of Constant-Rate Period
A_f	Pre-Exponential Factor of Fast-Rate Period
A'	Modified Paris' Law Parameter
b	Specimen Width
C	Radial Distance between the Aggregate Surface and the Wetting Front
CA_0	Intercept of the Constant-rate Line
CA_{tank}	Carbonyl Area of the Unaged Tank Asphalt
C_{agg}	Aggregate Property Constant
CR_i	Specific Surface Area of the Particle with Diameters in the Range between Sieve Sizes
$c.s.a$	Cracking Surface Area
D	Aggregate Particle Diameter
d	Specimen Thickness
E_{ac}	Activation Energy of Constant-Rate Period
E_{af}	Activation Energy of Fast-Rate Period
$E(z)$	Magnitude of the Complex Modulus at Depth z
E_d	Magnitudes of the Complex Modulus at the Bottom of the AC Layer
E_0	Magnitudes of the Complex Modulus at the Surface of the AC Layer
$\lvert E^*_{(\omega)} \rvert$	Magnitudes of the Moduli in the DT Test
$\left\lvert E^*_{(\frac{1}{2t})} \right\rvert$	Magnitudes of the Moduli in the OT Test
G_1, G_2, G_n	Individual Aggregate Bulk Specific Gravities
G_b	Specific Gravity of the Asphalt
G_{mm}	Maximum Theoretical Specific Gravity of the Mixture (ASTM D 2041)
G_{sb}	Bulk Specific Gravity of the Aggregate
G_{sb}	Bulk Specific Gravity for the Total Aggregate

G_{se}	Effective Specific Gravity of the Aggregate
K	Volume Factor
k	Model Parameter
k_c	Reaction Rate of Constant-Rate Period
k_f	Reaction Rate of Fast-Rate Period
k_r	Reference Stiffness
m_a	Mass of Aggregate
m_{ab}	Mass of Aggregate Coated with Binder
m_{ac}	Mass of Aggregate Coated with Coating Material
N	Number of Load Cycles
n	Model Parameter
n'	Modified Paris' Law Parameter
P_1, P_2, P_n	Individual Aggregate Percentages by Weight of Aggregate
P_b	Asphalt Content Expressed in Percent by Total Weight of Mixture
P_{ba}	Absorbed Asphalt Expressed in Percent by Weight of Aggregate
P_{mm}	Percent by Weight of Total Loose Mixture
$P_{LVE}(t)$	Linear Viscoelastic Force
$\max.P_{LVE}(z=c)$	Measured Maximum Viscoelastic Force Within the Specified Time Interval
R	Radius of the Spherical Aggregate
r	Pore Radius
r_i	Effective Density of Aggregate
$s(c)$	Area Under the Strain Profile above the Tip of the Crack Length
T	Tortuosity
t	Loading Time in the OT Test (Page 213)
t	Time of Absorption (Page 95)
t_d	Dimensionless Time
u	Percentage of the Completed Absorption
$W_R(N)$	Pseudo Strain Work for Each Loading Cycle

$\overline{\Delta\varepsilon_p}$	Rutting Susceptibility Parameter
ΔJ_R	Pseudo *J* Integral
θ	Contact Angle
μ	Liquid Viscosity
ρ_{ab}	Density of Aggregate Coated with Binder
ρ_{ac}	Density of Wax-Coated Aggregate
ρ_{av}	Bulk Density of the Aggregate
ρ_{aw}	Density of Aggregate Saturated With Water
ρ_b	Binder Density
ρ_c	Density of Coating Material
ρ_w	Density of Water at the Laboratory Temperature
σ	Surface Tension
ϕ	Damage Density of an Asphalt Mixture Specimen
ω	Angular Velocity of the DT Machine

CHAPTER 1. INTRODUCTION

BACKGROUND AND SIGNIFICANCE OF WORK

Warm mix asphalt (WMA) technologies employ reduced mixing and placement temperatures thereby allowing reduced fuel consumption, enhanced compaction, increased haul distances, and an extended paving season. Issues of concern in WMA are binder oxidation and absorption and their impact on pavement durability. TxDOT project 0-6009 quantified oxidation rates in HMA pavements and their impact on pavement durability, but did not address warm mixes or binder absorption (Glover et al., 2013).

Further descriptions of WMA technologies used in Texas, research project 0-5597, Evaluation of Warm Mix Asphalt Technologies, and of research project 0-6009, Evaluation of Binder Aging and Its Influence in Aging of Hot Mix Asphalt Concrete, are presented below (Estakhri et al., 2010; Glover et al., 2013).

DESCRIPTION OF WARM MIX ASPHALT TECHNOLOGIES

Warm mix asphalt (WMA) is generic term for a variety of technologies that allow the producers of hot-mix asphalt to lower the temperatures at which the material is mixed and placed on the road. Reductions of 50 to 100°F have been documented. These temperature reductions reduce fuel consumption, enhance compaction, allow for increase in haul distances, and extend the paving season.

WMA technologies can be broadly grouped into two categories:

- *Chemical Modifiers*, which rely on a variety of different mechanisms, such as surfactants to help coat the aggregate at lower temperatures or waxes that decrease the viscosity above their melting point.
- *Foaming Processes* that introduce small amounts of water into the plant that turns into steam, expanding the binder phase and reducing mix viscosity.

Several of the technologies which have been used in Texas are described below.

Evotherm and Akzo Nobel Redi-Set Wmx

Both the Evotherm and Redi-Set WMX processes are classified in company literature as surfactants. One of the problems with reducing the temperature of hot mix production is that the viscosity of the asphalt is reduced which can inhibit coating of the aggregate. A surfactant acts like a soap and aids in the coating process. However, there may be additional components in these two WMA processes and their effects are unknown. In fact, Evotherm has been marketed in the past as a "chemistry package" implying that the chemistry is changed and customized depending on the base binder used for the project.

Evotherm was developed in the U.S. by MeadWestvaco Asphalt Innovations, Charleston, South Carolina (http://www.evotherm.com). Evotherm uses a chemical additive technology customized for aggregate compatibility. The Evotherm technology can be delivered in three different forms as described below.

- Evotherm ET (Emulsion Technology)–a high AC content, water-based asphalt emulsion (~70 percent solids). Evotherm ET requires no plant modifications and simply replaces the liquid asphalt in your HMA design. Evotherm ET allows for temperature reductions greater than 100°F.
- Evotherm DAT (Dispersed Asphalt Technology)–a concentrated solution of Evotherm additives in-line injected at the mix plant. Evotherm DAT allows for flexibility in switching between warm mix and hot mix production while lowering mix temperatures 85–100°F.
- Evotherm 3G (Third Generation)–developed in partnership with Paragon Technical Services and Mathy Technology & Engineering, this water-free form of Evotherm is suitable for introducing the additives at the mix plant or asphalt terminal. Evotherm 3G generally lowers mix temperatures 60–85°F (33–45°C).

The Akzo Nobel Redi-Set WMX is delivered as a solid and ideally would be blended with the asphalt prior to introduction in the asphalt plant.

Sasobit

Sasobit is a product of Sasol Wax (formerly Schumann Sasol) of South Africa. Sasobit is a Fischer-Tropsch (F-T) or synthetic wax that is created in the coal gasification process (http://www.sasolwax.com/www_sasobit_de.html). These organic waxes have longer chemical chain lengths and are different from petroleum or paraffin waxes (which are normally considered undesirable in asphalt. The longer chains help keep the wax in solution, and it reduces binder viscosity at typical asphalt production and compaction temperatures. Sasobit has been used as a compaction aid and a temperature reducer. The Sasobit process incorporates a low melting point organic additive that chemically changes the temperature-viscosity curve of the binder. Both of these additives melt at about 210°F and produce a reduction in the binder viscosity by providing liquids in the binder above their melting points. Blending 3 to 4 percent Sasobit by weight allows a reduction in production temperatures of 18°F to 54°F.

The manufacturer anticipates that in-line blending of melted Sasobit with the asphalt binder stream at the plant will be finalized in the near future, thus eliminating the current use of the Sasobit distributor at the plant. Direct blending of solid Sasobit at the plant is not recommended because it will not give a homogeneous distribution of Sasobit in the asphalt. Further, Sasobit allows incorporation of Styrene Butadiene Styrene (SBS) modifier using a special cross-linking agent termed Sasoflex. Either Sasobit or Sasoflex can be blended into hot binder at the blending plant without the need for high-shear blending.

Sasol emphasizes the difference between naturally occurring bituminous waxes and F-T waxes in terms of their structure and physical properties. The main difference is the much longer chain lengths and the fine crystalline structure of the F-T waxes. The predominant chain lengths of the hydrocarbons in Sasobit range from 40 to 115 carbon atoms; whereas, those in bituminous paraffin waxes range from about 25 to 50 carbon atom, yielding lower melting points than F-T waxes. The longer carbon chains in the F-T wax yield a higher melting point. However, the smaller crystalline structure of the F-T wax, as compared to bitumen paraffin waxes, reduces the brittleness at low pavement service temperatures.

Sasol states that the melting point of Sasobit is approximately 210°F and that it is completely soluble in asphalt at temperatures above 248°F. It reduces the binder viscosity and,

thus, reportedly enables mix production temperatures to be reduced by 18°F to 54°F and improves compactability. At temperatures below its melting point, Sasobit forms a lattice structure in the asphalt binder that is the basis for the reported stability of asphalts that contain Sasobit. At service temperatures, Sasobit-modified mixes exhibit increased resistance to rutting.

Advera

Advera is supplied by PQ Corporation. It is a finely powdered synthetic zeolite (sodium aluminum silicate hydrate) that has been hydro-thermally crystallized. When Advera is added to the mix at the same time as the binder, water is released. This water release creates a foaming of the asphalt binder and, thereby, temporarily increases workability and enhances aggregate coating at lower temperatures. When it is heated above 185°F to 360°F, it gives up 21 percent water by mass, which microscopically foams the asphalt to aid coating of the aggregate. This foaming action of the liquid binder acts as a temporary asphalt volume extender and mixture lubricant, enabling the aggregate particles to be rapidly coated and the mix to be workable and compactable at temperatures significantly lower than those typically used for HMA. PQ states that the mix can be compacted until the temperature drops below 212°F.

PQ Corporation recommends the addition of 0.25 percent by weight of the mix, or 5 lb of Advera WMA per ton of asphalt mix. Since Advera WMA is an inorganic material it does not change the performance grade of the asphalt binder (Federal Highway Administration). Advera WMA is manufactured in plants located in Jeffersonville, Indiana, USA and Augusta, Georgia, USA. It is available in bags, bulk bags (supersacks), and bulk delivery by truck and rail.

Foaming Processes

Foaming processes are the most commonly used WMA method in the state. This process requires a modification to hot mix plant and introduces small amounts of water into the drum which turns into steam, expanding the binder phase and reducing mix viscosity. This very small amount of water is unlikely to have an effect on the long term properties of the mix since the water will be expelled during construction. Foaming processes which are currently being used in Texas today include the following: Astec Double Barrel Green, Terex WMA System, Gencor Green Machine, Maxam Aqua Black.

Until now, foaming processes have been difficult to simulate in the laboratory since it is a modification to the hot mix plant. Recently TTI acquired a Wirtgen laboratory scale bitumen foaming device as shown in Figure 1. This equipment can produce foamed asphalt binders and foamed asphalt mixtures and will be used for fabrication of foamed binders and mixtures in the proposed study. Two of TTI's asphalt laboratory technicians have completed an extensive training course on the use of this equipment.

Figure 1. Wirtgen Laboratory Scale Foamed Bitumen Equipment in TTI's Laboratory.

RESEARCH PROJECT 0-5597 EVALUATION OF WARM MIX ASPHALT TECHNOLOGIES

TxDOT research study 0-5597 was completed by TTI in August 2009. The study was initiated by the TxDOT in 2006 to evaluate warm mix asphalt as a new technology. Initially a literature search was completed and published in 2007 as the first research report from this study (0-5597-1) (Button et al., 2007). In addition, a laboratory and field evaluation of different WMA technologies was conducted (Estakhri et al., 2010). During the first half of the study, TxDOT had only placed 1000 tons of warm mix as a demonstration. By the end of the third year of the study, TxDOT had placed more than 1,000,000 tons of warm mix and allowed the use of warm mix in all dense-graded mixtures through the implementation of special provision 341---020. This research was focused on learning as much as possible during this span of time regarding the effects of WMA technologies on mixture design, lab performance characteristics, and field performance. An ongoing implementation study (5-5597) is underway by Cindy Estakhri of TTI to continue to monitor performance of warm mix field sections.

In terms of mixture design, researchers found that dense-graded WMA mixtures which are designed with the additive will have a significantly lower optimum asphalt content than the corresponding mixture without the WMA additive. Even when the mixing and compaction temperature is reduced to 60°F below that used for HMA, compaction was enhanced sufficiently to cause a reduction in density and, thus optimum asphalt content.

At the onset of this research, TxDOT procedures required a laboratory oven-curing procedure prior to molding specimens. This procedure consisted of a 2 hour cure of the mixture at the recommended compaction temperature. WMA mixtures which are cured at their respective compaction temperature exhibit Hamburg results as much as half that achieved for the corresponding HMA. Increasing the oven curing time from 2 hours to 4 hours and increasing the oven curing temperature to 275°F resulted in a significant increase in WMA Hamburg results that were comparable to the corresponding HMA. Increasing the oven curing time for HMA from 2 hours to 4 hours and to 275°F did not result in a significant increase in HWTT results.

The cracking performance (from fatigue and overlay testing) indicates that WMA has the potential to improve the cracking resistance of a mix. While WMA field mixtures did increase in stiffness during the first year of service, some WMA technologies still showed a slight improvement in cracking resistance.

Surface free energy tests and Hamburg wheel tracking test results indicate that WMA mixtures may be susceptible to moisture damage, particularly during the first few months of service. However, extensive field construction of warm mix projects has not revealed any moisture susceptibility issues.

Field performance of WMA projects evaluated in study 0-5597 has been equivalent to comparable HMA projects. The oldest WMA pavement in Texas was 3 years old and was performing similarly to the HMA control section. Cores from field projects taken one year after construction indicate a significant "stiffening" of the WMA mixes as measured by HWTT, Overlay test, and Indirect Tensile Strength. GPR of WMA projects indicate that they are as uniformly constructed (in terms of density) as corresponding control HMA sections. X-ray CT data indicate that the density or air void distribution with depth in the mat may be even more uniform than HMA and FWD data indicate the structural strength characteristics are similar to HMA.

RESEARCH PROJECT 0-6009 EVALUATION OF BINDER AGING AND ITS INFLUENCE IN AGING OF HOT MIX ASPHALT CONCRETE

Although evidence that binder oxidation in pavements occurs, that it occurs beyond the near-surface of the pavement, that it is ongoing throughout the life of the pavement, and that it has a very profound effect on pavement durability is mounting and gaining acceptance, important implementation issues remain to be better understood. Understanding how best to design mixtures in a way that takes binder oxidation into account to achieve maximum pavement durability is a very complex but important issue. A second, related issue is the use of maintenance treatments to impede or reduce binder oxidation in pavements. Project 0-6009 was designed to provide new information on these issues so as to achieve significant improvements to pavement durability, and significant life-cycle cost savings to TxDOT.

Specifically, the project goals included: 1) a new test procedure to characterize binder aging and predict service life for different applications, 2) an HMA mix design component that incorporates aging and its effect on fatigue cracking, 3) guidelines for optimizing HMA mixture resistance to aging, and 4) guidelines for best maintenance treatments to reduce aging of binders.

To accomplish these goals, a number of methods are being used: 1) measurements of binder oxidation to determine both fast-rate and constant-rate reaction kinetics and relationships between oxidation and hardening, 2) measurements of mixture property changes (such as fatigue) that result from binder oxidative hardening, 3) measurements of binder oxidation and hardening in the field, and the field mixture fatigue decline with binder oxidation, and 4) development of a model of binder oxidation and hardening in pavements that can be used to predict hardening over time. The pavement oxidation and hardening model uses the binder oxidation kinetics together with the effects of oxidation on mixture properties and a new model of pavement temperature as a function of time and depth to estimate oxidation and hardening in the field. These estimates are being compared to the measured oxidation and fatigue resistance decline. When fully developed, the model will be a key element to pavement design.

Figure 2 is an example of the binder reaction kinetics data that are being obtained. From such data for each asphalt, activation energy values can be determined that are essential to calculating reaction rates from pavement temperatures. Accurate oxidation kinetics are necessary for estimating binder oxidation in pavements and being able to compare model calculations to field measurements. Each binder has its own oxidation kinetics parameters.

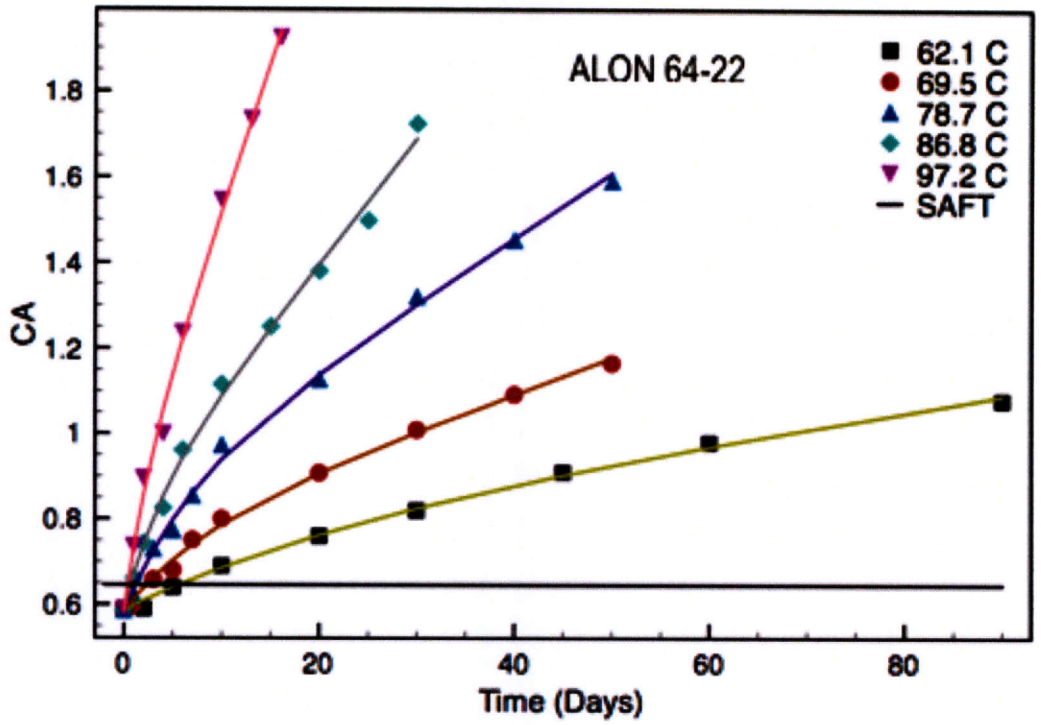

Figure 2. Oxidation of Alon 64-22 at Five Temperatures.

Figure 3 is an example of the type of correlation obtained between binder oxidation (carbonyl area, CA) and binder hardening, represented by a combination of elastic and viscous properties that relate to binder brittleness. The data in the figure are for binder that was extracted and recovered from pavement cores, both shoulder and wheel path locations. These data were obtained over the five-year duration of the project to obtain oxidation rates (CA versus time), and hardening rates that can be used to calibrate the oxidation model. The data are high quality and are providing the best understanding of binder oxidation in pavements available.

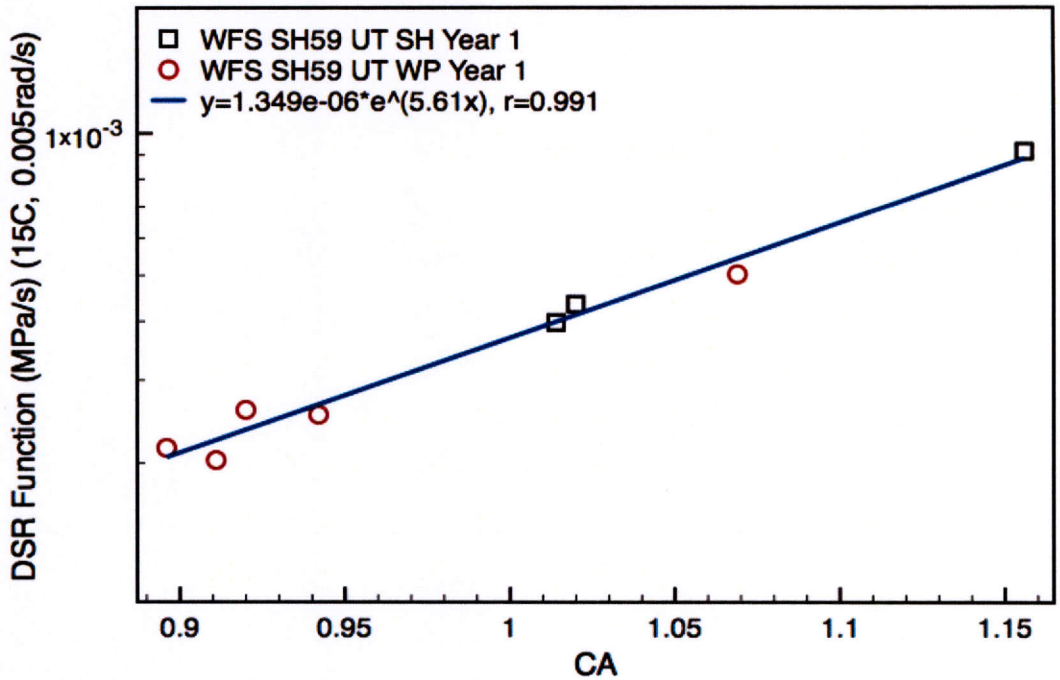

Figure 3. Binder Hardening in Pavements with Oxidation (CA Increase).

At the same time, field cores were used to provide measurements of the changes that occur to bulk mixture physical properties as the result of binder oxidation. These properties are being assessed with the VEC and RDT* tests of prismatic field specimens. The VEC test provides viscoelastic characterization of the mixture with test procedure damage. The RDT* test provides viscoelastic characterization but tracks damage (crack growth) as it occurs during the testing. These tests, conducted on field (or laboratory) specimens at various levels of oxidative aging, provide information on the effect of binder oxidation on mixture durability (e.g., fatigue resistance). This information is essential to being able to estimate pavement service durability in the presence of oxidative aging and traffic and thermal loads. This decline of fatigue resistance with binder hardening is a characteristic of each mixture that is probably a function of binder content, air voids, aggregate type, and other variables.

The procedures and results of project 0-6009 provide important background and resources for project 0-6613. It is anticipated that the methods of projecting warm mix durability for project 0-6613 will parallel durability methods of project 0-6009. Important to 0-6613, just as for 0-6009, will be fundamental characterization data on binder oxidation rates (and thus binder oxidation kinetics), binder hardening rates (directly related to the oxidation rates), and the impact of binder hardening on mixture durability (e.g., fatigue resistance). Also essential to the effort will be the pavement oxidation model, developed in 0-6009, that uses a pavement temperature model together with binder oxidation kinetics and diffusion parameters and hardening characteristics, to calculate oxidation and hardening in pavements for a binder durability specification.

However, also there will be some significant new requirements for project 0-6613. These will include assessments of binder absorption and its effect on durability, moisture susceptibility, and the effect of the various warm mix additives on these mixture characteristics.

CHAPTER 2. WMA FIELD TEST SECTIONS

In this project, two projects which employed the use of multiple WMA technologies were sampled and evaluated in the field and laboratory: FM 324 in the Lufkin District and FM 973 in the Austin District. The technologies and asphalt binder types used are shown below in Table 1.

Table 1. WMA Technologies Evaluated in Field Projects.

WMA Technology	FM 324	FM 973
Base Asphalt	PG 64-22	PG 70-22
Foaming		X
Evotherm	X	X
Akzo Nobel Redi Set	X	
Advera	X	
Sasobit	X	
None–Control HMA	X	X

LUFKIN FM 324

In February and March of 2008, the Lufkin district placed four different WMA technology field trials (Figure 4). A description of the project details is shown in Table 2.

Figure 4. Construction of Lufkin WMA Field Trials.

Table 2. Lufkin WMA Field Trial Project Details.

Project Location	FM 324, Lufkin
Construction Dates	February/March 2008
Warm Mix Tonnage	~ 4000 tons (~1000 tons/WMA technology)
Mix Design Information	• Item 341, Type D Dense Graded • PG 64-22 • Aggregate: 91% Hanson Chico LS 9 % Field Sand • Anti-strip: 1% lime for HMA and all WMA • AC Content: 4.6% (Both HMA and WMA)
Warm Mix Asphalt Technology	Sasobit, Evotherm DAT, Akzo Nobel Rediset, Advera
Mixture Production	Temperature at Load Out: HMA 270°F WMA 240°F
Laydown and Compaction	Mat Thickness: 1.5 inches

Table 3. Lufkin Mix Design Report.

TEXAS DEPARTMENT OF TRANSPORTATION

HMACP MIXTURE DESIGN : COMBINED GRADATION

Refresh Workbook

File Version: 12/09/04 11:12:14

SAMPLE ID:	32D4	SAMPLE DATE:	8-15-05
LOT NUMBER:		LETTING DATE:	
STATUS:	US 69	CONTROLLING CSJ:	
COUNTY:	Angelina	SPEC YEAR:	2004
SAMPLED BY:		SPEC ITEM:	341
SAMPLE LOCATION:	ETA	SPECIAL PROVISION:	
MATERIAL:	Type D	MIX TYPE:	ITEM341_D_Fine_Surface
PRODUCER:	East Texas Asphalt		
AREA ENGINEER:	David Collmorgan	PROJECT MANAGER:	

COURSE\LIFT:		STATION:		DIST. FROM CL:	

	BIN FRACTIONS																					
	Bin No.1		Bin No.2		Bin No.3		Bin No.4		Bin No.5		Bin No.6		Bin No.7			Combined Gradation						
Aggregate Source:	Hanson		Hanson		ETA		Texas Lime															
Aggregate Number:	Chico		Chico		Sand		Hydrated Lime															
Sample ID:	D-F		Scr.		Field Sand		Lime															
Rap?, Asphalt%:															Total Bin							
Individual Bin (%):	56.0	Percent	34.0	Percent	9.0	Percent	1.0	Percent		Percent		Percent		Percent	100.0%							
Sieve Size:	Cum.% Passing	*Wtd* Cum. %	Cum.% Passing	*Wtd* Cum. %	Cum.% Passing	*Wtd* Cum. %	Cum.% Passing	*Wtd* Cum. %	Cum.% Passing	*Wtd* Cum. %	Cum.% Passing	*Wtd* Cum. %	Cum.% Passing	*Wtd* Cum. %	Cum. % Passing	Lower & Upper Specification Limits		Within Spec's	Restricted Zone	Within Spec's	Individual % Retained	Cumulative % Retained	Sieve Size
3/4"	100.0	56.0	100.0	34.0	100.0	9.0	100.0	1.0		0.0		0.0		0.0	100.0	100.0	100.0	Yes			0.0	0.0	3/4"
1/2"	100.0	56.0	100.0	34.0	100.0	9.0	100.0	1.0		0.0		0.0		0.0	100.0	98.0	100.0	Yes			0.0	0.0	1/2"
3/8"	97.5	54.6	100.0	34.0	100.0	9.0	100.0	1.0		0.0		0.0		0.0	98.6	85.0	100.0	Yes			1.4	1.4	3/8"
No. 4	34.5	19.3	98.9	33.6	100.0	9.0	100.0	1.0		0.0		0.0		0.0	62.9	50.0	70.0	Yes			35.7	37.1	No. 4
No. 8	3.9	2.2	70.2	23.9	100.0	9.0	100.0	1.0		0.0		0.0		0.0	36.1	35.0	46.0	Yes			26.8	63.9	No. 8
No. 30	1.7	1.0	13.5	4.6	99.8	9.0	100.0	1.0		0.0		0.0		0.0	15.6	15.0	29.0	Yes			20.5	84.4	No. 30
No. 50	1.1	0.6	6.5	2.2	92.0	8.3	100.0	1.0		0.0		0.0		0.0	12.1	7.0	20.0	Yes			3.5	87.9	No. 50
No. 200	0.6	0.3	2.1	0.7	4.0	0.4	100.0	1.0		0.0		0.0		0.0	2.4	2.0	7.0	Yes			9.7	97.6	No. 200

Not within specifications # Not cumulative

Asphalt Source & Grade:	Fina 64-22	Binder Percent, (%):	4.6	Asphalt Spec. Grav.:	1.025
Antistripping Agent:	Hydrated Lime	Percent, (%):	1		

Mixture Production Properties

The mixture was produced by East Texas Asphalt and a summary of the production data from the project is presented in Table 4.

Table 4. Project Production Data for Lufkin Field Trials.

Mixture Type	AC Content, %	Lab Molded Density, %	In-Place Air Voids, %
PG 64-22 HMA	4.1	95.7	10.1
WMA Rediset	4.2	97.4	NA
WMA Advera	4.5	97.5	11.7
WMA Evotherm	4.3	97.3	10.6
WMA Sasobit	4.3	97.4	11.5

Summary of Mixture Properties

The mixture was produced by East Texas Asphalt and TTI technicians were onsite to sample and mold samples for later testing. Prior to molding, the plant mixes were cured for 2 hr at 250°F for the HMA and 220°F for all of the WMA technologies. The samples were brought back to TTI's laboratory for testing.

Results of the Hamburg Wheel tracking test are presented in Figure 5. For a PG 64-22, the specification limits the rut depth to no more than 1/2 in. at 10,000 cycles but this district does not enforce a Hamburg requirement since their mixes will often not meet the minimum though they have performed well historically. The Sasobit and HMA mix were the only samples passing the Hamburg criteria with this 2 hr oven curing time.

Results of HWTT on field cores are shown in Figure 5. All of the mixtures continued to become more rut-resistant with age. The different WMA mixtures performed similarly to the HMA. The Evotherm and Advera WMA showed better cracking resistance in the overlay test (Figure 6). With increasing age, the cracking resistance dissipated. The Sasobit and Rediset mixes seem to be stiffer than the other mixes as indicated by the indirect tensile strength (Figure 7).

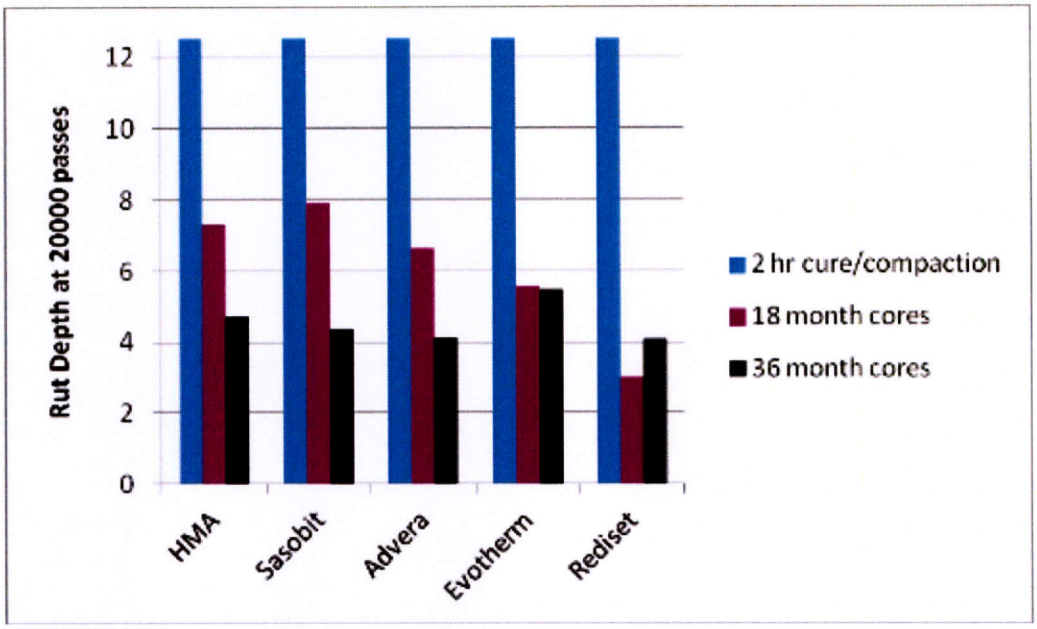

Figure 5. Hamburg Wheel Tracking Test Results for Lab Molded Warm Mix and Hot Mix Compared to Roadway Cores for FM 324.

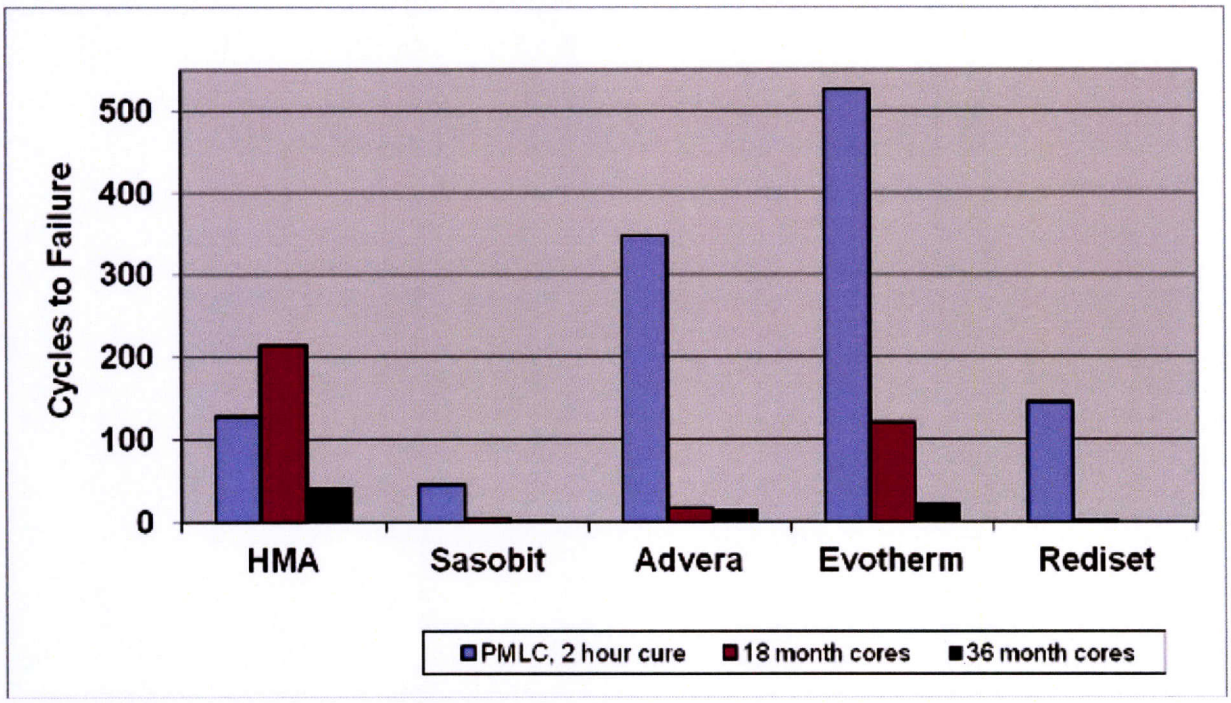

Figure 6. Overlay Test Results for Plant Mix-Lab Compacted HMA and WMA and Roadway Cores for FM 324.

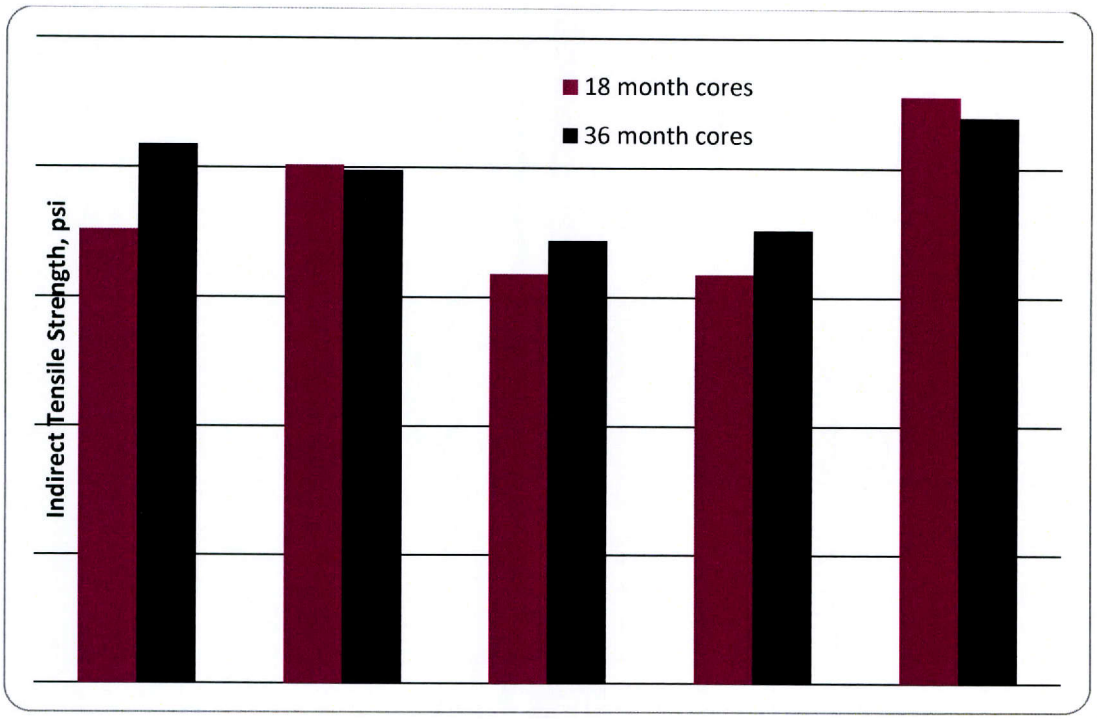

Figure 7. Indirect Tensile Strength Results for HMA and WMA Roadway Coresm FM 324.

Field Performance Evaluation

Field performance of all four of the warm mix asphalt technologies test sections well up until the third year of service. Significant cracking began to appear in 2011 but only in certain sections as shown in Table 5 below.

The district performed Falling Weight Deflectometer (FWD) testing at the time the cores were taken in 2011. A review of the FWD data revealed that the south end of the project (south of the railroad tracks) had significantly higher deflections than the northern portion of the project. This happened to be where the Rediset mix was placed. Observations during coring also revealed this base to be an iron ore gravel type whereas the rest of the project seemed to be a limestone base. Some short sections south of the tracks (in the Advera section) had very low deflections with similar characteristics of stabilized bases. Discussions with the maintenance engineer revealed that previous spot base repair had occurred on this roadway and would explain the low deflections.

While the Rediset mix is somewhat stiffer than some of the other mixes (IDT results), the measured properties of the field cores for all of the mixes are similar and would not explain the alligator cracking seen in Figure 8. This extensive cracking is attributed to the high deflections in the base layer in this portion of the project.

Table 5. Summary of Distress on US 71 WMA and HMA Test Sections.

Location	Transverse Cracking, linear ft			Longitudinal Cracking, linear ft			Alligator Cracking, linear ft of wheelpath		
	2009	2010	2011	2009	2010	2011	2009	2010	2011
SB Lane HMA	0	0	0	0	0	120	0	0	20
SB Lane Sasobit	0	0	0	0	0	0	0	0	20
SB Lane Evotherm	0	0	0	0	0	0	0	0	0
SB Lane Advera	0	0	0	0	0	0	0	0	0
SB Lane Rediset	0	0	0	0	0	230	0	0	160

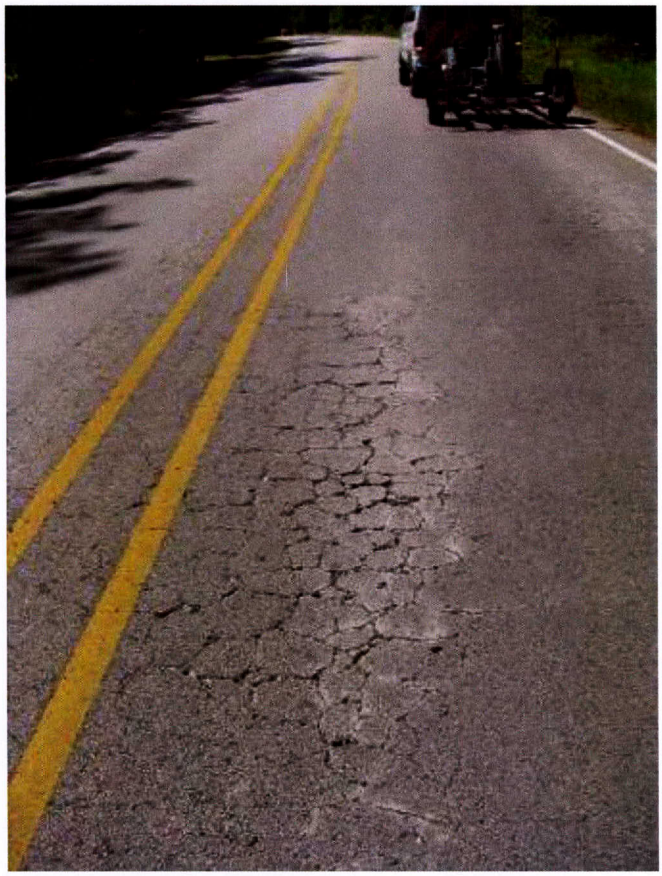

Figure 8. Alligator Cracking at South End of Project.

FM 973

The field project on FM 973 is near the Bergstrom International Airport at Austin, Texas. Limestone aggregate in four different sizes and a natural sand were used. Details of the project are shown in Table 6 and the mixture design report is shown in Table 7. A control HMA and two WMAs with a modified PG 70-22 binder were used and these are designated as Sections 1, 7, and 8 in Figure 9. Additional test sections were constructed using RAP and RAS in different combinations but those sections were not included for evaluation in this research project.

Evotherm DAT™ and a Foaming process were used as WMA technologies in this field project. Evotherm DAT™ has been designed to enhance coating, adhesion, and workability at lower production temperatures. In order to treat the binder with this chemical additive, the binder was heated to the mixing temperature and the additive was blended at 5 percent by weight of binder. Foamed binder was produced on-site by injecting 5 percent water and air into the hot binder inside a special expansion chamber.

Table 6. FM 973 Project Details.

Field Project	FM 973
Construction Dates	28-Nov-11
WMA Technologies	Evotherm DAT, Foaming
Mix Design Information	TxDOT Type C Binder: PG 70-22 Aggregate: Centex Limestone Optimal Binder Content: 5.2%
Production Temperature	HMA: 320°F
	Evotherm: 275°F
	Foaming: 275°F
Placement Temperature	HMA: 275°F
	Evotherm: 240°F
	Foaming: 235°F
Lab Curing (2 hours) at Temperature	HMA: 275°F
	Evotherm: 240°F
	Foaming: 275°F

Table 7. Mix Design Used for the HMA and WMA Sections on FM 973.

HMACP MIXTURE DESIGN : COMBINED GRADATION

Refresh Workbook

File Version: 04/28/11 08:20:35

SAMPLE ID:		SAMPLE DATE:	
LOT NUMBER:		LETTING DATE:	
SAMPLE STATUS:		CONTROLLING CSJ:	
COUNTY:	Jimmy Whited #652	SPEC YEAR:	2004
SAMPLED BY:		SPEC ITEM:	
SAMPLE LOCATION:		SPECIAL PROVISION:	
MATERIAL CODE:	Type C	MIX TYPE:	SS3224_C_Coarse_Surface
MATERIAL NAME:	64SC1500 #4	WMA Included in Design?	No
PRODUCER:	RTI Hot Mix, Ltd.	WMA TECHNOLOGY:	
AREA ENGINEER:		PROJECT MANAGER:	WMA RATE: / UNITS:
COURSE\LIFT: Surface	STATION:	DIST. FROM CL:	CONTRACTOR DESIGN # : 64SC1500 #4

Recycled Binder, %	
Bin No.8 :	0.0
Bin No.9 :	1.0
Bin No.10 :	0.0
Total	***1.0***

Use this value in the QC/QA template>>

Ratio of Recycled to Total Binder, %
(based on binder percent (%) entered below in this worksheet)
19.2

	AGGREGATE BIN FRACTIONS														"RECYCLED MATERIALS"						
	Bin No.1		Bin No.2		Bin No.3		Bin No.4		Bin No.5		Bin No.6		Bin No.7		Bin No.8		Bin No.9		Bin No.10		
Aggregate Source:	Limestone_Dolom		Limestone_Dolom		Limestone_Dolom		Limestone_Dolom		Gravel						Fractionated RAP		RAS				Material Type
Aggregate Pit:	Ruby		Ruby		Ruby		Ruby										Ramming LTD-Buda				Material Source
Aggregate Number:																					RAS Type
Sample ID:	Type C		Type D		Type F		Mfg. Sand		Field Sand												Sample ID
															Recycled Asphalt Binder (%)						
															5.0		20.0				
Hydrated Lime?:															0.0	% of Tot. Mix	5.0	% of Tot. Mix		% of Tot. Mix	
Individual Bin (%):	26.0	Percent	19.0	Percent	21.0	Percent	22.0	Percent	7.8	Percent		Percent		Percent		% of Aggreg	4.2	% of Aggreg		% of Aggreg	
Sieve Size:	Cum.% Passing	*Wtd* Cum. %	Cum.% Passing	*Wtd* Cum. %	Cum.% Passing	*Wtd* Cum. %	Cum.% Passing	*Wtd* Cum. %	Cum.% Passing	*Wtd* Cum. %	Cum.% Passing	*Wtd* Cum. %	Cum.% Passing	*Wtd* Cum. %	Cum.% Passing	*Wtd* Cum. %	Cum.% Passing	*Wtd* Cum. %	Cum.% Passing	*Wtd* Cum. %	

Sieve Size	Combined Gradation: Total Bin 100.0% Cum. % Passing	Lower & Upper Specification Limits: Lower	Upper	Within Spec's	*Restricted Zone: Lower*	*Upper*	*Within Spec's*	Individual % Retained	Cumulative % Retained
1"	100.0	100.0	100.0	Yes				0.0	0.0
3/4"	100.0	95.0	100.0	Yes				0.0	0.0
3/8"	83.1	70.0	85.0	Yes				16.9	16.9
No. 4	55.5	43.0	63.0	Yes				27.6	44.5
No. 8	38.3	32.0	44.0	Yes				17.2	61.7
No. 30	21.4	14.0	28.0	Yes				16.9	78.6
No. 50	15.1	7.0	21.0	Yes				6.3	84.9
No. 200	4.8	2.0	7.0	Yes				10.3	95.2

(Bold Italic) Not within specifications ***(Bold Italic)*** Not within specificaitons- Restricted Zone *(Italic)* Not cumulative

Lift Thickness, in:	2.00	Binder Substitution?	No	Binder Originally Specified:	PG 64-22	Substitute Binder:	PG 64-22 *Substitute binder doesn't comply with spec*
Asphalt Source & Grade:	Valero	Binder Percent, (%):	5.2	Asphalt Spec. Grav.:	1.033		
Antistripping Agent:		Percent, (%):					

FM 973
Between FM 969 and HWY 71

Section No.	Type	Binder	RAP	RAS
1	HMA	70-22	0	0
7	WMA Foaming	70-22	0	0
8	WMA Evotherm	70-22	0	0
9	WMA Evotherm	64-22	15	3
3	HMA	64-22	15	3
4	HMA	64-22	0	5
2	HMA	64-22	30	0
5	HMA	58-28	30	0
6	HMA	58-28	15	3

- Type C mix
- Limestone C, D, F, Mfg. Sand + Field Sand
- Section length ~ 2,040 ft
- Sections 1 & 7: 400 tons
- Sections 2-6, 8, 9: 800 tons

Figure 9. Test Section Layout on FM 973.

Field Sampling and Testing

TTI personnel were onsite during construction to obtain loose and to compact samples under different curing conditions. Cores were taken immediately after construction and then again throughout the project. The results of the laboratory testing are presented in subsequent chapters.

Field Performance

At 14 months of service, the pavement sections were beginning to exhibit the types of distress shown in Figure 10. This distress is summarized in Table 8. No significant difference is noted between the HMA and WMA sections at this time.

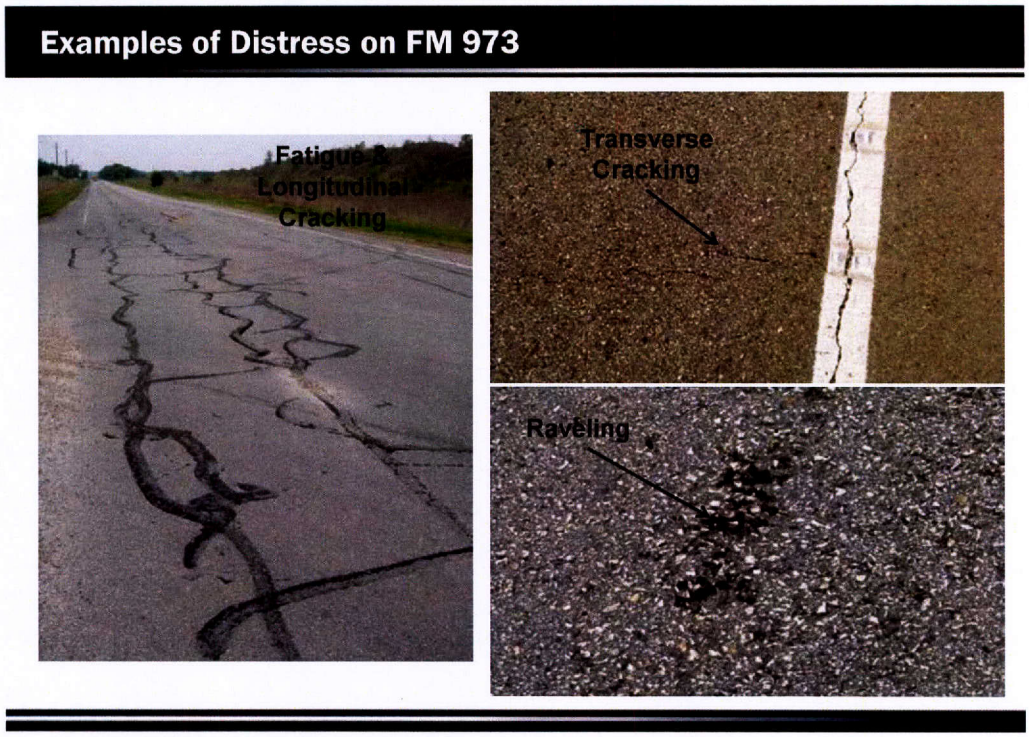

Figure 10. Types of Distress Being Exhibited on FM 973.

Table 8. Summary of Pavement Performance Distress on FM 973.

FM 973 Performance (14 Months) – WMA Sections

Section	Binder	RAP	RAS	Distress				
				Long WP (LF)	Fat. Crk.	Long N-WP (LF)	Trans. Crk	Raveling Index
1	70-22 (Control)	0	0	10	0	25	0	3.0
7	70-22 WMA Foaming	0	0	25	0	20	0	3.5
8	70-22 WMA Additive	0	0	30	0	25	0	4.0

CHAPTER 3. MEASURE WARM MIX BINDER OXIDATION AND HARDENING KINETICS

ABSTRACT

In order to evaluate the fundamentals of WMA binder oxidation in pavements and its impact on WMA pavement durability, oxidation and hardening kinetics need to be measured. Fundamental understanding of binder oxidation in WMA binders that is necessary for predicting binder oxidation in WMA pavements is determined. Activation energies and pre-exponential coefficients for base binder with/without WMA additives are determined.

At controlled temperature and pressure, initial asphalt oxidization occurs at a fast but decreasing rate as it transitions to a slower constant-rate period. The importance of fast-rate kinetics has been proved by both laboratory and field data (Jin et al., 2013). Therefore, both fast-rate and constant-rate kinetics are obtained in this study. This document is a report that addresses the aging experiment and determination of warm mix binder oxidation and hardening kinetics.

OBJECTIVE

In order to evaluate the effect of WMA technologies on asphalt binder oxidation kinetics, carbonyl area indicating the oxidation level would be tested continuously to estimate the reaction rate of asphalt binder with or without additives. Also, by calculating the chemical reaction rate at different temperatures and applying the Arrhenius equation, oxidation kinetics parameters (activation energy and pre-exponential factors) for the fast rate period and the constant rate period could be estimated.

MATERIALS AND METHODS

Valero PG70-22 binders used in FM973 pavements were selected for the oxidation kinetics study, including base binder and binder with WMA additives. Sample were prepared in aluminum trays, 2.4±0.05 g binders in each tray, and the thickness of the binder layer was 0.8 mm. These trays were put into Pressure Oxidation Vessels (POVs), where certain temperatures were maintained. After oxidation, these trays were taken out and tested under Fourier transform infrared spectroscopy (FTIR) machine and Dynamic Shear Rate (DSR) machine.

Two analytical techniques were used to characterize the unaged and aged binders. Infrared spectroscopy was used to measure the carbonyl area and a Carri-Med CSL 500 controlled stress rheometer was used to measure both the low shear rate limiting viscosity and the DSR function. The low shear rate limiting viscosity is obtained from a frequency sweep at 60°C from 0.1 rad/s to 100 rad/s. The DSR function is measured at 44.7°C and 10 rad/s then time-temperature shifted to 15°C, 0.005 rad/s (Ruan et al., 2003).

Valero PG70-22 base binder, Valero PG70-22 binder with Evotherm additive, and foamed Valero PG70-22 were tested using Pressure Oxygen Vessel. Figure 11 shows the timelines and temperatures.

Binder	Aging Time (Day)			
	140°F	163°F	186°F	208°F
Valero PG70-22 with Evotherm	2, 5, 10, 20, 35, 55	1, 3, 5, 8, 15, 30, 50	1, 2, 4, 6, 10, 20, 30	1, 2, 4, 6, 10, 20
Valero PG70-22	2, 5, 10, 20, 35, 55	1, 3, 5, 8, 15, 30, 50	1, 2, 4, 6, 10, 20, 30	1, 2, 4, 6, 10, 20
Valero PG70-22 Foamed	2, 5, 10, 20, 30, 45, 62, 91	1, 2, 3, 5, 7, 10, 15, 20, 30, 40, 55	1, 2, 3, 5, 6, 7, 10,15, 20, 30, 40, 55	1, 2, 4, 6, 10, 15, 20, 25, 30

Figure 11. Sampling Times for Asphalt at Different Aging Temperature.

RESULTS AND DISCUSSION

Analysis of Carbonyl Area Data

Carbonyl area (CA), low shear rate limiting viscosity and DSR function were measured. Figure 12 shows the CA growth with time at four aging temperatures asphalt binder (foamed Valero not shown).

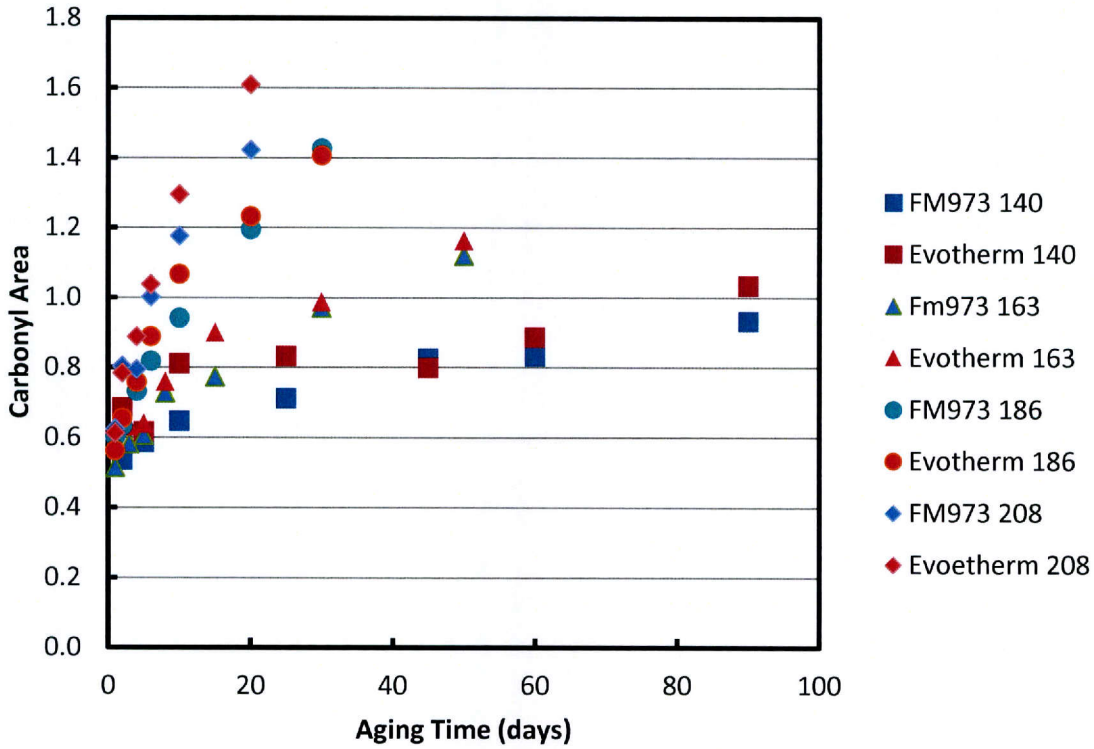

Figure 12. CA Growth of Valero PG70-22 with/without Evotherm Additives at Five Temperatures in Air.

The carbonyl area formation with time at each temperature is modeled according to the following equations:

$$CA = CA_{tank} + M\left(1 - e^{-k_f t}\right) + k_c t \tag{3-1}$$

$$k_f = A_f e^{-\frac{E_{af}}{RT}} \tag{3-2}$$

$$k_c = A_c e^{-\frac{E_{ac}}{RT}} \tag{3-3}$$

where $M = (CA_0 - CA_{tank})$, CA_{tank} is the carbonyl area of the unaged tank asphalt, CA_0 is the intercept of the constant-rate line, k_f and k_c are two reaction constants that are temperature dependent according to the Arrhenius equation. Using the current model (Jin et al., 2011), oxidation kinetic parameters A_f, E_{af}, A_c and E_{ac} were determined and showed below.

Table 9. Calculation of Oxidation Kinetic Parameters.

Binder	CA_{tank}	A_f (1/Day)	E_{af} (kJ/mol)	A_c (CA/Day)	E_{ac} (kJ/mol)
Valero PG 70-22 with Evotherm	0.583	1.19×10^7	51.4	6.47×10^8	72.1
Valero PG 70-22 without Evotherm	0.559	3.45×10^6	49.8	4.49×10^7	64.1
Valero PG 70-22 foamed	0.574	2.45×10^6	47.1	8.22×10^7	65.8

Correlation between Oxidation Kinetic Parameters

Jin et al. (2011) reported that the two activation energies for asphalts plotted against each other reveal a good linearity. This correlation is further validated on binder with WMA additives.

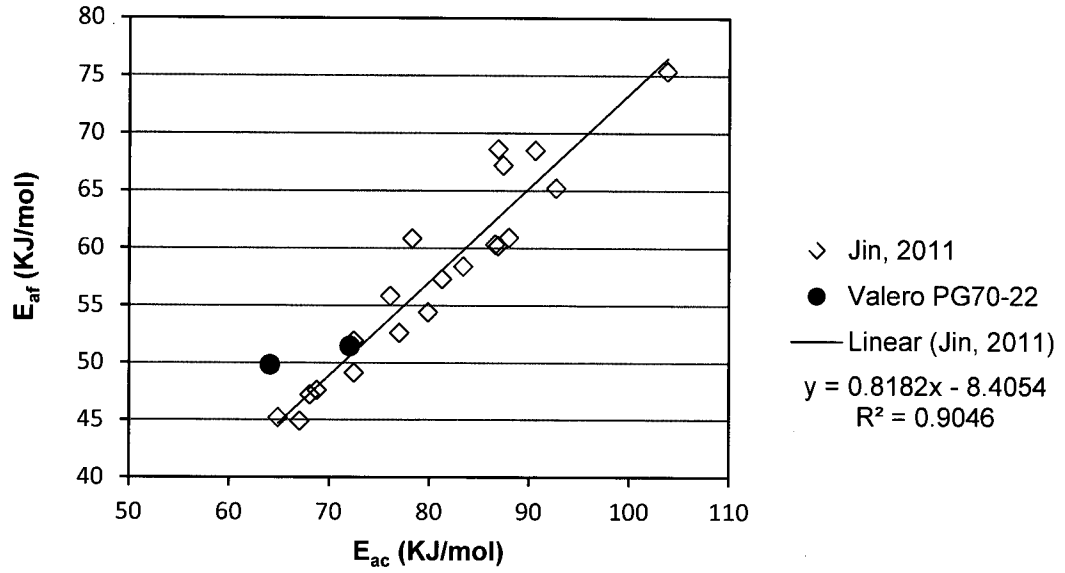

Figure 13. Empirical Linear Correlation between the Fast-Rate and Constant-Rate Activation Energies.

Linear correlation between rate activation energies and logarithmic frequency factors were also consistent with reported data (Jin et al., 2011; Domke et al., 2000; Liu et al., 1996). Figure 14 and Figure 15 show that Evotherm additive does not change the fundamental correlations between oxidation kinetic parameters in asphalt binders.

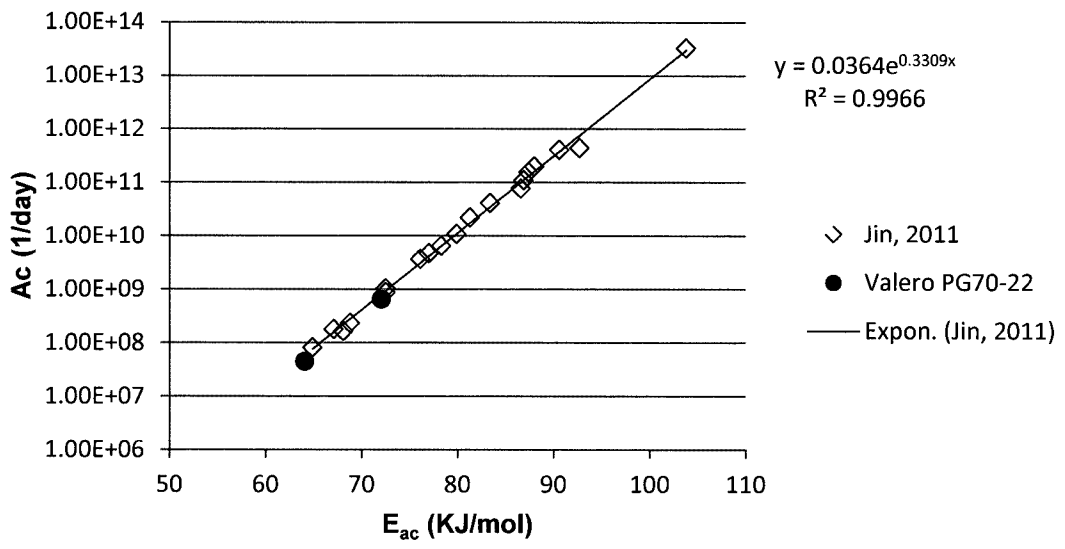

Figure 14. The Correlation between Constant-Rate Kinetics Parameters.

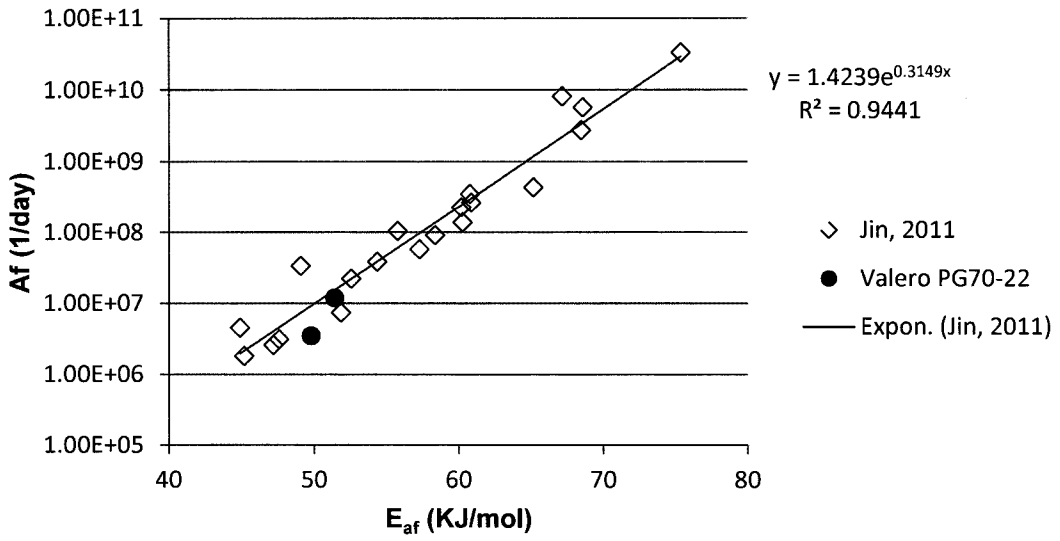

Figure 15. The Correlation between Fast-Rate Kinetics Parameters.

Analysis of Rheological Data

Hardening susceptibilities (HS) of low shear rate limiting viscosity and DSR function are shown in Figure 16, Figure 17, Figure 18, Figure 19, Figure 20, and Figure 21, in semi-log scale.

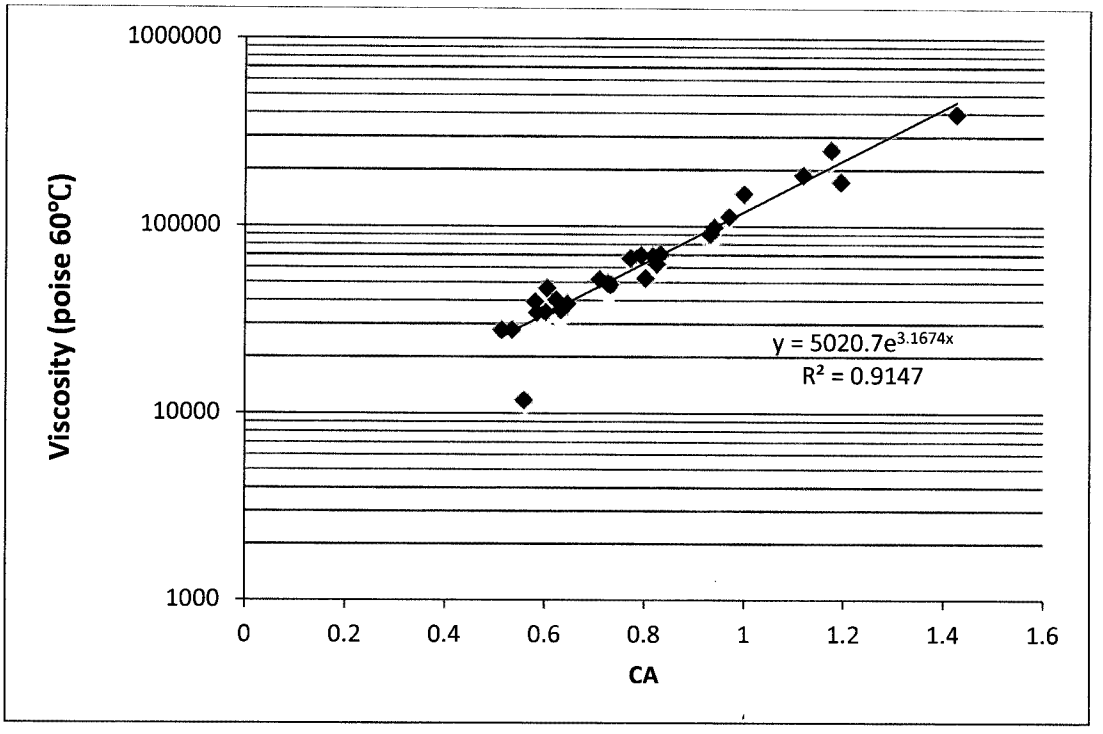

Figure 16. HS of Limiting Viscosity of Valero PG70-22.

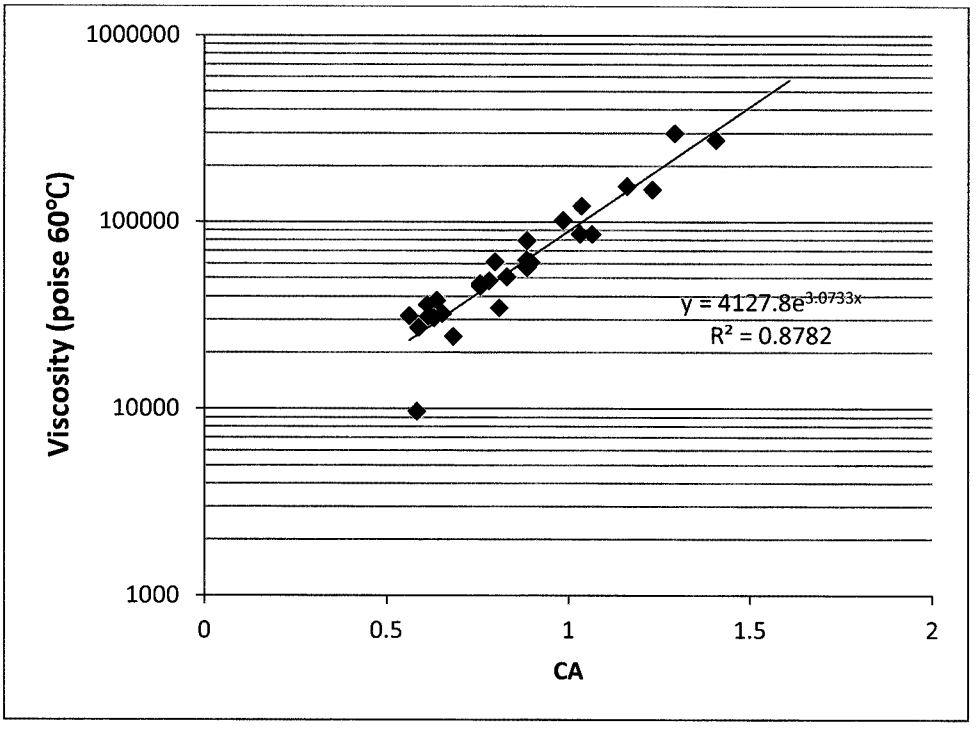

Figure 17. HS of Limiting Viscosity of Valero PG70-22 with Evotherm Additives.

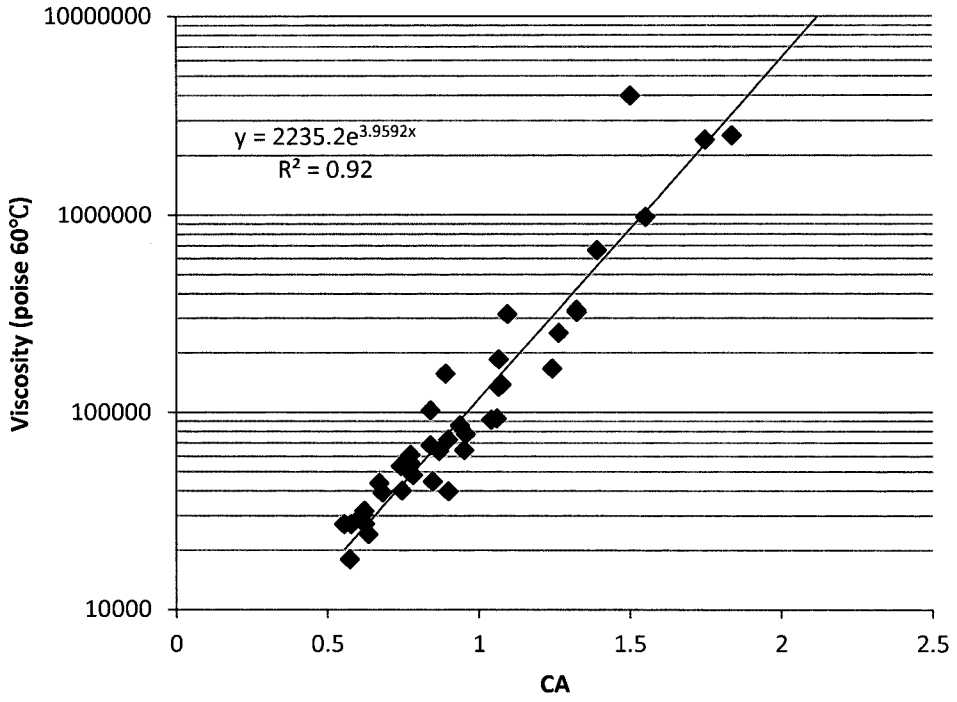

Figure 18. HS of Limiting Viscosity of Foamed Valero PG70-22.

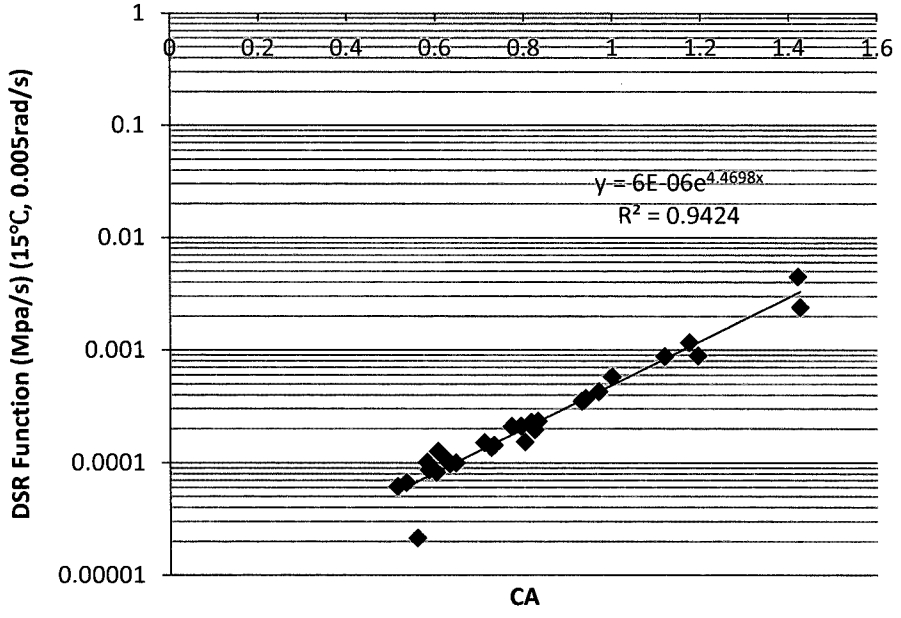

Figure 19. HS of DSR Function of Valero PG70-22.

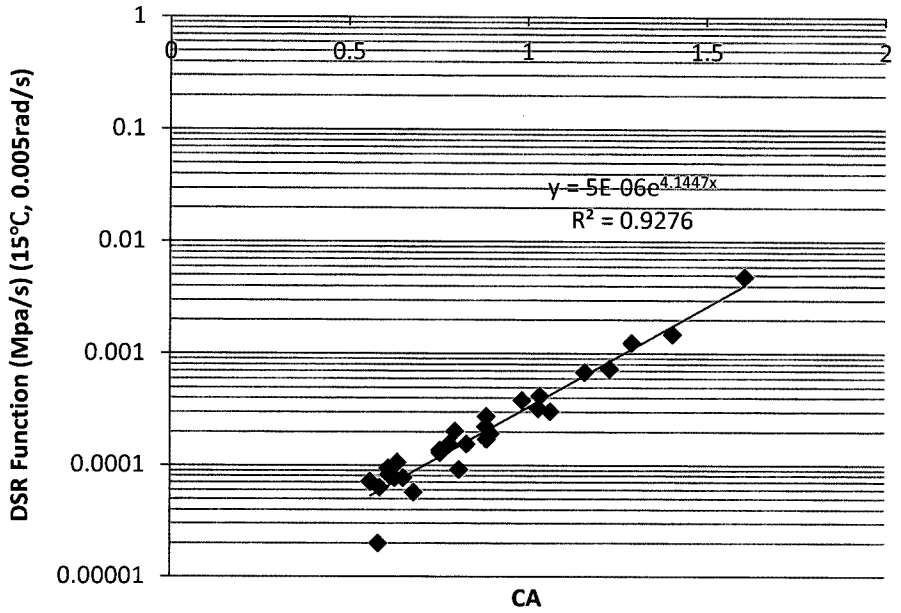

Figure 20. HS of DSR Function of Valero PG70-22 with Evotherm Additives.

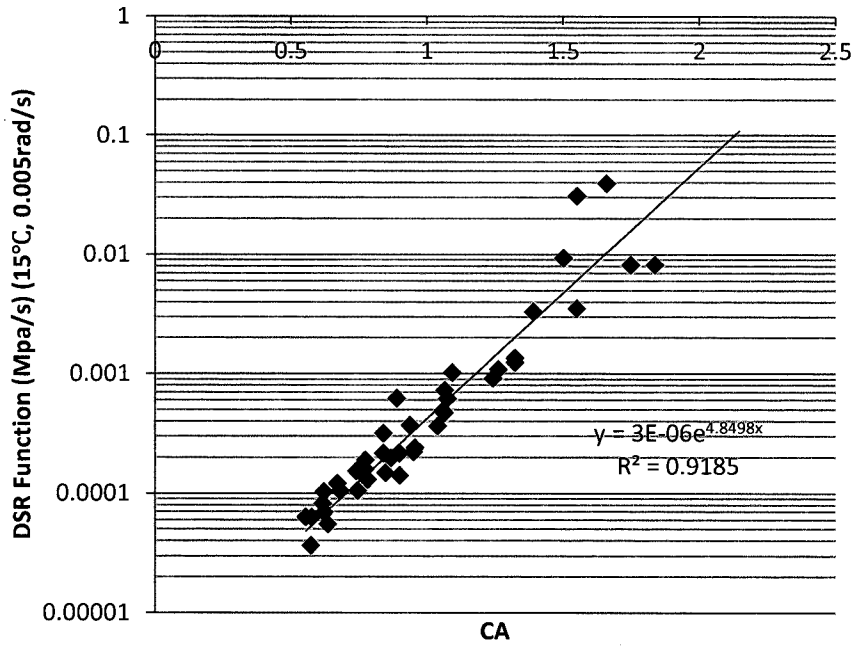

Figure 21. HS of DSR Function of Foamed Valero PG70-22.

CONCLUSIONS

Valero PG70-22 neat, Evotherm modified, and foamed binders have been aged in POV apparatuses from which kinetics data were obtained. Model parameters were obtained from global optimization using the method of Jin et al. (2011).

All three binders have similar reaction kinetics parameters although the Evotherm binder shows slightly higher activation energies, both in fast-rate period and constant period. Also, empirical correlations were found between model parameters. Correlation between E_{ac} and E_{af} are verified in Valero PG70-22 binder, which is consistent with former data (Jin, 2011). This result indicates that WMA additives do not change the fundamental correlations between oxidation parameters.

Rheological data confirmed that hardening susceptibilities also exist in binder with WMA additives. With oxidative reaction kinetics parameters and hardening susceptibility, it is possible to predict WMA binder oxidation and hardening as a function of time and temperature. This capability is important for pavement oxidation models to predicting WMA pavement performance.

CHAPTER 4. ESTIMATE WMA BINDER OXIDATIVE AGING BY A TRANSPORT MODEL

ABSTRACT

Aging of binder in the field with and without warm mix additive is simulated. The simulation is performed using an aging modeled developed in TxDOT project 0-6009 (Glover et al., 2013). Earlier in this report (Measure Warm Mix Binder Oxidation And Hardening Kinetics), reaction kinetics parameters for both unmodified binder and binder with warm mix additive were reported. Likewise, rheological properties were reported. These reaction kinetics parameters and rheological properties are used in the aging model, along with a site specific temperature profile, to simulate 10 years of aging in the field.

INTRODUCTION

Binder field aging of both unmodified Valero PG 70-22 binder and the same binder with Evotherm additive is simulated using an aging model developed in TxDOT project 0-6009 (Glover et al., 2013). Aging is measured in terms of asphalt carbonyl ("CA") content and asphalt DSR function. The model is described in detail in chapter 9 of the 6009 report, and considers both fast-rate and constant-rate kinetics (Jin et al., 2011). The binders simulated were each used in the construction of at least one section of FM973 (located near Austin, TX). A pavement temperature profile based on the Austin location was created for use with the aging model (Han et al. 2011). Two binders are compared: Valero PG 70-22 and Valero PG 70-22 with Evotherm additive. To give additional insight into the aging phenomena two pavement depths have also been selected: 0.5 and 1.5 inches.

MODEL BACKGROUND AND PARAMETER DETERMINATION

The aging model is based on oxygen transport, and oxygen/asphalt reaction kinetics. As such, a distinct set of model input parameters are required to simulate field aging. The parameters include asphalt binder parameters, a site specific temperature profile, and mixture parameters.

The binder parameters required include reaction kinetics parameters, rheological properties, and initial aging state. The reaction kinetics parameters (except M_{RTFOT}) are those described earlier in this report and are taken directly from that work. A value of 0.15 was selected as a reasonable value for M_{RTFOT}. The rheological properties required include: viscosity hardening susceptibility, DSR function hardening susceptibility, and the DSR function zero-CA intercept. Like the reaction kinetics parameters, these parameters were taken directly from the work presented in the chapter: *Measure Warm Mix Binder Oxidation And Hardening Kinetics*. The CA_{tank} value could be used as an estimate of the initial aging state, but in this work that estimate was improved. The estimate was improved by multiplying the CA_{tank} value by a factor of 1.2. The factor of 1.2 was determined by comparing CA values for several binders (not specifically listed here) before and after RTFOT. The development of this factor is closely related to the rule of thumb that the viscosity (in units of Poise) doubles when unaged asphalt is subjected to RTFOT.

A pavement temperature profile based on climatic data for Austin, TX, was developed specifically for the binder aging simulations performed. In addition to being site specific, the temperature profile accounts for temperature variations due to depth below the pavement surface and due to time of year. The details of the pavement temperature model used are fully described in Chapter 6 of TxDOT report 0-6009 (Glover, 2013). The year 2005 was selected as a representative year for climatic inputs (i.e., hourly air temperature, solar radiation, and wind speed, in addition to pavement albedo, the emission coefficient, and the absorption coefficient). The simulated pavement temperature for a single year (here 2005) was repeated 10 times to provide an estimated 10-year-pavement-temperature profile.

Representative mixture parameters were chosen for this aging simulation. In particular, a diffusion depth of 1 mm and a field calibration factor of 5 were selected.

RESULTS AND DISCUSSION

The model described above was implemented using MATLAB® software to produce the results that are shown and described below. Figure 22 shows the simulated increase in binder CA content over a 10 year period in the field. The results are shown for unmodified Valero PG 70-22 and the same binder with Evotherm additive. Additionally, for both binders, two representative pavement depths (0.5 inches and 1.5 inches) are shown. A summary box showing CA levels at 5 and 10 years of aging, along with total CA increase, is also provided.

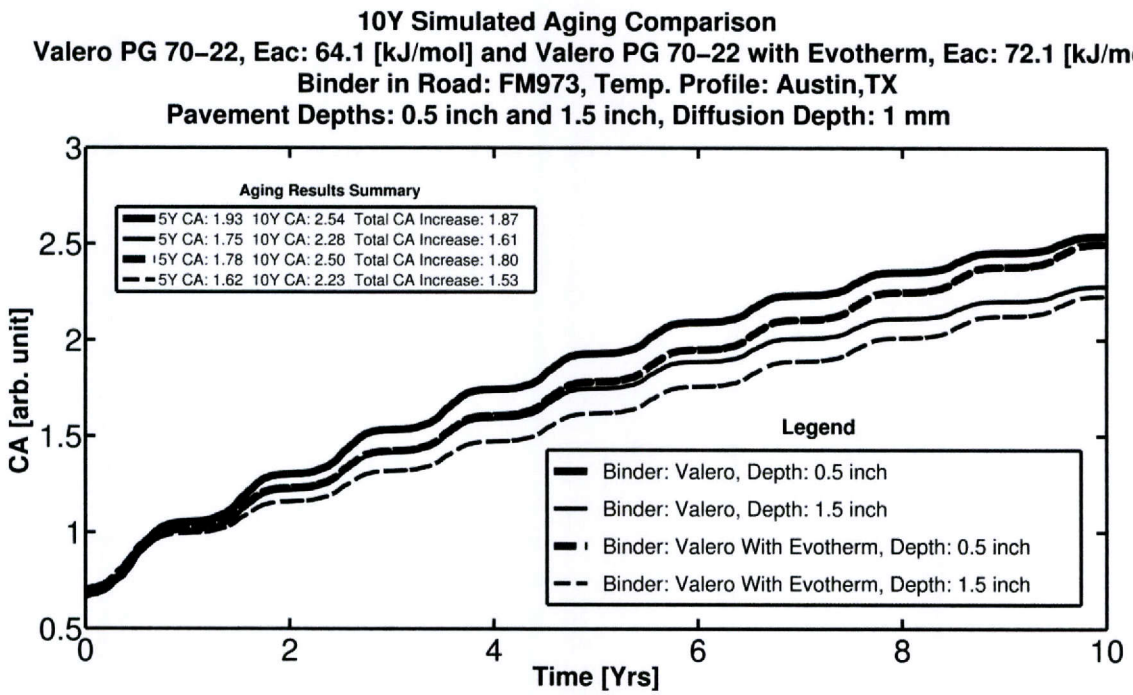

Figure 22. Comparison of the Increase in Binder Carbonyl Content with Time for Both Valero PG 70-22 Binder and Valero PG 70-22 Binder with Evotherm Additive.

Examining Figure 22, the unmodified Valero binder had a somewhat greater increase in CA content than the Evotherm-modified binder. The binders have nearly equal initial viscosities,

hardening susceptibilities, and initial CA levels. Therefore, the greater CA increase in the unmodified Valero binder can be attributed to its slightly lower activation energy (64.1 kJ/mol compared with 72.06 kJ/mol for the Evotherm-modified binder). Although the unmodified Valero binder showed a greater increase in CA content, the difference is modest, and reflects the fact that the Evotherm-modified binder remains kinetically and rheologically similar to the unmodified binder.

Comparing the two pavement depths (0.5 inch and 1.5 inch), for either binder, the CA level increased more quickly at the 0.5 inch depth than at the 1.5 inch depth. The greater increase in binder CA content near the pavement surface results from higher pavement temperatures near the pavement surface.

Figure 23, below, shows the simulated increase in binder DSR function with time over a 10 year period in the field. As in Figure 22, the results are shown for unmodified Valero PG 70-22 and the same binder with Evotherm additive. For both binders, two representative pavement depths (0.5 inches and 1.5 inches) are shown. A summary box showing DSR function levels at 5 and 10 years of aging, along with total DSR function increase, is provided.

DSR function values can be determined using binder CA content, the DSR function hardening susceptibility, and the DSR function zero-CA intercept. The DSR function can be correlated with pavement ductility and, therefore, pavement failure.

The results displayed in Figure 23 reflect the fact that the natural logarithm of the DSR function is linearly related to the CA content of the binder. For this reason the trends in Figure 23 are analogous to the trends in Figure 22. The unmodified Valero binder shows a greater increase in DSR function than the Evotherm-modified binder, and both binders show greater increases in DSR function at the 0.5 inch pavement depth than at the 1.5 inch pavement depth. As with CA content, although the unmodified binder has a greater DSR function increase than the modified binder, the difference is modest.

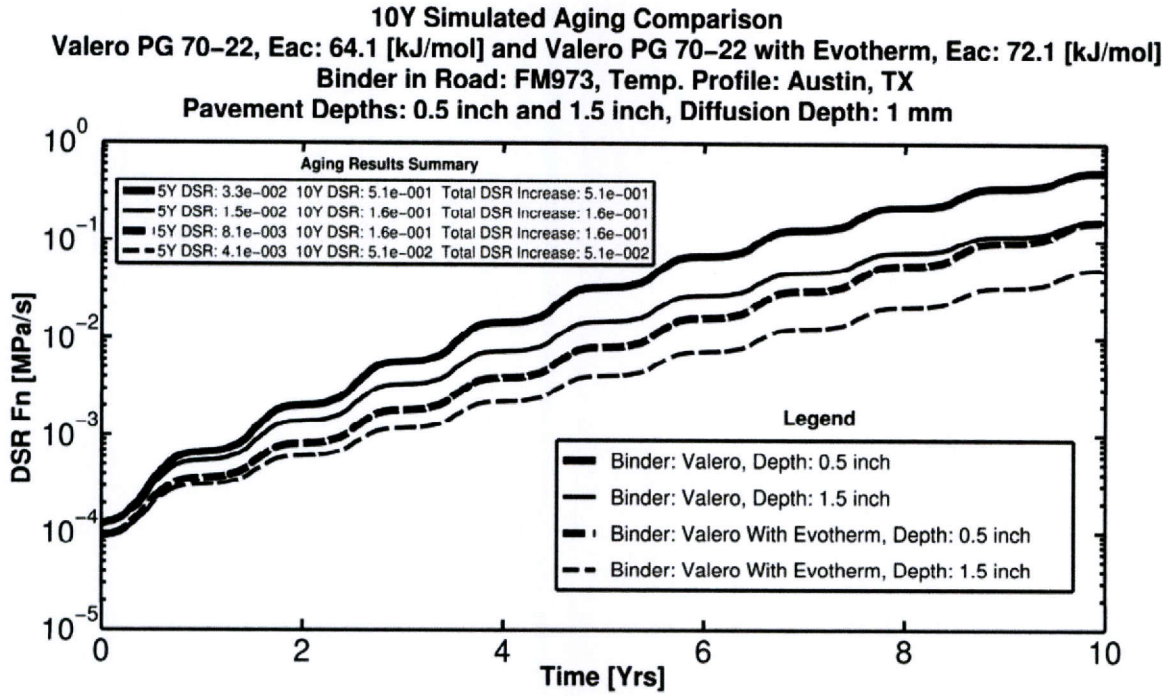

Figure 23. Comparison of the Increase in DSR Function with Time for Both Valero PG 70-22 Binder and Valero PG 70-22 Binder with Evotherm Additive.

CONCLUSIONS

A TxDOT project 6009 pavement aging model was used to simulate field aging of unmodified Valero PG 70-22 binder and Valero PG 70-22 binder modified with an Evotherm additive. Binder reaction kinetics parameters and rheological parameters were taken directly from the results of the earlier chapter: *Measure Warm Mix Binder Oxidation And Hardening Kinetics*. A site specific pavement temperature profile for Austin, TX was developed to estimate the pavement temperature as a function of depth and time of year. Representative mixture parameters were used.

The unmodified Valero binder displayed slightly greater aging, in terms of both binder CA content and DSR function. A review of the binder properties indicates that this difference is primarily due to the slightly lower activation energy of the unmodified binder. Despite this slight difference, overall the modified and unmodified binders have similar aging properties and aging differences are modest.

CHAPTER 5. CHARACTERIZATION OF LAB MIXED LAB COMPACTED (LMLC) WARM MIX SPECIMENS AND RECOVERED BINDERS

MIXTURE STIFFNESS EVALUATION (RESILIENT MODULUS)

The "Schmidt" Resilient Modulus Device (ASTM D 4123) shown in Figure 24 is a simple, quick, nondestructive test for determining the modulus of field cores and laboratory compacted specimens. This test will be particularly useful for the laboratory aging portion of the study since the test is nondestructive and the same specimens may be tested throughout the aging process to determine measure their change in stiffness. The test may be performed at different temperatures and at one or more loading frequencies, 0.33, 0.5, and 1.0 Hz.

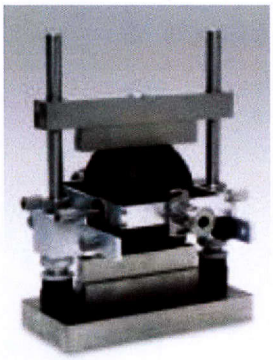

Figure 24. Schmidt Device for Measuring Resilient Modulus (ASTM D 4123).

Figure 25 presents the MR stiffness for LMLC specimens aged at 140°F (60°C) over a series of periods for the Texas FM 973 field projects. Each bar represents the average value of three replicate specimens, and the error bars represent ± one standard deviation from the average value.

Figure 25 indicates that the stiffness of HMA and WMA LMLC specimens increased significantly with aging in the laboratory at 140°F (60°C). As illustrated, the slopes of the curves, referring to the rate of change in mixture stiffness over the same period, were similar for HMA and WMA mixtures. In addition, for both HMA and WMA mixtures the change in MR stiffness during the first week of laboratory aging was higher than the change in stiffness recorded afterwards.

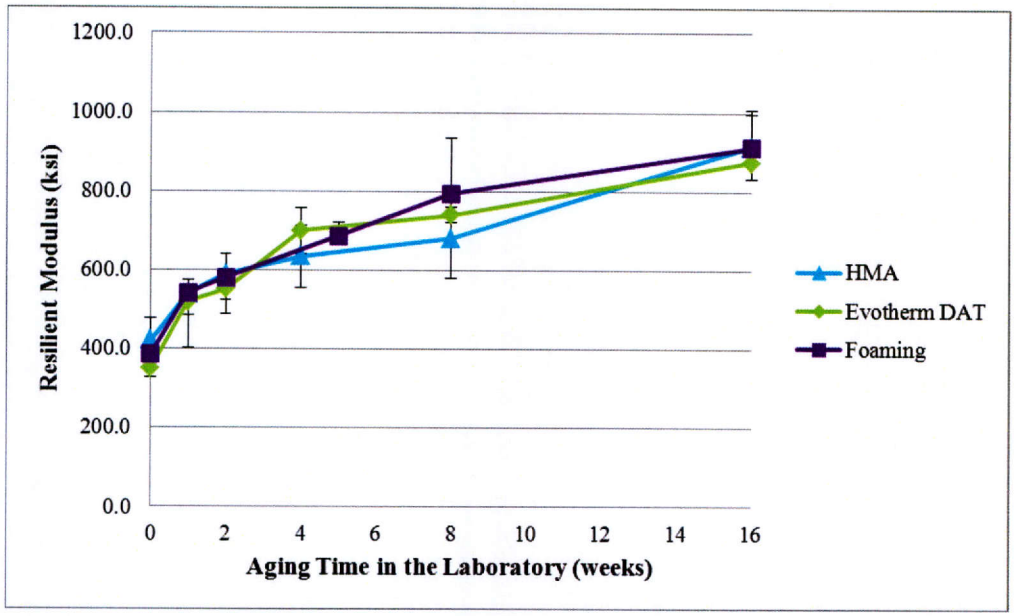

Figure 25. Evolution of MR Stiffness with Laboratory Aging for the Texas Field Project.

Figure 26 presents the MR stiffness of Plant Mixed-Field Compacted (PMFC) cores and LMLC specimens with different aging times in the field and laboratory for the Texas field pavements, respectively. In each graph, the specimen types are arranged from lowest to highest stiffness from left to right. Each bar in Figure 25 represents the average value of three replicate specimens, and the error bars represent ± one standard deviation from the average value.

To explore the differences between mixture stiffness in the field and laboratory, a statistical analysis was completed to account for the variability in the MR stiffness. Analysis of Variance (ANOVA) and Tukey-Kramer Honestly Significant Difference (Tukey's HSD) tests were conducted with a 5 percent significance level (i.e., alpha = 0.05) to verify the difference in MR stiffness between LMLC specimens with and without Long-Term Oven Aged (LTOA) protocols versus PMFC cores with different in-service times. The general results of Tukey's HSD test on different aging stages are shown in Figure 26 with capital letters above the MR stiffness bars. The MR stiffness decreases as letters change from A to F. Different letters indicate MR stiffness that are significantly different from each other.

Comparison of MR stiffness for the PMFC cores and LMLC specimens from the Texas field project (Figure 26) showed that for HMA, similar stiffness was exhibited between PMFC cores at construction and LMLC specimens with aging protocols of 0 (i.e., no LTOA) to 4 weeks at 140°F (60°C) in the laboratory. Laboratory aging for 8 weeks and 16 weeks were able to simulate the field aging after summer at 8 months in-service in Texas. For MR stiffness of Texas WMA Evotherm DATTM, the laboratory aging protocols of 0 weeks and 4 to 8 weeks at 140°F (60°C) were representative of the field aging at construction and after summer at 8 months in the service, respectively. Similar results were shown by MR stiffness of Texas WMA Foaming, with a slight difference that a statistically equivalent stiffness was attained between PMFC cores at construction and LMLC specimens with up to 2 weeks of laboratory LTOA at 140°F (60°C).

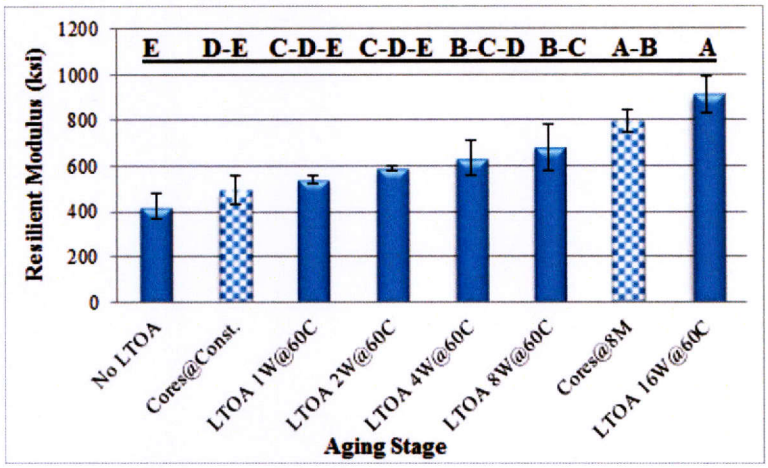

(a) HMA

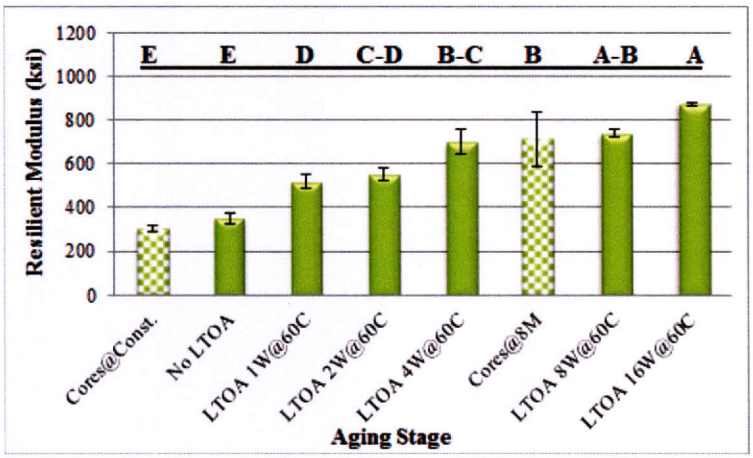

(b) Evotherm DAT

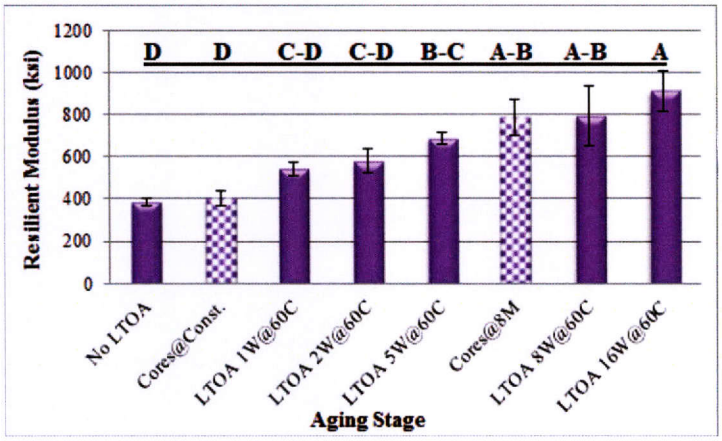

(c) Foaming

Figure 26. MR Results of PMFC Cores and LMLC Specimens with Different Aging for the Texas Field Project.

RUTTING AND MOISTURE SUSCEPTIBILITY TESTING (HAMBURG WHEEL TRACKING) TRA

The Hamburg Wheel Tracking Test (HWTT) is a laboratory test that utilizes repetitive loading in the presence of water, and measures combined mixture resistance to stripping and rutting. Two sets of Superpave Gyratory Compacted (SGC) specimens are submerged in warm water at 122°F (50°C) and subjected to 52 passes of a steel wheel per minute. Each set of the specimens is loaded for a maximum of 20,000 load cycles or until 0.5in (12.5mm) of deformation occurs.

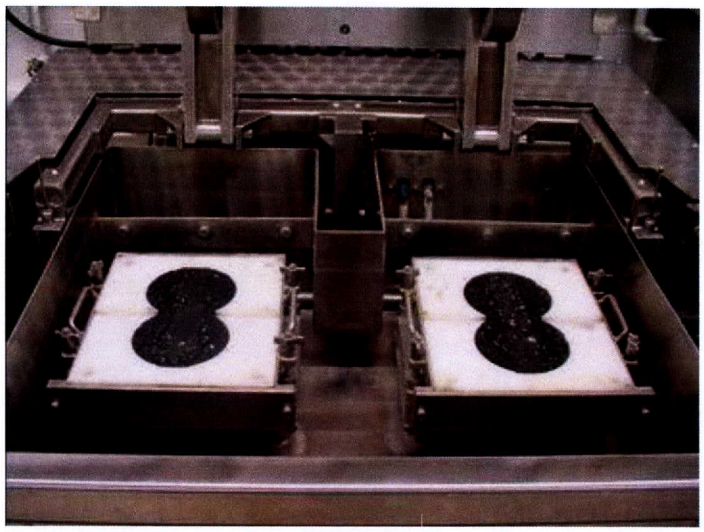

Figure 27. HWTT Machine with Cylindrical SGC Specimens.

A novel methodology to analyze HWTT test results is provided in this study, and three test parameters are proposed, which are able to accurately evaluate the mixture resistance to both stripping and rutting. As with the monotonic loading criterion, it is desirable to develop single numbers that are derived from the test data themselves without subjective interpretation that will allow a direct comparison between mixtures with different exposure and conditioning histories. It is also desirable, if possible, to propose single numbers that combine the results of more than one test on the same mixture. The HWTT is the only test that was conducted with multiple load applications so it has posed a problem in finding a repeated loading performance number that combines the results of more than this one test. The critical point in the HWTT is where the curvature of the curve of permanent strain versus load cycles changes from negative to positive, i.e., at the mathematical point of inflection. A number of measurements are proposed in the following that compare the performance of the mixture prior to the "Stripping Number" as this point of inflection is termed and the subsequent resistance to stripping of the same mixture after stripping has begun.

Two separate forms of performance curve are used in developing these repeated loading performance numbers. One of these is the power law form that fits the rut depth versus load cycles curve prior to the Load Cycles at the Stripping Number. The second is the three parameter model that is used in the Mechanistic Empirical Pavement Design Guide (MEPDG) to model the three phases of rutting, including the third phase in which the rutting accelerates

beyond the "Flow Point" (NCHRP 1-37A, 2002). The point of inflection that is determined with this three parameter curve and is named the "Stripping Number" is the equivalent in the HWTT to the Flow Point in rut depth predictions. One of the advantages of using the three parameter model is that it determines a maximum number of load cycles that the mixture will not be able to exceed. The difference between this asymptote value and the Stripping Number is the Remaining Life of the mixture which is a measure of the ability of the mixture to resist stripping once stripping has begun. A number of performance measures are proposed which make use of the data from these two curves and from the IDT Test under wet conditions. All of these numbers have physical significance and are taken directly from the curves themselves without any subjective interpretation. In this regard, we have allowed the curves to "speak for themselves."

Results

HWTT test results of several Texas mixtures are analyzed in this study with the proposed analysis methodology. The plots of rut depth versus load cycles are presented in Figure 28, for each mixture type.

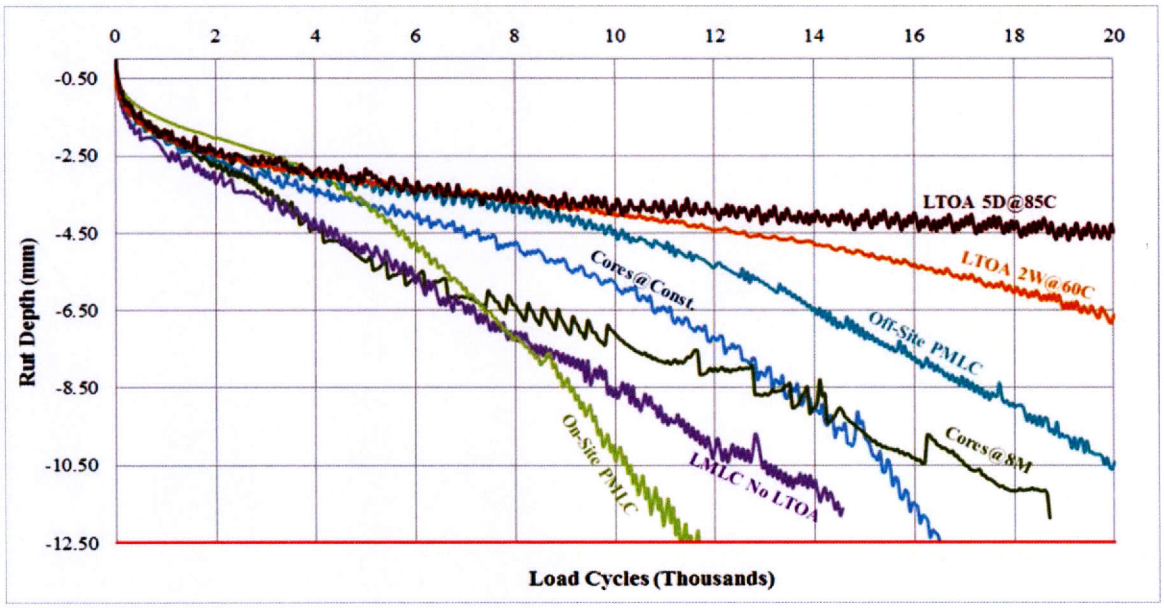

(a)HMA

Figure 28. HWTT Load Cycles versus Rut Depth by Mixture Type for the Texas Mixtures.

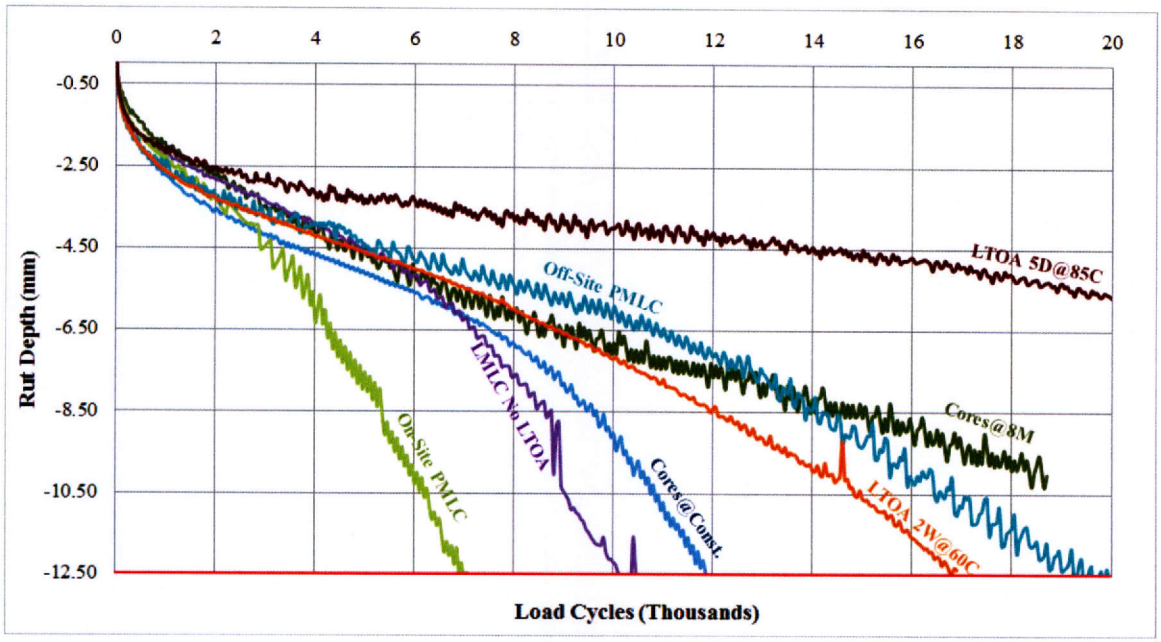

(b)Evotherm DAT™

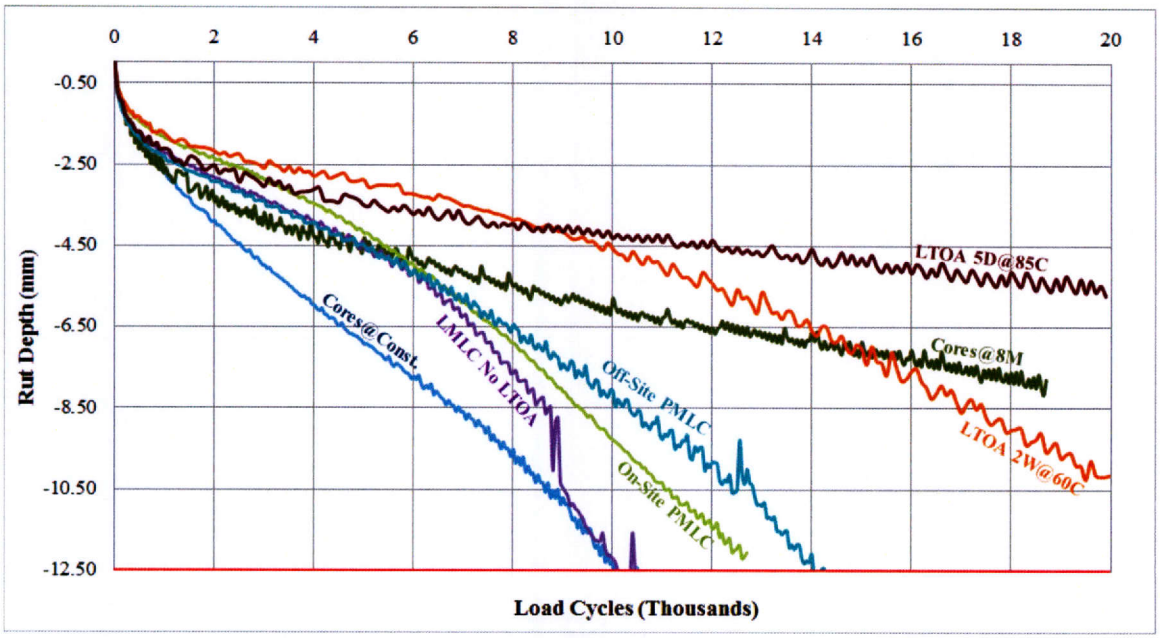

(c)Foaming

Figure 28. HWTT Load Cycles versus Rut Depth by Micture Type for the Texas Mixtures (cont'd.).

Test parameters of the number of load cycles at the stripping number (LC_{SN}) and the remaining life load cycles (LC_R) of Texas mixtures are summarized in Figure 29 and Figure 30, respectively.

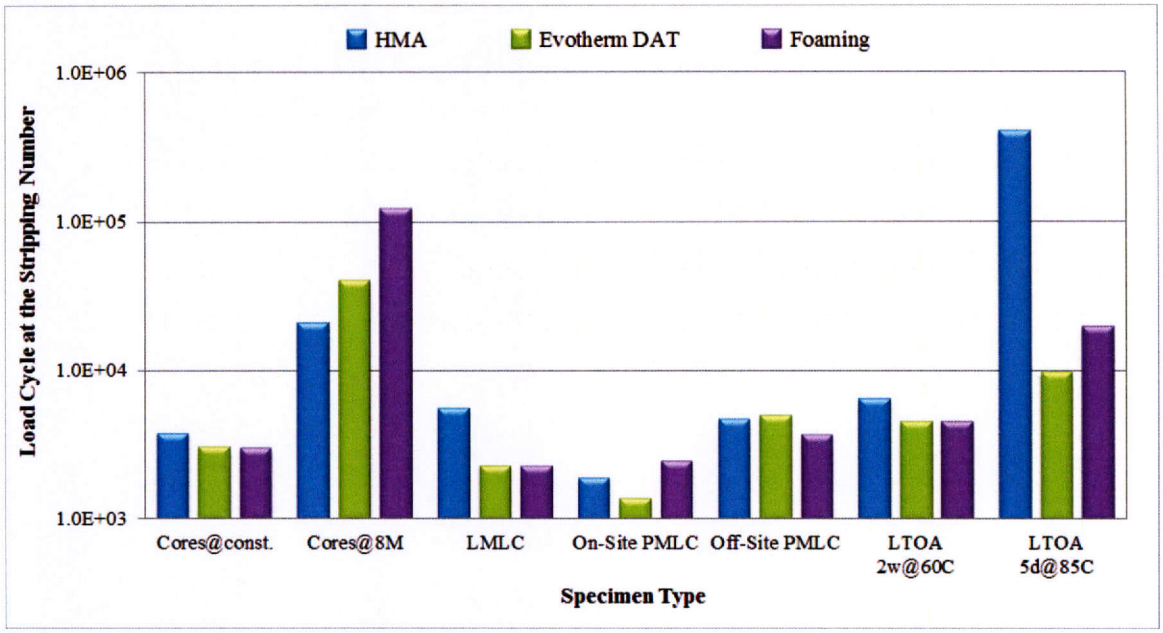

Figure 29. HWTT Test Parameter of LC_{SN} for Texas Mixtures (log scale).

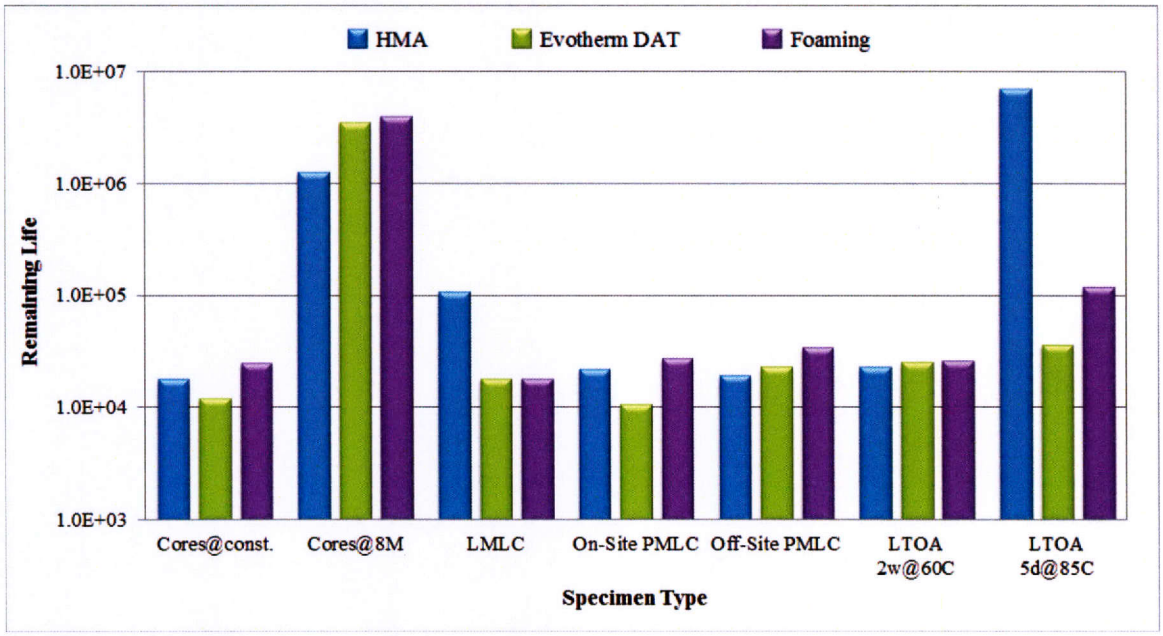

Figure 30. HWTT Test Parameter of Remaining Life for Texas Mixtures (log scale).

Figure 31 summarizes the rutting susceptibility parameters of $\overline{\Delta\varepsilon_p}$ of Texas mixtures. This is the mean slope of the curve of rut depth versus load cycles prior to the stripping number. This indicates the resistance of the mixture to rutting under wet conditions.

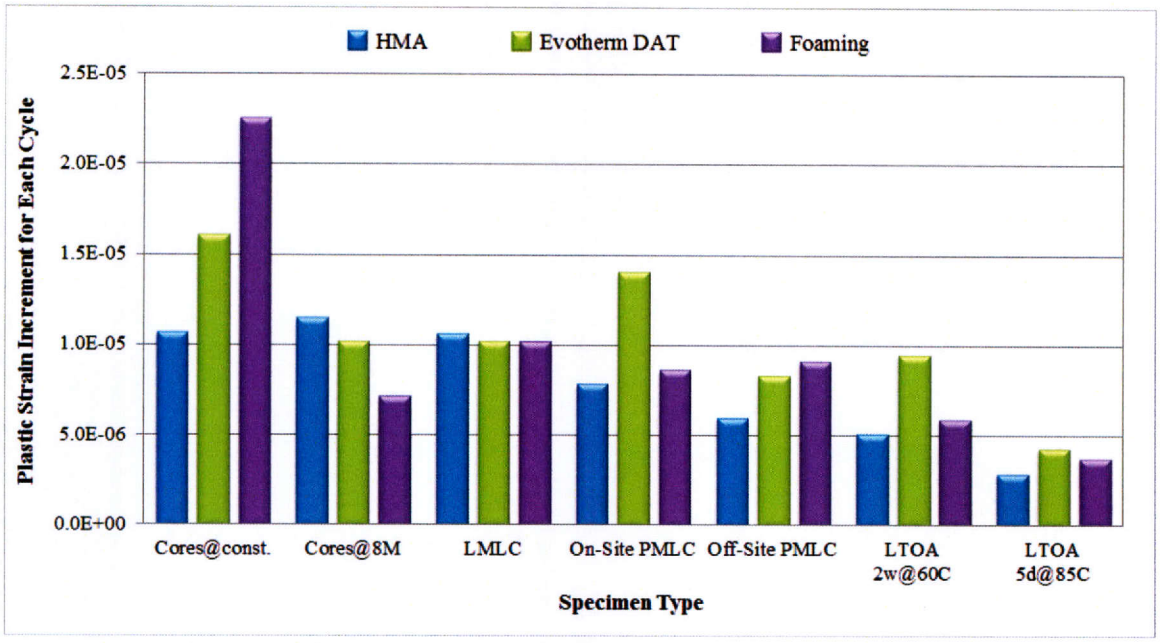

Figure 31. HWTT Test Parameter $\overline{\Delta\varepsilon_p}$ for Texas Mixtures.

Figure 32 illustrates the slope of the rut depth versus load cycles curve at the Stripping Number as it is calculated by the three parameter MEPDG model. This indicates the rate at which the mixture is rutting at the instant it begins to strip.

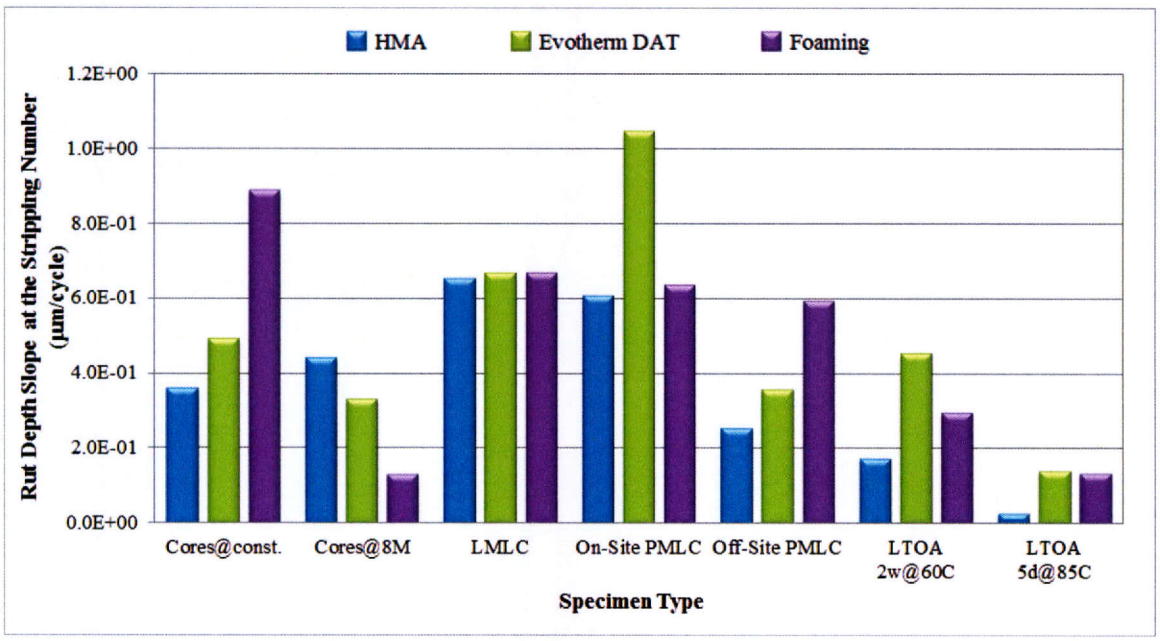

Figure 32. Rut Depth Slope at the Stripping Number for Texas Mixtures (Three Parameter MEPDG Fitting Model).

Figure 33 is the slope of the permanent strain versus load cycles curve as determined by the FHWA VESYS rutting criteria. Similar to the slope in Figure 32, this slope also indicates the rate at which rutting is developing at the instant that stripping begins to occur.

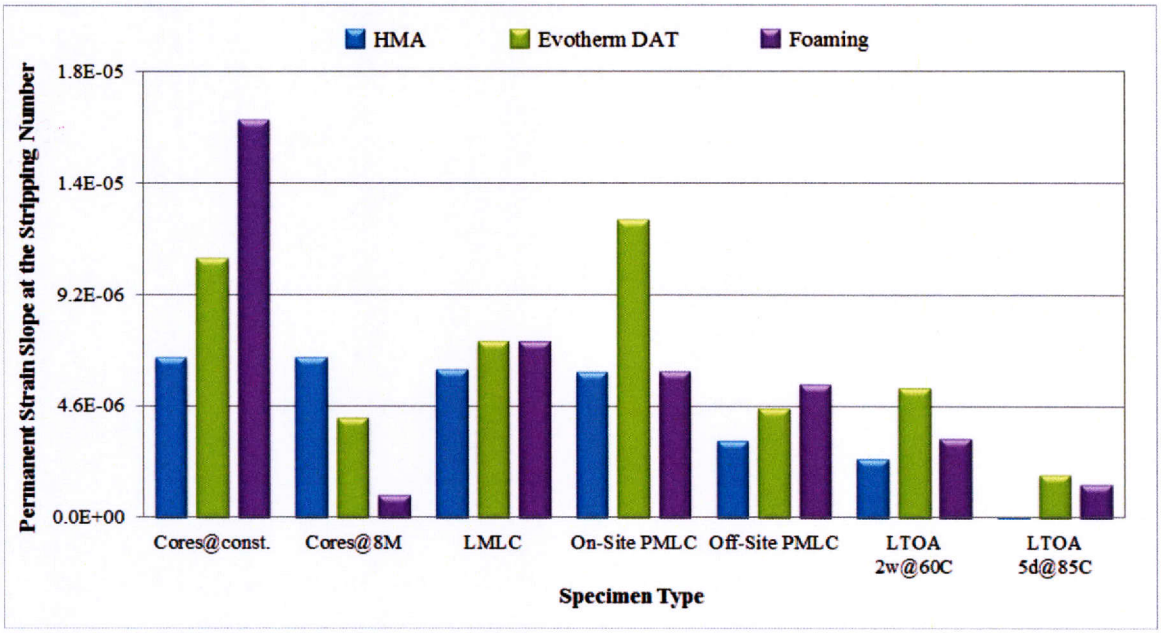

Figure 33. Permanent Strain Slope at the Stripping Number for Texas Mixtures (FHWA-VESYS Power Model).

The Crack Speed Index is illustrated in Figure 34. This calculated value is a negative exponential and the more negative the exponent, the better able the mixture is to resist crack growth after the Stripping Number.

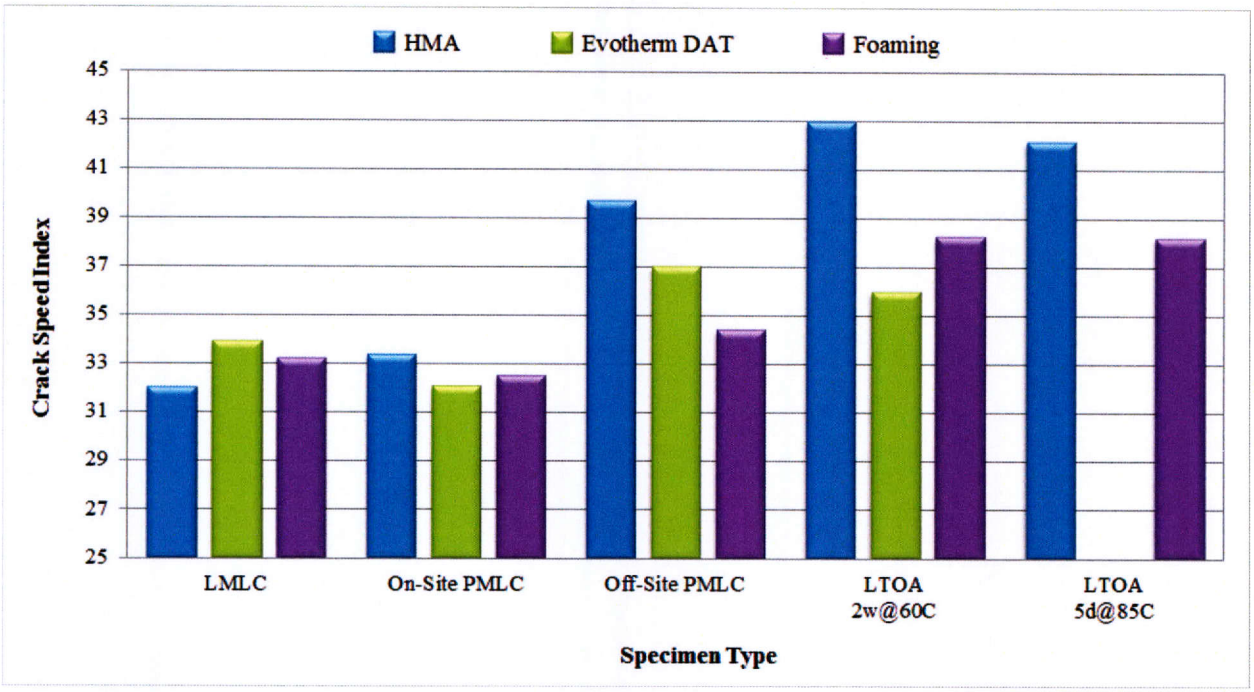

Figure 34. HWTT Test Parameter of Crack Speed Index for Texas Mixtures (Larger Positive Number Means Better Performance in Terms of Crack Speed Index).

COMPRESSIVE PERMANENT DEFORMATION PROPERTIES OF LAB COMPACTED MIXES

To characterize the material properties of undamaged and damaged asphalt mixtures, an experimental protocol was developed in the preliminary studies (Zhang et al. 2012; 2013) that included a sequence of three tests:

1) Nondestructive compressive creep test (VEC).

2) Nondestructive compressive dynamic modulus test (VEC).

3) Destructive compressive dynamic modulus test (RDC).

All three tests in the testing protocol were conducted using the Universal Testing Machine (UTM). The same testing protocol was used in this study and the loading sequence is shown in Figure 35.

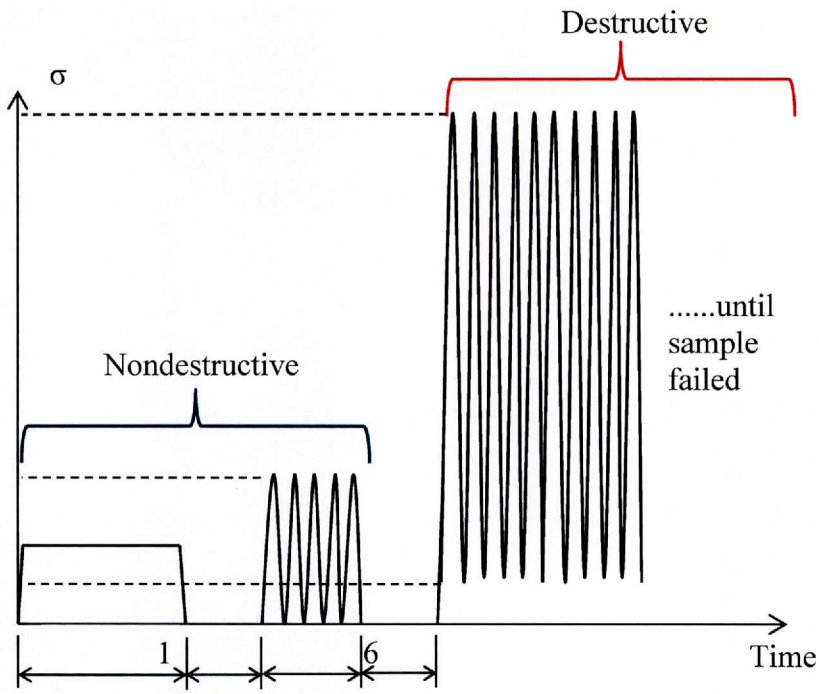

Figure 35. Schematic Plot of the Loading Sequences Used in the Tests (Not Scaled).

Before the tests, the asphalt mixtures specimens were stored in an environmental chamber at a constant temperature of 40°C for at least 3 hours to reach the equilibrium temperature. The nondestructive creep test was firstly conducted, which applied a constant compressive stress of 25 kPa to the specimens for 120 sec. The total strain at the end of the creep test was controlled at less than 150 με which was the linear viscoelastic limit for the asphalt mixture in compression (Levenberg and Uzan 2004). Then the compressive load was removed and the specimen was at rest for 1 hour. The 1-hour rest period was used for the following purposes: 1) the viscoelastic strains produced in the nondestructive tests were fully recovered and would not affect the results of the following tests; and 2) the 1-hour rest period was needed to compensate for the temperature loss due to opening the door of the UTM chamber during the setup and operation of the tests.

After the 1-hour rest period, the nondestructive dynamic modulus test was performed on the same specimen, in which a compressive haversine stress with a maximum stress value of 70 kPa was applied to the sample for 600 loading cycles at a frequency of 1 Hz. After another 1-hour rest period, the destructive dynamic modulus test was performed on the same undamaged specimen, in which a shifted sinusoidal compressive load with a minimum stress of 15 kPa and a maximum stress of 615 kPa was applied to the specimen at a frequency of 1 Hz. The three tests had the same testing configuration that is shown in Figure 36.

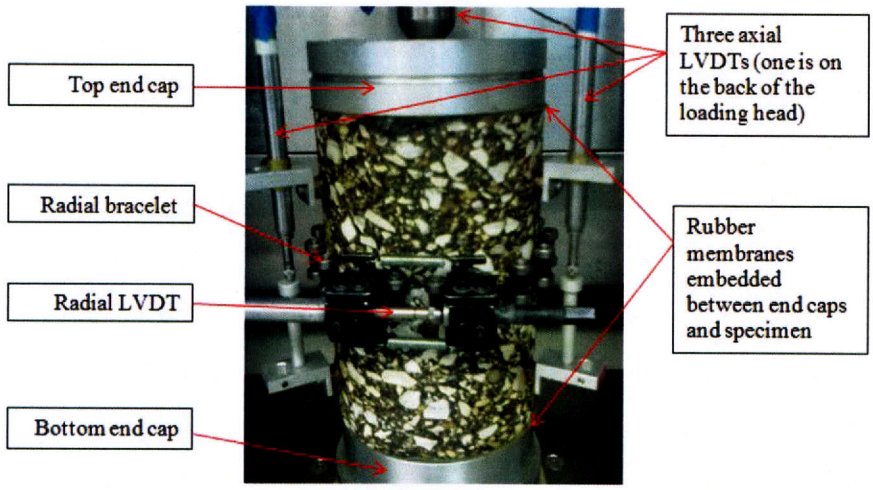

Figure 36. Testing Configurations of the Compressive Tests.

In the three tests, the total axial deformation was recorded with respect to time using three vertical linear variable differential transformers (LVDTs). The axial strain was determined by dividing the average axial deformation by the axial gauge length (i.e., 90 mm in this study). A radial LVDT was mounted on a bracelet which surrounds the specimen to record the change of the specimen's circumference. The radial strain was calculated as the ratio of the circumferential deformation to the original circumference of the specimen (i.e., 314.2 mm).

The conditions at the ends of all the tested specimens were treated to produce an identical and approximately idealized end conditions (i.e., axial load was applied with very little lateral constraint or friction). The treatments as shown in Figure 36 included: 1) two soft rubber membranes were placed between the end caps and the specimens; and 2) wax-based petroleum jelly was used between the rubber membranes and the end caps. With the help of these treatments, the asphalt mixture specimens were found to be able to deform freely in the radial direction at the ends of the cylindrical specimens. The tested specimens also showed that the end constraints were negligible and a uniform radial deformation was produced along the height of the specimens.

TENSILE PROPERTIES OF LAB COMPACTED MIXES

The tension fatigue properties are measured by conducting controlled-strain Repeated Direct Tension (RDT) test using the Material Test System (MTS). The environment chamber of the MTS controls the temperature at 20°C. The test specimen is 102 mm in diameter and 150 mm high. The specimen is glued to a pair of end-caps and then set up in the environmental chamber of the MTS. The ends of the test specimen should be smooth and parallel so that the load is concentric with the axis of the specimen to avoid possible bending moment imposed on the specimen. Three axial linear variable differential transformers (LVDTs) are mounted on the middle part of the test specimen. They are placed at 120° apart from each other around the specimen surface and the average of the three LVDTs is used as the axial deformation of the specimen.

The test procedure of the controlled-strain RDT test is designed to determine the threshold between the undamaged state and damaged state of an asphalt mixture, and the

destructive behavior of the asphalt mixture, which characterizes the cracking damage generated in the material. The threshold between the undamaged state and damage state is used as the reference based on which the fatigue damage can be quantified and is examined by performing a series of consecutive controlled-strain RDT tests with different strain levels on the same specimen. From these tests, the material properties of the asphalt mixture specimen under different strain levels are measured. As a result, the behavior of the asphalt mixture under different strain levels can be identified, which in sequence includes the linear viscoelastic, nonlinear viscoelastic, and damaged behavior. The stress-strain diagrams and material properties of an asphalt mixture at these three different material states have the following characteristics, as illustrated in Figure 37:

- In the linear viscoelastic state, the loading path (OA) and the unloading path (AO) are the same; the material properties do not change with the increase of the loading cycles at a given strain level, and they do not change with the change of the strain levels;
- In the nonlinear viscoelastic state, the loading path (OBC) and the unloading path (CO) are different, and the deformation can fully recover after unloading; the material properties do not change with the increase of the loading cycles at a given strain level, but they change with the change of the strain levels
- In the damaged state, the loading path (OCE) and the unloading path (EF) are different, and the deformation cannot be fully recovered after unloading; the material properties change with the increase of the loading cycles at a given strain level, and they change with the change of the strain levels.

The linear and nonlinear viscoelastic behaviors belong to the undamaged region, separated by Point B in Figure 37. The dividing point between the nonlinear viscoelastic state and the damaged state (Point D) is the threshold between the undamaged and damaged state. Such a threshold is defined as the critical nonlinear viscoelastic state. The material properties measured at the threshold strain level are defined as the critical nonlinear viscoelastic properties.

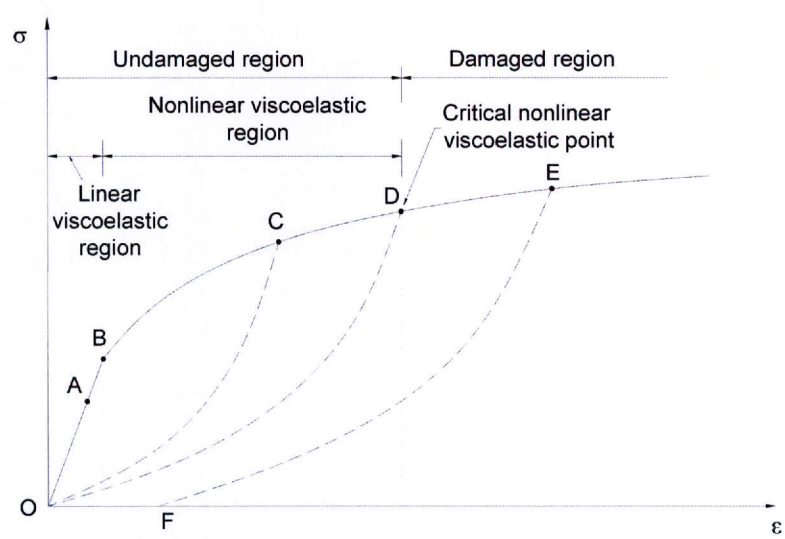

Figure 37. Different Material States of an Asphalt Mixture.

Once the stress level is in the damaged region, the cracks will begin to grow from the air voids and the mixture will develop many small fracture zones distributed within the mixture. The damage density is the ratio of the area of these air voids or cracks to the total cross sectional area.

Application of the damage density into the Paris' Law can be modified in the following way:

$$\frac{d\emptyset}{dN} = A'(J_R)^{n'} \tag{5-1}$$

where $(d\emptyset)/dN$ represents the evolution of the damage density of an asphalt mixture specimen per cycle; A' and n' are fracture coefficients associated with the evolution of the damage density; and J_R is the pseudo J integral that is calculated based on the pseudo strain energy and used to model crack growth in asphalt mixtures. In contrast to the traditional experimental methods of measuring the fracture coefficients, A' and n' can be determined using the damage density calculated above.

In the two figures shown below, Figure 38 and Figure 39, the material codes are as follows: H stands for Hot Mix; F stands for Foaming; and E stands for Evotherm. The symbols A0, A2, andA6 stand for laboratory aging for 0, 2, and 6 weeks at 60°C. The symbol RH95% refers to the fact that the sample was exposed to 95 percent Relative Humidity for a period of six months at 25°C.

As is clearly observed in Figure 38, as the conditioning relative humidity increased to 100 percent, the fracture parameter n' tended to increase for both WMA and HMA specimens, which indicates that the water vapor pressure in the specimens significantly increased the fatigue potential of the asphalt mix material. As shown in Figure 39, the modified Paris' law parameter A' tended to decrease as the conditioning relative humidity increased; however, this decrease was not adequate to offset the increase of n'. Therefore, it is concluded that the moisture presence in the asphalt due to vapor diffusion increases the fatigue cracking of the asphalt mix significantly. These findings demonstrate that cracks grow faster in specimens with a higher RH level. Computations have shown that within six months of laydown, the asphalt mixture in a pavement surface layer will reach at least 95 percent Relative Humidity because of the upward diffusion of subsurface water vapor. This accelerates the deterioration of the asphalt layer of a flexible pavement. As a result, the RH level should be taken into consideration when predicting the fatigue life of any asphalt mixture and when designing asphalt pavements.

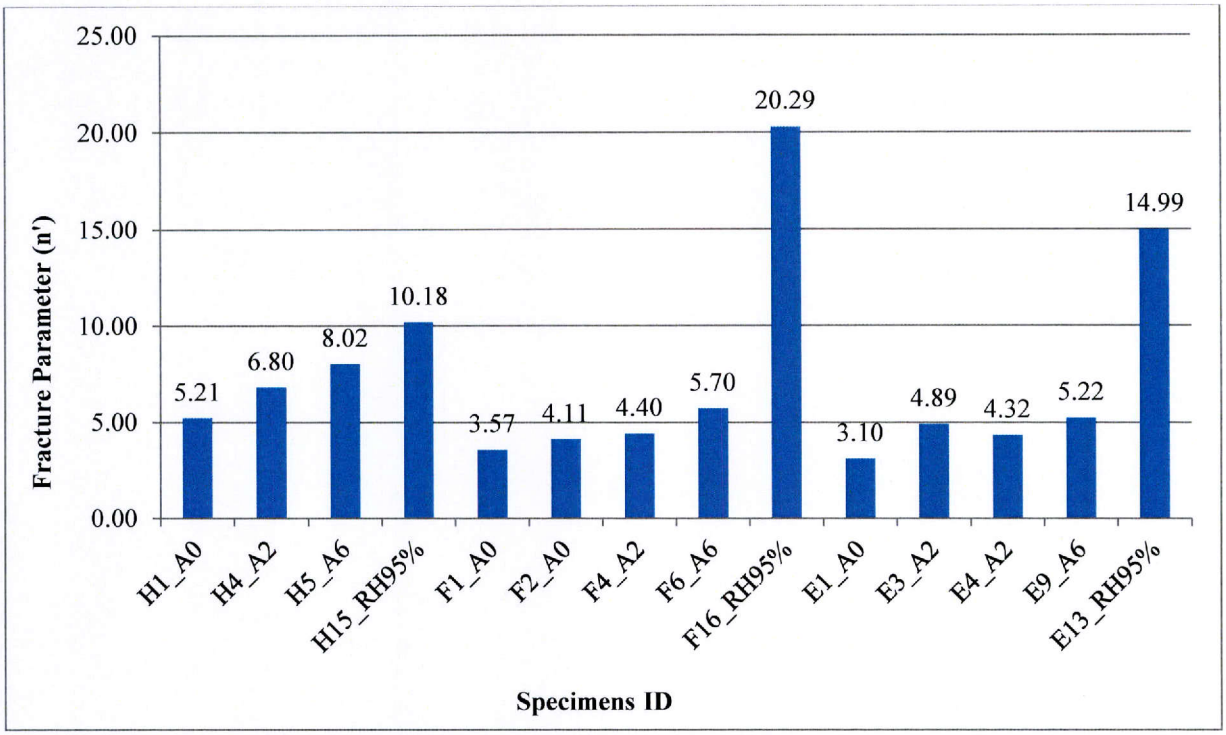

Figure 38. Test Results n' for HMA and WMA.

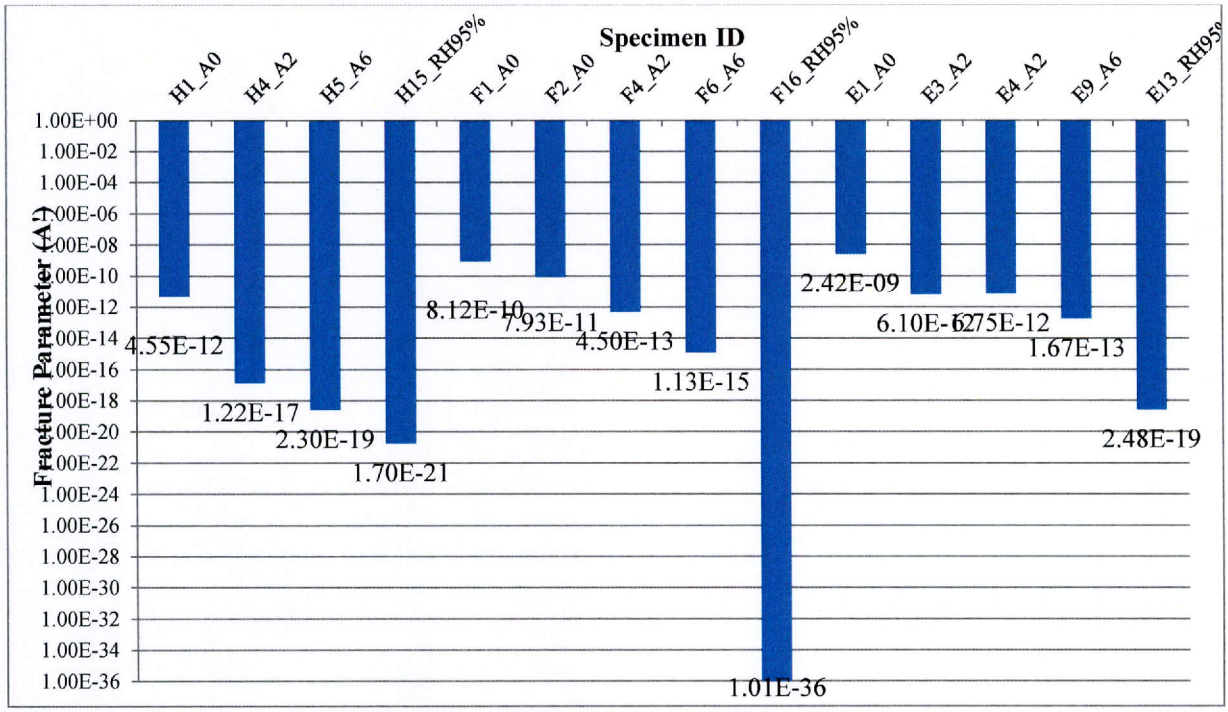

Figure 39. Test Results of A' for HMA and WMA.

The relation of log A′ and n′ is found to be highly linear as illustrated in Figure 40. In general, the fracture parameter n′ will increase as the A′ is decreasing, which indicates that the A′ and n′ are highly correlated with each other. Sensitivity analyses have shown that the fracture exponent, n' is a reliable indicator of the speed of crack propagation.

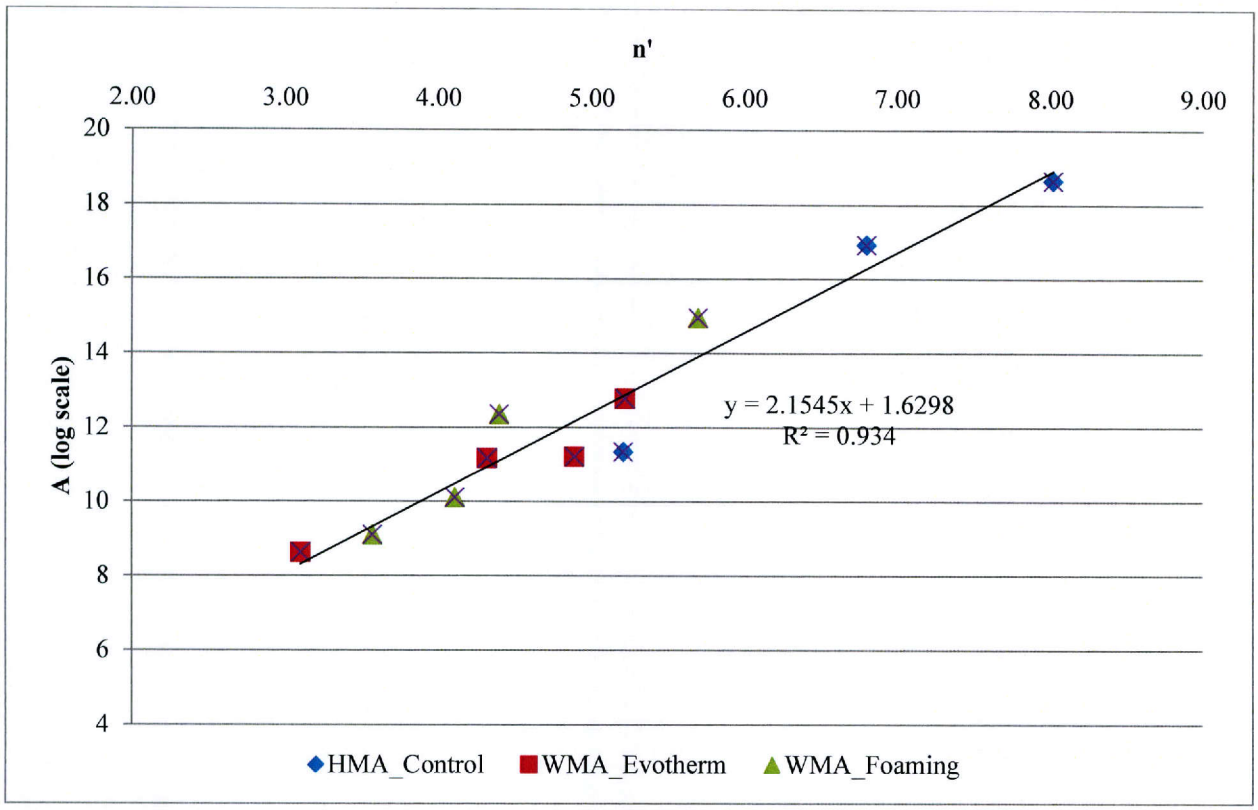

Figure 40. Plot of log A′ vs. n′.

Water vapor has a significant effect on asphalt pavement materials. Water vapor accumulates in the asphalt pavement surface layer at a rapid rate and it reaches nearly saturated vapor pressure within a period of 6 months. Moreover, wetting processes in the pavement layer brought by the subsurface water vapor diffusion occurs continuously, both day and night. Therefore, the presence of water due to vapor diffusion in the asphalt surface layer is one of the major water movement mechanisms in pavement and it greatly accelerates the deterioration of the asphalt mixture. Reviewing the information in Figure 38, and comparing the sizes of the fracture exponent, n', the WMA Evotherm DAT and foaming technologies improve the fatigue crack growth resistance of WMA compared to the HMA, even after six months aging. However, taking the effect of the moisture vapor conditioning into account, the Hot Mix is more resistant to fatigue cracking than either of the Warm Mix mixtures.

CHAPTER 6. CHARACTERIZE FIELD CORE DURABILITY AND CHARACTERIZE BINDER OXIDATION AND HARDENING IN TEST SECTIONS

CHARACTERIZE FIELD CORE DURABILITY

Introduction

The stiffness profile in field asphalt layers, unlike that in laboratory compacted specimens, is not uniform because of the non-uniform air void distribution with depth and the aging phenomenon. X-ray CT scan analysis of field layers shows that the initial stiffness profile is a C shaped curve. The asphalt layers immediately after placement have higher stiffness in the center of layer compared to the upper and lower edges because the center part is hotter and receives more compaction energy compared to the layers near the surface and bottom layer. This initial C-shaped stiffness profile changes due to binder aging with time. Binder aging also is more severe near the surface due to higher oxygen availability and sun radiation at the surface. In addition, recent studies confirm that oxygen can penetrate to depths well below the surface through interconnected air voids.

In this subtask, viscoelastic characterization (VEC) test was used to characterize the stiffness gradient of field-aged asphalt mixtures. Since the aging of asphalt layer in field is non-uniform with pavement depth, the stiffness gradient is much more accurate than the average resilient modulus to characterize the field core. After the characterization of stiffness gradient of field core, the Texas Overlay Tester (OT) was conducted to determine the fracture properties of the same field core based on viscoelastic fracture mechanics principles.

Methodology

The methodology described in this study includes:

- The DT test outputs are analyzed using the stiffness gradient calculation module;
- The OT test and the stiffness gradient outcomes are plugged into the functionally graded material (FGM) numerical module to calculate the crack growth pattern;
- The FGM output is used in another analytical module to calculate the fracture properties of the AC.

The DT test is a nondestructive test; therefore, the same sample can be used for both VEC test and OT test. Figure 41 shows the main modules of the methodology which are described in this study. The analytical and numerical models will be discussed in detail in the following sections.

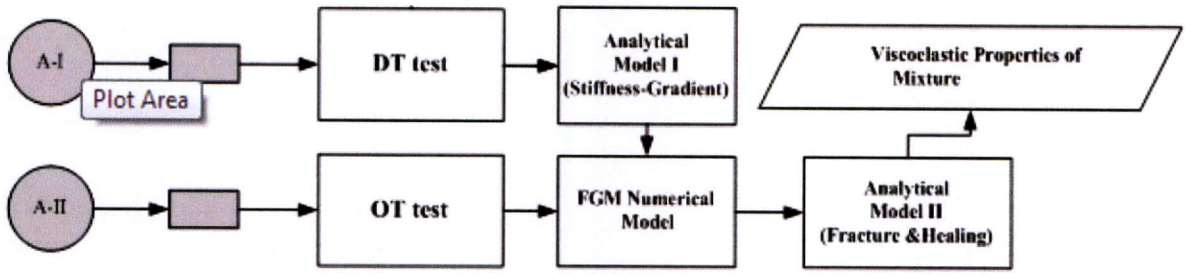

Figure 41. Procedures of the Test Protocol of Field Samples.

Stiffness Gradient Calculation Module

A rectangular specimen is cut from the field core used for the DT test and steel end-caps are glued to both ends of the rectangular specimen. Four Linear Variable Differential Transformers (LVDTs) are installed on each specimen of which four LVDTs measure the strain at the surface, bottom and the center of the asphalt layer. The rectangular field specimens oscillate under the monotonically increasing loads and these oscillations can be tracked in the strain outputs. The oscillations occur due to the effect of the feedback frequency and the stiffness gradient. The test is conducted at two different temperatures and each test takes about 3 hours to complete including the time required for the test sample to reach to the equilibrium temperature.

The analytical model assumes that the strain changes linearly with depth and the complex modulus of the asphalt layer changes from a higher modulus at the surface to a lower modulus at the bottom following a power function. Equations 6-1 and 6-2 show the stiffness gradient function and the relation between the modulus at the surface and the modulus at the bottom of the asphalt concrete layer in the field.

$$E(z) = E_d + (E_0 - E_d)\left(\frac{d-z}{d}\right)^n \tag{6-1}$$

$$E_0 = kE_d \tag{6-2}$$

where E(z) is the magnitude of the complex modulus at depth z; E_0 and E_d are the magnitudes of the complex modulus at the surface and the bottom of the AC layer, respectively; n and k are model parameters; and d is the thickness of the specimen. The exponent n is an indication of the sharpness of the stiffness profile. In the other words, as n value increases, the stiffness profile becomes sharper near the surface.

The analytical model uses a procedure which includes the signal processing to find the amplitude and frequency of the oscillations at the surface, center and the bottom of the AC layer. Then, using an analytical method based on linear viscoelasticity and the correspondence principle, the complex modulus gradient function is calculated. The detailed process has been described in a previously published paper (Koohi et al., 2012a; 2012b).This test and the corresponding analytical model estimates the stiffness gradient function with depth for the field specimen in the feedback frequency at two different temperatures.

Development of FGM Numerical Model

Less oxygen is available for the aging mechanism for the deeper portions of asphalt layer within the pavement structure. Therefore, asphalt mixtures in the field are usually stiffer at the surface because of more oxygen availability and more solar radiation at the surface. The stiffness gradient in the pavement layers usually is defined by dividing the pavement layer into smaller sub-layers each of which has different stiffness modulus. Obviously , this method increases the errors in the strain and stress calculations in the FE models (Dave et al., 2008). In this approach, every single layer will have different stiffness modulus and these properties should be redefined once the number of sub-layers is increased to obtain more accurate results.

The error caused by assuming multiple layer, each with a discrete stiffness can be remedied by assigning a continuous function for the stiffness as a function of depth, such that the stiffness modulus changes as a function of the coordinates of each material point inside the pavement. Therefore, in this dissertation a FGM-UMAT is used, such that the user has the flexibility to assign a function of the structural coordinate without the need to redefine the values of the stiffness modulus for each sub-layer. More accurate results can be obtained simply by redefining the FE mesh without the need to redefine the stiffness modulus of every single layer. Therefore, the accuracy of the gradient function can be defined by the user with the coarseness of the FE mesh because the UMAT is defined at the integration points in the mesh and the number of the integration points can be increased by using a finer mesh. A user defined material subroutine (UMAT) in ABAQUS was developed to define the stiffness gradient with depth in the asphalt layer. The model has been developed for a general case which includes three dimensional stress, plane stress and plane strain cases. It can be used as a subroutine along with the various simulated field asphalt concrete models to define the aging, stiffness, and Poisson's ratio changes with the thickness of the asphalt concrete layer.

Estimation of the Fracture Properties for Field Samples

The OT test was initially designed to test asphalt overlays on rigid pavements for the prediction of reflective cracking. The test apparatus consists of a stationary and a moving plate. A rectangular AC specimen is needed for this test similar to that used for the DT test. The specimen is glued onto the aluminum plates which are then fixed on the machine. The repeated displacement is applied to the specimen by moving one of the plates back and forth. The load and the displacement with time are recorded via an acquisition system. The machine has been used as a torture test to compare the performance of different asphalt mixtures; however, a high degree of variability has been reported by the users. The test consists of two steps; the first step is a nondestructive test which is used to measure the undamaged properties such as m value and the relaxation modulus and the second step is the destructive test which is used to measure the fracture and healing properties of the AC. This method includes the calculation of the viscoelastic force in each cycle as a function of the area under strain profile above the crack tip. By measuring the force in each cycle the area under the strain profile in the intact thickness above the crack is calculated; furthermore, the FE output gives the strain profiles for different crack lengths. Therefore, as the area under strain profile above the crack in each cycle is calculated, the corresponding crack length in each load cycle can be found. Equations 6-3 and 6-4 give the calculated viscoelastic force for each loading and unloading cycle.

$$\max. P_{LVE}(z = c) = \frac{E_1 b t^{1-m}}{(1-m)t_1} s(c) \qquad 0 < t < t_1 \tag{6-3}$$

$$\max. P_{LVE}(z = c) = bs(c)\frac{E_1 t^{1-m}}{(1-m)t_1} - 2bs(c)\frac{E_1 (t-t_1)^{1-m}}{(1-m)t_1} \qquad t_1 < t < 2t_1 \tag{6-4}$$

where max.P_{LVE}(z=c) is the measured maximum viscoelastic force within the specified time interval, b is the width of specimen, and s(c) is the area under the strain profile above the tip of the crack length.

Additionally, the pseudo displacement is calculated by Equation 6-5:

$$U_r(t) = \frac{P_{LVE}(t)}{k_r} \tag{6-5}$$

where $P_{LVE}(t)$ is the linear viscoelastic force and k_r is the reference stiffness which is the value of the maximum load in the first load cycle divided by the maximum opening. After the crack length in each load cycle is calculated, the viscoelastic force and pseudo displacement for each cycle are calculated. By graphing the pseudo displacement versus the measured force, a closed loop is obtained in which the area under the loop is the pseudo work for each cycle. The change of the pseudo work is used to find the Paris's laws fracture parameters, which are shown in Equation 6-6:

$$\frac{dC(N)}{d(N)} = A\left[\frac{W_R(N)}{c.s.a}\right]^n \tag{6-6}$$

where c.s.a is cracking surface area, and $W_R(N)$ is the pseudo strain work for each loading cycle.

A similar methodology to that for the laboratory compacted specimen is used for the field-aged asphalt concrete layers with few modifications. The strain profiles for the field aged asphalt concrete layers are estimated using the previously described FGM-FE model and a smaller displacement is applied to the field specimen because they are more brittle.

The output of the stiffness gradient model from the DT test gives the magnitude of the complex modulus at the feedback frequency which is 20 Hz in the machine that was used in the test. However, the modulus obtained from the OT test is measured at a different frequency; therefore, the Equation 6-7 is used to transfer the modulus to the desired frequency if it is needed in the calculations.

$$\left|E^*_{\left(\frac{1}{2t}\right)}\right|(OT) = \left|E^*_{(w)}\right|(DT)\left(\frac{1}{2tw}\right)^m \tag{6-7}$$

where $\left|E^*_{\left(\frac{1}{2t}\right)}\right|$ and $\left|E^*_{(w)}\right|$ are the magnitudes of the moduli in the OT test and DT tests, respectively. The m is the undamaged parameter which is obtained from the nondestructive part

vertical displacement of the specimen at different locations during the loading process. The test is a non-destructive tension test with monotonically increasing load. The maximum allowable tensile strain is 70 micro-strains. The test was conducted at 10°C and 20°C to evaluate the effect of temperature on the stiffness gradient of the specimen. The rest time of the test between two temperatures is 2 hours, in order to allow the specimen to reach the temperature equilibrium and eliminate the interaction between the tests. Figure 43 is the configuration of the VEC test.

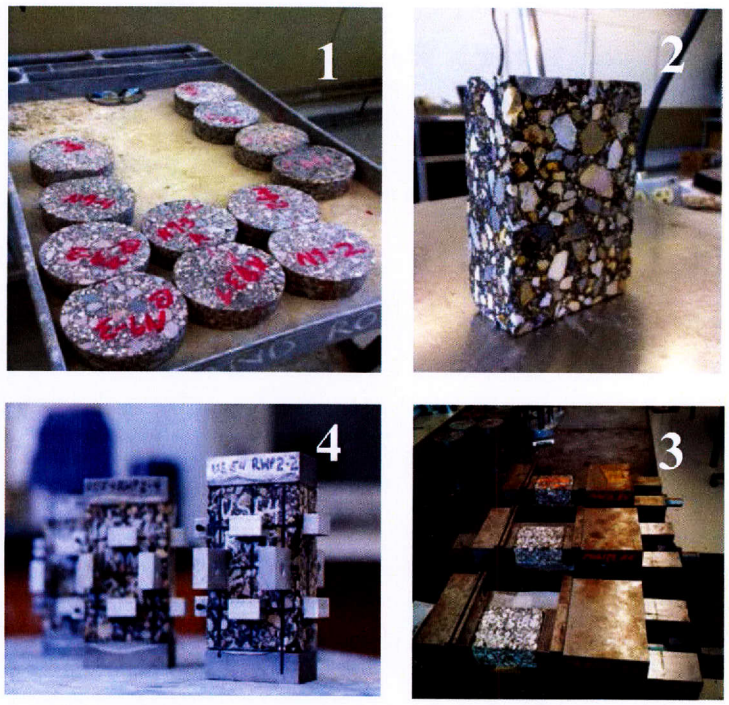

Figure 42. Sample Preparation for VEC Test.

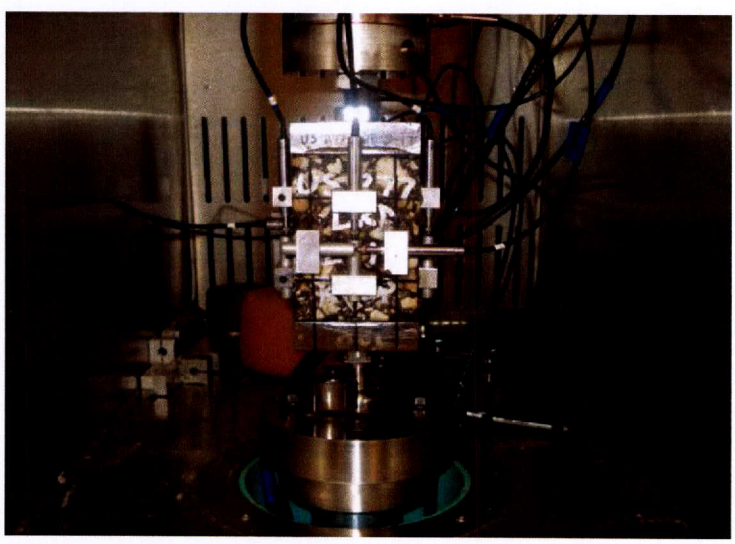

Figure 43. Configuration of VEC Test.

of the OT test, t is the loading time in the OT test and ω is the angular velocity of the DT machine.

Experiment

Sample Collection

Texas Department of Transportation (TxDOT) setup an experimental overlay on Texas Farm to Market (FM) Highway 973 in Travis County, Austin District, in order to conduct testing and long-term performance monitoring for Foaming and Evotherm WMA mixes. HMA is paved as control group. The overlay construction started in December 2011, and ended in January, 2012. Table 10 presents the construction information of experimental sections in FM 973. The field asphalt mixtures were cored from HMA, Foaming, and Evotherm WMA sections after 1 month aging, 8 months aging, and 14 months aging. Some underlying asphalt layers are also cored. Table 11 summarizes the number of field cores for each section.

Table 10. Summary of Construction Information of Experimental Sections in FM 973.

Section Number	Mixture Description				Date of Paving	Station	Comment
	Type	Binder	RAP	AS			
1	HMA	PG 70-22	0	0	12/01/2011		Control Mix
7	WMA (Foaming)	PG 70-22	0	0	12/01/2011		
8	WMA (Evotherm)	PG 70-22	0	0	01/04/2012		

Table 11. Number of Field Cores for Each Section.

Aged Month	Section 1	Section 7	Section 8	Total Number
0	8	9	12	29
8	5	4	4	13
14	6	6	6	18

Sample Preparation for VEC Test

The sample preparation for viscoelastic characterization (VEC) test is shown in Figure 42. The test sample is in rectangular shape, which is cut from a cylindrical field core. The length and width of the sample are 4 inches and 3 inches, respectively. The thickness of the sample varies from 1 inch to 2.5 inches on the basis of the thickness of asphalt layer. After cutting the specimen, a pair of steel caps was glued on the specimen. A special gluing jig was used to make sure that the specimen was centered between the steel caps. For VEC test, four pairs of LVDTs were glued on the top, center, and bottom surface of the specimen, in order to measure the

Sample Preparation for OT Test

Since the VEC test is a non-destructive test, the same specimen can be used for OT test after removing the LVDTs and steel caps from the specimen. Sample preparation for OT tests is shown in Figure 44. The specimen was glued on a pair of aluminum plates. The force was loaded through the aluminum plates to the specimen repeatedly. The OT test is conducted in two steps: the non-destructive test and the crack growth test. Figure 45 illustrates the non-destructive and destructive loading patterns. The non-destructive step includes 10 load cycles with an opening of 0.002 inch, and the destructive step includes 300 load cycles with a maximum opening displacement of 0.0125 inch for 1-inch thickness sample and 600 load cycles with the same opening displacement for 1.5-inch thickness sample. The test was conducted at 25°C.

Figure 44. Sample Preparation for OT Test.

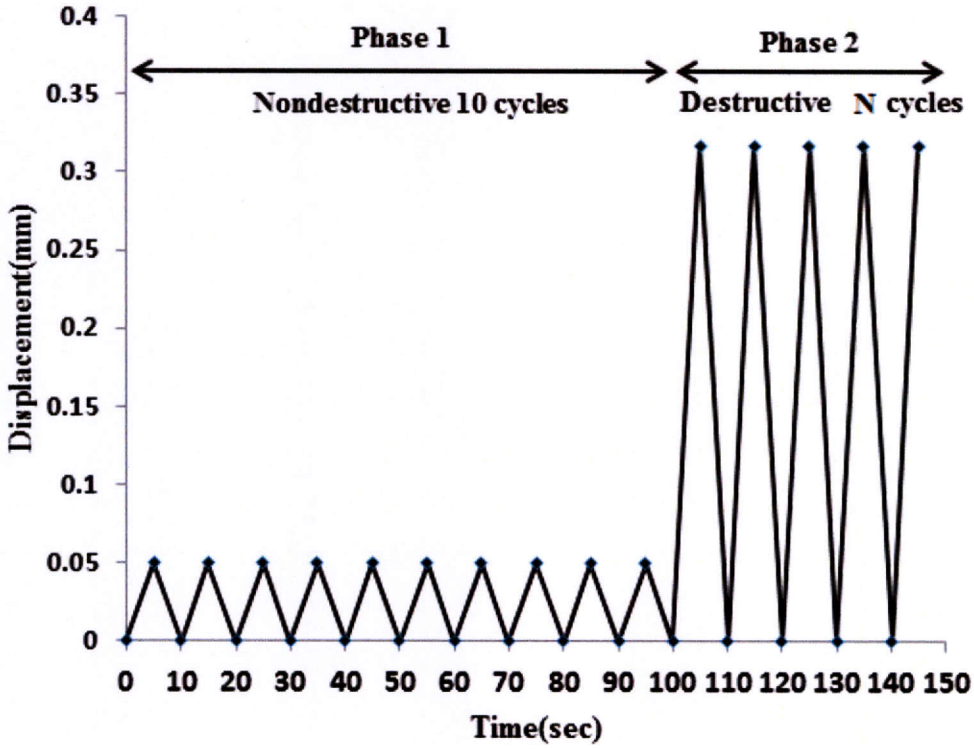

Figure 45. Loading Pattern for Field Specimen in OT Test.

Result and Discussion

Results for Stiffness Gradient Analysis

The outputs of the VEC test were analyzed using the stiffness gradient calculation methodology. Table 12 presents the results of the stiffness gradient analysis for field cores. The modulus of surface is larger than that of the bottom, because the surface suffered more aging than the bottom. The parameters k and n indicate the shape of the stiffness gradient curve. Parameter k is the ratio of the modulus at the surface to the modulus at the bottom of the layer. The high n values indicate that the stiffness gradient is very high near the surface.

Figure 46 is the stiffness gradient profiles for the top layer of experimental sections after 1 month aging. As shown in Figure 46, the complex modulus of 1-month aged HMA is larger than that of Foaming WMA, and the complex modulus of 1-month aged Foaming WMA is larger than that of Evotherm WMA. The modulus of the surface layer is slightly larger than that of the bottom of the layer after 1 month aging in winter. Figure 47 shows the difference of stiffness gradient profiles of field cores at different temperatures. The results show that the stiffness gradient curve is a function of loading frequency and temperature.

Table 12. Results of the Stiffness Gradient Analysis for Field Cores (First Set: F; Second Set: S; Third Set: T).

Sample ID	Test Temperature (°C)	n	k	Surface Modulus (ksi)	Bottom Modulus (ksi)
F1-13-1	10	4.98	1.36	486	359
F1-13-2	10	4.14	1.89	1044	553
F1-13-3	10	4.96	1.71	1050	611
F1-20-1	10	4.77	1.51	620	410
F1-26-1	10	4.93	1.44	557	386
F1-27-1	10	3.78	1.43	479	336
F1-28-1	10	3.53	1.30	487	375
S1-2-1	10	3.93	1.70	905	534
S1-13-1	10	3.51	1.80	802	447
S1-20-1	10	3.38	1.72	900	524
S1-24-1	10	3.71	1.65	831	504
T1-1-1	10	4.99	1.64	927	565
T1-18-1	10	4.11	2.06	1070	518
T1-9-1	10	4.16	1.53	866	566
F7-5-1	10	5.57	1.18	423	357
F7-15-1	10	5.36	1.35	474	352

Sample ID	Test Temperature (°C)	n	k	Surface Modulus (ksi)	Bottom Modulus (ksi)
S1-13-1	20	3.85	1.67	688	411
S1-24-1	20	5.36	1.65	662	400
T1-1-1	20	4.99	1.64	927	565
T1-18-1	20	4.11	2.06	1070	518
T1-9-1	20	4.16	1.53	866	566
F7-16-1	20	4.93	1.39	307	222
F7-21-1	20	4.10	1.22	253	206
F7-24-2	20	4.13	1.76	708	402
F7-24-3	20	5.24	1.81	855	473
S7-5-1	20	5.00	1.84	644	418
S7-12-1	20	4.07	1.76	709	404
S7-15-1	20	4.91	2.02	721	357
S7-16-1	20	4.10	1.64	626	380
T7-1-1	20	3.89	1.62	623	385
T7-15-1	20	4.17	1.70	693	408
T7-3-1	20	3.88	1.81	701	387
F8-8-1	20	4.93	1.38	262	190
F8-12-1	20	4.76	1.27	322	253
F8-18-1	20	4.02	1.41	308	218
S8-12-1	20	4.23	1.84	567	309
S8-18-1	20	5.19	1.92	519	271
T8-15-1	20	3.27	1.91	692	362
T8-12-1	20	4.13	1.59	560	352
T8-10-1	20	3.77	1.82	599	329

Sample ID	Test Temperature (°C)	n	k	Surface Modulus (ksi)	Bottom Modulus (ksi)
F7-16-1	10	5.12	1.29	421	325
F7-21-1	10	4.75	1.22	403	331
F7-24-1	10	4.93	1.25	477	382
F7-24-2	10	4.12	1.87	1026	548
F7-24-3	10	4.11	2.03	1270	628
S7-5-1	10	4.30	1.88	771	410
S7-12-1	10	3.96	1.61	810	502
S7-15-1	10	4.69	1.95	931	478
S7-16-1	10	4.15	1.75	776	444
T7-1-1	10	4.10	1.74	908	522
T7-3-1	10	4.10	1.86	821	441
T7-15-1	10	4.72	1.54	755	490
F8-4-1	10	4.86	1.22	354	289
F8-8-1	10	4.94	1.31	324	248
F8-12-1	10	4.15	1.37	396	290
F8-18-1	10	5.03	1.38	305	221
F8-20-1	10	4.12	1.37	410	300
F8-24-1	10	4.12	1.28	341	266
S8-4-1	10	4.73	2.12	671	317
S8-8-1	10	4.09	2.02	743	368
S8-12-1	10	4.91	1.76	756	431
S8-18-1	10	5.02	1.84	695	378
T8-13-1	10	4.34	2.03	879	433
T8-15-1	10	4.42	1.81	739	408
T8-12-1	10	4.98	1.62	692	427
T8-10-1	10	3.89	1.52	741	488
F1-13-1	20	4.10	1.38	450	326
F1-13-2	20	5.61	1.68	783	467
F1-13-3	20	4.14	1.84	846	459
F1-26-1	20	4.89	1.53	446	291
F1-27-1	20	3.99	1.31	383	293
F1-28-1	20	4.93	1.50	357	237
S1-2-1	20	4.15	1.77	755	426

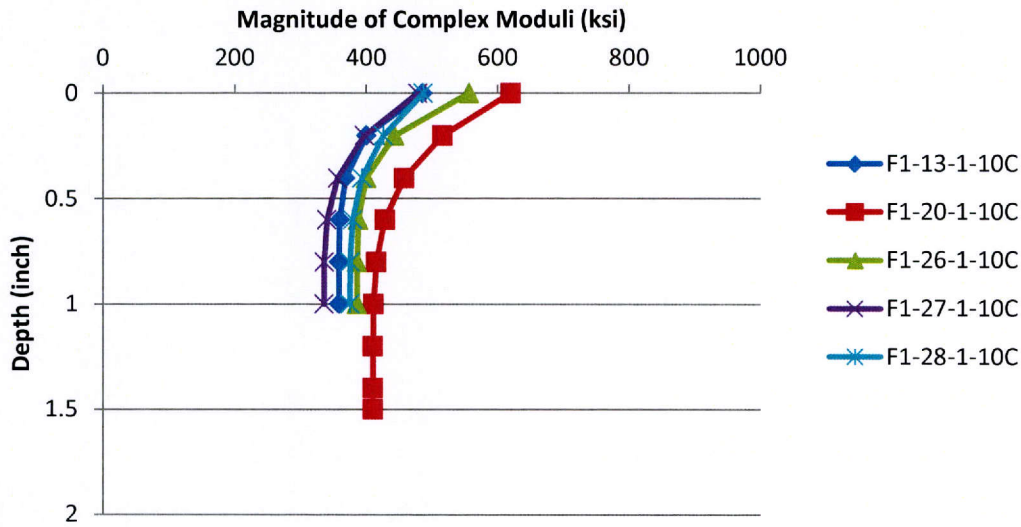

(a)

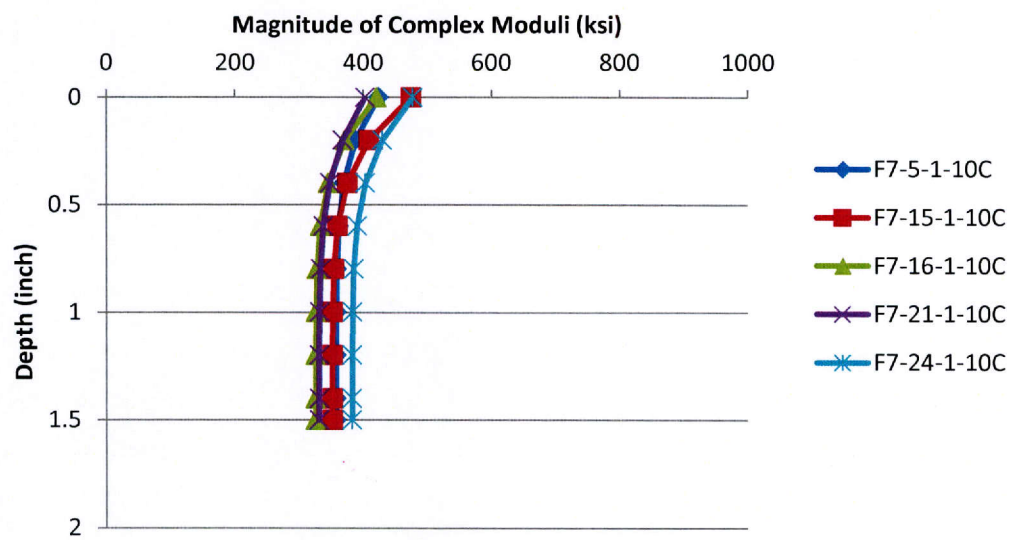

(b)

Figure 46. Stiffness Gradient Curves of 1 Month Aged Top Layers from Each Section.

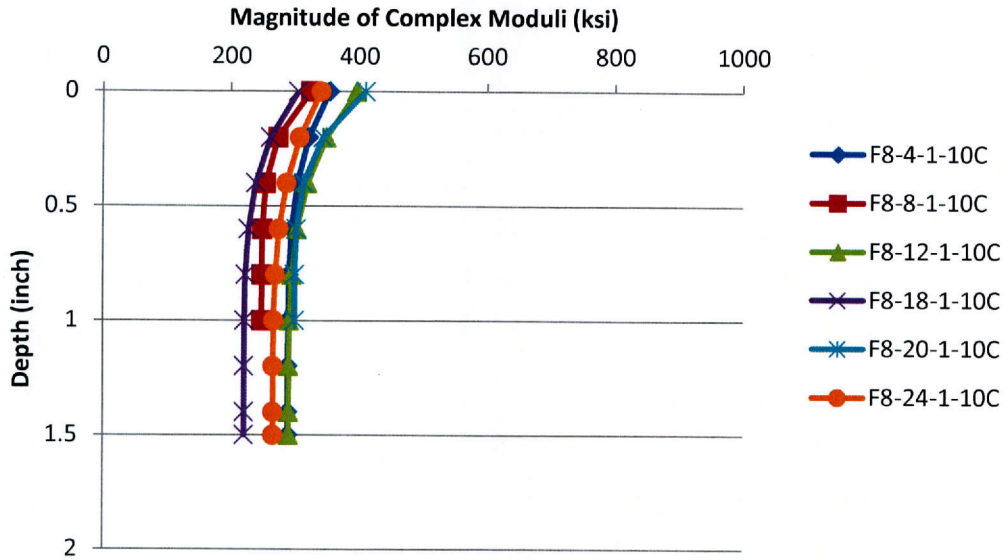

(c)

Figure 46. Stiffness Gradient Curves of 1 Month Aged Top Layers from Each Section (cont'd).

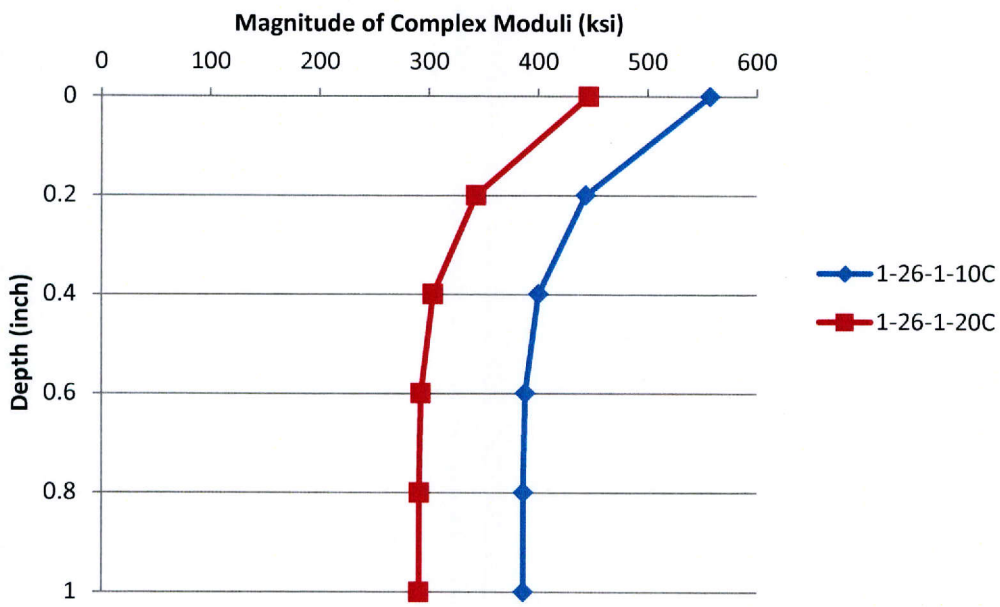

Figure 47. Stiffness Gradient Curves of Field Core 1-26-1 at Different Temperatures.

Figure 48 shows the variation of stiffness gradient curves of field cores after 8 months aging. As can be seen from Figure 48, the surface modulus increased much more rapidly than the bottom modulus, which leads to a higher k values. The stiffness gradient curves of field cores

from underlying layers are also presented in Figure 49. Contrary to what might have been expected, the complex moduli of the underlying layers are higher than that of the top layer, which means the aging of underlying layers are severer than the aging of the top layer. That is because these layers all served as overlays, but were not paved at the same time. Figure 50 is the pavement performance information of the experimental section, which indicates that the third layer was constructed in 2005 after five years of aging, and the second layer was constructed in 2009. Figure 51 presents the average stiffness values at the top and bottom of the surface layers for each section, which illustrates the variation of complex modulus for each section with the aging time.

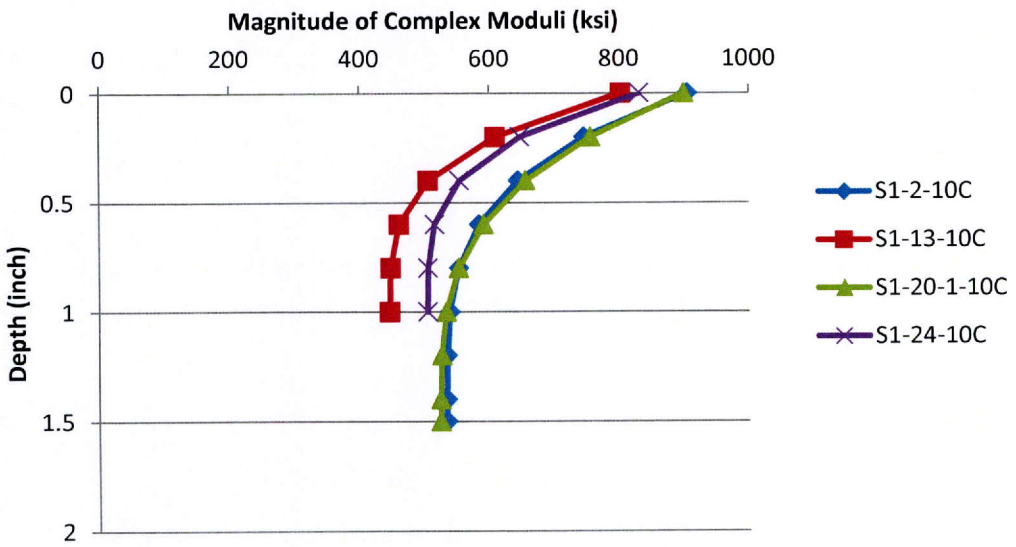

(a)

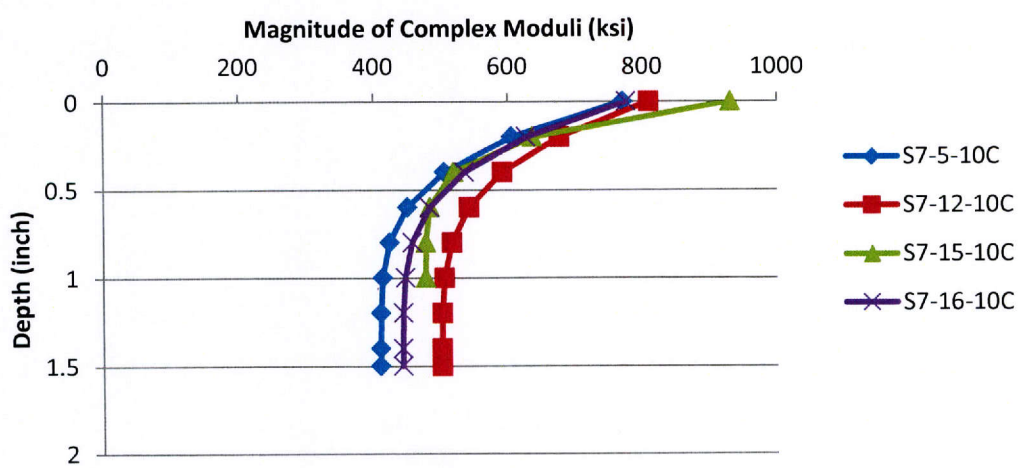

(b)

Figure 48. Stiffness Gradient Curves of 8 Months Aged Top Layers from Each Section.

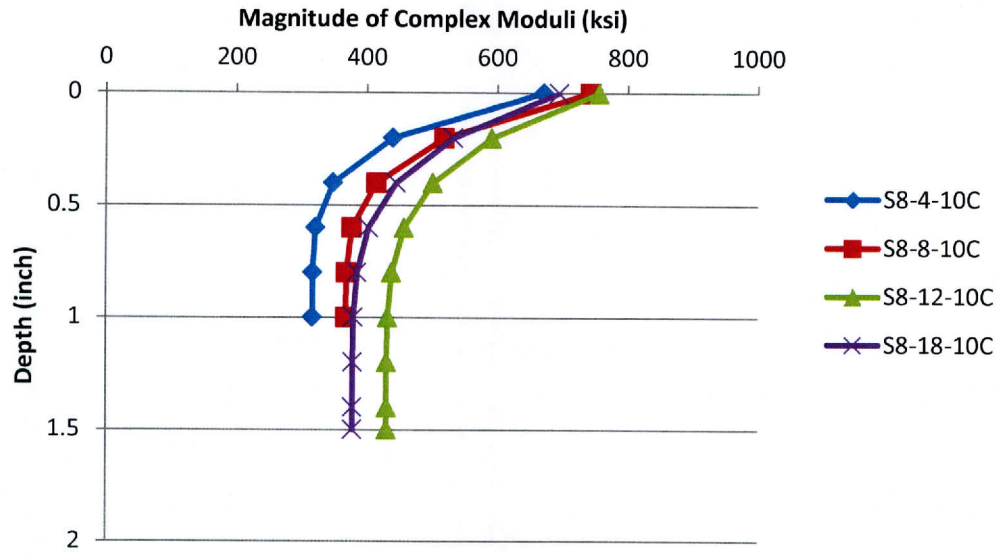

(c)

Figure 48. Stiffness Gradient Curves of 8 Months Aged Top Layers from Each Section (cont'd).

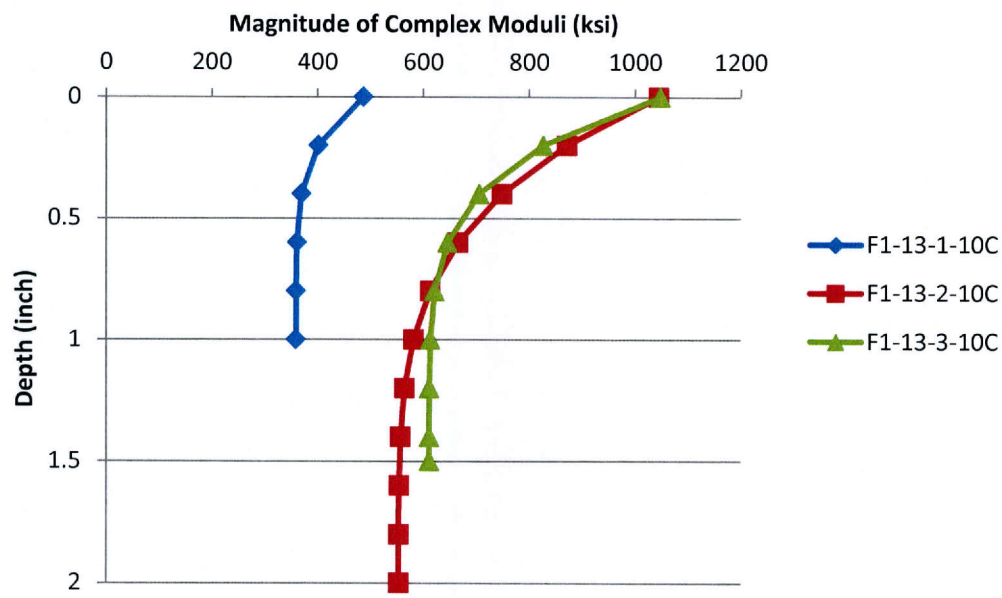

Figure 49. Stiffness Gradient Curves of Top and Underlying Layers from HMA Section.

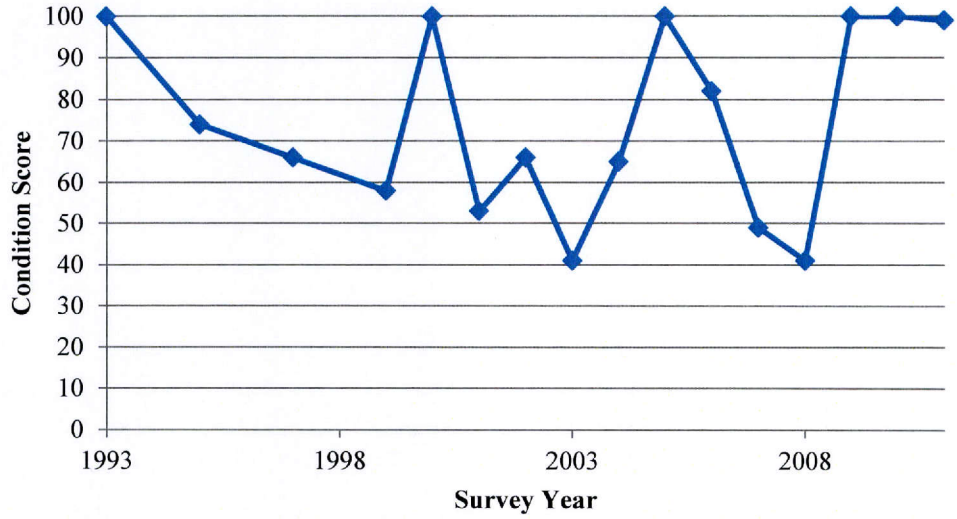

Figure 50. Pavement Performance Information of the Experimental Section.

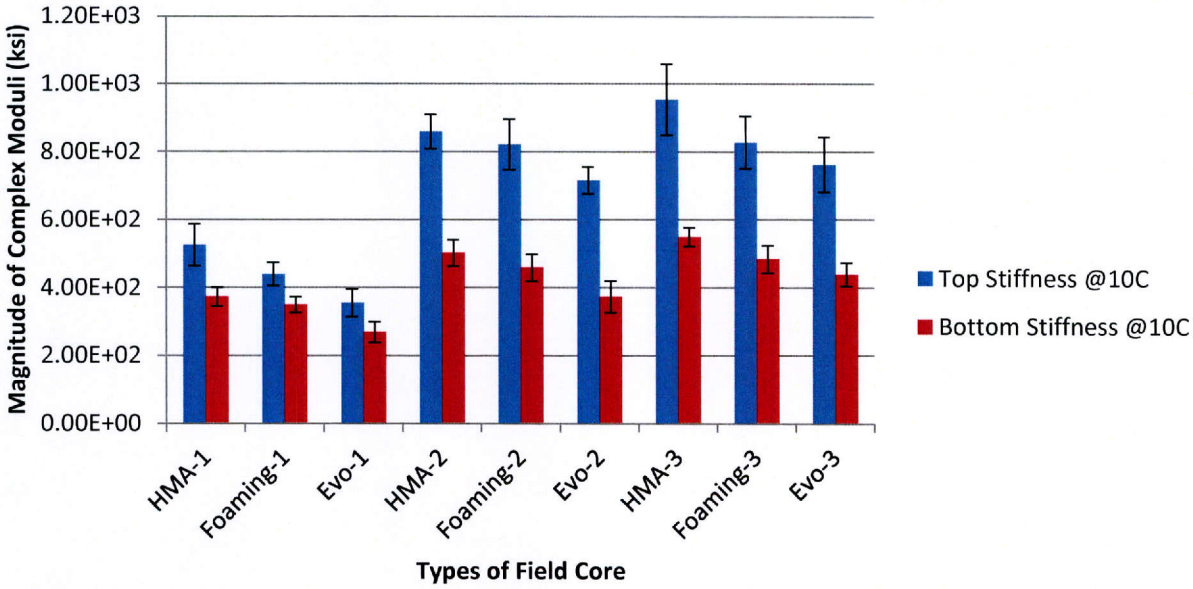

Figure 51. Average Stiffness Values of Top and Bottom Layers for Each Section.

Results for the Fracture Properties Analysis

The OT test was conducted in two steps (non-destructive and destructive) to determine the fracture and healing properties of the field specimens. The analysis methodology is based on the principles of fracture mechanics. As shown in Equations 5-8, the modified Paris's law was applied to characterize the crack propagation during the OT test. The parameters A and n are the fracture properties of the field specimens. The OT test results of the field samples are presented in Table 13. Figure 52 illustrates the variation of fracture properties A and n with the aging time.

As can be observed from Figure 52, A tended to decrease as the aging time increased. Meanwhile, the exponential parameter n increased with the aging time. No significant difference of fracture properties can be found between warm mixes and hot mix. Additionally, a linear relationship between n and –logA was detected and shown in Figure 53. It is shown that the slope of the trend lines increased with the aging time.

$$\frac{dC(N)}{d(N)} = A\left[\frac{W_R(N)}{c.s.a}\right]^n \tag{6-8}$$

where c.s.a is cracking surface area, $W_R(N)$ is the pseudo strain work for each loading cycle.

Table 13. Viscoelastic Properties of Field Samples.

Sample ID	Sample Thickness (inch)	Undamaged Modulus (ksi)	Failure Cycles	A	n
F1-13-1	1	141	221	0.035	2.38
F1-20-1	1.5	154	600+	0.027	2.61
F1-27-1	1	130	300+	0.031	2.56
F7-12-1	1	156	231	0.0145	2.38
F7-15-1	1.5	128	600+	0.022	2.15
F7-16-1	1.5	116	600+	0.0179	2.23
F8-4-1	1.5	120	600+	0.0219	2.44
F8-12-1	1.5	136	600+	0.019	2.66
F8-18-1	1.5	101	600+	0.033	2.37
S1-2-1	1.5	187	600+	0.008	3.64
S1-13-1	1	203	170	0.006	3.83
S1-24-1	1	201	36	0.0041	3.93
S7-5-1	1.5	187	600+	0.0062	3.71
S7-15-1	1	181	35	0.0033	3.86
S7-16-1	1.5	194	218	0.012	3.42
S8-4-1	1	190	105	0.0157	3.48
S8-8-1	1	182	92	0.0097	3.64
S8-12-1	1.5	176	600+	0.0083	3.75

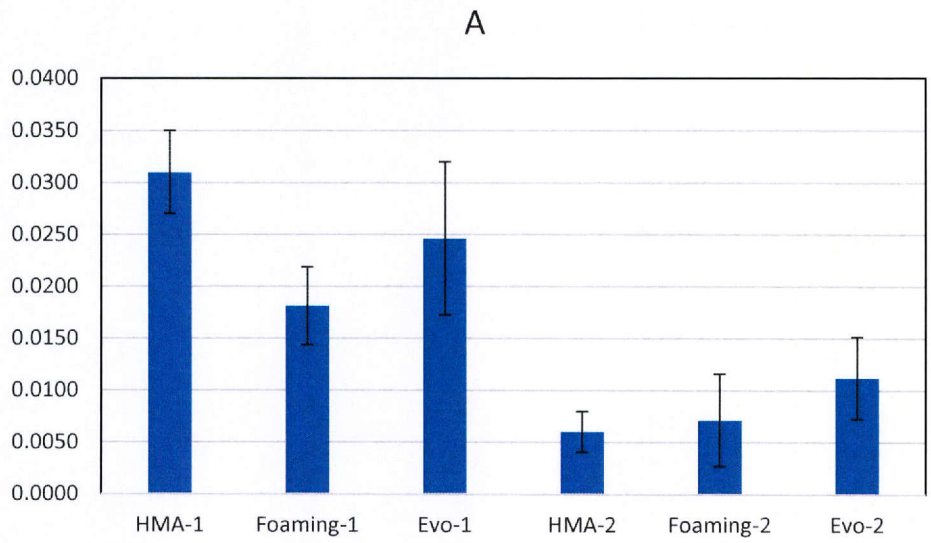

(a)

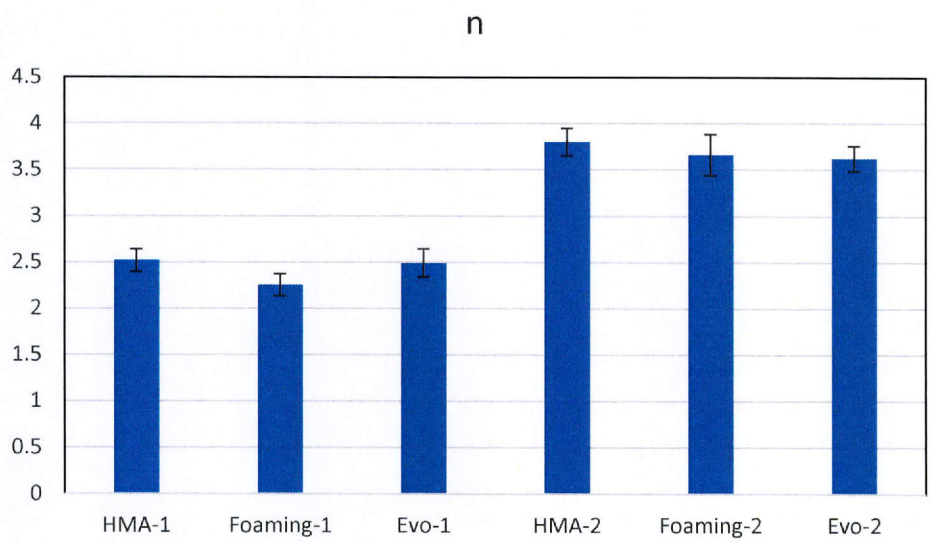

(b)

Figure 52. Variation of Fracture Properties of Field Samples with Aging Time.

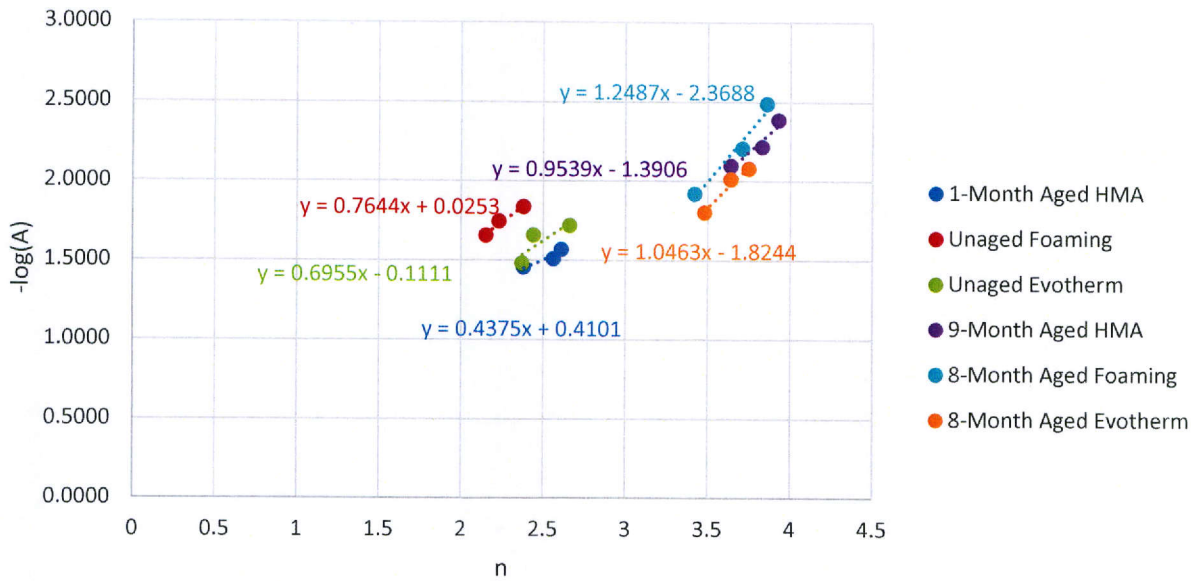

Figure 53. Correlation between n and –log(A).

Conclusion

The characterization of the viscoelastic properties of field-aged asphalt mixture is more challenging than that of the laboratory-compacted specimen because of the non-uniform aging in the asphalt layer. The VEC test was applied to characterize the stiffness gradient of field cores successfully. According to the VEC test results, the surface modulus of field-aged asphalt mixture increased much more rapidly than that of the bottom modulus after 8 month aging. The ranking order of the modulus of1 month aged field core is HMA, Foaming, and Evotherm WMA. After 8 months aging, the modulus of Foaming warm mix is close to that of hot mix, and still larger than that of Evotherm warm mix. Only slight increase of modulus can be observed from 8 months aging time to 14 months aging time. The OT test was used to determine the fracture properties of field-aged asphalt mixture on the basis of the principles of fracture mechanics. The fracture parameter A tended to decrease as the aging time increased. The exponential parameter n increased with the aging time. No significant difference of fracture properties can be found between warm mixes and hot mix. A linear relationship between n and –log(A) was detected. The slope of the trend lines increased with the aging time.

CHARACTERIZE BINDER OXIDATION AND HARDENING IN TEST SECTIONS

Introduction

A representative set of the FM 973 field cores tested above where selected for binder extraction, recovery, and evaluation. The cores were selected based on quality and availability of remaining portions. To the extent possible cores were selected for which successful overlay and VEC tests were completed for comparative purposes. For the 0/1 and 8 month samples, rounded core edge pieces were available for extraction and recover. From a binder aging point of view there is no reason to think that binder extracted and recovered from rounded edge core edge pieces would be any different than binder extracted and recovered from whole cores. For the 14 month samples, whole cores were available for extraction and recovery. Table 14 lists the exact cores and core pieces selected (for cross reference to other sections of this report).

Table 14. Selection of Core Material for Binder Extraction and Recovery.

	Section		
Aging Time [Months]	**1 (HMA)**	**7 (Foaming)**	**8 (Evotherm)**
0/1	Not Available	**Rounded** 7-16-1	**Rounded** 8-8-1
8	**Rounded** S1-2	**Rounded** S7-16	**Rounded** S8-4
14	**Whole Core** 1-3-12	**Whole Core** 7-3-13	**Whole Core** 8-3-5

The cores, or available pieces of cores, were cut into layers. Core heights were around 1.5 inches. Three layers, each a nominal 0.5 inches were cut. The layers represent material at the surface, in the middle of the lift, and at the bottom of the lift. In general it is expected that aging will proceed more quickly near the pavement surface due to higher temperatures, which increase reaction rates. Availability of oxygen may also be a factor, but in general it appears that oxygen is available at all core depths and temperature is the dominant factor.

Extraction, recovery, and evaluation was conducted following the methods described in TxDOT report 6009 Chapter 8 (Glover, 2013). In particular, the results of Burr et al. were taken into account with regards to solvent selection, and timely and complete solvent removal (Burr et al., 1990; Burr et al., 1991; Burr et al., 1993; Burr et al., 1994). A Nicolet 6700 Fourier Transform Infrared Spectroscopy spectrometer was used to measure the carbonyl area and a DSR machine was used to measure the rheological property DSR function. A Carri-med CSL 500 controlled stress rheometer was used to measure the rheological property DSR function. The DSR function measurement was made at 44.7°C and 10 rad/s, in the time-sweep mode. A 2.5-cm composite parallel plate geometry was used with a 500 μm gap between the plates.

Table 15 shows the results of the FTIR and DSR measurements for the extracted and recovered binder from selected FM973 Field Cores. Measurements on the neat binder are also provided here for easy comparison. The rounded pieces and the whole cores are assumed to be equivalent, but for completeness the samples are labeled appropriately.

Table 15. FTIR and DSR Results for Extracted and Recovered Binder.

Aging Time [Months]	Section								
	1 (HMA)			7 (Foaming)			8 (Evotherm)		
Original	Zero Aging Time POV Tray			Zero Aging Time POV Tray			Zero Aging Time POV Tray		
	FTIR [arb. unit]	DSR [MPa/s]		FTIR [arb. unit]	DSR [MPa/s]		FTIR [arb. unit]	DSR [MPa/s]	
	0.56	2.13E-05		0.57	3.67E-05		0.58	1.97E-05	
0/1	Rounded			Rounded 7-16-1			Rounded 8-8-1		
	N/A			Layer	FTIR [arb. unit]	DSR [MPa/s]	Layer	FTIR [arb. unit]	DSR [MPa/s]
				1	0.78	1.49E-04	1	0.79	1.31E-04
				2	0.70	1.03E-04	2	0.68	5.74E-05
				3	0.67	7.95E-05	3	0.76	1.11E-04
8	Rounded S1-2			Rounded S7-16			Rounded S8-4		
	Layer	FTIR [arb. unit]	DSR [MPa/s]	Layer	FTIR [arb. unit]	DSR [MPa/s]	Layer	FTIR [arb. unit]	DSR [MPa/s]
	1	0.90	3.62E-04	1	0.94	2.21E-04	1	0.91	3.21E-04
	2	0.86	2.20E-04	2	0.80	2.71E-04	2	0.79	1.33E-04
	3	0.86	2.03E-04	3	0.84	4.00E-04	3	0.80	1.84E-04
14	Whole Core 1-3-12			Whole Core 7-3-13			Whole Core 8-3-5		
	Layer	FTIR [arb. unit]	DSR [MPa/s]	Layer	FTIR [arb. unit]	DSR [MPa/s]	Layer	FTIR [arb. unit]	DSR [MPa/s]
	1	0.95	2.01E-04	1	0.89	1.81E-04	1	0.86	1.89E-04
	2	0.88	1.72E-04	2	0.82	2.24E-04	2	0.79	1.91E-04
	3	0.87	2.02E-04	3	0.95	3.00E-04	3	0.83	1.89E-04

Most, if not all of the measurable, aging occurred during construction and the first 8 months. The construction process appears to have increased CA levels between about 0.1 CA to 0.2 CA. The first 8 months of aging saw another jump of approximately 0.15 CA. This makes sense because the pavements were constructed in December and January. The first 8 months encompassed a summer when pavement oxidation occurs most rapidly due to high temperatures. The remaining 6 month before the 14 month coring were primarily cooler months.

From the above table in can be seen that differences in binder aging between the control HMA cores and the two WMA cores are comparable. Total aging for all three types of pavements in terms of CA was about 0.35 CA. In terms of rheology, the binder DSR function increased essentially as expected from the known linear relationship between binder CA levels

and DSR function values. The near equivalence of aging between the three pavement materials is expected from the results of the kinetics studies which showed similar reaction kinetics parameters.

Despite the relatively short aging period, aging model predictions made (reported earlier in this report) were fairly accurate. The predictions put CA levels at around 1 after approximately 1 year of again. The above results show CA levels were around 0.9 CA at this time. Early period aging is generally difficult because of the complicating factors of construction aging and fast-rate kinetics. The slight over prediction here could be contributed to the use of a field calibration factor ("fcf") of 5. While this is a typical value, a reduction in this value would give a more perfect match at the end of the first year of aging. Since the pavement aging period was relatively short, adjustment of the field calibration factor for long term predictions is a bit uncertain, but without further information a slight downward adjustment of the fcf is suggested.

CHAPTER 7. INTRODUCTION TO THE STANDARD METHOD FOR MEASURING ABSORPTION WITH STATISTICAL DISCUSSION

ABSTRACT

To determine whether significant differences exist between WMA and HMA binder absorption, method precision must be carefully considered. The most popular approach for determining binder absorption uses standard methods and practice (ASTM D4469, AASHTO T84 and AASHTO T85). Using these methods, binder density, binder content, bulk specific gravity and theoretical maximum specific gravity are measured, and binder absorption is calculated using the standard practice D4469. However, precision and bias statements for binder absorption are not included.

In this chapter, water and binder absorption background concepts and procedures are reviewed. Also, statistical analyses are presented. This chapter provides detailed information about the sources of error and the precision of the various standard methods that are used to measure asphalt binder absorption in aggregates.

INTRODUCTION

One objective of this project is to determine if, and by how much, asphalt absorption is reduced by the lower temperatures used in the warm mix process, compared to hot mix temperatures.

The precision with which absorption measurements can be made is a critical issue because of the desire to detect, not just values of absorption, but also differences between warm mix absorption and hot mix absorption. If the accuracy and precision of absorption measurements are not high enough in the presence of relatively small differences between warm mix and hot mix absorption, then no determination of the differences will be possible. These precision issues also compound the difficulty of measuring increases in absorption over time which may be overwhelmed by measurement error.

OBJECTIVES

The objectives of this work were:

- To study the standard procedure for measuring binder absorption.
- To understand the sources and magnitudes of error in binder absorption measurements.
- To estimate the statistical precision of binder absorption that derives from standard methods.
- To provide an improved understanding of the level of precision required for binder absorption and issues that might be addressed to achieve improvement.

BACKGROUND

Concepts of Mixture Properties

When a sample of HMA/WMA is prepared in the laboratory, it is analyzed to determine the probable performance in a pavement structure. The analysis focuses on five volumetric

characteristics and the influence those characteristics are likely to have on HMA/WMA behavior. The five characteristics are:

- Mixture Density
- Air Voids
- Voids in the Mineral Aggregate (VMA)
- Voids Filled with Asphalt (VFA)
- Binder Content

Mixture properties are most affected by volume rather than weight; however, production and testing of HMA/WMA are by weight. Weight and volume properties of HMA/WMA are given in Figure 54. Example volumetric properties that determine long term pavement performance of HMA and WMA are air Voids, voids in mineral aggregate (VMA), and voids filled with asphalt (VFA).

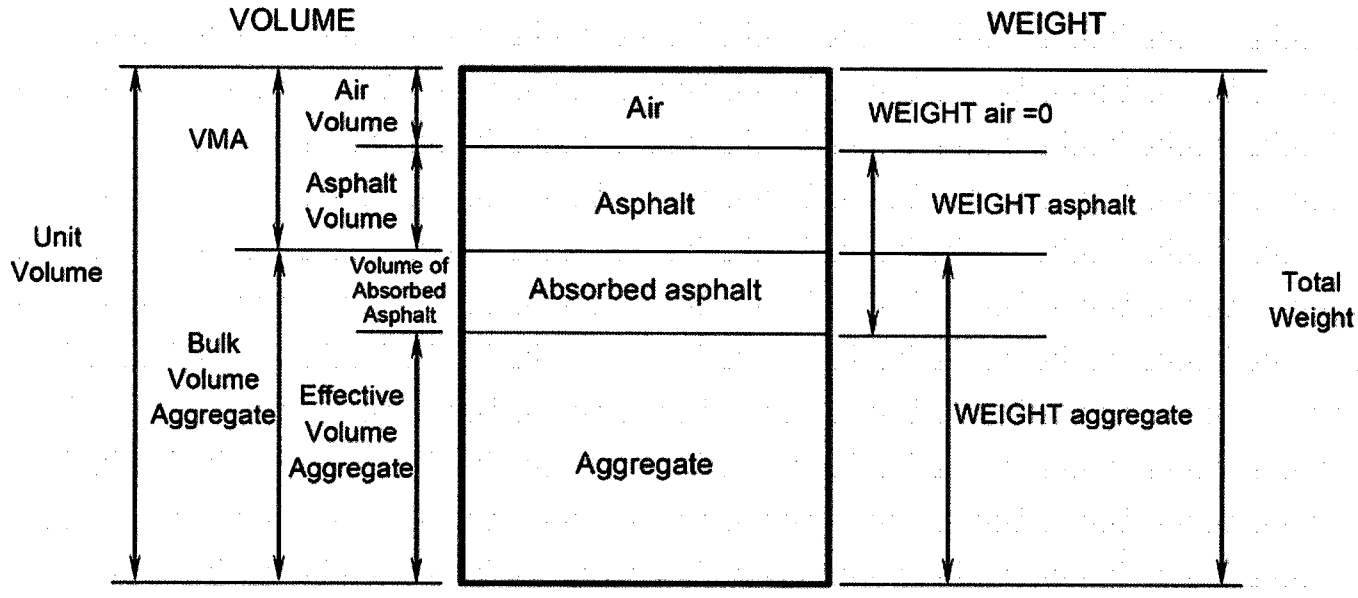

Figure 54. Component Diagram of Compacted Sample.

Background and Literature

One issue with warm mix asphalt processes is if, and by how much, asphalt absorption is reduced by the lower temperatures used in warm mix processes, compared to hot mix temperatures. Asphalt absorption can be beneficial by providing mechanical interlocking between asphalt and aggregate. On the other hand, excessive absorption that is not compensated for by additional binder reduces the asphalt available for filling (to the appropriate degree) the interstitial voids among aggregate, thereby yielding a too-thin asphalt film that is more susceptible to raveling and weathering. And going too far by providing too much asphalt for the interstitial voids leads to permanent deformation (rutting) and perhaps bleeding of asphalt at the surface, a severe safety hazard. Finally, a highly absorptive aggregate carries a penalty cost in that the extra binder required to produce the correct volumetric properties adds cost to the pavement design. Therefore, achieving the right balance between not providing enough asphalt

in the presence of absorption and providing too much is a critical part of the mixture design process. Incorrect estimates of asphalt absorption translate to erroneous calculations of air voids, VFA, and VMA, all important parameters used in mixture design to control pavement durability and stability.

Asphalt absorption depends on asphalt properties, such as composition, viscosity, and surface energy. Aggregate properties reported to be relevant to absorption include porosity, permeability, pore size distribution, surface area, roughness, presence of fines, aggregate size distribution (gradation), and surface chemical composition (Lee et al., 1993a). A discussion of various laboratory methods available to measure these aggregate properties can be found elsewhere (Lee et al., 1993b). The presence or absence of water also influences the degree of absorption. The driving force of asphalt into the aggregate pores is mainly determined by capillary action and thus absorption is expected to be a nonlinear function of time. Additionally, the issue of preferential absorption is a concern because the absorbed and non-absorbed fractions of the asphalt may have different rheological, physical, chemical, and aging characteristics. The amount of absorption is of interest as it affects the amount of asphalt needed for a durable mix design; preferential absorption is of interest to the extent it changes the asphalt composition of the remaining interstitial asphalt and thereby affects pavement durability.

Fundamental to accurate measurements of absorption and preferential absorption is the precision with which absorption measurements can be made. This is a critical issue especially when the desire is to detect, not just values of absorption, but also differences between warm mix absorption and hot mix absorption. If the accuracy and precision of absorption measurements are not high enough, and if the differences between warm mix and hot mix absorption are small enough, then no determination of the differences will be possible. These precision issues also compound measurements of absorption over time, since changes over time may be overwhelmed by measurement error.

Water Absorption

In principle, measuring water absorption is straightforward. Water absorbed into the pores of aggregate is simply the weight of the saturated aggregate (i.e., aggregate plus absorbed water) less the weight of the dry aggregate, expressed per weight of dry aggregate. However, accurate measurements are complicated by the issue of determining the saturated weight absent surface (non-absorbed) water. Furthermore, the smaller the water absorption, the greater precision that is required in measuring the weights in order to determine absorption to within a reasonable accuracy. Finally, in order to define absorption, one must accurately be able to determine the volume of voids inside the aggregate that are able to absorb water, i.e., accurate measurements of the aggregate bulk specific gravity versus its apparent specific gravity are essential. All of these issues pose challenges to the precision of water absorption measurements.

Measurement precision is therefore fundamental to accurate absorption determinations, and any issue that reduces precision jeopardizes meaningful determinations. In the case of direct measurements of water absorption, either excess water coating the saturated aggregate or excessive drying of the surface to remove the coating that results in removal of absorbed water from pores, are the major sources of error. Saturated surface dry (SSD) methods (ASTM C 127 and C 128 for coarse and fine aggregates, respectively) attempt to achieve exactly the correct surface dry condition, but the methods are subjective and therefore the reproducibly is difficult.

To avoid the complication of errors in surface dry determinations, other methods require total immersion of the aggregate in water and measurements either of the immersed volume in water or the submerged weight in water. An example of this method is the Corelok® AggPlus System, where two oven-dried aggregate samples are used; one sample is subjected to vacuum and then submerged in water to determine its apparent density and the other is submerged in water inside a calibrated volume to determine its bulk specific gravity. The combination of the results of both tests is used to calculate aggregate absorption. A study comparing the vacuum-sealing method vs. the standard AASHTO methods found that the standard deviation of replicate tests was lower for the vacuum-sealing method. In addition, a good correlation was observed between test results performed on aggregate blends in the vacuum-sealing method and test results obtained after mathematically combining values of the individual aggregate fractions as prescribed by the standard AASHTO methods. However, further refinement was recommended because some of the results were statistically different and the vacuum-sealing method tended to systematically underestimate the value of absorption (especially for higher absorption values) and overestimate the apparent and bulk specific gravities (Hall, 2004).

Other challenges associated with water displacement methods include the precision of the volume measurements (inherently less precise than weight) plus the requirement of a bulk volume of the specimen (without water absorption). This volume is difficult to measure accurately because water immersion immediately results in encroachment of water into the pores. One approach is to determine the weight in water over time as aggregate absorbs water and extrapolating back to time zero to obtain the zero-absorption value (Kandhal and Lee, 1972; Lee, 1971). Finally, a measurement of ultimate absorption potential is desirable but somewhat difficult to achieve because air in dead-end pores prevents total absorption. Evacuating the air before saturation can be used to achieve total absorption but there still remains the difficulty of obtaining an accurate measurement of the weight with zero absorption.

Given these challenges, water absorption methods are still being evaluated with respect to accuracy, precision, usability, and cost. NCHRP 4-35 is an ongoing effort on "Improved Test Methods for Specific Gravity and Absorption of Coarse and Fine Aggregate." AASHTO T 85 for coarse aggregates and T 84 for fine aggregates indicate absorption measurements with one standard deviation (SD) of about 0.1 percentage point up to an absorption level of 2.5 percent for coarse aggregate and one percent for fine aggregate (percent water absorption is 100 x mass of water absorbed per mass of aggregate). So, if coarse aggregate water absorption is 2.5 percent, then 1 SD variation would be from about 2.4 to 2.6 percent. For fine aggregate absorption of 1 percent, 1 SD variation would range from about 0.9 to 1.1 percent. These levels of precision might be good enough to assess differences between HMA and WMA absorption if they were representative of asphalt absorption as well. However, as discussed subsequently, there are additional challenges with asphalt measurements that result in significantly reduced precision.

Previous Research on Water Absorption

Hughes and Bahramian (1967) recognized that the standard methods available for determining water absorption (i.e., ASTM C 127 and C 128) were subjective and that the results varied when individual aggregate size fractions were tested separately versus tests performed on single continuously graded material. Therefore, they proposed a saturated air laboratory test method for determining the absorption of aggregates. The method, based on principles of vapor absorption in capillary tubes, achieved an accurate SSD aggregate condition by circulating

saturated air over wet aggregates. The authors observed that periodic weight measurements of wet aggregates that were subjected to drying conditions followed a characteristic trend: a faster initial rate of moisture loss up to a clear inflection point where the rate decreased significantly. The inflection point was labeled the "critical absorption value" and defined as the point of transition from moisture escaping from the surface of the aggregates to moisture escaping from the pore within the aggregates (i.e., the SSD condition). The rate of moisture loss after the critical absorption value was controlled by the aggregate pore size and relative humidity of the saturated air stream.

The saturated air laboratory test method consisted of soaking the aggregate samples for 24 hours, drying them to an approximate SSD condition based on the standard methods, placing them in a container of known weight, measuring the aggregate sample weight, and placing it inside the test apparatus. During the test, a constant air flow rate at a fixed relative humidity is drawn over the aggregate using a vacuum pump. The aggregate sample was weighed at periodic intervals of about 15–30 min (depending on the number of simultaneous samples being tested) until the critical condition was detected. Afterward, the sample was oven dried at 110°C for 24 hr and its weight measured again. The percent absorption was calculated as:

$$\% \text{ Absorption} = 100 \frac{W_{\text{critical}} - W_{\text{oven dry}}}{W_{\text{oven dry}}} \tag{7-1}$$

Tests were performed by Hughes and Bahramian (1967) at constant relative humidity while varying the temperature and also at a constant temperature with varying relative humidity. The critical absorption value did not change with different temperatures, but it did change with different relative humidity values. The higher the relative humidity, the higher the absorption value due to the decreased rate of moisture loss from the aggregate. Another set of tests was conducted with varying relative humidity but using a sample of dry aggregates. As expected, the time required to reach the critical absorption value was longer, and the absorption values were always below the values obtained when wet aggregates were employed.

Comparison of the saturated air method to the standard ASTM C 128 test method showed less variability in the results and lower percent absorption values. In addition, the saturated air method yielded consistent results when individual aggregate fractions and single continuous graded material were tested.

Asphalt Absorption

Complicating the measurement of asphalt absorption, compared to water absorption and in addition to the issues mentioned above, are ease-of-handling factors including higher asphalt viscosity compared to that of water (even at HMA temperatures), asphalt stickiness, and the wettability of aggregate by asphalt. These issues make establishing an accurate SSD condition with asphalt impossible. And each time the asphalt-coated aggregate is handled, asphalt will be lost, creating error in the asphalt mass measurement, so care must be taken to measure the various mixture weights required by the methods without intermediate handling.

The conventional standard method for determining asphalt absorption in pavement mixtures, ASTM D 4469, uses specific gravity determinations (ASTM C 127, C 128, and D

2041), together with asphalt content (ASTM D 2172) and asphalt density (ASTM D 3289, ASTM D 3142 or ASTM 3142). Volumetric properties of compacted paving mixtures use the following expression to estimate asphalt absorption:

$$P_{ba} = 100 \frac{G_{se} - G_{sb}}{G_{sb} G_{se}} G_b \tag{7-2}$$

where:
P_{ba} = absorbed asphalt expressed in percent by weight of aggregate.
G_{se} = effective specific gravity of the aggregate.
G_{sb} = bulk specific gravity of the aggregate.
G_b = specific gravity of the asphalt.

The effective specific gravity of the aggregate includes all void spaces in the aggregates except those that absorb asphalt. G_{se} is determined as follows:

$$G_{se} = \frac{P_{mm} - P_b}{\frac{P_{mm}}{G_{mm}} - \frac{P_b}{G_b}} \tag{7-3}$$

where:
P_{mm} = percent by weight of total loose mixture (i.e., 100 percent).
P_b = asphalt content expressed in percent by total weight of mixture.
G_{mm} = maximum theoretical specific gravity of the mixture (ASTM D 2041).

The bulk specific gravity of the asphalt (G_b) is usually determined with AASHTO T 228 or ASTM D 70 standard method. The bulk specific gravity of the aggregate (G_{sb}) is determined by combining fractions of coarse aggregate, fine aggregate, and mineral filler based on their individual percentages and bulk specific gravities:

$$G_{sb} = \frac{P_1 + P_2 + \cdots + P_n}{\frac{P_1}{G_1} + \frac{P_2}{G_2} + \cdots + \frac{P_n}{G_n}} \tag{7-4}$$

where:
G_{sb} = bulk specific gravity for the total aggregate.
P_1, P_2, P_n = individual aggregate percentages by weight of aggregate.
G_1, G_2, G_n = individual aggregate bulk specific gravities.

The individual bulk specific gravity of the coarse aggregate is determined with AASHTO T 85 or ASTM C 127, for the fine aggregate AASHTO T 84 or ASTM C 128 is used, and for the mineral filler AASHTO T 100 or ASTM D 854 is the standard method.

The standard test methods listed above usually suffer from the same accuracy problems as the methods used to estimate water absorption methods. As noted by Lee, et al. (1990), "Using the acceptable ranges of two results by a single operator specified by ASTM of 0.011for G_{mm} and 0.025 for G_{sb}, for a range of asphalt contents between 5–7 percent, the calculated

asphalt absorption can vary up to 1.1 percent by weight...of the aggregate." In a mixture that is 94 percent aggregate and 6 percent asphalt (of which 1 percentage point, say, is absorbed in the aggregate), then that 1.1 percent of the aggregate weight error would translate to approximately 20 percent of the interstitial asphalt in the mix. Thus the amount of this error (uncertainty) in the measurement would be comparable to the total amount of absorption. Of course, for more absorptive aggregates, this measurement error would translate to a smaller percentage of the total absorption; if the total absorption is 4 percent of the aggregate weight (probably a value that is at the high end of typical absorption range) then the 1 percent uncertainty would be 25 percent of the amount absorbed. Then, to measure differences between warm mix and hot mix absorption within the context of this variability is also challenging. More recent reproducibility values (2008 Annual Book of ASTM Standards) are consistent with those above (G_{mm}: 0.023, G_{sb}: 0.035 by vacuum sealing; 0.023 for 12.5 mm nominal maximum aggregate size). In actuality, the Rice method more typically produces a variability of 0.2–0.4 percent, less than half the value determined from the ASTM indicated errors (Kandhal and Khatri, 1991). Other methods (immersion method of Goshorn and Williams, 1942, and the bulk impregnated method of the U.S. Corps of Engineers, 1954 and Ricketts et al., 1954) provide comparable variability.

The challenge of accurately determining asphalt absorption is further supported by ASTM D 4469 in a table that indicates the effect of measurement errors on absorption calculations. Using typical measurement values for each variable and reported ASTM reproducibility precision limits for each variable in the method's calculation, the method reports that due to random measurement errors, an example calculated value of asphalt absorption may range from −0.38 to +3.05 percent (of dry aggregate weight). While this method is for pavement mixtures and the errors can be better controlled in the laboratory, the same fundamental difficulties exist for measurements on laboratory specimens. These ranges of uncertainty make the determination of differences between warm mix and hot mix asphalt absorption problematic.

If measuring the amount of absorption is difficult, then measuring preferential absorption is even much more so, especially because, along with composition changes due to preferential absorption (if it occurs), are the composition changes due to asphalt oxidation which most certainly are affected by the hot aggregate surface.

Previous Research on Asphalt Absorption

For many decades, asphalt absorption has been a topic of interest among the asphalt research community. Researchers have been interested in developing test methods and models to measure and predict asphalt absorption as well as to understand the aggregate characteristics (i.e., physical and chemical properties) that have an impact on the absorption process.

One of the first attempts at evaluating asphalt absorption by aggregates was through the correlation with kerosene absorption. Hveem (1942) developed the centrifuge kerosene equivalent (CKE) test, which measures the kerosene quantity absorbed by an aggregate sample under soaking and applied centrifuge force. The CKE standard test method (ASTM D 5148) determines the percent kerosene absorbed by the fine aggregate fraction, the percent oil absorbed by the coarse aggregate fraction, and a combined index (designated as the *K* factor) that indicates the relative particle roughness and surface capacity of the combined aggregates based on porosity. Both aggregate fractions are first dried to constant weight at 230°F and the test is

performed at elevated temperatures (140°F) when the oil is soaking into the coarse aggregate fraction to simulate HMA production.

Goshorn and Williams (1942) also developed a method to measure asphalt absorption. The Immersion Method, which was later considered to produce maximum absorption values yet not realistic values expected in conventional HMA, consisted of heating a coarse aggregate sample to 300°F, placing it in a wire basket, and submerging it in an asphalt bath heated at 275°F for 2 hours. The immersed sample was then cooled to room temperature and then reheated to 275°F for 1 additional hour. The basked was then removed from the asphalt bath and allowed to drain in air at 275°F. After cooling, the coarse aggregate sample was removed from the basket and weighed in air and under water. The absorption was calculated as follows:

$$P_{ba} = \frac{(W_{coat\ agg} - W_{dry\ agg}) - \left((W_{coat\ agg} - W_{coat\ agg\ sub}) - (W_{agg\ SSD} - W_{sat\ agg})G_b\right)}{W_{agg\ dry}} \tag{7-5}$$

A similar procedure was developed for fine aggregate but using a flask rather than a wire basket and subjecting the mix of fine aggregate and hot asphalt to vacuum to remove the entrapped air.

A few years later, Ricketts et al. (1954) as part of a U.S. Corps of Engineers study (U.S. Corp of Engineers, 1954), developed the Bulk Impregnated Specific Gravity Method. The procedure prescribed heating an aggregate sample to constant weight and slowly adding it to a gallon pail of asphalt heated to 280°F that had been previously weighed in air and submerged in water. After 2 minutes of mixing, the contents were cooled and weighed in air and under water. The dry weight of the aggregate, the weight of the asphalt-filled pail in air and submerged in water, and the weight of the mixture in air and submerged in water is used to estimate asphalt absorption using the following relationship (G_{sbi} is the bulk impregnated specific gravity):

$$G_{sbi} = \frac{W_{dry\ agg}}{(W_{mixture\ dry} - W_{mixture\ sub}) - (W_{pail\ dry} - W_{pail\ sub})} \tag{7-6}$$

$$P_{ba} = \left(\frac{1}{G_{sb}} - \frac{1}{G_{sbi}}\right) G_b \tag{7-7}$$

One of the first comprehensive evaluations of the absorption methods described above was done by Lee (1969). Using eight different aggregates (absorptive limestone, non-absorptive limestone, pit-run gravel, and carbonate rocks) and six different asphalts with a range of penetration values, the author measured several physical and chemical properties including bulk and apparent specific gravities, water absorption, CKE, oil capacity, total porosity, pore-size distribution, and chemical/mineral composition. Absorption measurements were done using the Immersion, Bulk Impregnated Specific Gravity, and Rice methods. The bulk, apparent, water absorption, CKE, and oil capacity were determined via the standard ASTM methods. The total porosity was determined with powder density measurements made on the coarse aggregate fraction. The pore-size distribution was determined with the mercury porosimeter measurements

and the mineral composition by the ethylene diamine tetraacetic Acid (EDTA) and X-ray diffraction methods.

Lee (1969) found that the absorption values obtained with the Immersion Method were higher likely due to the unlimited supply of asphalt at low viscosity for an extended period. The absorption results in the Immersion Method increased with time at a decreasing rate, with most of it occurring during the first minutes of the test. The viscosity of the asphalt also had an effect on the level of absorption with lower viscosities yielding higher absorption values. Also, regardless of the absorption method used, there was a high degree of variability among different particles belonging to the same aggregate type. The author explained this behavior based on the mineral composition of the aggregate and the porosity and pore-size distribution in each particle. A good correlation was observed between water absorption and binder absorption, with binder absorption ranging between 50–80 percent of the water absorption values, yet it was recommended to use water absorption values just as an indicator of *potential* asphalt absorption. The correlation between binder absorption and CKE and oil capacity was not as strong as the correlation with water absorption was. The best correlation was observed between absorption and porosity and pore size distribution for pores larger than 0.5μm. The Immersion Method was considered to provide the maximum potential asphalt absorption, the Bulk Impregnated Specific Gravity method the maximum practical absorption, and the Rice Method the minimum practical asphalt absorption.

In a subsequent study, six Iowa limestone aggregates (crushed rock and cylinders) and two asphalts (low and high penetration values) were used to evaluate the effects of asphalt absorption on mixtures, establish a criteria for specifying aggregates used in mixtures with regard to asphalt absorption, and to develop remedies for utilizing absorptive aggregates in asphalt mixtures (Lee, 1971). Aggregate absorption was evaluated with respect to water, CKE, oil, asphalt (Rice, Bulk-Impregnated Specific Gravity, and Immersion methods), and the photometer (dye) method. The water, CKE, and oil methods were not recommended as indirect asphalt absorption methods due to their poor reliability. The photometer method (reduction of asphalt concentration due to absorption of the asphalt by the aggregate that results in a change in the absorbance of the solution) was found to have a good correlation to asphalt absorption with the advantage that various asphalt sizes and gradations could be analyzed. The independent factors considered for the asphalt absorption study were asphalt type, aggregate type and size, temperature, and absorption time. The most important factors that controlled asphalt absorption were total porosity and pore-size distribution of the aggregate, viscosity of the asphalt, and absorption time. The absorption versus time curves measured via the Rice method showed an exponential relationship, with most of the absorption occurring during the first 10–30 days and leveling off after about 3 months. The absorption trend increased with time (at a decreasing rate) and with higher temperature (i.e., lower asphalt viscosity). A later study by Kandhal and Koehler (1985) confirmed the absorption versus time exponential relationship.

The issue of pore-size distribution related to the degree of asphalt absorption was further studied by Kandhal and Lee (1972). They applied the mercury porosimetry method to evaluate the effective porosity (i.e., interconnected pores), pore size distribution, and pore-volume distribution of limestone aggregate cores obtained from six different quarries in the state of Iowa. The authors correlated the pore characteristic to asphalt absorption measurements performed using the Immersion Method and the Bulk Impregnated Specific Gravity Method. Based on regression analysis, they established that pore sizes between 0.1–0.05μm controlled the amount

of water absorption, while larger pore sizes between 0.7–0.05μm controlled asphalt absorption. A similar study by Kandhal and Khatri (1992) performed on various aggregates and asphalt SHRP materials confirmed that a pore diameter of 0.05μm was the threshold size below which no apparent asphalt absorption occurred.

In another research study, Kandhal and Khatri (1991) applied the Immersion, the Bulk Impregnated Specific Gravity, and the Rice methods to measure the absorption of 3 standard aggregates used in the Strategic Highway Research Program (SHRP). Certain modifications were done to the methods; the Immersion test was done without reheating, submerging for 1 and 3 hours, at a temperature of 290°F, and the measurements performed without removing the aggregate sample from the wire basket. The Bulk Impregnated Specific Gravity was also modified by using a smaller aggregate and binder sample size and a test temperature of 290°F. The Rice maximum specific gravity method was used to study the time-dependent behavior of absorption by aging the asphalt mixtures for 1, 2, 4, 6, and 8 hours at 290°F. The materials that were tested consisted of 3 aggregates (McAdam limestone with high water absorption, Watsonville granite with medium water absorption, and Frederick Limestone with low water absorption), glass beads (to evaluate operator and procedural errors), and two asphalts (AAM-1 – AC-20 from West Texas and AAB-2 – low viscosity AC-5 from Wyoming Sour). Only coarse aggregate fractions (3/8–1/2 in) were considered.

The authors confirmed that the Immersion Method produced the highest absorption values and the time-dependency of the absorption mechanism since after 3 hours of immersion the results were significantly higher than after1 hour of immersion (Kandhal and Khatri, 1991). In addition, as expected, the lower-viscosity asphalt (AAB-2) yielded higher absorption values. With respect to aging, asphalt absorption increased with aging time following a hyperbolic curve trend (see equation below). The absorption values obtained with the Rice method after 8 hours of oven aging were similar to the ones obtained after 1 hour of immersion with the Immersion Method, and the absorption results after about 4 hours of oven aging were similar to the ones obtained with the Bulk Impregnated Specific Gravity Method. The rate of absorption decreased after about 4 hours of oven aging and thus the authors' recommendation was to measure absorption after a 4-hour aging period. With available absorption measurements at zero time and two other aging times the following equation was recommended to estimate asphalt absorption at other aging times:

$$A = A_0 + \frac{t}{a+bt} \tag{7-8}$$

where:
A = asphalt absorption at any given time t
A_0 = asphalt absorption at time zero

$$a = \frac{t_1 t_2}{t_2 - t_1}\left(\frac{1}{\Delta A_1} - \frac{1}{\Delta A_2}\right)$$

$$b = \frac{1}{t_2 - t_1}\left(\frac{t_2}{\Delta A_2} - \frac{t_1}{\Delta A_1}\right)$$

$\Delta A_1 = A_1 - A_0$
$\Delta A_2 = A_2 - A_0$

In addition, the maximum value of absorption was estimated as follows:

$$A_1 = A_0 + \frac{1}{b} \tag{7-9}$$

Also related to absorption time, Musselman et al. (2001) studied the effect of laboratory conditioning/curing time on asphalt absorption. They observed that many asphalt mixtures in Florida that were designed using the Superpave method were failing during the quality control (QC) and quality acceptance (QA) tests due to low air voids and VMA. Their hypothesis was that since the QC and QA tests were done at the plant, immediately after production, the absorption time was not sufficient or equivalent to the absorption time the mixtures experienced during design, especially because the main type of aggregate used was absorptive Florida limestone. They measured the asphalt absorption and air void content of 7 mixtures prepared with limestone aggregates from various parts of the state that were laboratory mixed laboratory compacted (LMLC) and subjected to the standard design conditioning/curing condition and plant mixed laboratory compacted (PMLC) with no conditioning/curing, after haul time, and after 1 hour, and 2 hours of conditioning/curing. The results were compared against measurements performed on field cores. The PMLC mixtures with no conditioning/curing underestimated the air void content of absorptive mixtures by approximately 0.5 percent for absorptive aggregates and by 0.25 percent for non-absorptive aggregates. Based on their observations, the recommendation was to continue the standard conditioning/curing for mixture design and to implement a 1 hour conditioning/curing for PMLC mixtures before compaction.

With regard to asphalt absorption modeling, Guin et al. (1992) used a physicochemical model to predict asphalt absorption and compared it to measurements on model liquids, asphalt, alumina aggregates, and limestone. The selected model, which was developed by Wade et al. (1978) to describe the rate of liquid absorption by an evacuated porous sphere, is based on material balance, pressure drop and flow rate (Darcy's Law), and capillary pressure. Thus, the advantage was that parameters related to the liquid asphalt and aggregate properties were included. The model expression used was:

$$t_d = \frac{r\sigma t \cos\theta}{4\mu R^2 T^2} = \frac{t\sigma}{4\mu} C_{agg} \tag{7-10}$$

where:
t_d = dimensionless time
r = pore radius
σ = surface tension
t = time of absorption
θ = contact angle
μ = liquid viscosity
R = radius of the spherical aggregate
T = tortuosity
C_{agg} = constant that depends on aggregate properties

According to the model, absorption is a function of the properties of the liquid (σ, μ), the properties of the aggregate (r, R, and T), and the wettability of the aggregate by the liquid (θ). The time required for absorption is directly proportional to the viscosity of the liquid and the aggregate size (squared), and inversely proportional to the pore radius. Temperature is not directly included in the expression, but taken into account indirectly as a function of the viscosity and surface tension. Some of the limitations of the model with respect to its application to the experiments performed by Guin et al. (1992) were that it did not account for the aggregate pore size distribution and that it considered that the voids were subjected to vacuum rather than initially filled with air or water. In addition, the authors assumed that the contact angle was constant between the aggregate and all liquids and thus C_{agg} was the same for all liquid-aggregate combinations.

Two methods were used to measure absorption and correlate it to the model predictions. One was a pycnometer method (conservation of volume) and the other a buoyancy method (change in buoyant force). Porous synthetic alumina and natural limestone aggregates submerged in glycerol-water solutions, decane, ethanol, and water were tested using both methods. During the test, the fluid properties were kept at a constant temperature to avoid changes in their properties. When asphalt was used, a nitrogen purge was introduced in the buoyancy method to prevent oxidation. The results from both methods provided similar results. When absorption vs. actual time data was used, the time range was very wide from a few minutes to many hours for the same absorption value. The authors attributed this behavior to the wide range of liquid properties, especially viscosity. When dimensionless time was used (i.e., *td*), the data from the different liquids aligned closer together and the remaining variability was explained by the authors as a function of the contact angle between aggregates and the liquids, which was assumed to be equal for all liquids in the calculations. For the natural porous limestone aggregate (cylindrical core specimens) the results did not follow the model approximation, achieving high values of absorption rapidly and not showing a significant increase afterwards. The reasons for this behavior were attributed to trapped air in the pores, the non uniform pore size distribution within the aggregate, the natural variability of the aggregate specimens, and the shape of the specimens (i.e., cylindrical vs. spherical).

Previous Research on Selective Asphalt Absorption

One of the earliest studies regarding selective asphalt absorption was done by Lettier et al. (1949). They measured the absorption properties of dolomite, calcite, and quartz aggregates that were used in two pavement field projects that showed early distress and where asphalt absorption by the aggregate was hypothesized as the main cause of the observed failures. One field project was located in the Wabash River Valley and used 5 percent PEN 60/70 asphalt and local crushed dolomite stone and sand. During mixture production, the stone was difficult to dry and tended to absorb all the supplied asphalt, yielding a mixture that lacked tackiness. In addition, individual aggregate particles appeared dry in the mixture and were easily dislodged from the pavement surface after compaction. From visual inspection of aggregates extracted from forensic field cores, it was determined that the depth of asphalt absorption into the aggregate was between 1/16-3/16 in. The other field project was located in the Missouri River Valley and used an MC-1 cutback asphalt and calcite aggregate. Soon after construction, sections of the road began showing signs of raveling even though limited amount of traffic was allowed. Visual examination of aggregate particles that became dislodged from the surface of

the pavement indicated that the failure of the pavement was possibly a result of selective absorption of the asphalt material.

Using water absorption measurements as an indicator of asphalt absorption capacity, Lettier et al. (1949) concluded that absorption was a function of the aggregate bulk specific gravity, the crystalline structure (percent of interstices), and the quantity and shape of the surface voids. Aggregates with high bulk specific gravities (about >2.6) were non-absorptive, whereas aggregates with low bulk specific gravity tended to absorb more asphalt. In addition, after exploring the surface of the aggregates under magnification, it was apparent that aggregates that non-absorptive aggregates had compact and small-grained dense crystalline masses, whereas the absorptive aggregates had numerous interstices between crystals or were composed of large grained crystals. Further, the composition of the asphalt that was removed from the outside of the aggregates was compared to the composition of the asphalt that was chemically extracted from the aggregate. The results showed that the maltenes and other oil-wax components of the asphalt penetrated more readily than the asphaltenes did. The difference in asphaltene content was about 25 percent of asphaltenes inside the aggregate versus 35 percent outside.

In a separate study on selective asphalt absorption, Lee (1968) conducted experiments to understand the changes in the chemical composition of the effective asphalt film due to absorption and *adsorption*. A series of successive extractions were performed on 13 mixtures prepared with absorptive and non-absorptive aggregates using centrifuge and trichloroethylene extraction methods. The first extraction was done after submerging the loose mixture in the solvent for 3 minutes before subjecting it to the centrifuge, the second extraction after submerging the loose mixture for an additional 5 minutes in the solvent, and the third extraction after soaking the loose mixture for an additional 45 minutes in the solvent. The material recovered after the first extraction was assumed to belong to the non-absorbed fraction of the asphalt, while the material recovered after the third extraction was assumed to belong to the asphalt absorbed in the asphalt pores. The material obtained after the second extraction was assumed as the asphalt fraction *adsorbed* to the surface of the aggregate. Based on the results of the study, Lee (1968) concluded that selective absorption occurred in mixtures prepared with both type of aggregates (absorptive and non-absorptive). He also observed a lower asphaltene content and viscosity of the asphalt that was recovered from inside the aggregate pores (third extraction) compared to the asphalt obtained after the first extraction. The differences in asphaltene content and viscosity were more pronounced in the mixtures prepared with absorptive aggregates.

A later study on asphalt selective asphalt absorption used size exclusion chromatography to measure the composition of asphalt extracted from mixtures with a tetrahydrofuran method (Chen, 1992). The measurements showed no evidence of selective absorption, only evidence of *adsorption* of the polar fraction of the asphalt to the aggregate surface. Ideally, however, the composition of the absorbed and non-absorbed fractions of the asphalt should be able to be determined without the need of extraction solvents.

RESULT AND DISCUSSION

Statistical Analysis of Standard Method on Water Absorption and Binder Absorption

Measurement precision is so important in water/binder absorption measurements, thus, a system study about the precision of current popular methods of absorption measurement is

necessary. However, due to the characteristics of asphalt absorption measurement, asphalt coating or mixing is an irreversible process, introducing great difficulty to judge the precision of a method by repeating it on exact same sample. Moreover, complicating the measurement of asphalt absorption, compared to water absorption and in addition to the issues mentioned above, are ease-of-handling factors including higher asphalt viscosity compared to that of water, even at HMA temperatures, asphalt stickiness, and the wettability of aggregate by asphalt. These issues make establishing an accurate SSD condition with asphalt virtually impossible. And each time the asphalt-coated aggregate is handled, asphalt likely is lost, creating error in the asphalt mass measurement.

In order to get a complete understanding about the precision of water and asphalt absorption, a system literature review was conducted. ASTM D4469 and related ASTM documents involves aggregate/asphalt characteristics are carefully reviewed and summarized. Furthermore, using statistical analysis method, error propagation function, the final uncertainty of absorption tests was estimated.

AMRL Statistics on Water Absorption

AASHTO Materials Reference Laboratory (AMRL) has a large database, including compilations of statistics water absorption and aggregate apparent and bulk densities for both coarse and fine aggregates. Table 16 and Table 17 show the single operator and multilaboratory precision for both coarse and fine aggregate absorption.

Table 16. AMRL Compilation of Statistics: Coarse Aggregate Water Absorption.

		Multilaboratory Precision					Multilaboratory Precision					Single Operator Precision					
		1st Sample					2nd Sample					1st SMPL 2nd SMPL					
Sample No	No. Labs	Avg.	1S	D2S	1S%	D2S%	Avg.	1S	D2S	1S%	D2S%	1S	D2S	1S%	D2S%	1S%	D2S%
177/178	1329	0.306	0.066	0.187	21.6	61.1	0.302	0.061	0.173	20.3	57.3	0.026	0.073	8.4	23.8	8.5	24
173/174	1269	0.577	0.109	0.309	18.9	53.6	0.578	0.111	0.315	19.2	54.4	0.035	0.098	6.03	17.1	6.03	17.1
169/170	1256	1.383	0.409	1.156	29.5	83.6	1.434	0.411	1.163	28.7	81.1	0.155	0.438	11.2	31.7	10.8	30.5
165/166	1138	0.304	0.063	0.177	20.6	58.3	0.294	0.061	0.174	20.9	59	0.025	0.072	8.37	23.7	8.63	24.4
161/162	1171	3.064	0.277	0.783	9.03	25.6	3.03	0.277	0.783	9.14	25.9	0.128	0.362	4.17	11.8	4.22	11.9
157/158	1059	0.551	0.109	0.307	19.7	55.8	0.544	0.102	0.29	18.8	53.2	0.036	0.101	6.49	18.4	6.57	18.6
153/154	994	2.021	0.15	0.425	7.43	21	2.012	0.154	0.435	7.65	21.6	0.056	0.157	2.75	7.77	2.76	7.8
149/150	1059	0.358	0.13	0.368	35.6	103	0.35	0.12	0.339	34.1	97	0.054	0.152	15	42.4	15.3	43.4
145/146	1008	0.443	0.11	0.311	25.1	70.2	0.441	0.11	0.311	25.2	70.6	0.059	0.168	13.4	37.9	13.5	38
141/142	912	0.498	0.12	0.339	24.8	68.2	0.494	0.12	0.339	25.1	68.7	0.062	0.175	12.4	35.2	12.5	35.5
137/138	836	0.394	0.11	0.311	27.7	79	0.403	0.12	0.339	30.4	84.2	0.07	0.197	17.7	49.9	17.3	48.8
133/134	765	0.356	0.1	0.283	28.9	79.5	0.362	0.11	0.311	29	85.9	0.046	0.132	13.1	36.9	12.8	36.3
129/130	680	0.289	0.11	0.311	38.3	108	0.286	0.1	0.283	35.9	98.9	0.051	0.144	17.6	49.8	17.8	50.3
125/126	575	0.398	0.12	0.339	30.1	85.3	0.398	0.12	0.339	30.1	85.3	0.074	0.21	18.7	52.8	18.7	52.8
121/122	541	0.742	0.2	0.566	27.1	76.2	0.747	0.19	0.537	25.3	71.9	0.083	0.234	11.1	31.5	11.1	31.3

Table 17. AMRL Compilation of Statistics: Fine Aggregate Water Absorption.

		Multilaboratory Precision					Multilaboratory Precision					Single Operator Precision					
		1st Sample					2nd Sample					1st SMPL			2nd SMPL		
Sample No	No. Labs	Avg.	1S	D2S	1S%	D2S%	Avg.	1S	D2S	1S%	D2S%	1S	D2S	1S%	D2S%	1S%	D2S%
179/180	1316	0.61	0.153	0.431	25	70.7	0.609	0.157	0.443	25.7	72.7	0.071	0.201	11.7	33	11.7	33.1
175/176	1271	0.631	0.139	0.394	22.1	62.4	0.634	0.137	0.389	21.7	61.3	0.065	0.184	10.3	29.1	10.3	29
171/172	1165	0.812	0.151	0.426	18.5	52.4	0.803	0.154	0.435	19.1	54.1	0.073	0.207	9.01	25.5	9.12	25.8
167/168	1136	0.574	0.135	0.383	23.6	66.7	0.591	0.142	0.402	24.1	68.1	0.061	0.172	10.6	30	10.3	29.1
163/164	1141	0.718	0.198	0.56	27.6	78	0.701	0.196	0.555	28	79.2	0.079	0.223	11	31.1	11.2	31.8
159/160	1067	0.91	0.199	0.563	21.9	61.8	0.906	0.196	0.555	21.7	61.3	0.078	0.222	8.6	24.3	8.64	24.4
155/156	976	0.748	0.159	0.45	21.3	60.2	0.746	0.154	0.436	20.7	58.4	0.069	0.195	9.19	26	9.22	26.1
151/152	1026	0.865	0.25	0.707	29	81.7	0.88	0.29	0.82	32.4	93.2	0.132	0.375	15.3	43.3	15.1	42.6
147/148	921	0.87	0.27	0.764	30.6	87.8	0.86	0.26	0.735	30.2	85.5	0.114	0.323	13.1	37.2	13.3	37.6
143/144	934	0.716	0.25	0.707	35.5	98.8	0.71	0.26	0.735	36.4	104	0.109	0.308	15.2	43	15.3	43.3
139/140	851	0.799	0.39	1.103	48.5	138	0.782	0.39	1.103	49.6	141	0.131	0.371	16.4	46.5	16.8	47.5
135/136	725	0.771	0.25	0.707	32.9	91.7	0.777	0.25	0.707	32.7	91	0.113	0.321	14.7	41.6	14.6	41.3
131/132	642	0.676	0.31	0.877	45.9	130	0.682	0.31	0.877	44.9	129	0.125	0.354	18.5	52.4	18.4	51.9
127/128	579	1	0.47	1.329	46.8	133	0.939	0.44	1.245	47.3	133	0.196	0.556	19.6	55.6	20.9	59.2
123/124	542	0.993	0.29	0.82	29.5	82.6	0.999	0.32	0.905	32.4	90.6	0.128	0.363	12.9	36.5	12.8	36.3

For these AMRL data, the level of multilaboratory precision for fine aggregate water absorption, expressed as the difference two-sigma limit in percent (d2s%), ranges from 50 to 141 percent and for coarse aggregate water absorption, the range is from 21 to 108 percent. The single operator d2s% precision values range from 24 to 60 percent for fine aggregate, and for coarse aggregate the range is from eight to 53 percent. These are all quite large values for water absorption uncertainty and should be noted by practitioners. Asphalt absorption precision would be expected to have worse precision than these water absorption numbers.

Furthermore, the large decrease in precision from single operator to multilaboratory (60 percent maximum d2s% compared to over 100 percent maximum) likely can be largely attributed to the subjectivity of operator judgment, specifically concerning the saturated surface dry condition. This conjecture is consistence with the literature review on water absorption presented in a preceding section of this chapter.

Asphalt Absorption Error Calculation in ASTM D4469

ASTM D4469, a standard practice for calculating asphalt absorption based upon measurements from several standard methods, provides a discussion of the impact of error propagation on uncertainties in the absorption result. Specifically, four variables in the asphalt absorption calculation equation are considered:

These four variables affecting the final error of absorption are:

- The theoretical maximum specific gravity of an oven-dry paving mixture.
- The asphalt content expressed either as percent of the mass of the sample of oven-dry paving mixture, or as percent of the mass of oven-dry total aggregate in the sample of oven-dry paving mixture.
- The apparent specific gravity of the asphalt in the paving mixture.
- The weighted average ASTM bulk specific gravity of the oven-dry total aggregate in the paving mixture.

The discussion includes example results that show the type of sensitivity that may derive from each of these four factors. Table 18, adapted from D4469, shows these four factors, for which the measured value for each of these four variables plus the calculated absorption value for a specific asphalt paving mixture are listed in the first row. In other rows of the Table, the effect on asphalt absorption of changing one of the variables within the limits of the ASTM precision statement for reproducibility is shown while the other three variables are held constant. Each changed variable within its range of reproducibility is marked by the symbol (a).

Table 18. Effect of Measurement Errors on Calculated Percent Asphalt Absorption in ASTM D4469 (adapted from Table XX, ASTM D4469, 2011).

Theoretical Maximum Specific Gravity	Asphalt Content %*	Asphalt Apparent Specific Gravity	Weighted Average ASTM Oven-Dry Bulk Specific Gravity of Total Aggregate	% Asphalt Absorption
2.501	6.2	1.015	2.673	1.32
2.482(a)	6.2	1.015	2.673	0.98
2.520(a)	6.2	1.015	2.673	1.64
2.501	5.39(a)	1.015	2.673	0.77
2.501	7.01(a)	1.015	2.673	1.87
2.501	6.2	1.013(a)	2.673	1.33
2.501	6.2	1.017(a)	2.673	1.31
2.501	6.2	1.015	2.615(a)	2.16
2.501	6.2	1.015	2.731(a)	0.51

*Asphalt Content based on mass of sample of total oven dry mix (kg of asphalt per 100 kg of oven dry total mix)

From Table 18 we see that of these four factors, the theoretical maximum specific gravity, asphalt content, and bulk specific gravity have the largest effect on asphalt absorption. The fourth factor, asphalt apparent specific gravity, does not have as strong an effect.

Furthermore, ASTM D4469 provides calculated absorption values for the combination of errors listed in Table 18 that produce the most extreme ranges. In the sample asphalt absorption calculation of ASTM D4469, even when errors in each variable in the calculation are within its ASTM reproducibility precision limits, the value for percent asphalt absorption, in principle, can span a large range, from −0.38 to 3.05 g per g of aggregate, as extreme limits.

Error Propagation for Asphalt Absorption

For standard methods, performance statistics (1s, d2s) are provided based on experimental determinations by hundreds of laboratories. The large number of experiments (n) provides a very good understanding of the method's inherent precision, even though it says nothing about accuracy.

D4469 is a standard practice that provides a calculation procedure for asphalt absorption that is based on standard methods for determining the four variables described above. However, statistical measures of precision are not provided. The only information related to errors is that presented in the table from which Table 10, above, is adapted. The purpose of this section is to provide calculated estimates of 1s and d2s to allow an improved understanding of the reliability of an asphalt absorption measurement.

In order to further evaluate combined asphalt absorption measurement uncertainties, an error propagation function is used to estimate the error in standard methods. Assuming

interactions between independent variables are negligible, a common formula for calculating error propagation is the variance formula:

$$s_f = \sqrt{\left(\frac{\partial f}{\partial x}\right)^2 s_x{}^2 + \left(\frac{\partial f}{\partial y}\right)^2 s_y{}^2 + \left(\frac{\partial f}{\partial z}\right)^2 s_z{}^2 + \cdots} \tag{7-11}$$

where s_f represents the standard deviation of error in measuring the function f(x, y, z,...) that results from random errors in the independent variables x, y, z,..., variables that are characterized by standard deviations s_x, s_y, s_z, ... It is important to note that this formula is based on the linear characteristics of the gradient of f and therefore is a good estimation for the standard deviation of f as long as s_x, s_y, s_z... are small compared to the partial derivatives (Ku, 1966; Arnaut, 2008; Clifford, 1973).

As an example, we present calculated estimates of the statistical 1s values for water absorption and compare them to the reported AMRL corresponding values that derived from the hundreds of laboratory measurements. Then, we present a corresponding calculation for asphalt absorption, for which there are no laboratory 1s values available.

In AMRL data, water absorption can be represented as:

$$\text{Water absorption (mass percent)} \equiv \frac{\text{mass of absorbed water}}{\text{mass of aggregate}} \text{ x } 100$$

$$= \frac{\text{volume of absorbed water}}{\text{mass of aggregate}} \text{ x water density x } 100$$

$$= \frac{100}{\text{bulk specific gravity of aggregate}} - \frac{100}{\text{apparent specific gravity of aggregate}} \tag{7-12}$$

From the reported precision for bulk specific gravity and apparent specific gravity of sample 165, we can perform an error propagation calculation for water absorption, presented in Table 19.

Table 19. Error Propagation on Water Absorption, Based on AMRL Coarse Aggregate Sample 165, Multilaboratory.

	Aggregate Bulk Specific Gravity	Aggregate Apparent Specific Gravity
Value	2.713	2.735
s	0.0063	0.0048
$\frac{\partial f}{\partial x}$	−0.136	0.134
$\left(\frac{\partial f}{\partial x}\right)^2 s_x^2$	7.34×10^{-7}	4.14×10^{-7}

Based on the calculation, the multilaboratory1S for water absorption is estimated to be 0.107 mass percent whereas from the water absorption AMRL database, it is 0.063 mass percent. So, the estimated error of water absorption on AMRL coarse aggregate sample #165 is in reasonable agreement to the experimental determination provided in the AMRL database. From this example, we can see error propagation function does provided meaningful information.

Now, recall the equation for calculating asphalt absorption in ASTM D4469 (ASTM D4469, 2011):

$$Aac = 100\left[\frac{P_{tac}}{100-P_{tac}} + \frac{G_{ac}}{G_{ag}} - \frac{100G_{ac}}{(100-P_{tac})G_{tm}}\right] \tag{7-13}$$

where:
A_{ac} = absorbed asphalt as percent by mass of the oven-dry aggregate.
P_{tac} = asphalt content as percent by mass of the total mix in the sample of oven- dry paving mixture.
G_{ac} = apparent specific gravity of the asphalt in the paving mixture sample.
G_{ag} = weighted average ASTM oven-dry bulk specific gravity of the total aggregate in the sample of paving mixture.
G_{tm} = theoretical maximum specific gravity of the sample of oven-dry paving mixture.

Taking the example calculation in ASTM D4469 as an example and referring to ASTM D2041, D6307, D3289, and C127, four variables in the example calculations of ASTM D4469 come into play and their values and distribution statistics are listed in Table 20. The single lab and multiple lab standard deviations were obtained from the other ASTM methods referenced by D4469.

Table 20. Error of Variables Related to ASTM D4469.

Variables in D4469	Value	Standard Deviation Single Lab*	Standard Deviation Multiple Lab*
Asphalt Content Weight Percent of Mix	6.2000	0.04%	0.06%
Asphalt Specific Gravity	1.0150	0.0006	0.0007
Bulk Specific Gravity of Aggregate	2.6730	0.0090	0.0250
Theoretical Maximum Specific Gravity	2.5010	0.0080	0.0160

Table 21 lists calculated estimates of asphalt absorption errors for the example given in ASTM D4469 based on the error propagation function and values of P_{tac}, G_{ac}, G_{ag}, and G_{tm} for the sample calculation in ASTM D4469; standard deviations for the four variables were obtained from the standard methods: ASTM D2041, D6307, D3289, and C127.

Table 21. Error Propagation Calculation on Asphalt Absorption, ASTM D4469.

		P_{tac}	G_{ac}	G_{ag}	G_{tm}
Value	Single Lab	6.2000	1.0150	2.6730	2.5010
	Multiple Lab	6.2000	1.0150	2.6730	2.5010
s	Single Lab	0.0400	0.0006	0.0090	0.0080
	Multiple Lab	0.0600	0.0007	0.0250	0.0160
$\frac{\partial f}{\partial x}$	Single Lab	0.6753	−5.2157	−14.2059	17.2996
	Multiple Lab	0.6753	−5.2157	−14.2059	17.2996
$\left(\frac{\partial f}{\partial x}\right)^2 s_x^2$	Single Lab	0.0007	0.0000	0.0163	0.0192
	Multiple Lab	0.0016	0.0000	0.1261	0.0766

Based on these data and using the error propagation function, the estimated statistical information for asphalt absorption in the example in D4469 calculation is estimated in Table 22.

Table 22. Estimated Error Statistics for Binder Absorption in ASTM D4469.

	Asphalt Absorption	Calculated Error Propagation Estimates			
		1s	d2s	1s%	d2s%
Single lab	1.30	0.19	0.54	15	41
Multiple lab	1.30	0.45	1.28	35	98

This error propagation function result is can be compared to the error discussions in ASTM D4469; For this example, the Difference Two-Sigma Limit in percent (d2s%) for multilaboratory measurements, d2s%, can range up to 98 percent, compared to the range provided by the extreme limits shown in Table 18 of 125 percent of the absorption level for this example. Different levels of absorption will result in more or less percent variation relative to the level of absorption.

SUMMARY

This chapter presented a comprehensive review of the current standard methods for measuring asphalt absorption. AASHTO T84/T85, ASTM D 4469, and ASTM C127/128 are the most popular methods to measure the specific gravities, water absorption and asphalt absorption of aggregate. This discussion also included measurement precision; especially notable are the measurement uncertainties for both water and binder absorption.

The AMRL database provides statistical evaluations of precision for aggregate specific gravities and water absorption. These data show that considering the difference two sigma limit in percent (d2s%), which represents the acceptable difference of two measurements, the coefficient of variance can be as high as 141 percent, for some samples. These results illustrate that the water absorption measurement precision can be quite problematic. This poor precision in large part can be attributed to the subjective standards of determining the saturated surface dry condition, which is highly dependent on the operator's judgment, coupled with a low absorption value.

Asphalt absorption, calculated from the aggregate bulk specific gravity, the binder content of the mixture, the mixture maximum specific gravity, and the binder specific gravity, suffers from even greater precision difficulties than water absorption. While the binder specific gravity is determined quite precisely, the other three variables are subject to considerably more uncertainty that propagates into the total uncertainty of the absorption. The contributions to high asphalt absorption uncertainty are especially significant from the aggregate bulk specific gravity and the mixture theoretical maximum specific gravity. As an example, using the sample error analysis given by ASTM D4469, and with contributions from all four variables in the absorption calculation, values of 1s% equal to 15 percent (single operator) and 35 percent (multilaboratory) are calculated at an asphalt absorption level of 1.3 percent. Still following this example, if a single operator were to conduct absorption measurements in triplicate (n=3), then the statistical 95 percent confidence interval for the absorption (mean of the three replicate measurements) is calculated to be +/- 37 percent. Using the multilaboratory statistics (multiple laboratories conducting the three replicates), the 95 percent confidence interval for the mean of the three replicates is calculated to be +/-87 percent. Fewer replicates will provide a wider range of uncertainty; more replicates will reduce the range.

The point of this chapter is that the uncertainty in asphalt absorption measurements inherently tends to be quite high, deriving primarily from uncertainties in the aggregate bulk specific gravity and the mixture theoretical maximum specific gravity, invariably resulting in subtracting two numbers that are fairly close to each other. The actual uncertainty for a specific mixture will vary from this example, depending on the actual values of the aggregate and mixture properties and whether the level of absorption is higher or lower.

The standard practice D4469 does not provide the normal standard method statistical information (e.g., 1s, d2s) but practitioners need to be aware of the uncertainties associated with asphalt absorption calculations. The discussion and analysis presented in this chapter provide a methodology for estimating the uncertainty of absorption methods plus an example of the generally poor precision that is obtained.

CHAPTER 8. INTRODUCTION TO USING THE DENSITY GRADIENT COLUMN (DGC) FOR AGGREGATE AND ABSORPTION MEASUREMENTS

ABSTRACT

As noted in the preceding chapter, measurements of asphalt absorption using the standard methods and the standard practice D4469 are subject to very significant measurement error. The problem is fundamental in that the measurement inevitably requires subtracting two numbers that are quite close to each other: total mass of binder in the mixture minus the binder mass that is not absorbed. And the less the absorption, the more challenging it is to determine the absorption accurately with a reasonable percent error. Contributing to measurement errors are errors in measurements of aggregate bulk and apparent densities, densities that differ because of air voids within the aggregate.

To improve the precision and accuracy of measurements of aggregate densities and asphalt absorption, an alternative test method has been adapted and applied to aggregates and mixtures. The density gradient column method (DGC) is based on the direct measurement of density in a precisely calibrated density gradient fluid. The method does not involve measuring particle volume and thus the measurement is simple and more direct with the potential for improved accuracy and precision. Details of this method and its application to asphalt absorption measurements are given below.

MATERIALS AND METHODS

The Density Gradient Column Method and Procedure

The density gradient method is based on the direct measurement of particle density in a column of fluid that has a linear density gradient, generated by continuously blending two completely miscible make-up fluids of different densities and gravity feeding them to the bottom of the column. The linearly variable density column fluid for asphalt binder measurements is generated by continuously blending water and a brine solution of appropriate density. For aggregate measurements, the two make-up fluids are appropriate water blends of a heavy liquid (lithium metatungstate, density 2.95 g/ cm^3, LMT Liquid, LLC, 3093 Willowwood Circle, Ammon, ID 83406).

Because the method does not involve a separate measurement of particle volume, it is direct and efficient, but the accuracy of the method depends upon an accurate calibration of the density variation with height in the column. Two sets of glass beads (American Density Materials, Inc., 3826 Spring Hill Road. Staunton, VA 24401-6318), traceable to NIST weights and measures, have been used in our determinations; one set (for asphalt density determinations) provides density calibrations at 23°C from 0.94 to 1.10 g/cm^3 ±0.0002 g/cm^3 and the other set (for aggregate density determinations) provides density calibrations from 2.0 to 2.8 g/cm^3 ±0.0005 g/cm^3. The thermal expansion coefficient of the beads was reported as 0.000037 g/cm^3/°C. An example calibration is presented in the Results and Discussion section.

The measurement requires generating a linear density fluid in an appropriate graduate cylinder containing the calibration beads. The beads, each of different density, settle at the point

in the column equal to their density. Particles of asphalt or aggregate are dropped into columns having different density ranges and settle at the height corresponding to their density. The height of each bead or asphalt or aggregate particle is read with a cathetometer to within 0.001 cm precision; the accuracy, however, is reduced because of the uncertainly of the location of the center of mass of the irregularly shaped asphalt and aggregate pieces. The asphalt and aggregate densities are determined by linear interpolation of the density versus height calibration.

Binder Absorption Calculation

The DGC methodology requires coating the aggregate with asphalt binder at 121°C for 15 seconds on a hot plate followed by curing the coated aggregate at 143°C for 2 hours in the oven. The mass of binder absorbed by aggregate $m_{abs\text{-}b}$ is determined by subtracting the aggregate mass from the mass of aggregate plus absorbed and coated binder and then correcting for the mass of binder coating:

$$m_{abs-b} = \mathrm{func}(m_{ab}, m_a, \rho_b, \rho_{ab}, \rho_{av}) = m_{ab} - m_a - \frac{m_{ab}\rho_b}{\rho_{ab}} - \frac{m_a\rho_b}{\rho_{av}} \tag{8-1}$$

In this equation, m_{ab} is the mass of aggregate coated with binder (including both absorbed binder and any extra binder coating), m_a is the mass of aggregate (including air voids of negligible mass), ρ_b is the binder density, ρ_{ab} is density of aggregate coated with binder (including both absorbed binder and any extra binder coating), ρ_{av} is bulk density of the aggregate, i.e., the density of the aggregate including its air voids. The masses are measured using a precision balance, and densities are measured using the DGC. While the first four properties can be measured directly, ρ_{av} is measured using the wax-coating method described below.

Bulk Density from the Wax Coating Method

The coating method is based on assuring that the coating material (paraffin wax, Avantor Performance Materials, Inc. Philipsburg, NJ08865) is not absorbed by the aggregate. The likelihood that this assumption is satisfied is increased by chilling the aggregate in a refrigerator and heating the wax to just beyond its melting temperature. Then, using a fine brush, the wax is coated onto the surface of aggregate, being careful to fill the surface pits and valleys with wax. The cold aggregate is intended to prevent the wax from penetrating into the aggregate pores. The wax coating is determined from the above equation for binder absorption, but with the amount of absorption (in this case of wax) equal to zero:

$$0 = m_{ac} - m_a - \frac{m_{ac}\rho_c}{\rho_{ac}} + \frac{m_a\rho_c}{\rho_{av}} \tag{8-2}$$

from which the aggregate bulk density ρ_{av} is calculated as:

$$\rho_{av} = \frac{m_a\rho_c}{m_a + m_{ac}\frac{\rho_c}{\rho_{ac}} - m_{ac}} \tag{8-3}$$

In this equation, m_{ac} is the mass of aggregate coated with coating material (wax), m_a is mass of the clean aggregate, ρ_c is the density of coating material (determined from the DGC method), ρ_{ac} is density of wax-coated aggregate, ρ_{av} is bulk density of the aggregate (including the air voids).

Apparent Density and Vacuum Water Saturation

Vacuum water saturation is applied before measuring the density of the water-saturated aggregate in the DGC. After 45 min vacuum saturation and subsequent 24 hours water saturation, it is assumed that all air voids are filled with water. Then, the apparent density of the aggregate is determined from the following equation:

$$\rho_a = \frac{1}{\frac{1}{\rho_{av}} - \frac{1}{\rho_w}\left(\frac{\rho_{aw}}{\rho_{av}} - 1\right)} \tag{8-4}$$

where ρ_a is the apparent density of the aggregate, ρ_{av} is bulk density of the aggregate, ρ_{aw} is density of aggregate saturated with water (measured directly in the DGC), ρ_w is density of water at the laboratory temperature.

RESULT AND DISCUSSION

DGC Calibration

Lithium metatungstate (LMT) heavy liquid, with a density of 2.95 g/cm^3, and water were used to create the DGC for aggregate density measurements. Water has a density of 0.9980 g/mL at a lab temperature of 21°C. Then, if LMT and water are mixed, a linear density gradient column can be prepared with densities ranging from 0.998–2.95 g/ cm^3.

An example DGC, with a range designed for aggregate density measurements, and its linear calibration are shown in Figure 55. The density of the aggregate is determined by measuring each aggregate's vertical position in the column using the telescopic cathetometer having a precision of 0.001 cm; however, the exact center of mass of the irregularly shaped aggregate pieces is uncertain, leading to a somewhat reduced precision of the density measurement. Additionally, the density of paraffin wax and the Alon PG 64-22 un-aged binder were measured. The binder density ρ_b was 1.058 g/cm^3; the density of paraffin wax was measured as 0.917 g/cm^3. The two column fluids used to create the DGC for measuring the wax density were water and isopropyl alcohol, a poor solvent for the wax.

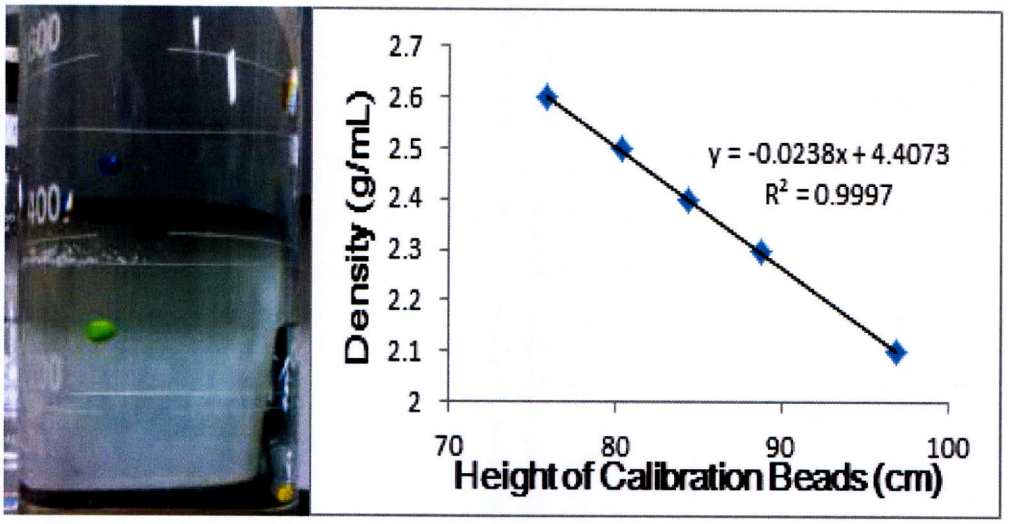

Figure 55. Example DGC Density versus Height Calibration.

Aggregate and Absorption Characteristics

From DGC measurements of density and using Equations 8-1 through 8-4, aggregate characteristics (ρ_{av}, ρ_a) and binder absorption ($m_{abs\text{-}b}$) were determined for a number of individual aggregate pieces.

Additionally, characteristic aggregate and absorption volumes were calculated. Each aggregate's void volume (V_{void}) is calculated as its bulk volume minus the aggregate apparent volume (volume of the aggregate excluding the void volume):

$$V_{void} = \frac{m_a}{\rho_{av}} - \frac{m_a}{\rho_a} \tag{8-5}$$

where ρ_a is the apparent density of the aggregate, ρ_{av} is the aggregate bulk density, m_a is the mass of aggregate piece. The volume of the absorbed binder ($V_{abs\text{-}b}$) is given by:

$$V_{abs-b} = \frac{m_{ab}-m_a}{\rho_b} - \frac{m_{ab}}{\rho_{ab}} + \frac{m_a}{\rho_{av}} \tag{8-6}$$

where, as before, m_{ab} is mass of aggregate coated with binder, m_a is mass of aggregate with air void, ρ_b is density of binder, ρ_{ab} is density of aggregate coated with binder, ρ_{av} is density of aggregate with air void.

These aggregate and absorption characteristics for three aggregate types (Delta Sandstone, Martin Marietta Granite, and Hanson Limestone) were determined by the DGC measurements and the data are shown in Table 23, Table 24, and Table 25. Other aggregate materials selected for study are TX1 Lightweight Streetman, Jones Mill, and Hoban rhyolite grade 6. Interestingly, the void fraction of the sandstone aggregate is significantly higher than

either the granite or limestone samples. Also of note is the wide variation in void fraction between the several different pieces of aggregate.

Table 23. Aggregate and Absorption Characteristics for Delta Sandstone (9 Pieces).

Piece							Void Fraction
1	1.0003	2.557	2.805	0.0190	0.034	0.018	0.0869
2	0.7561	2.502	3.059	0.0254	0.054	0.025	0.1787
3	0.8566	2.219	3.037	0.0406	0.104	0.039	0.2694
4	0.9971	2.445	3.073	0.0330	0.083	0.032	0.2035
5	1.7243	2.447	2.924	0.0147	0.115	0.042	0.1632
6	1.3735	1.919	3.294	0.1235	0.298	0.119	0.4165
7	0.9550	2.264	3.111	0.0462	0.115	0.045	0.2726
8	0.4209	2.378	3.233	0.0188	0.046	0.018	0.2599
9	0.7123	2.383	3.022	0.0245	0.063	0.024	0.2108

Table 24. Aggregate and Absorption Characteristics for MM Granite (7 Pieces).

Piece							Void Fraction
1	0.4416	2.377	3.090	0.0165	0.043	0.016	0.2309
2	0.5625	2.498	2.931	0.0108	0.033	0.010	0.1479
3	0.4722	2.493	2.796	0.0098	0.021	0.009	0.1083
4	0.3183	2.539	2.825	0.0044	0.013	0.004	0.1014
5	0.5024	2.525	2.778	0.0042	0.018	0.004	0.0905
6	0.8285	2.553	2.776	0.0093	0.026	0.009	0.0806
7	0.3860	2.543	2.755	0.0026	0.012	0.003	0.0770

Table 25. Aggregate and Absorption Characteristics for Hanson Limestone (10 Pieces).

Piece							Void Fraction
1	0.9145	2.491	2.798	0.0179	0.040	0.017	0.1097
2	0.9289	2.560	2.787	0.0138	0.029	0.013	0.0813
3	0.5146	2.510	2.739	0.0053	0.017	0.005	0.0838
4	1.2332	2.635	2.718	0.0049	0.014	0.005	0.0305
5	0.4096	2.624	2.712	0.0036	0.005	0.004	0.0324
6	0.4866	2.587	2.673	0.0026	0.006	0.003	0.0323
7	0.7165	2.513	2.903	0.0121	0.038	0.012	0.1344
8	0.5355	2.612	2.697	0.0024	0.006	0.002	0.0317
9	0.8588	2.597	2.753	0.0098	0.019	0.009	0.0565
10	1.0510	2.645	2.688	0.0006	0.006	0.001	0.0162

These data indicate that the volume of the absorbed binder is highly correlated with the void volume of the aggregates. Generally, the volume of absorbed binder was about 40 percent of the total void volume (Figure 56). This correlation is found on all three types of aggregates (Delta Sandstone, Martin Marietta Granite and Hanson Limestone), indicating that the void volume of the binder plays a key role in determining the amount of asphalt binder absorption.

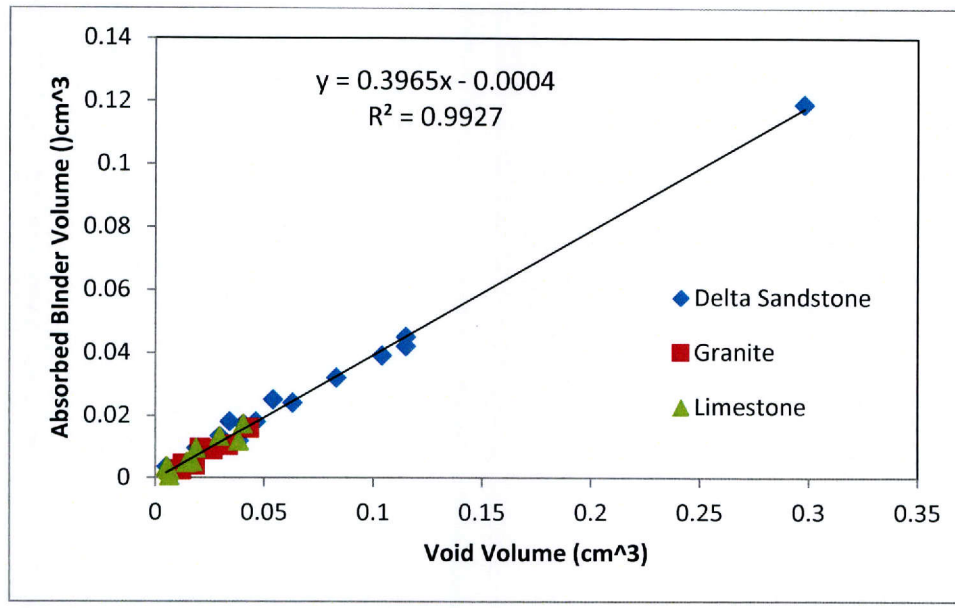

Figure 56. Correlation between Absorbed Binder Volume and Void Volume.

CONCLUSION

As described above, reducing error measurements is critical to accurate binder absorption measurements. While this work suggests improved accuracy in determining binder absorption over standard techniques, additional improvements are believed possible and are being investigated. These improvements include more accurately coating the aggregate with wax to measure the aggregate bulk specific gravity and decreasing the density gradient (change in density per height of column) to more accurately measure the density of the aggregate, wax-coated aggregate, and binder-coated aggregate. These issues are discussed further below.

The bulk density is a critical determination that is subject to error in all of the absorption measurement methods, including the DGC method. The problem is to accurately exclude surface roughness from the determination but also to include all of the internal void volume that has a void volume path to the aggregate surface. (Trapped void volume that has no open path to the surface cannot be detected and serves to decrease the aggregate apparent density.) With the wax coating method, it is important to avoid bridging surface pits and valleys; otherwise additional void volume will be created and erroneously included in the measurement. At the same time, absorption by wax into the void volume must be prevented. Concerning DGC measurements of wax-coated or binder-coated or water-saturated aggregate density, a principal source of error appears to be the irregular shape of each piece. Because of such irregularities, the center of buoyancy of each piece is not precisely known. Thus, the accuracy of the location of

this center in the DGC is subject to additional error beyond the precision of the cathetometer. This error can be improved if the density gradient in the column is decreased, thereby expanding the vertical distance between calibrations beads, resulting in a decrease in the location error, relative to the calibration precision.

In this chapter, the concept of the Density Gradient Column and its use for asphalt materials measurement was introduced. Experiment results indicate that the Density Gradient is an efficient way to measure the absorption and aggregate is demonstrated as a main for aggregate characterization and absorption tests.

CHAPTER 9. AGGREGATE CHARACTERISTICS

ABSTRACT

In this subtask, we selected typical aggregates which are commonly used in Texas and measured the following characteristics of the aggregates, piece by piece:

- Mass.
- Bulk specific gravities, specific gravity including accessible voids.
- Apparent Specific Gravity, specific gravity without accessible voids.
- Air Void Volume.
- Aggregate Volume.

Also, the following characteristics are determined using Aggregate Image Measurement System (AIMS) or gathered from database:

- Angularity, Shape.
- Surface Energy.

MATERIALS AND METHODS

Density Gradient Column

Lithium metatungstate (LMT) heavy liquid, with a density of 2.95 g/cm^3, and water were used to create the DGC for aggregate density measurements. Water has a density of 0.9980 g/mL at a lab temperature of 21°C. Then, if LMT and water are mixed, a linear density gradient column can be prepared with densities ranging from
0.998–2.95 g/cm^3.

Aggregate Image Measurement System (AIMS)

The AIMS image based particle analysis provides an objective characterization of particle angularity, form, and surface texture. Save time and gain valuable new insights about your aggregates. Simply load the tray with the material sample, place into the AIMS system. The system then automatically acquires the images of each particle and analyzes the shape characteristics.

Aggregates

These aggregate and absorption characteristics for six aggregate types (Delta Sandstone, Martin Marietta Granite, Hanson Limestone, TX1 Lightweight Streetman, Jones Mill Quartzite, and Hoban rhyolite grade 6 Gravel) have been determined by DGC measurements.

RESULTS AND DISCUSSION

Aggregate Volumetric Measurement by Density Gradient Column

From DGC measurements, aggregate characteristics can be determined, on a piece by piece basis. Table 26 to Table 31 show the bulk density, apparent density and void fraction for a

number of pieces of each of six aggregate types: Delta Sandstone, Martin Marietta Granite, Hanson Limestone, Hoban rhyolite grade 6 Gravel, Jones Mill Quartzite and TX1 Lightweight Streetman. Mean and standard deviation values for these data are given in Table 32.

Table 26. Aggregate Characteristics, Delta Sandstone (n=9).

Aggregate	Mass (g)	Bulk Density (g/cm^3)	Apparent Density (g/cm^3)	Void Volume (cm^3)	Aggregate Volume (cm^3)
Delta Sandstone	1.0003	2.557	2.805	0.034	0.391
Delta Sandstone	0.7561	2.502	3.059	0.054	0.302
Delta Sandstone	0.8566	2.219	3.037	0.104	0.386
Delta Sandstone	0.9971	2.445	3.073	0.083	0.408
Delta Sandstone	1.7243	2.447	2.924	0.115	0.705
Delta Sandstone	1.3735	1.919	3.294	0.298	0.716
Delta Sandstone	0.9550	2.264	3.111	0.115	0.422
Delta Sandstone	0.4209	2.378	3.233	0.046	0.177
Delta Sandstone	0.7123	2.383	3.022	0.063	0.299

Table 27. Aggregate Characteristics, Granite (n=7).

Aggregate Type	Mass (g)	Bulk Density (g/cm^3)	Apparent Density (g/cm^3)	Void Volume (cm^3)	Aggregate Volume (cm^3)
Granite	0.4416	2.377	3.090	0.043	0.186
Granite	0.5625	2.498	2.931	0.033	0.225
Granite	0.4722	2.493	2.796	0.021	0.189
Granite	0.3183	2.539	2.825	0.013	0.125
Granite	0.5024	2.525	2.778	0.018	0.199
Granite	0.8285	2.553	2.776	0.026	0.325
Granite	0.3860	2.543	2.755	0.012	0.152

Table 28. Aggregate Characteristics, Hanson Limestone (n=10).

Aggregate	Mass (g)	Bulk Density (g/cm^3)	Apparent Density (g/cm^3)	Void Volume (cm^3)	Aggregate Volume (cm^3)
Hanson Limestone	0.9145	2.491	2.798	0.040	0.367
Hanson Limestone	0.9289	2.560	2.787	0.029	0.363
Hanson Limestone	0.5146	2.510	2.739	0.017	0.205
Hanson Limestone	1.2332	2.635	2.718	0.014	0.468
Hanson Limestone	0.4096	2.624	2.712	0.005	0.156
Hanson Limestone	0.4866	2.587	2.673	0.006	0.188
Hanson Limestone	0.7165	2.513	2.903	0.038	0.285
Hanson Limestone	0.5355	2.612	2.697	0.006	0.205
Hanson Limestone	0.8588	2.597	2.753	0.019	0.331
Hanson Limestone	1.0510	2.645	2.688	0.006	0.397

Table 29. Aggregate Characteristics, Gravel (n=14).

Aggregate	Mass (g)	Bulk Density (g/cm^3)	Apparent Density (g/cm^3)	Void Volume (cm^3)	Aggregate Volume (cm^3)
Gravel	0.3318	2.527	2.602	0.004	0.131
Gravel	0.4817	2.440	2.765	0.023	0.197
Gravel	0.3944	2.332	2.986	0.037	0.169
Gravel	0.3816	2.419	2.754	0.019	0.158
Gravel	0.5708	2.396	2.749	0.030	0.238
Gravel	0.8383	2.413	2.793	0.047	0.347
Gravel	0.3859	2.486	2.844	0.020	0.155
Gravel	0.8289	2.396	2.839	0.054	0.346
Gravel	0.3784	2.414	2.759	0.020	0.157
Gravel	0.7940	2.377	2.811	0.052	0.334
Gravel	0.8154	2.322	2.817	0.061	0.351
Gravel	0.9034	2.318	2.954	0.083	0.390
Gravel	0.5911	2.400	2.895	0.042	0.246
Gravel	0.3632	2.347	3.130	0.038	0.155

Table 30. Aggregate Characteristics, Jones Mill Quartzite (n=7).

Aggregate	Mass (g)	Bulk Density (g/cm^3)	Apparent Density (g/cm^3)	Void Volume (cm^3)	Aggregate Volume (cm^3)
Jones Mill Quartzite	0.5587	2.369	2.802	0.036	0.236
Jones Mill Quartzite	0.2840	2.536	2.806	0.011	0.112
Jones Mill Quartzite	0.3256	2.492	3.041	0.024	0.131
Jones Mill Quartzite	0.6626	2.412	3.098	0.061	0.275
Jones Mill Quartzite	0.2766	2.550	2.908	0.013	0.108
Jones Mill Quartzite	0.2705	2.579	2.831	0.009	0.105
Jones Mill Quartzite	0.3184	2.519	2.888	0.016	0.126

Table 31. Aggregate Characteristics, Lightweight (n=7).

Aggregate	Mass (g)	Bulk Density (g/cm^3)	Apparent Density (g/cm^3)	Void Volume (cm^3)	Aggregate Volume (cm^3)
Lightweight	0.3093	1.551	2.139	0.0548	0.199
Lightweight	0.5759	1.475	2.504	0.1603	0.390
Lightweight	0.1940	1.465	2.314	0.0486	0.132
Lightweight	0.1575	1.508	2.372	0.0380	0.104
Lightweight	0.2817	1.446	2.127	0.0624	0.195
Lightweight	0.1689	1.522	2.377	0.0399	0.111
Lightweight	0.5296	1.563	2.047	0.0803	0.339

From this table, we can see that bulk density, apparent density and void fraction varies, not only from different types of aggregate, but even also from different pieces in the same type of aggregate. This result indicates that at the piece by piece level, aggregate properties are not uniform.

Based on these aggregate mass and specific gravity data, air void volume and volumetric void fraction was calculated. Also, a statistical analysis was done on these data, providing the mean value and the standard deviations.

Table 32. Statistical Analysis on Aggregate Characteristics.

		Mass (g)	Bulk Density (g/cm^3)	Apparent Density (g/cm^3)	Void Volume (cm^3)	Aggregate Volume (cm^3)	Void Fraction
Delta Sandstone (n=9)	AVG	0.9773	2.346	3.062	0.101	0.423	0.2291
	SD	0.3807	0.192	0.147	0.080	0.180	0.0920
Granite (n=7)	AVG	0.5016	2.504	2.850	0.024	0.200	0.1195
	SD	0.1643	0.060	0.121	0.011	0.064	0.0545
Hanson Limestone (n=10)	AVG	0.7649	2.577	2.747	0.018	0.297	0.0609
	SD	0.2863	0.050	0.070	0.012	0.108	0.0379
Gravel (n=14)	AVG	0.5756	2.399	2.835	0.038	0.241	0.1208
	SD	0.2157	0.060	0.127	0.021	0.093	0.0370
Jones Mill (n=7)	AVG	0.3852	2.494	2.911	0.024	0.156	0.1418
	SD	0.1583	0.076	0.117	0.019	0.069	0.0472
Light-weight (n=7)	AVG	0.3167	1.504	2.269	0.069	0.210	0.3334
	SD	0.1713	0.044	0.166	0.043	0.113	0.0601

Figure 57 and Figure 58 show the statistical data for the mass and volume properties of the six aggregate types. While certainly there are errors to the data, it is clear that for the same type and source of aggregate, densities and especially volumetric properties show significant differences between individual pieces that reflect more than measurement error; air voids, for example, are not distributed evenly among the separate aggregate pieces. This conclusion is supported by additional data in Chapter 9 on the dependence of asphalt absorption on aggregate air voids. Also notable is the variation in average void fraction among the six aggregates, ranging from 0.067 for the Hanson Limestone to 0.23 for the Delta Sandstone (not counting the artificially manufactured lightweight aggregate for which the void fraction is 0.33).

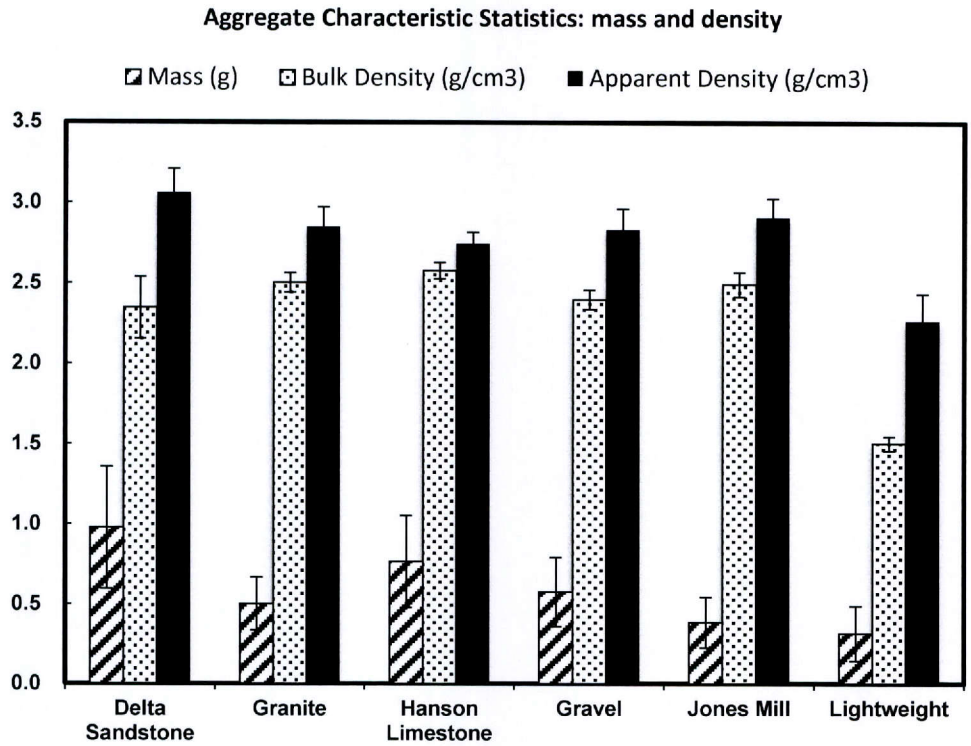

Figure 57. Aggregate Characteristics Statistics, Mass, and Density, Results Plot as Mean ± 1SD (n for Each Aggregate Type Is Given in Table 32).

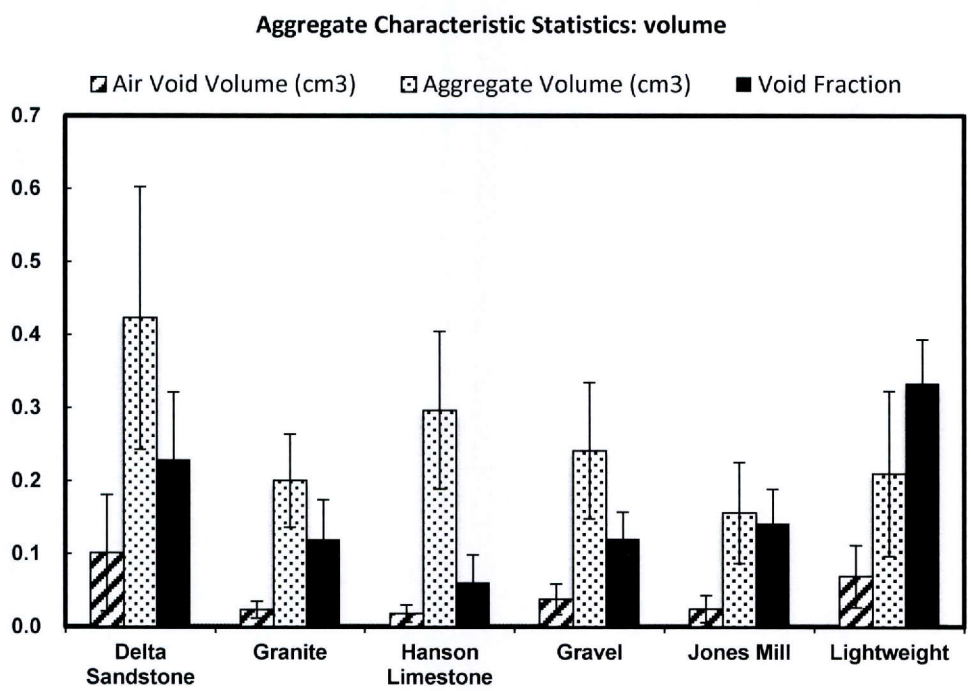

Figure 58. Aggregate Characteristics Statistics, Volume, and Void Fraction, Results Plot as Mean ± 1SD (n for Each Aggregate Type Is Given in Table 32).

Aims Test and Surface Energy of Aggregates

In this work, we selected from our extensive database two of the aggregates with characteristics that are significantly different, one an absorptive limestone and another one a non-absorptive quartzite, for further tests of asphalt absorption, aggregate compliance, dynamic mechanical analyzer tests and bulk mixture tests. We have compiled a database of aggregate surface energy test results. We selected two of these aggregates and determined for them the specific gravity, gradation, and shape, angularity and texture spectra.

Immediately below is presented the Specific Gravity, both apparent (excluding pores) and bulk (including pores) specific gravities for both of the aggregates used in this project for standard specific gravity determinations. The results are summarized in Table 33.

Table 33. Aggregate Specific Gravity.

Aggregate Type	Bulk Specific Gravity	Apparent Specific Gravity
Limestone	2.578	2.652
Quartzite (coarse)	2.682	2.746
Quartzite (fine)	2.551	2.832

Surface Pore Size Distribution with Mercury Porosimeter

This method was reviewed with respect to safety issues and procedures in the use and handling of mercury and it is found that safety concerns prevent using this method.

Aggregate Imaging System (AIMS) Measurements of the Cumulative Spectra of the Shape, Angularity, and Texture of Each Aggregate

The aggregate used in this project for the lab mixture is quartzite and its full mix design gradation is shown as follows.

Table 34. Quartzite Full Mix Design Gradation.

Sieve Size	Cum. Passing %	Individual Passing %
1/2"	100.0	0.0
3/8"	93.1	6.9
No. 4	64.6	28.5
No. 8	40.7	23.9
No. 16	26.2	14.5
No. 30	14.6	11.6
No. 50	8.5	6.1
No. 200	3.5	4.9
Pan	N/A	3.5

For the AIMS test, four different sizes of clean aggregates were collected which are retained on sieve sizes 3/8", No.4, No.8, and No.16. The AIMS angularity chart provides an objective characterization of the material edge characteristics. AIMS angularity characterizes the particle edge sharpness characteristics on a scale of 0–10,000.

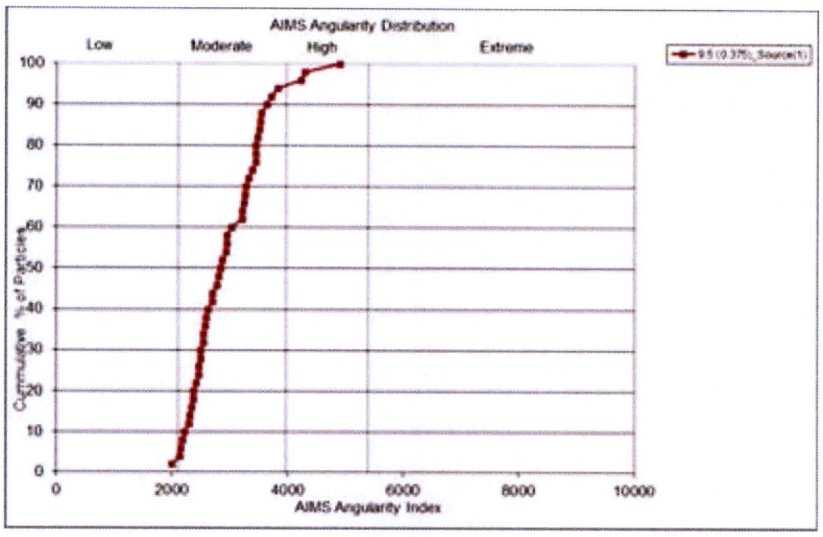

Figure 59. AIMS Angularity Chart (3/8").

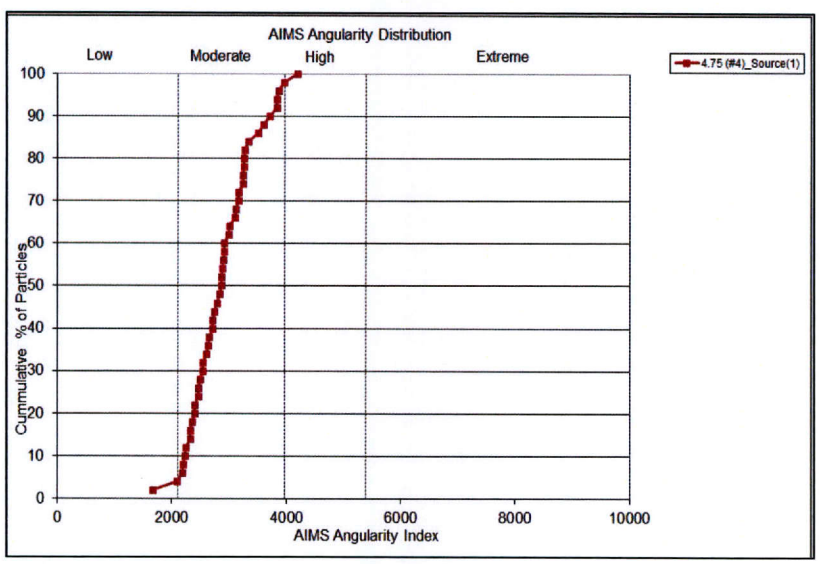

Figure 60. AIMS Angularity Chart (#4).

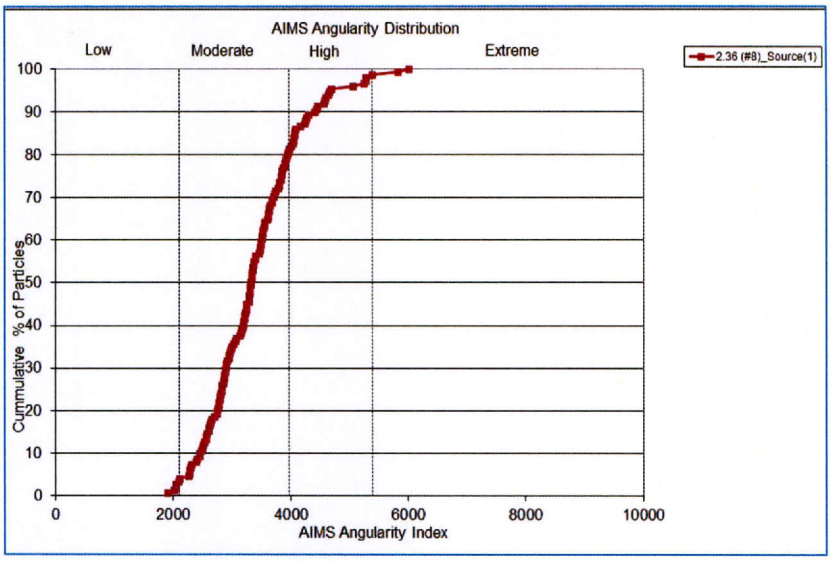

Figure 61. AIMS Angularity Chart (#8).

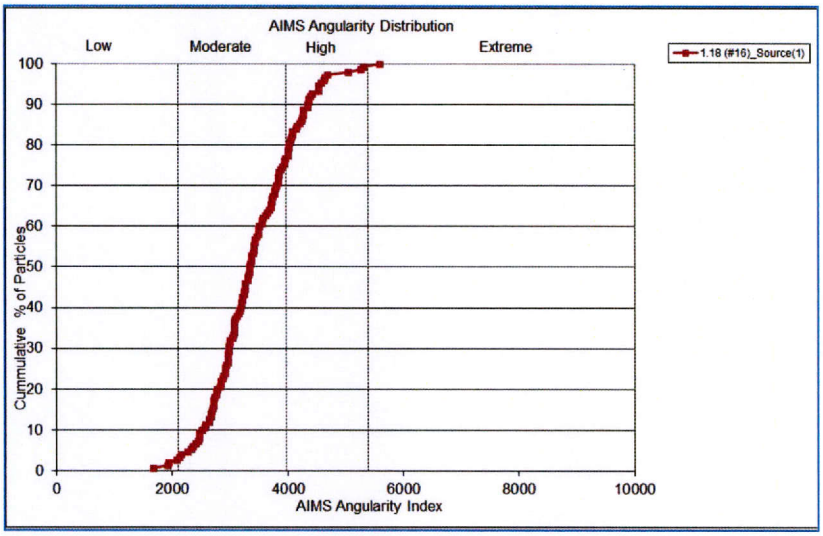

Figure 62. AIMS Angularity Chart (#16).

Existing manual methods for "flat and elongated" analysis can be tedious, labor intensive, and group to a specific range. The AIMS system captures coarse particle 3D shape data and presents the information in multiple formats.

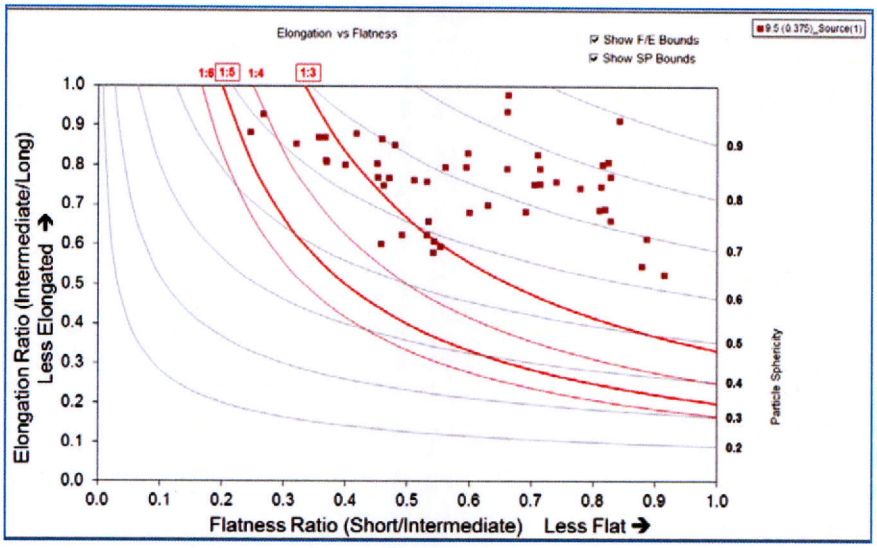

Figure 63. AIMS 3D Shape Ratio Chart (3/8").

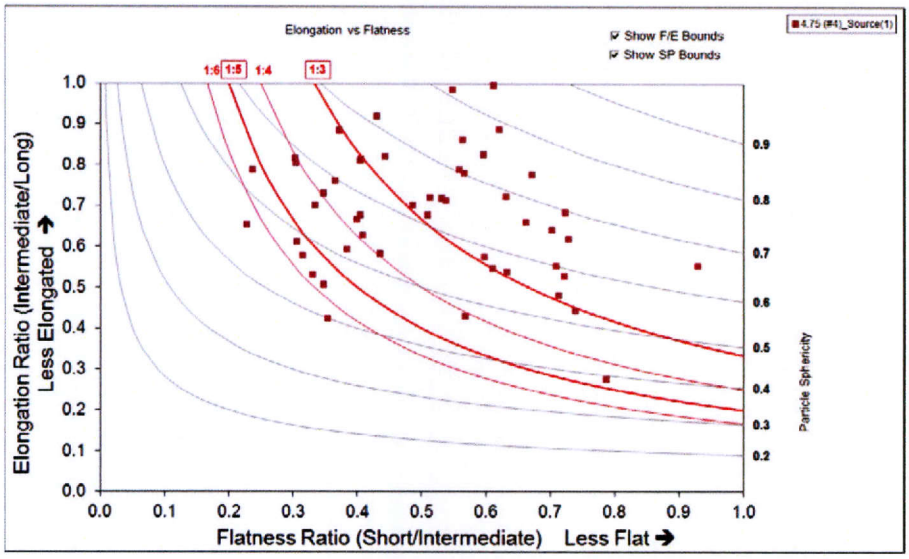

Figure 64. AIMS 3D Shape Ratio Chart (#4).

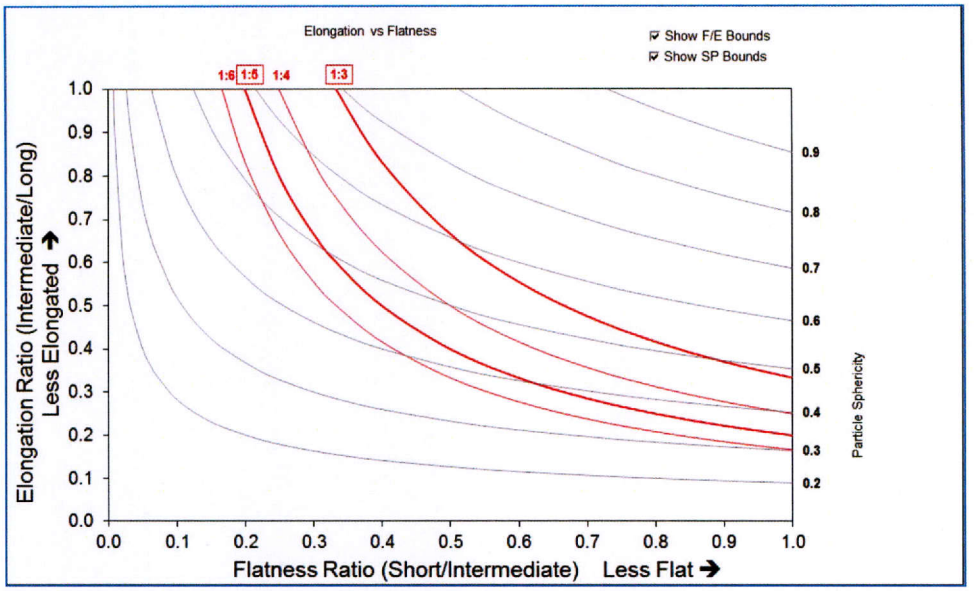

Figure 65. AIMS 3D Shape Ratio Chart (#8).

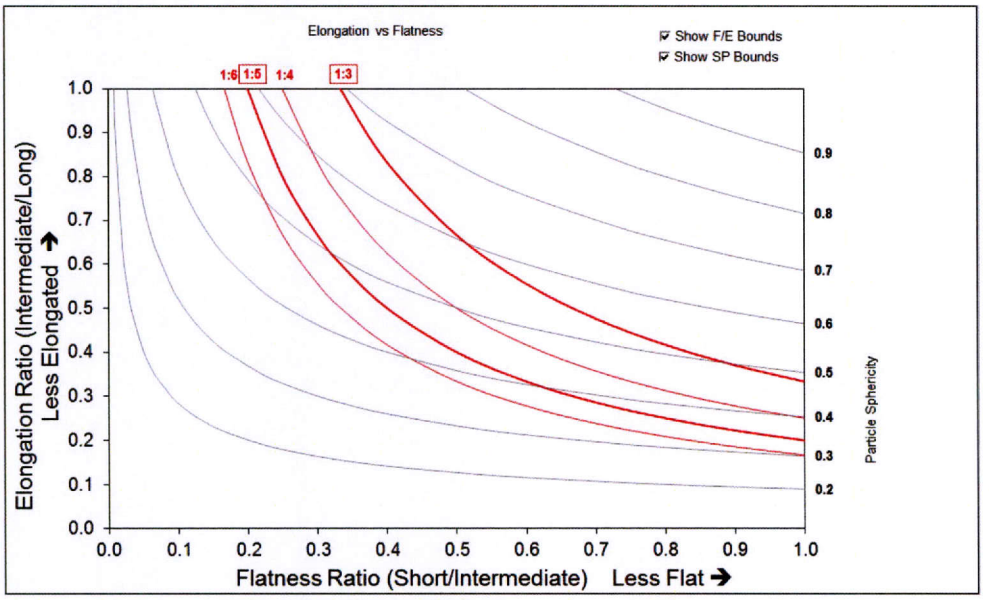

Figure 66. AIMS 3D Shape Ratio Chart (#16).

The AIMS also characterizes surface texture on a scale of 0–1000.

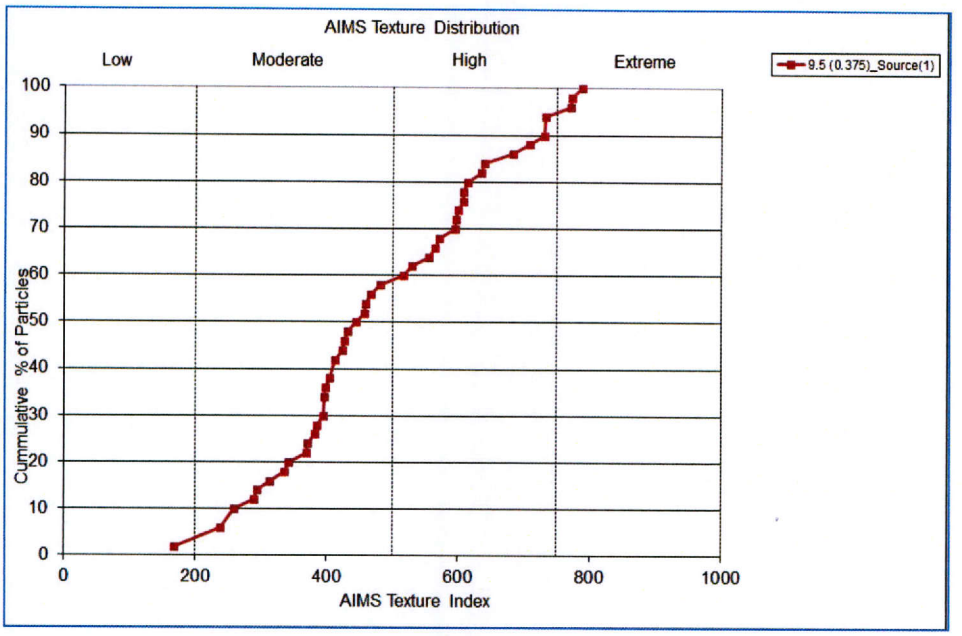

Figure 67. AIMS Texture Chart (3/8").

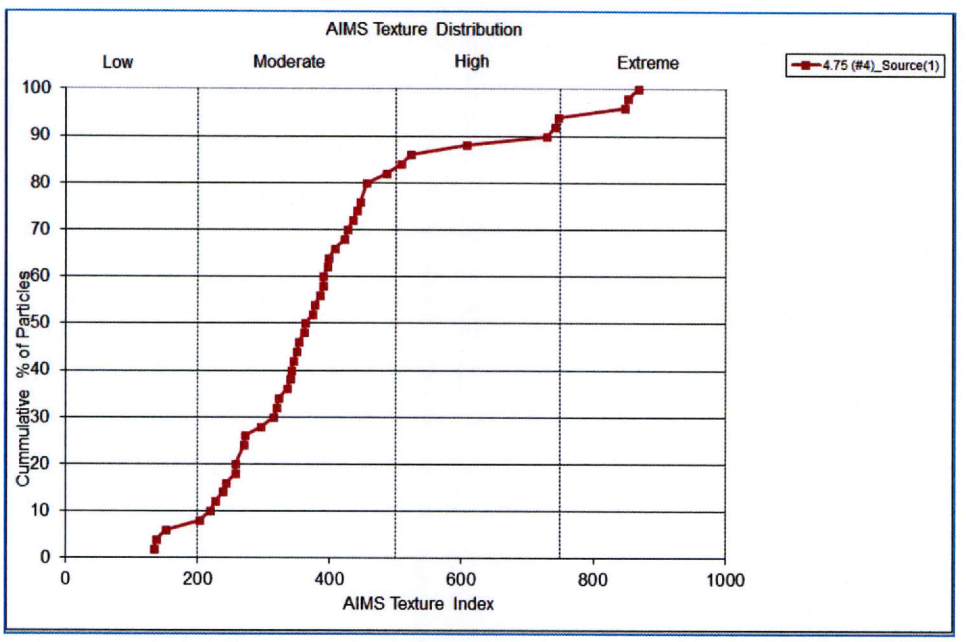

Figure 68. AIMS Texture Chart (#4).

Surface Energy Components with the Universal Sorption Device (USD) in Our Advanced Characterization of Infrastructure Materials Laboratory

The surface energy components for different aggregates are summarized in the Table 35 and Table 36. The abbreviation SSA means the Specific Surface Area as determined by the USD measurement with water vapor. The symbol Γ in these tables means the surface energy. The superscript LW means Lifshitz-van der Waals and is the non-polar surface energy component.

The superscript AB stands for Acid-Base. The superscript + means Acid and the subscript – means Base. The symbol with no super- or subscript stands for the total surface energy.

Table 35. Surface Energy Component for Different Aggregates.

Aggregate	Γ	Γ^{LW}	Γ^{AB}	Γ^{+}	Γ^{-}
Texas River Gravel	111.26	44.37	66.9	1.63	687.89
Limestone	95.53	45.17	50.36	1.33	474.99
Georgia Granite	229.40	133.20	96.20	24.10	96.00
Colorado Limestone	88.99	79.90	9.09	0.10	206.50
Texas Limestone	107.87	86.50	21.37	0.40	285.50
Meuse River Gravel	259.79	142.30	117.49	6.30	547.80
Rhine River Moraine Gravel	278.20	137.30	140.90	8.30	598.00
Quenast Porphyry	250.75	135.40	115.35	8.80	378.00
Glansanda Crushed Granite	185.24	151.30	33.94	0.70	411.40
Limestone Filler	134.53	68.30	66.23	2.90	378.10

Table 36. Surface Energy Components for Different Aggregates Used in Texas.

Material	Γ	Γ^{LW}	Γ^{AB}	Γ^{+}	Γ^{-}	SSA
Water	72.80	21.80	51.00	25.50	25.50	
Limestone - El Paso, TX	271.00	152.00	119.00	236.00	15.00	2.30
Vulcan Materials - Limestone (2004) - Brownwood, TX	124.84	51.97	72.87	3.23	410.97	0.62
Vulcan Materials - Traprock (2004) - Knippa, TX	521.73	53.43	468.30	1.93	28,406.90	0.27
Limestone - Odessa, TX	115.95	50.30	65.65	2.05	525.59	0.74
Fordyce - River Gravel (2003) - Murphy, TX	162.05	50.21	111.84	1.91	1637.18	0.54
Vulcan Materials - Limestone (2007) - Brownwood, TX	111.25	50.33	60.92	3.45	268.95	1.01
Fordyce - River Gravel (2007) - Murphy, TX	111.34	44.37	66.97	1.63	687.89	0.47
Vulcan Materials - Traprock (2007) - Knippa, TX	422.39	51.09	371.30	3.60	9573.80	0.96
Martin Marietta - Granite (2004) - Snyder, OK	425.18	56.35	368.83	43.45	782.70	0.67
Martin Marietta - Quartzite (2004) - Jones Mill, AK	200.07	60.86	139.21	8.89	544.98	1.35
Martin Marietta - Sandstone (2004) - Sawyer, OK	104.98	62.46	42.52	2.03	222.61	0.83
Hanson - River Gravel (2004) - Prescott, AK	96.54	59.49	37.05	1.20	285.98	0.80
Texas Industries - Limestone (2004) - Bridgeport, TX	265.41	59.89	205.52	18.82	561.11	0.49
Martin Marietta - Granite (2007) - Snyder, OK	43.48	31.79	11.69	0.05	683.39	0.47
Martin Marietta - Sandstone (2007) - Sawyer, OK	108.92	48.57	60.35	2.90	314.00	0.94
Smith/Buster - Sandstone (2006) - Sawyer, OK	94.78	41.46	53.32	1.17	607.45	0.64
Hanson - Limestone (2006) - New Braunfels, TX	95.44	45.17	50.27	1.33	474.99	0.37

SUMMARY

The density gradient column provides an efficient method for measuring aggregate volumetric properties and with good precision. The measurements are for individual pieces of aggregate and as such provide interesting insight to the nature of aggregates and, as is seen in Chapters 10 and 11, to asphalt absorption.

Aggregate specific gravities, void volume and void fraction for Delta Sandstone, Granite, Hanson Limestone, Gravel, Jones Mill and lightweight were measured by the density gradient

column method. Statistical analysis shows these aggregates possess inherently different volumetric properties. Interestingly, even for the same aggregate type, there can be significant variability among individual aggregate pieces in their void volume and void fraction. For example, the void fraction (void volume per bulk volume) for Hanson Limestone varied from 1.5 percent to 13 percent for the sample of 10 pieces of aggregate with the range in average void fraction for the six natural aggregates varying from six to 33 percent. These inherently different aggregate volumetric characteristics among the various aggregate types affect asphalt absorption and must be taken into account. Other detailed studies on the essential factor controlling asphalt absorption are discussed in the following chapters.

AIMS experiments provided cumulative spectra of the shape, angularity, and texture of aggregates. These results, together with our database of aggregate surface energy, provide necessary information to further study HMA and WMA.

CHAPTER 10. MEASUREMENT OF BINDER ABSORPTION

Asphalt absorption represents an economic loss of effective binder, and may change binder properties. In pavement design, determination of asphalt absorption by standard methods is used to estimate air voids. However, a more precise method is necessary to provide an improved fundamental understanding of asphalt binder absorption.

Density gradient columns (DGC), fluid columns of linear density gradient, allow measurements of bulk density, apparent density, void volume, water absorption and asphalt absorption for individual aggregate pieces. The DGC method allows accurate measurements, superior to those of standard methods of absorption, as a function of aggregate characteristics such as mass of aggregate or void volume or aggregate type, thereby providing an improved fundamental understanding of asphalt absorption. Also, the DGC method is unique in that it allows the absorption for a specific aggregate piece to be related to that aggregate's specific characteristics of bulk density, apparent density, and void fraction.

In this research, asphalt absorption at various conditions was measured. Experimental data show that even though aggregates may possess totally different bulk and apparent densities and void volume fractions from piece to piece, the asphalt binder absorption correlates very well with the void volume and not well that establishes binder absorption.

INTRODUCTION

Asphalt absorption is the process in which asphalt flows into a porous aggregate, under the driving force of capillary pressure (Lee, 1969; Guin et al., 1993). Excessive absorption may reduce the available asphalt for binding aggregates particles together, thereby yielding a thin asphalt film that would be more susceptible to raveling and weathering. Incorrect estimates of asphalt absorption translate into erroneous calculations of percent air voids, voids filled with asphalt (VFA), and voids in the mineral aggregate (VMA), all important parameters used in mixture design to control pavement durability and stability.

Asphalt absorption depends on asphalt properties, specifically its composition, viscosity, and surface tension (Lettier et al., 1949). Aggregate properties relevant to absorption include porosity, permeability, pore size distribution, surface area, roughness, presence of fines, aggregate size distribution (gradation), and surface chemical composition (Kandhal and Lee, 1972; Guin et al., 1993; Chang et al., 1990; Kandhal and Khatri, 1992; Lee, 1969). A discussion of various laboratory methods available to measure the aggregate properties listed above can be found elsewhere (Rice, 1953; Rice, 1956; Lee, 1969; Guin et al., 1993; Doyle and Howard, 2012). The presence or absence of water also influences the degree of absorption. The driving force for asphalt absorption is mainly determined by capillary action and thus absorption is expected to be a nonlinear function of time (Kandhal and Khatri, 1991). The amount of absorption is of interest as it affects the amount of asphalt needed for a durable mix design.

Previous research has indicated that asphalt absorption correlated with water absorption, and fundamentally related to void volume (Lettier et al., 1949; Lee, 1969). These correlations are based on measurements of samples consisting large numbers of aggregate pieces of variable properties. Because it is possible that averages veiled individual differences between aggregate samples, research on absorption of asphalt by smaller, more specifically characterized samples could be helpful to better understanding the fundamentals of absorption. In the extreme limit,

these smaller samples become measurements on individual aggregate pieces. Such experiments require precise measurement of aggregate characteristics, water and asphalt absorption, aggregate void volume and aggregate mass, for each single piece of aggregate. The density gradient column introduced for asphalt absorption measurements in Chapter 7 and applied to aggregate characterization in Chapter 8 allows this kind of investigation at improved accuracy and precision than conventional, standard methods.

The density gradient column, often used for determining the densities of small samples of polymers and other materials (Fortuin, 1960), is based on the preparation of a stable column of liquid having a known variation of specific gravity along its length. A specimen introduced into the column will settle at a level of known specific gravity, where it is in hydrostatic equilibrium with the fluid in the column (Coombs, 1981). Thus, the density of specimen can be measured precisely. By combining the densities and masses of aggregate at different conditions, the DGC method allows precise calculation of bulk density, apparent density, void volume, water absorption, and asphalt absorption for each specific aggregate piece. The DGC method does not involve measurement of particle volume and thus the measurement is simple and direct.

In the work described below, asphalt absorption was measured for individual aggregate pieces. Aggregate properties and asphalt absorption for six different kinds of aggregate were assessed. Experimental data show that aggregates possess very different bulk density, apparent densities and void volume fractions even within the same aggregate type. However, although asphalt absorption is not well correlated with aggregate mass, it does correlate very well with the void volume of each aggregate piece. This kind of correlation, consistent with previous reported work (Lee, 1969), indicates that void volume, rather than aggregate mass, is a fundamental factor that establishes binder absorption.

MATERIALS AND METHODS

Asphalt

An Alon PG 64-22 asphalt was used for absorption measurements on a number of aggregate types. A Lion PG 64-22 was used for studies of the effect of mixing and curing contact time and temperature.

Aggregate

Six aggregate types used in Texas were evaluated with respect to their aggregate and asphalt absorption characteristics: Delta Sandstone, Martin Marietta Granite, and Hanson Limestone, TX1 Lightweight Streetman, Jones Mill, and Hoban rhyolite grade 6.

Density Gradient Column

Lithium metatungstate (LMT) heavy liquid, with a density of 2.95 g/cm^3, and water were used to create the DGC for aggregate density measurements. Water has a density of 0.9980 g/mL at a lab temperature of 21°C. When LMT and water are mixed, a linear density gradient column can be prepared with densities ranging from 0.998–2.95 g/ cm^3. For the absorption measurement, aggregate pieces that have been fully characterized in their mass, and bulk and apparent specific gravities, are immersed in asphalt at 143°C for 15 seconds and then cured at 121°C for 2 hours. The asphalt coated aggregates were then further measured to obtain asphalt absorption.

RESULT AND DISCUSSION

Asphalt Absorption in Each Aggregate Piece

With the aggregate densities together with precisely measured aggregate mass, the air void and binder absorption volumes can be calculated. Each aggregate's void volume (V_{void}) is calculated as its bulk volume minus the aggregate apparent volume (volume of the aggregate excluding the void volume):

$$V_{void} = \frac{m_a}{\rho_{av}} - \frac{m_a}{\rho_a} \tag{10-1}$$

where ρ_a is the apparent density of aggregate, ρ_{av} is bulk density of aggregate, m_a is the mass of the aggregate piece. The volume of the absorbed binder ($V_{abs\text{-}b}$) is given by:

$$V_{abs-b} = \frac{m_{ab}-m_a}{\rho_b} - \frac{m_{ab}}{\rho_{ab}} + \frac{m_a}{\rho_{av}} \tag{10-2}$$

where, as before, m_{ab} is mass of aggregate coated with binder, m_a is mass of aggregate with air void, ρ_b is density of binder, ρ_{ab} is density of aggregate coated with binder, ρ_{av} is density of aggregate with air void.

The absorption of Alon 64-22 binder by six different types of aggregates were measured using the Density Gradient Column method. Table 37 and Table 38 as two examples show the detailed data for Hanson Limestone and Jones Mill quartzite aggregates.

Table 37. Absorption Data for Hanson Limestone.

Piece#	m_a	ρ_{av}	ρ_a	m_{abs}	V_{void}	V_{abs}	Void Fraction
1	0.9145	2.491	2.798	0.0179	0.040	0.017	0.1097
2	0.9289	2.560	2.787	0.0138	0.029	0.013	0.0813
3	0.5146	2.510	2.739	0.0053	0.017	0.005	0.0838
4	1.2332	2.635	2.718	0.0049	0.014	0.005	0.0305
5	0.4096	2.624	2.712	0.0036	0.005	0.004	0.0324
6	0.4866	2.587	2.673	0.0026	0.006	0.003	0.0323
7	0.7165	2.513	2.903	0.0121	0.038	0.012	0.1344
8	0.5355	2.612	2.697	0.0024	0.006	0.002	0.0317
9	0.8588	2.597	2.753	0.0098	0.019	0.009	0.0565
10	1.0510	2.645	2.688	0.0006	0.006	0.001	0.0162

Table 38. Absorption Data for Jones Mill Quartzite.

Piece#	m_a	ρ_{av}	ρ_a	m_{abs}	V_{void}	V_{abs}	Void Fraction
1	0.5587	2.369	2.802	0.014	0.036	0.013	0.1543
2	0.2840	2.536	2.806	0.003	0.011	0.003	0.0964
3	0.3256	2.492	3.041	0.008	0.024	0.008	0.1806
4	0.6626	2.412	3.098	0.022	0.061	0.021	0.2214
5	0.2766	2.550	2.908	0.005	0.013	0.005	0.1233
6	0.2705	2.579	2.831	0.003	0.009	0.003	0.0890
7	0.3184	2.519	2.888	0.005	0.016	0.004	0.1277

Table 37 and Table 38 show that for both Hanson Limestone and Jones Mill quartzite, the DGC method can measure asphalt absorption as it varies from piece to piece, thus providing the capability of correlating the absorption with other properties of aggregate to explore which factors control the binder absorption. The traditional approach to characterizing binder absorption is to report it as absorption per mass of aggregate; Figure 69 and Figure 70 show binder absorption versus aggregate mass.

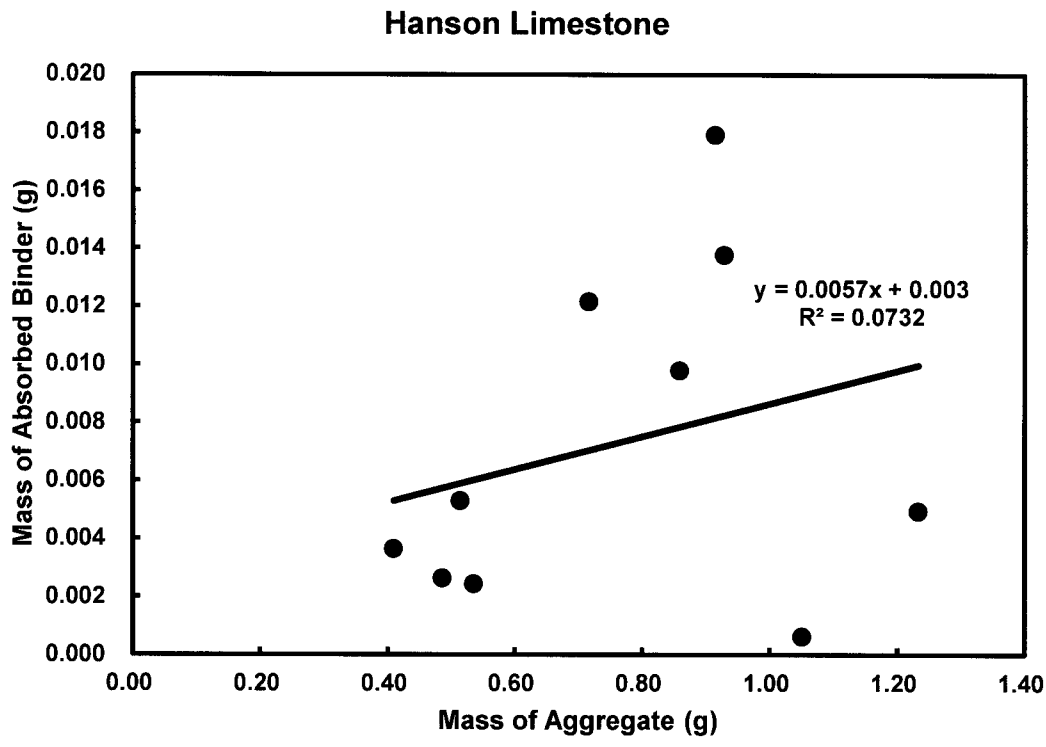

Figure 69. Asphalt Absorption versus Aggregate Mass, Hanson Limestone.

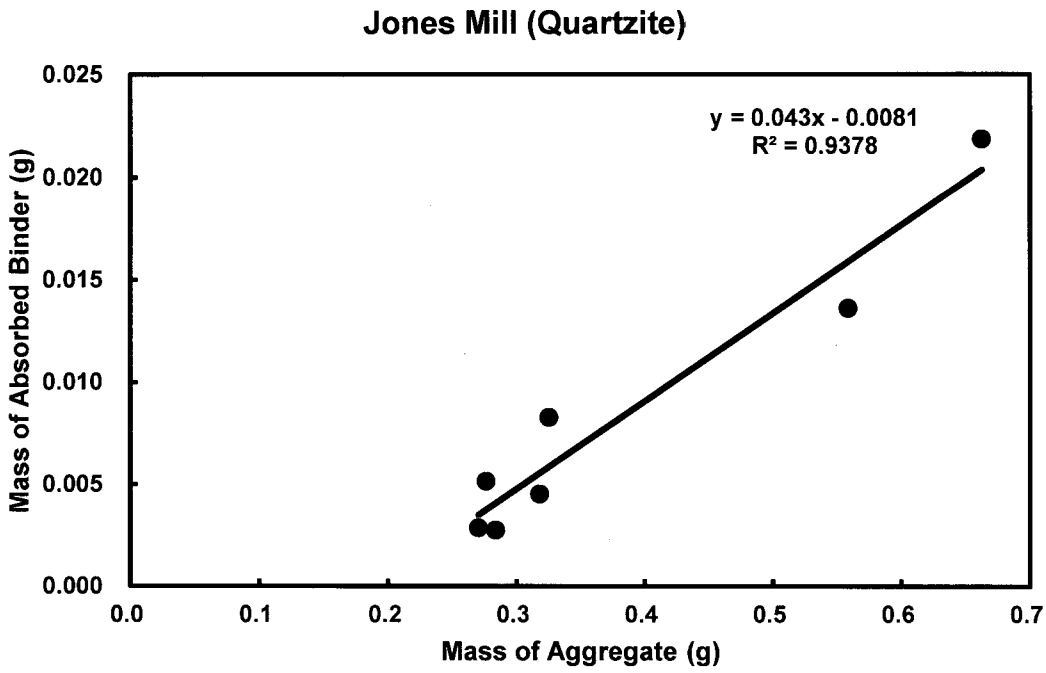

Figure 70. Asphalt Absorption versus Aggregate Mass, Jones Mill Quartzite.

Figure 69 and Figure 70 show that even though it is commonly accepted that absorption per mass of aggregate describes something fundamental about absorption, these data on individual aggregate pieces show that such a relationship is not universal. There may be a linear correlation on a per mass basis, as for the Jones Mill aggregate, or, there may not be, as is the case for the Hanson Limestone.

Aggregate Void Volume per Mass of Aggregate

The air void distribution and its relation with aggregate mass in these aggregate pieces are studied. Figure 71 and Figure 72 show the relationship of aggregate void volume to aggregate mass.

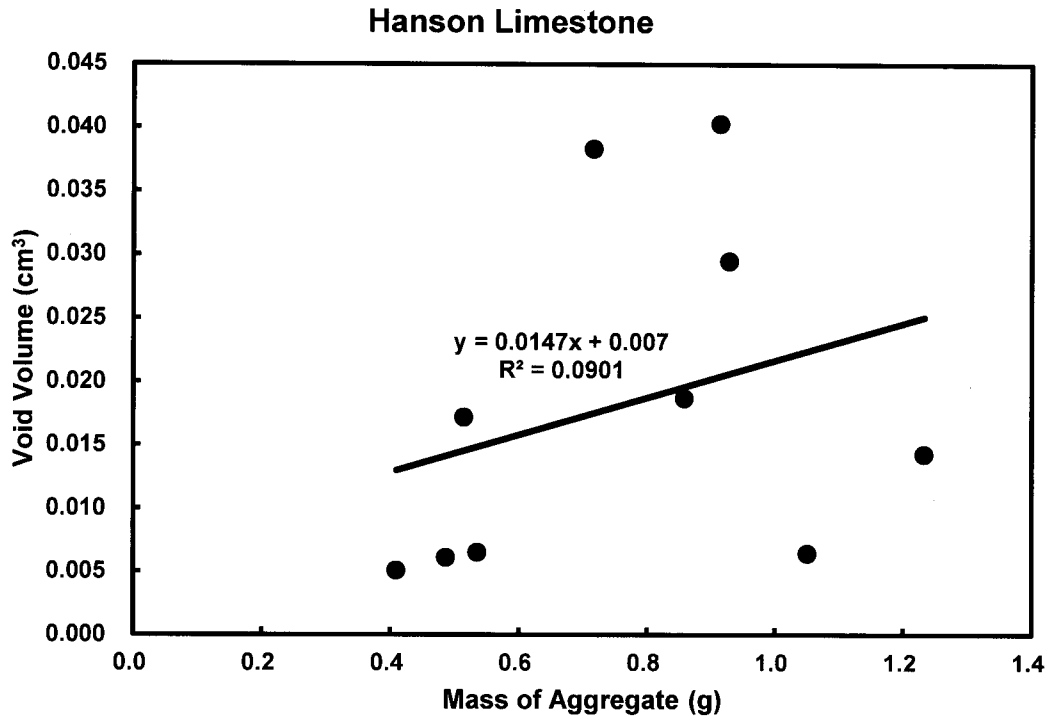

Figure 71. Air Void Distribution in Hanson Limestone Aggregates.

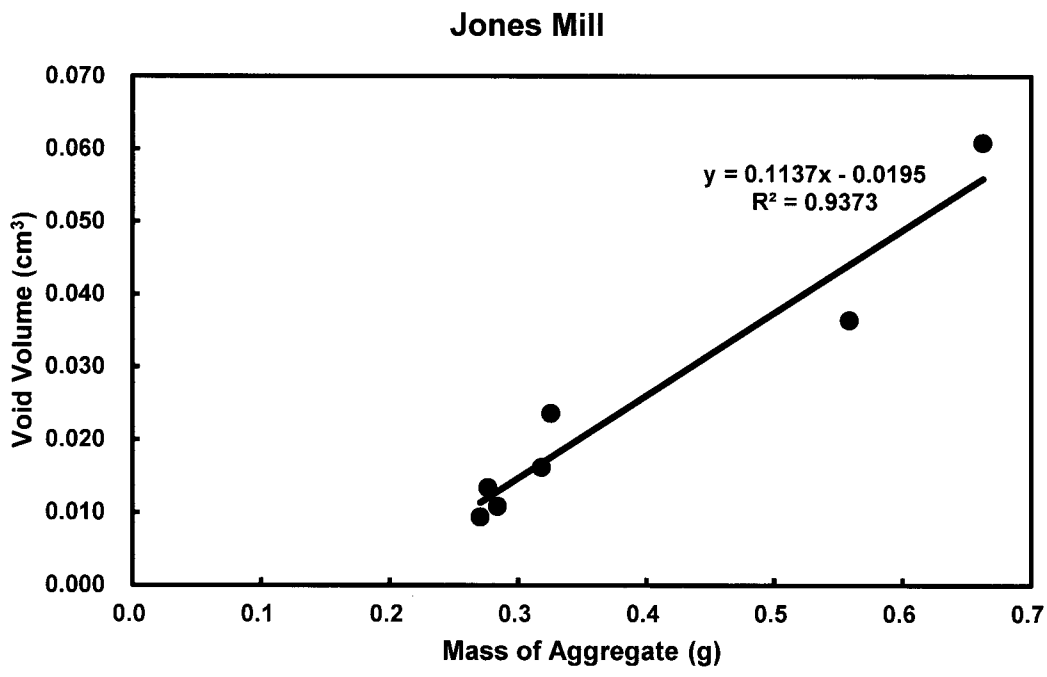

Figure 72. Air Void Distribution in Jones Mill Aggregates.

As was true of absorption versus mass relations, two different types of aggregate void versus mass plots were obtained for the Hanson Limestone and Jones Mill quartzite. For the Hanson Limestone, there is no correlation seen in the data whereas for the Jones Mill quartzite aggregates, the void volume has a very nice linear correlation with aggregate mass. These two different relations are consistent with those shown in Figure 69 and Figure 70 and suggest that the volume of absorbed binder relates to the aggregate void volume; the relationships are shown in Figure 73 and Figure 74.

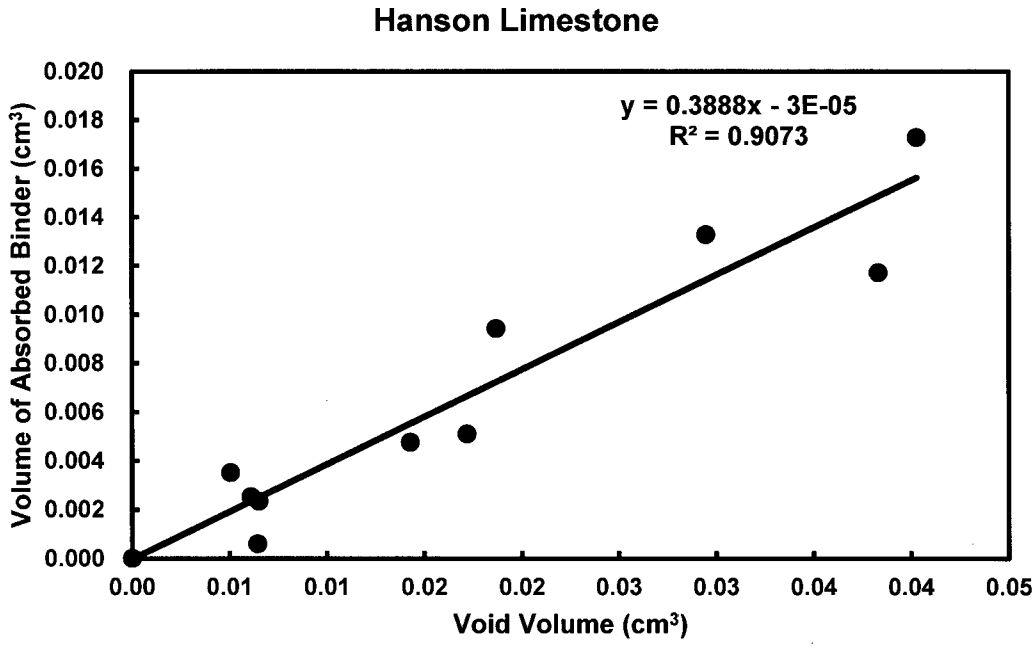

Figure 73. Relationship of Void Volume and Volume of Absorbed Binder, Hanson Limestone.

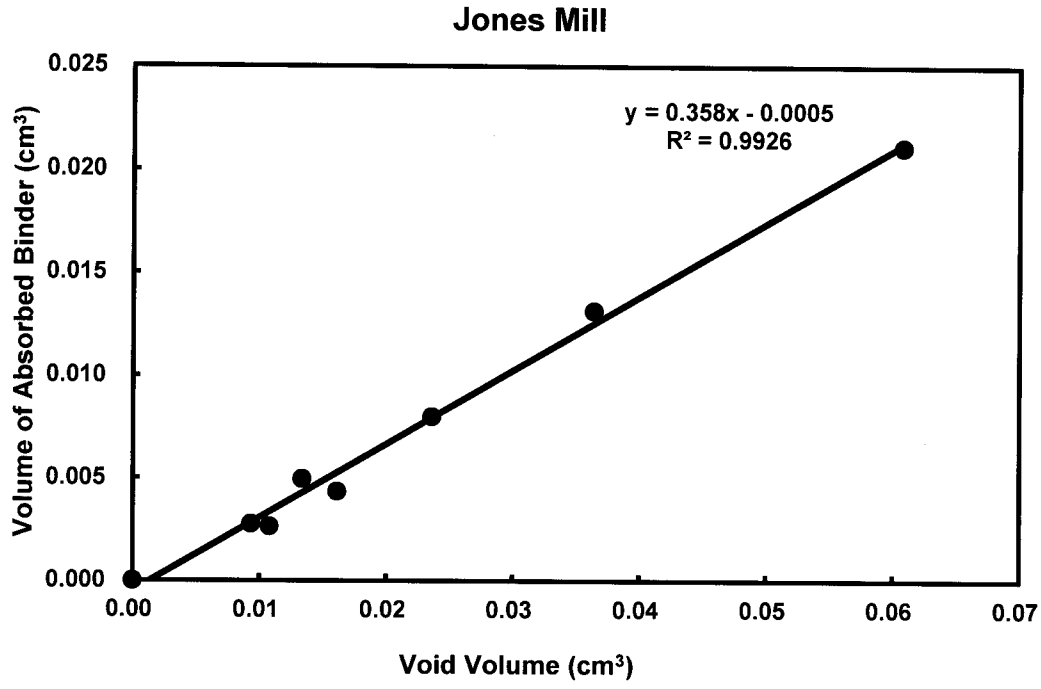

Figure 74. Relationship of Void Volume and Volume of Absorbed Binder, Jones Mill.

On the basis of volumetric calculation, the volume of absorbed binder versus void volume, in each single aggregate piece, is plotted. The origin for each data set is considered to be an a priori data point and is included in these plots. From Figure 73 and Figure 74, it is clear that there are very good linear relationships between absorbed asphalt volume and void volume. Thus, void volume is considered to be a more fundamental property for describing and correlating asphalt absorption than is aggregate mass.

Importance of Void Volume in Asphalt Absorption

In order to verify the importance of void volume in absorption research, DGC absorption data were obtained for additional types of aggregate. Delta Sandstone, Granite, Gravel, and Leightweight aggregate also were evaluated. All of these experiments used Alon 64-22 binder with 15 seconds mixing (immersion) time at 143°C followed by 2 hours curing time at 121°C. Figure 75 shows absorbed binder volume versus aggregate void volume for these four aggregates.

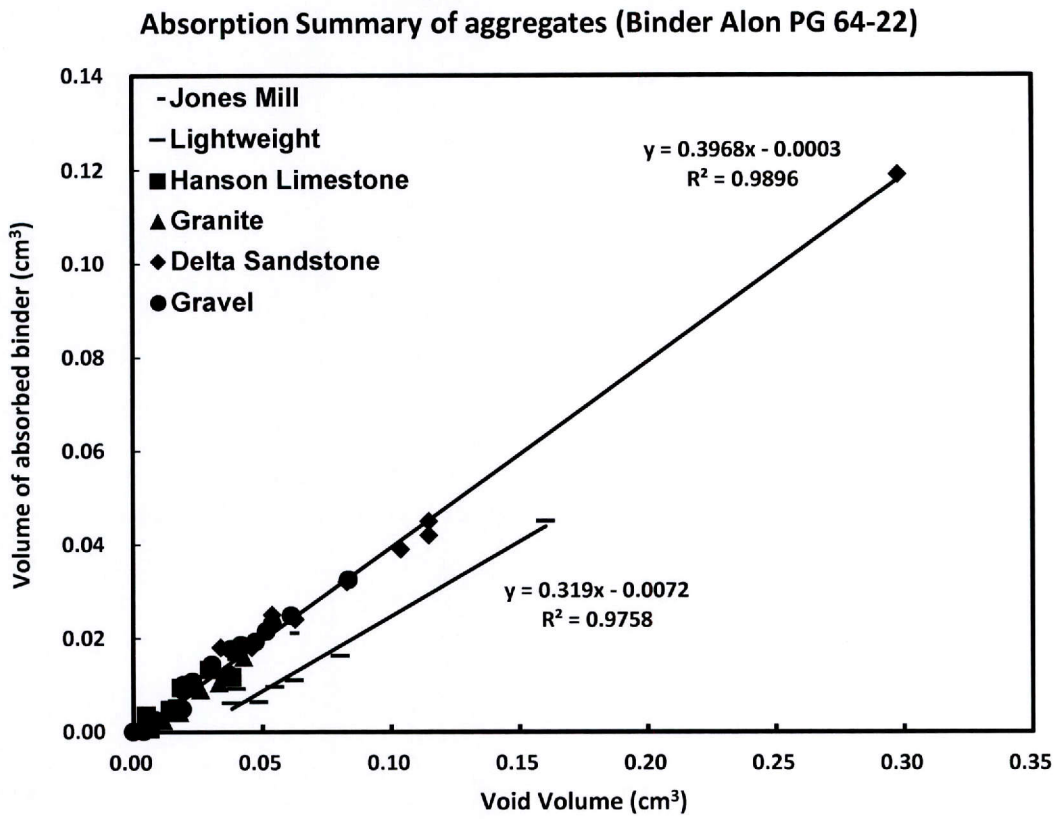

Figure 75. Correlation of Void Volume and Absorbed Binder Volume for Six Types of Aggregate.

Again, the asphalt absorbed (by each aggregate piece) is highly correlated with the aggregate air voids (of each aggregate piece). Moreover, this correlation is found for all six types of aggregates (Delta Sandstone, Martin Marietta Granite, Hanson Limestone, Jones Mill quartzite, gravel, and lightweight manufactured aggregate), indicating that the void volume of the binder plays a key role in determining the amount of asphalt binder absorption.

Additionally, except for the man-made lightweight aggregate, the slopes of the correlations on the other five types of aggregates are essentially the same at a value of 0.4, indicating that for the same asphalt and identical mixing/curing condition protocol, the percentages of void volume ultimately occupied by the asphalt is the same for the five different aggregate types.

The Linear correlation between water absorption and binder absorption, both expressed as mass percent of aggregate, has been report in previous research (Lee, 1969). Figure 76 shows this linear correlation. Using fixed water and binder density values, this correlation can be converted directly to volume asphalt absorbed versus volume of water absorbed (which is the same as aggregate void volume).

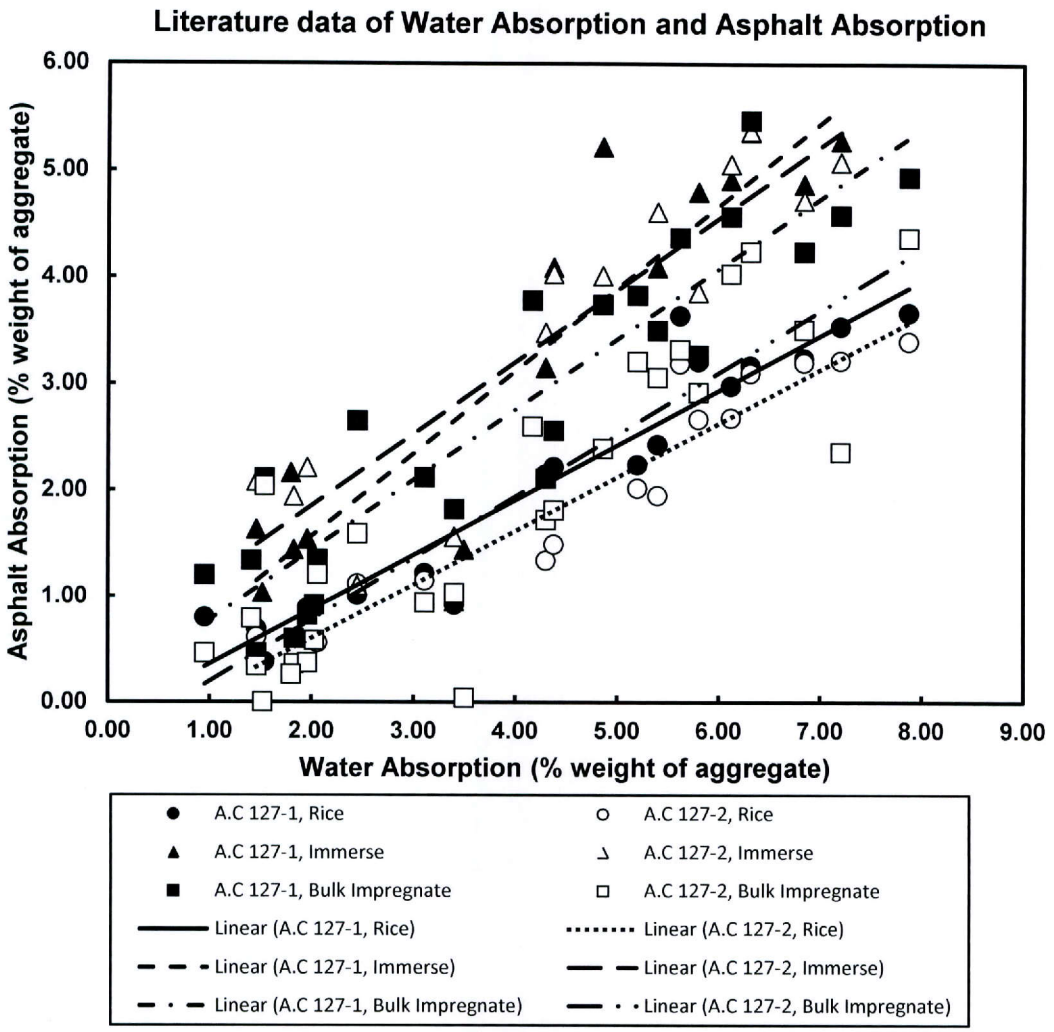

Figure 76. Linear Correlation of Water Absorption and Asphalt Absorption from Literature Data, Traditional Method.

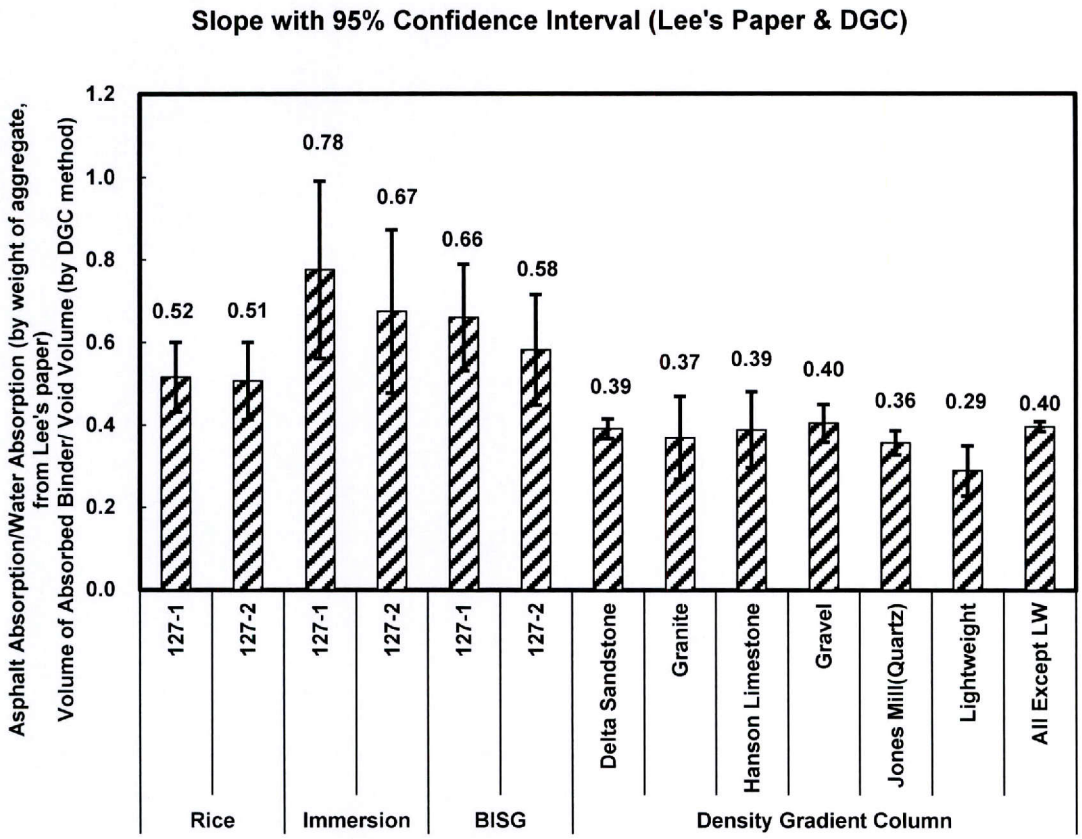

Figure 77. Statistical Analysis on the Ratio of Occupied Void Volume, DGC Method, and Traditional Methods.

Figure 77 summarizes the statistical analyses and comparison of the DGC method presented in Figure 75 to the Rice, Immersion and BISG methods evaluated by Lee (1969), shown in Figure 76.

Effect of Time and Temperature on Asphalt Absorption

Asphalt absorption is a dynamic process in which time and temperature each play important roles. With an important element of this effort being to establish the difference between HMA and WMA absorption, a study of the effect of temperature on absorption was conducted. The density gradient column was adopted as an efficient method for exploring absorption fundamentals, including the effects of time (both mixing and curing) and temperature.

Following the steps that occur in the hot mix (or warm mix) coating and curing process, the density gradient column method requires aggregates to be immersed in asphalt for a specified period of time at a specified temperature and then cured in an oven at a different temperature for a much longer period of time. In order to distinguish the different effects on asphalt absorption under these two conditioning periods, a study of mixing time and curing time was conducted using Jones Mill quartzite aggregate and Lion 64-22 asphalt binder. The results are reported below.

Mixing Time

The effect of mixing time on asphalt absorption was evaluated using multiple (from four to eight) pieces of one aggregate type (Jones Mill quartzite) and one asphalt binder (Lion PG 64-22). All aggregates were immersed in the well-stirred asphalt at 143°C for five periods: 15 seconds, 1 minute, 3 minutes, 5 minutes and 10 minutes. After immersion, these aggregates were quenched in cold water (room temperature) for 1 minute to stop the absorption process and measured immediately.

Figure 78 and Figure 79 show the fraction of aggregate void occupied by asphalt during the trial time period. Clearly, the aggregate has a high capacity to fill a large fraction of the aggregate void with asphalt, given a sufficient contact time while totally immersed in asphalt. After 10 minutes, the asphalt fills nearly 90 percent of the available voids in the aggregate. On the other hand, after 15 seconds, the absorption is greatly less than it is at the 10 minute mark, and only a little over one-fourth of the 40 percent value obtained during the baseline test of 15 seconds plus two hours cure time. Evidently, there is significant absorption that occurs while the mixture is hot but after the coating process.

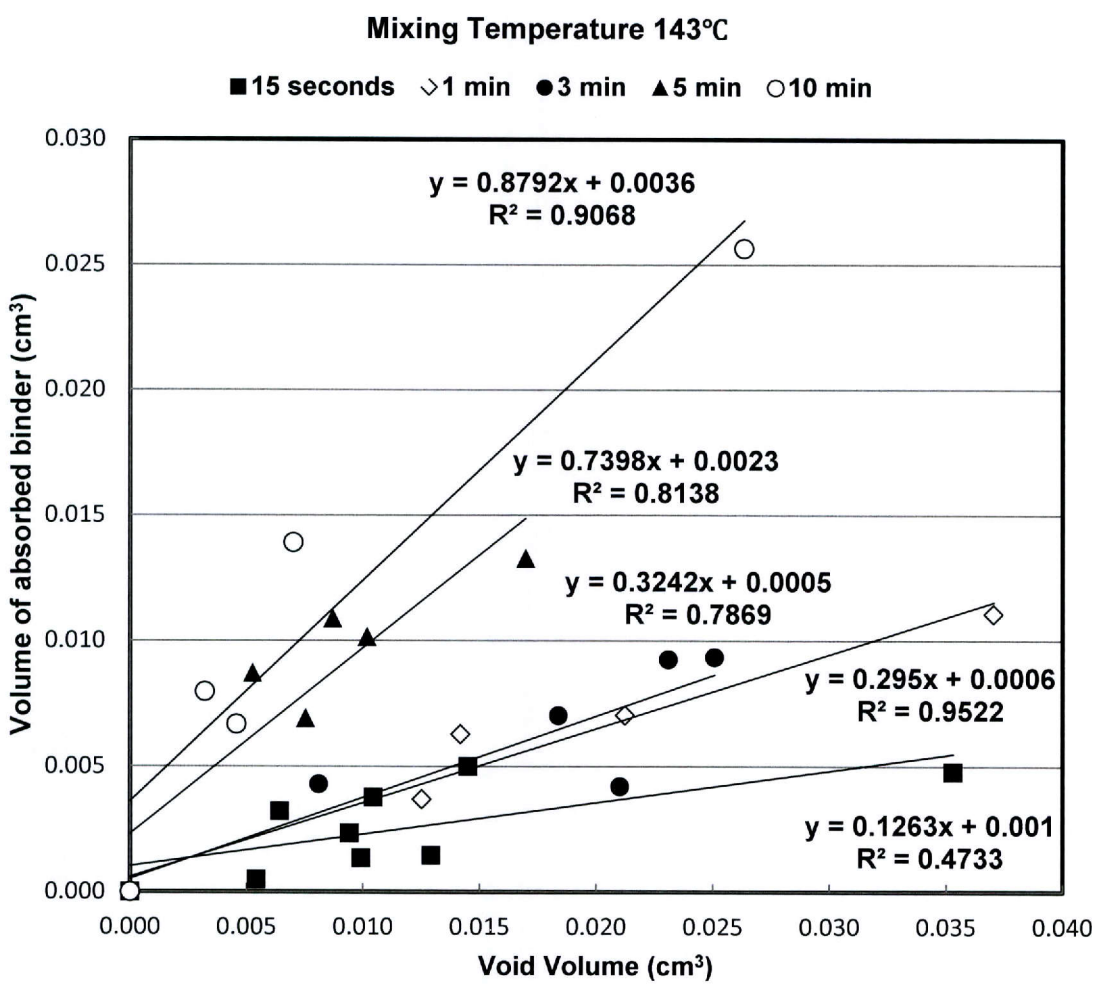

Figure 78. Linear Correlations of Void Volume and Absorbed Asphalt Volume at Different Mixing Times.

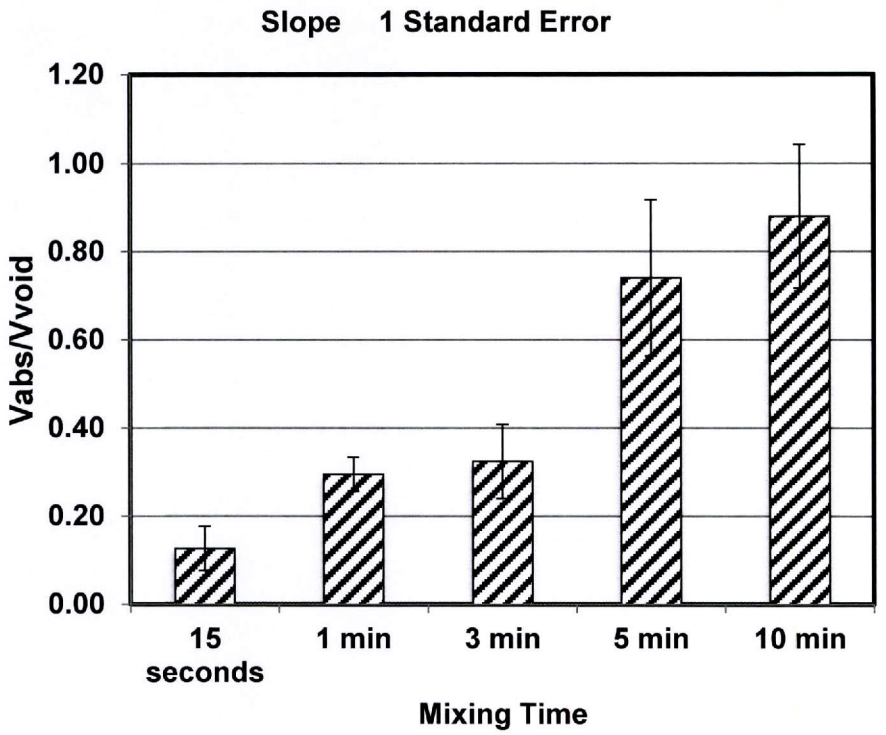

Figure 79. Statistical Analysis of Asphalt Absorption and Mixing Time.

Curing Time

Also a series of tests were conducted to evaluate the effect of curing time (after immersing the aggregate in hot asphalt) on asphalt absorption. All aggregates were pre-immersed under Lion 64-22 asphalts for 15 seconds at 143°C and then further cured in a constant temperature oven at 121°C. The curing times are 0.5 hour and 2 hours. Additional data were obtained to fill in the time gaps and establish the progression of absorption over time. Figure 80, Figure 81, and Figure 82 show these effects of variable curing time after a mixing time of 15 seconds. At these conditions, approximately one hour is required to approach the baseline absorption level of 0.4 aggregate void fraction filled with asphalt.

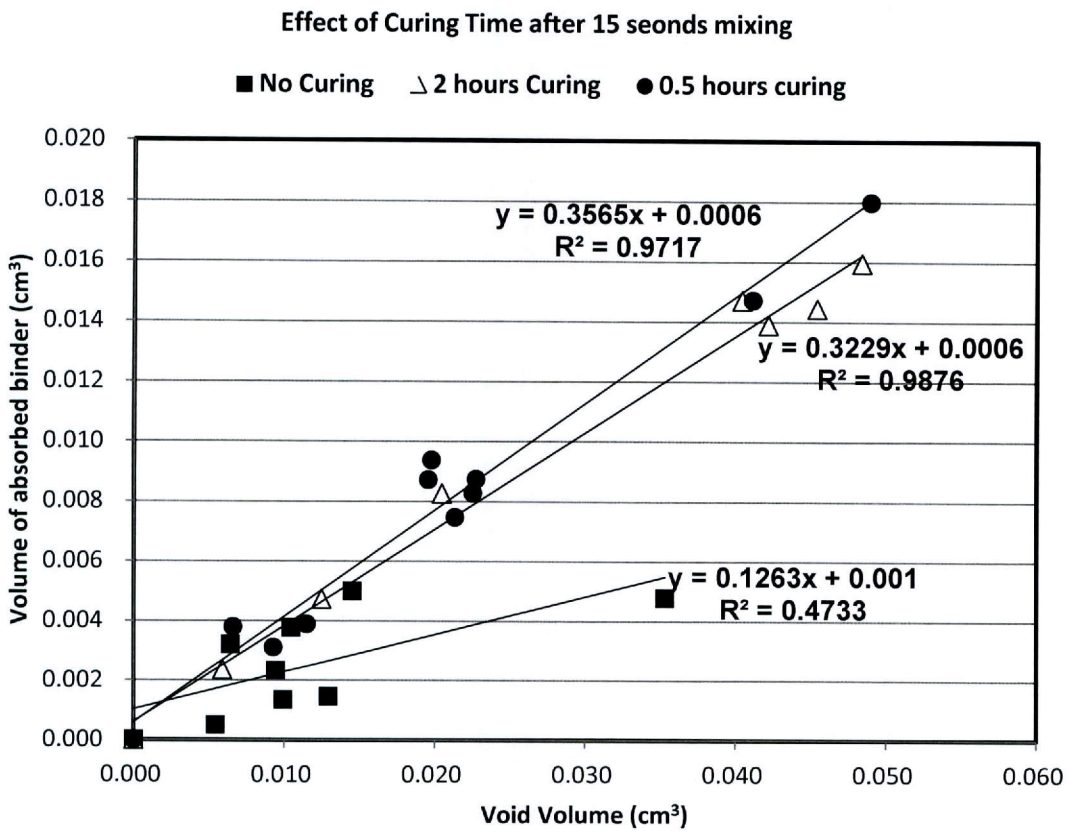

Figure 80. Linear Correlations of Absorbed Asphalt and Volume of Air Voids on Different Curing Time at 121°C.

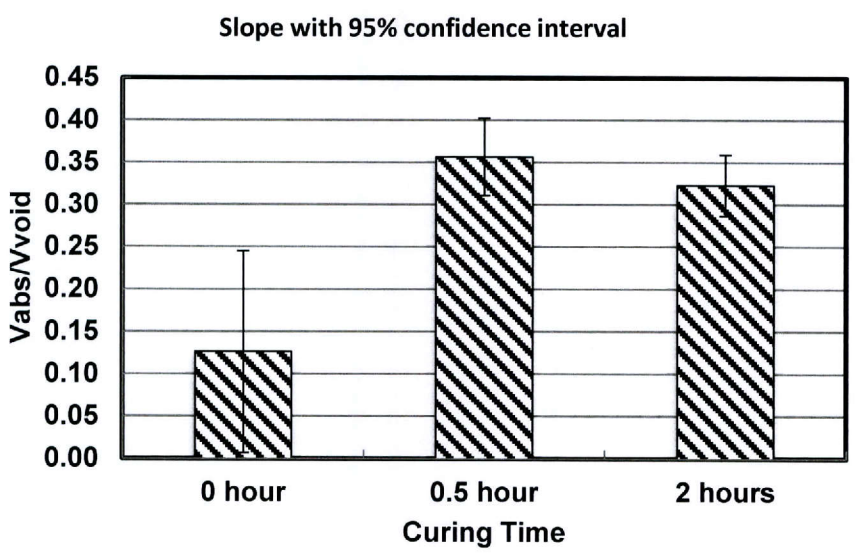

Figure 81. Statistical Analysis of the Volume Fraction of Air Voids Occupied by Asphalt.

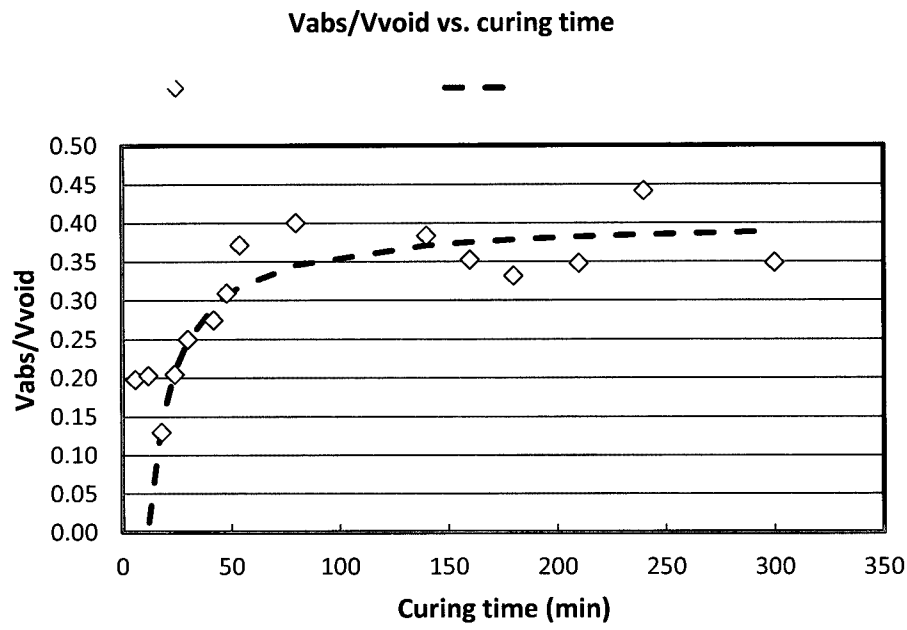

Figure 82. Hyperbolic Trendline of Curing Time and Asphalt Binder Absorption 121°C Curing, after 15 Seconds Mixing.

Temperature and Asphalt Absorption

In order to determine the effect of curing temperature and mixing temperature, a set of experiments are performed. The following tables show the effect of temperature on asphalt absorption.

Table 39. Effect of Mixing and Curing Temperature on Asphalt Absorption.

Temperature vs. V_{abs}/V_{void}		
Mixing (°C), 15 s	Curing (°C), 2 h	V_{abs}/ V_{void}
163	141	0.3260
143	121	0.3126
123	101	0.2602

CONCLUSION

Former research showed that asphalt absorption could be related to water absorption, in aggregates. However, this relationship is based on experiments using large samples of aggregate (Lettier et al., 1949; Lee, 1969). In this research, an improved method to measure asphalt absorption in aggregates was developed. The density gradient column provides a more precise means of measuring aggregate bulk density and apparent density, but for one piece of aggregate at a time. While this procedure may seem to have the disadvantage of requiring many measurements to characterize an aggregate source, it has the advantage of providing specific absorption data that correspond to specific aggregate density characteristics. As such, it provides an improved understanding of absorption fundamentals.

The density gradient column provides the capability to determine asphalt absorption for individual aggregate pieces, thus providing correlations between the amount of asphalt absorption and other properties, most importantly void fraction. Experimental results indicate that asphalt binder absorption correlates better with aggregate void volume than with aggregate mass. This kind of correlation exists for all six aggregate types that have been characterized in this work, indicating that a volumetric based correlation is fundamental to aggregate absorption.

This fraction of the aggregate void volume occupied by absorbed asphalt has been established as a fundamental factor important to understanding the effects of time and temperature on absorption. It is clear that as the contact time increases, asphalt absorption increases, and vice versa. When an aggregate is immersed into asphalt for more than 5 minutes, more than 70 percent of the air voids were filled with asphalt. Curing aggregate with asphalt at 121°C can also increase the asphalt absorption, but at a much slower rate than that at higher temperatures. Temperature experiments evaluated absorption at three different temperatures over a 40°C range. Basically, higher temperatures will cause more absorption, most certainly because of the reduced asphalt viscosity at higher temperatures. Based on these results, less absorption might be expected in WMA because of the lower temperatures, with the caveat that WMA additives may well alter the absorption trends. Absorption of asphalt from WMA is reported in the next chapter.

CHAPTER 11. ASPHALT ABSORPTION MEASUREMENT OF LOOSE MIX SAMPLES USING THE DENSITY GRADIENT COLUMN

ABSTRACT

Asphalt absorption on clean aggregate using well-controlled laboratory conditions and the DGC method has been demonstrated. Yet direct absorption measurements of mixtures are needed to provide a calibration of mixture processes to laboratory methods and to compare actual technologies (such as WMA), as implemented in the field, to conventional methods. The field and proprietary aspects of commercial processes provide their own challenges to duplicating field results in the laboratory and thus necessitate a valid measurement on the field mixtures.

By reversing the Density Gradient Column procedure, asphalt absorption in loose mixes was measured. Conceptually, the method could be used on compacted mixtures (pavement cores) also, although not without some additional difficulties. As with DGC binder absorption studies that start with clean aggregate, loose mixture measurements also found that binder absorption depends linearly on aggregate void volume, thereby supporting the conclusion that void volume is a fundamental factor in establishing asphalt absorption. The dominant feature of these absorption measurements is that in each case, the WMA loose mixes exhibited less absorption than the HMA control.

Linear correlations of the various recovered binder properties (log low-shear rate viscosity, log DSR function, and CA) with binder absorption (expressed as volume of binder absorbed per aggregate void volume) were found for the HMA control, Sasobit, Evotherm and Advera asphalts. The data suggest that a combined effect of binder rheology, WMA process conditions plus technology formulations that affect surface energies and asphalt aggregate wettability may alter absorption.

OBJECTIVE

There were three primary objectives of this work:

- To directly measure the level of asphalt absorption achieved in Lufkin loose mixes.
- To compare asphalt absorption with standard method calculations.
- To evaluate the various factors affecting absorption in loose mixtures.

MATERIALS AND METHODS

This chapter documents absorption measurements on hot mix and warm mix loose mixes from a single pavement test site. In February and March of 2008, the Lufkin District placed four different WMA technology field trials together with a hot mix control section. The 1.5 inch mat was a mix design with the following characteristics: Item 341, Type D dense graded mix having 4.6 percent PG 64-22 binder (the same base binder for both HMA and WMA test sections), aggregate that was 91 percent Hanson Chico limestone and 9 percent field sand, an anti-strip of 1 percent lime in all test sections (both HMA and WMA). The warm mix technologies that were placed were Sasobit, Evotherm DAT, Akzo Nobel Rediset, and Advera. The mixture production temperatures at load out were 270°F for the HMA and 240°F for the WMA technologies.

Materials Characterization

Two analytical techniques were used to characterize the oxidation level of unaged and aged binders. Infrared spectroscopy was used to measure the carbonyl area as discussed in the literature review and a Carri-Med CSL 500 controlled stress rheometer was used to measure both the low shear rate limiting viscosity and the DSR function. The low shear rate limiting viscosity is obtained from a frequency sweep at 60°C from 0.1 rad/s to 100 rad/s. The DSR function is measured at 44.7°C and 10 rad/s then time-temperature shifted to 15°C, 0.005 rad/s (Ruan et al., 2003).

Density Gradient Column

In order to measure the absorption of loose mix by DGC, a reverse process was applied. This process is the reverse of the method described in Chapters 8 and 10 in that the coated aggregate is measured first; then the aggregate is characterized after it is stripped of the binder. Specifically, the steps are:

- Measure the mass and density of the aggregate coated with asphalt.
- Extract and recover the aggregate with THF solvent.
- Measure the cleaned aggregate bulk density and apparent density using the wax coating and water saturation methods described and applied in Chapters 8 and 10.
- Adjust the binder density with any filler aggregate mixed with asphalt.

The reverse process necessarily started with measuring the density of the binder-coated aggregate followed by stripping the aggregate of coated and absorbed binder and then measuring the aggregate bulk and apparent densities. These aggregate densities, together with the recovered binder density, were used in the DGC method calculation. Measuring the binder density was complicated by the presence of fillers in the mix. A calculation procedure based on measuring the recovered binder (but absent filler) density and mass and the recovered filler mass was used to estimate the binder/filler density that existed in the mixture.

RESULT AND DISCUSSION

Asphalt Absorption Calculated by ASTM Method

Bulk Specific gravity and water absorption of Lufkin raw aggregates are listed in Table 40.

Table 40. Aggregate Properties of Lufkin Aggregates.

Aggregate	Gradation	Bulk Specific Gravity (Oven Dry)	Bulk Specific Gravity (SSD)	Apparent Specific Gravity	Water Absorption %
Fine	Screen	2.592	2.636	2.712	1.7
	Sand	2.593	2.620	2.666	1.1
Coarse	D/F	2.629	2.662	2.718	1.2

In the Lufkin field mixes, bulk specific gravity, theoretical maximum specific gravity, effective specific gravity, and binder content also were either measured or obtained from the mix design process. The binder content was measured by extraction and recovery (REF). These data are listed in Table 41. Water absorption for the Lufkin aggregates was 1.27 mass percent.

Table 41. Aggregate Properties for the Lufkin Project.

Asphalt Type	P_b, %	$G_{sb,blend}$	G_{mm}	G_{se}
HMA Control	3.76	2.613	2.490	2.637
Sasobit	3.60	2.613	2.480	2.619
Evotherm	3.50	2.613	2.485	2.620
Advera	3.94	2.613	2.479	2.632
Rediset	3.48	2.613	2.496	2.632

The absorbed asphalt by weight percent (P_{ba}) is calculated using the following equations.

$$P_{ba} = 100 \times \left(\frac{G_{se}-G_{sb}}{G_{sb}\times G_{se}}\right) \times G_b \tag{11-1}$$

and

$$G_{se} = \frac{P_{mm}-P_b}{\left(\frac{P_{mm}}{G_{mm}}-\frac{P_b}{G_b}\right)} \tag{11-2}$$

where G_{se} is the effective specific gravity of aggregate, G_{sb} is the bulk specific gravity of aggregate, G_b is the specific gravity of binder, and Pmm=100+Pb. By calculation, binder absorption and water absorption are listed in Table 42.

Table 42. Binder and Water Absorption, Lufkin Samples.

Asphalt Type	P_{ba}, %	Water Absorption Percent	P_{ba}/Water Absorption Percent
HMA Control	0.361	1.27	0.284
Sasobit	0.087	1.27	0.069
Evotherm	0.110	1.27	0.087
Advera	0.285	1.27	0.225
Rediset	0.286	1.27	0.225

This result show that binder absorption does change with different warm mix additives. Figure 83 shows this change clearly. From the view of mass percent, warm mix with Evotherm and Sasobit technologies, strongly reduced the asphalt binder absorption.

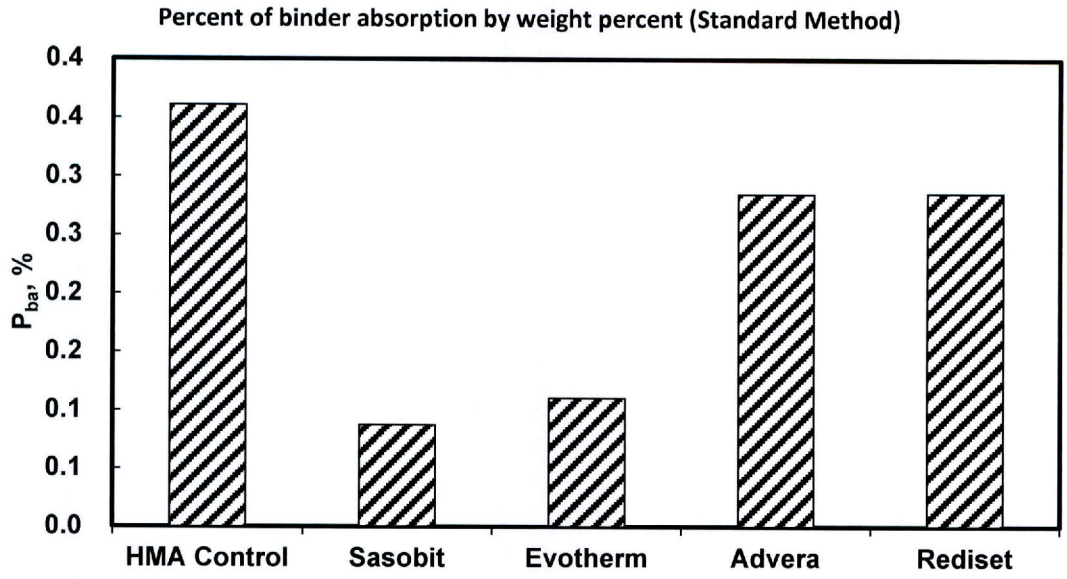

Figure 83. Binder Absorption of Lufkin Samples, Calculated Using ASTM Method.

Asphalt Absorption Calculated by Density Gradient Column Method

The density gradient column method was applied to measurements of asphalt absorption of Lufkin loose mix samples. In the DGC method, binder absorption of individual pieces of coarse aggregate was measured. Aggregate properties, such as bulk density, apparent density and void volume were also measured. Table 43 shows data from DGC method for the Lufkin loose mix samples. For each aggregate piece, binder volume absorbed and the aggregate void volume are calculated to provide an average value (of several aggregate pieces) of the volume of absorbed binder per aggregate void volume.

Table 43. Lufkin Loose Mix Asphalt Absorption by Density Gradient Column Method.

Asphalt Type	Mass of Aggregate	Bulk Density (g/cm^3)	Apparent Density (g/cm^3)	Void Volume (cm^3)	Volume of absorbed binder (cm^3)	Void Fraction
Control	1.2920	2.561	2.891	0.057	0.027	0.1140
Control	1.2176	2.593	2.835	0.040	0.018	0.0851
Control	0.8616	2.593	2.802	0.025	0.009	0.0746
Control	1.0465	2.594	2.876	0.040	0.015	0.0980
Control	0.3154	2.484	3.066	0.024	0.009	0.1900
Sasobit	0.2472	2.529	3.036	0.016	0.010	0.1670
Sasobit	0.6119	2.567	2.942	0.030	0.013	0.1277
Sasobit	0.2745	2.586	2.912	0.012	0.004	0.1119
Sasobit	1.0202	2.503	3.057	0.074	0.029	0.1814
Sasobit	0.4809	2.489	2.973	0.031	0.013	0.1629
Sasobit	0.2839	2.548	2.828	0.011	0.006	0.0990
Sasobit	0.4049	2.476	3.073	0.032	0.014	0.1943
Sasobit	1.0239	2.506	2.980	0.065	0.028	0.1592
Sasobit	0.6589	2.573	2.916	0.030	0.014	0.1176
Sasobit	0.6560	2.507	3.034	0.045	0.018	0.1736
Evotherm	0.3720	2.493	3.098	0.029	0.010	0.1953
Evotherm	0.5176	2.478	3.055	0.039	0.013	0.1889
Evotherm	0.6507	2.326	3.321	0.084	0.028	0.2996
Evotherm	0.5346	2.417	2.963	0.041	0.011	0.1843
Evotherm	0.1741	2.501	3.017	0.012	0.005	0.1711
Evotherm	0.5748	2.534	2.981	0.034	0.012	0.1501
Advera	0.4775	2.469	2.765	0.021	0.007	0.1070
Advera	0.8093	2.557	2.900	0.037	0.009	0.1183
Advera	0.3627	2.513	2.972	0.022	0.006	0.1546
Advera	0.6297	2.581	2.885	0.026	0.007	0.1054
Advera	0.5647	2.499	2.932	0.033	0.007	0.1474
Advera	1.1301	2.525	2.972	0.067	0.018	0.1506
Advera	0.4978	2.522	3.038	0.034	0.010	0.1700
Advera	0.6371	2.595	2.814	0.019	0.002	0.0777
Rediset	0.4464	2.630	2.805	0.011	0.003	0.0623
Rediset	0.9930	2.528	2.865	0.046	0.016	0.1176
Rediset	0.3152	2.574	2.814	0.010	0.003	0.0855
Rediset	0.6356	2.557	2.821	0.023	0.009	0.0936
Rediset	0.2835	2.641	2.778	0.005	0.002	0.0493
Rediset	0.2728	2.582	2.785	0.008	0.002	0.0729
Rediset	0.3003	2.488	2.882	0.016	0.005	0.1367
Rediset	0.5293	2.550	2.934	0.027	0.009	0.1310
Rediset	0.5085	2.625	2.795	0.012	0.003	0.0607
Rediset	0.6220	2.531	3.010	0.039	0.010	0.1592

DGC measurements indicate that the volume of asphalt absorption correlates well with the void volume, whether HMA or any of the four WMA mixtures. However, the slope of this correlation for the different mixtures varies, suggesting that asphalt binder type, temperature, and additives affect asphalt absorption. Figure 84 and Figure 85 show these results.

The dominant feature of these absorption measurements is that in each case, the WMA loose mixtures exhibited less absorption than the HMA control. The difference between the control and Sasobit mixtures could be considered not significant (p=0.09) but the differences from the control mix are much better defined for the other WMA processes (Evotherm: p=0.008, Advera: p=0.002, Rediset: p=0.01).

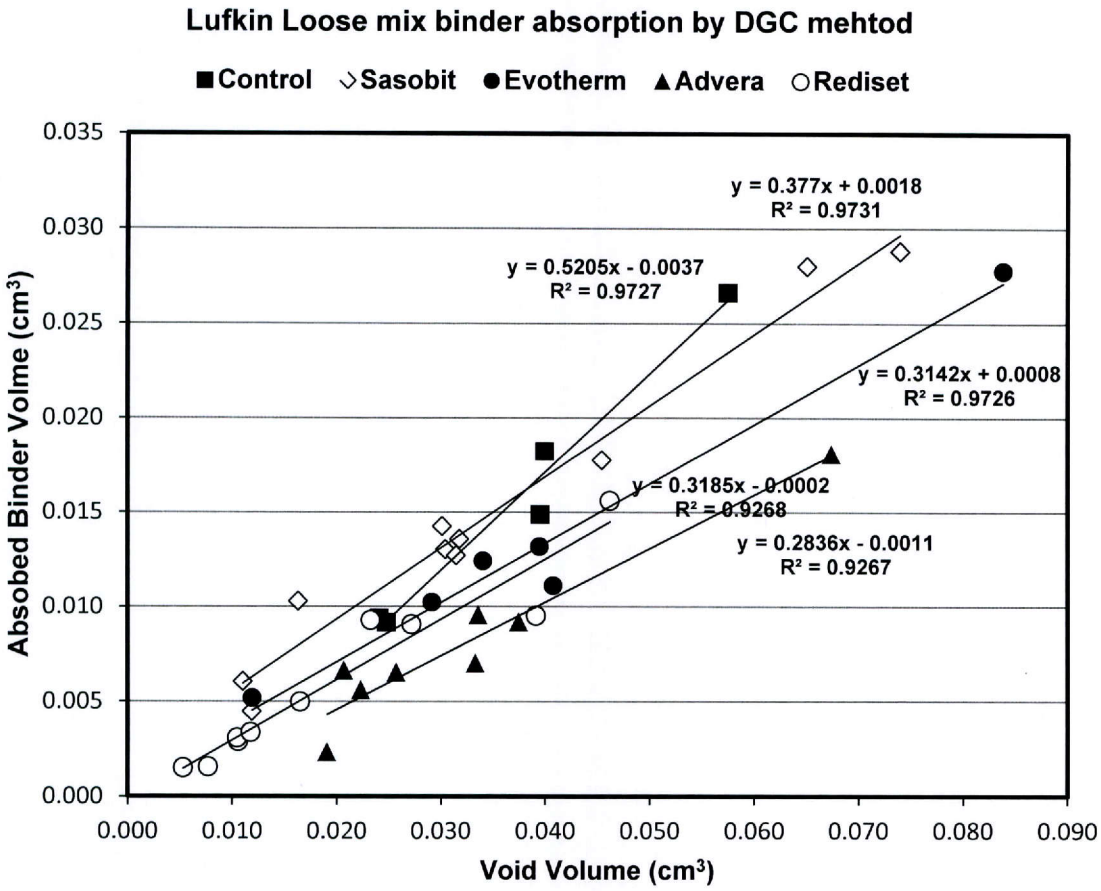

Figure 84. Linear Correlations of Asphalt Absorption and Air Void, Volumetric View.

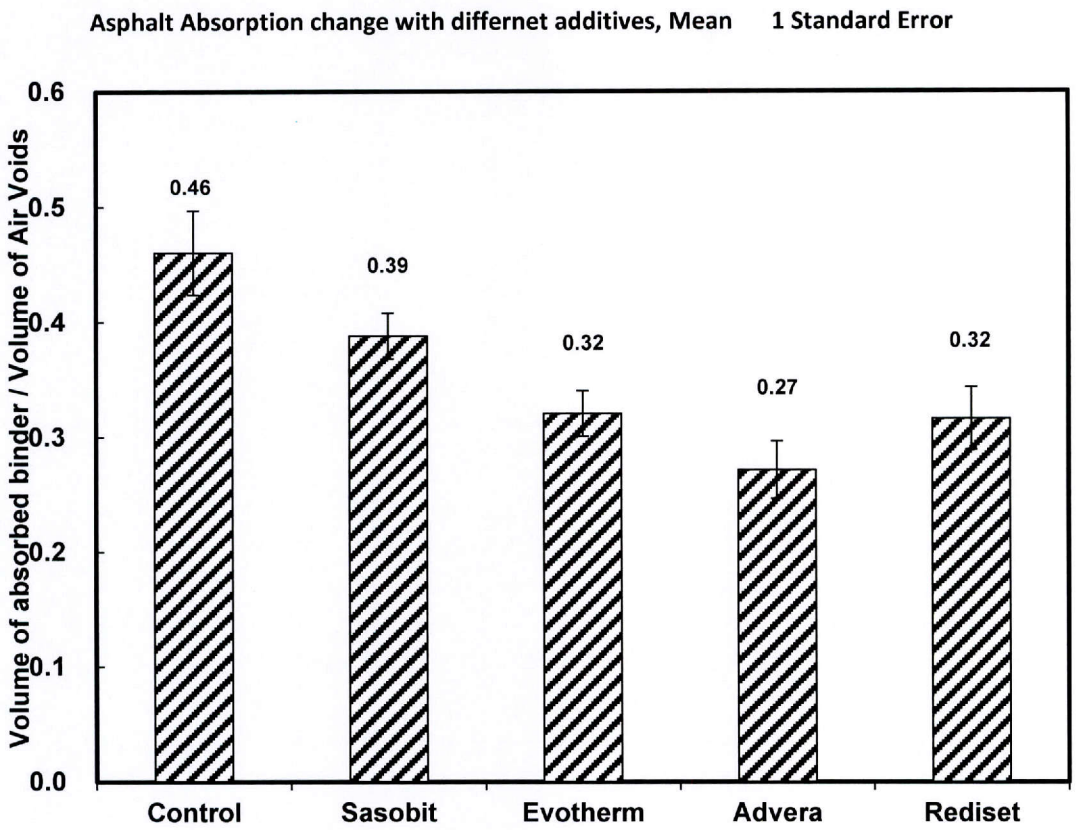

Figure 85. Mean Slope and 95 Percent Confidence Interval of the Mean.

Characteristics of Recovered Lufkin Binder

Using extracting and recovery method, asphalt binders are successfully recovered from Lufkin loose mix. Subsequently, the DSR function, the 60°C low shear-rate limiting viscosity, and the FTIR carbonyl area were measured. Table 44 shows these data.

Table 44. Characteristics of Recovered Lufkin Binder.

Asphalt Type	60°C Limiting Viscosity	DSR Function	Carbonyl Area
HMA Control	13770.04	0.000070	0.877
Sasobit	18328.64	0.000096	0.888
Evotherm	21935.24	0.000133	0.924
Advera	20761.36	0.000130	0.945
Rediset	15999.90	0.000071	1.009

Interestingly, linear correlations of the various recovered binder properties (log low-shear rate viscosity, log DSR function, and CA) with binder absorption (expressed as volume of binder

absorbed per aggregate void volume) were found for the HMA control, Sasobit, Evotherm, and Advera asphalts. Figure 86, Figure 87, and Figure 88 show these correlations.

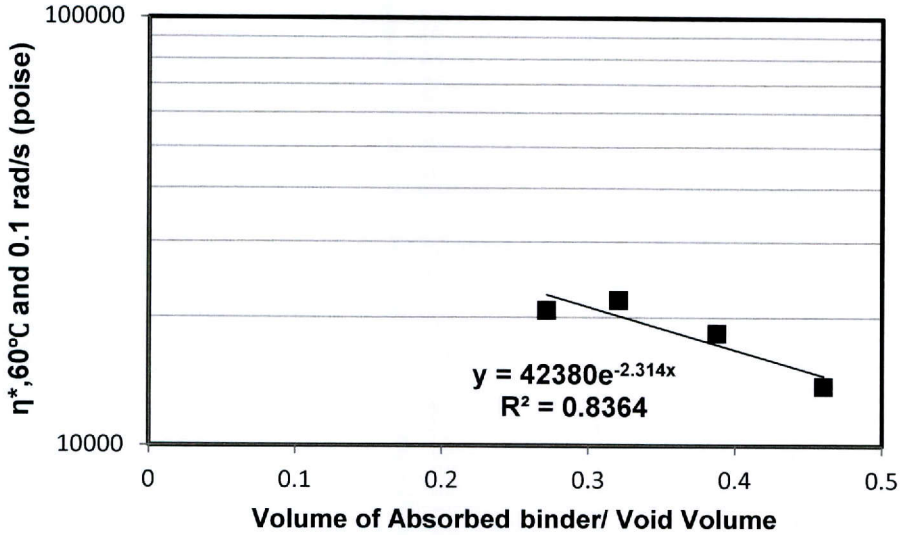

Figure 86. Exponential Correlation of Absorption Fraction and 60°C Limiting Viscosity.

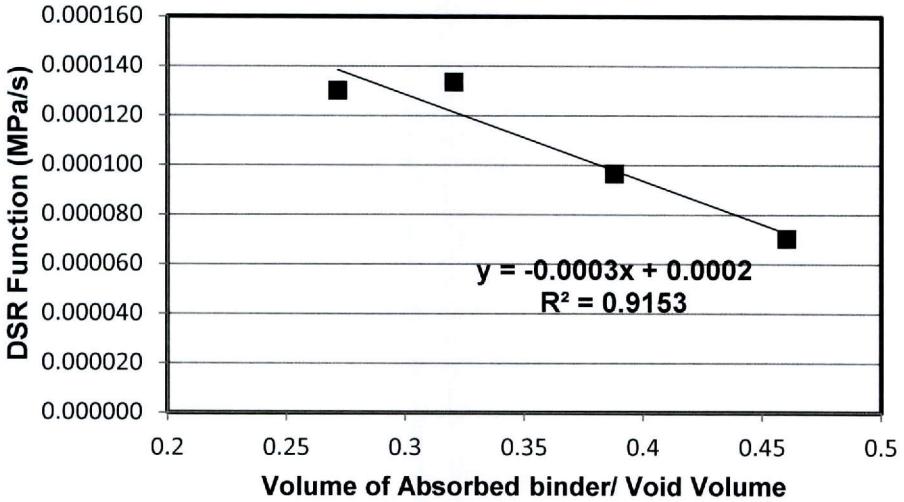

Figure 87. Linear Correlation of Absorption Fraction and DSR Function.

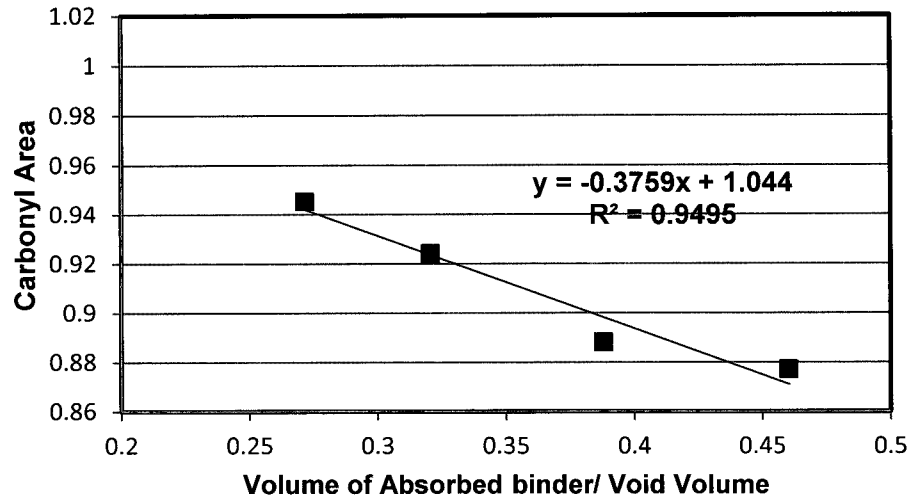

Figure 88. Linear Correlation of Absorption Fraction and Carbonyl Area Value.

The reason for these correlations is not understood. At first glance, it would make sense that the less "stiff" the binder rheology (expressed either as the 60°C low shear rate limiting viscosity or as the DSR function), the higher the absorption, and indeed, this is the case. Plus the fact that CA also shows a correlation is simply a reflection of the HS relation between the binder rheology and level of oxidation. However, what does not seem to fit is the fact that the HMA binder is the binder that is less "stiff" and less oxidized, rather than the WMA binders. Furthermore, we would expect that the lower WMA processing temperatures (compared to the HMA process) would result reduced absorption for the WMA process. And, it may well be true that without the reduced temperature, the binder absorption differences in the loose mix samples would have been even more accentuated than the data show.

The Rediset WMA recovered binder did not fit the correlation of the other binders for in a couple of ways. First, the Rediset CA was inordinately high in comparison to its rheology; this places it well above the line shown in Figure 88. Perhaps this anomaly was because of an additive to the Rediset binder that registered as an increase in CA independent of its absorption. However, an additional, although lesser, anomaly may exist with the absorption as it is affected by the binder rheology. The Rediset binder shows less absorption than its rheology would suggest, based upon the other binders. The rheology is similar to the hot mix recovered binder but its absorption is more in line with the Evotherm binder. Both of these anomalies may relate to the surface active nature of this Rediset WMA process. The additive may affect the CA reading but may also affect the binder absorption through aggregate wettability by the binder or the binder-air interfacial tension. A non-wetting contact angle and/or a reduced binder-air interfacial tension could, in principle, decrease the extent of binder absorption.

SUMMARY

In this study, by reversing the process of Density Gradient Column, asphalt absorption in loose mixes was measured. The reverse process necessarily started with measuring the density of the binder-coated aggregate followed by stripping the aggregate of coated and absorbed binder

and then measuring the aggregate bulk and apparent densities. These aggregate densities, together with the recovered binder density, were used in the DGC method calculation. Measuring the binder density was complicated by the presence of fillers in the mix. A calculation procedure based on measuring the recovered binder (but absent filler) density and mass and the recovered filler mass was used to estimate the binder/filler density that existed in the mixture.

As with DGC binder absorption studies that start with clean aggregate, loose mixture measurements also found that binder absorption depends linearly on aggregate void volume. This result supports the conclusion that void volume is a fundamental factor in establishing asphalt absorption. For each mixture type, HMA or the several WMA formulations evaluated, measurements on the individual pieces of aggregate gave a consistent absorption versus void volume correlation together with statistical estimates of the 95 percent confidence intervals for the absorption values.

The dominant feature of these absorption measurements is that in each case, the WMA loose mixes exhibited less absorption than the HMA control. However, whereas the difference between the control and Sasobit mixtures could be considered not significant, the differences from the control mix are much better defined for the other WMA processes.

Interestingly, linear correlations of the various recovered binder properties (log low-shear rate viscosity, log DSR function, and CA) with binder absorption (expressed as volume of binder absorbed per aggregate void volume) were found for the HMA control, Sasobit, Evotherm and Advera asphalts. Quantitatively, the reasons for these correlations are not understood. The data suggest, however, that there is a combined effect of binder rheology, WMA process conditions and technology formulations that affect surface energies and asphalt aggregate wettability.

CHAPTER 12. ABSORPTION SPECTRUM TESTS

It has been found that aggregates used in paving asphalt mixtures absorb the asphalt binder into the porous structure of the aggregates. National test methods are available to measure the aggregate absorption. However, most research and measurements on aggregate absorption are limited to the accessible voids at the aggregate surface. This paper presents recent findings on the selective absorption of asphalt binder by aggregate particles in asphalt mixtures. The selective absorption of the binder is visualized on the aggregate surface under natural light and UV light. Rings with different colors are identified on the cross-sections of the aggregates in both Hot Mix Asphalt and Warm Mix Asphalt, which indicates different asphalt components at different radial distances from the center of the aggregates. The asphalt components penetrating into aggregates are verified using the Laser Desorption Ionization – Ion Mobility – Mass Spectrometer. Significantly higher concentration of asphalt components is identified at the edge of the limestone sample than in its center after it is soaked in the AAD asphalt binder for 32 hours. Creep tests are also conducted on fresh limestone samples and limestone samples soaked in the AAD binder. The fresh limestone sample behaves elastically and is approximately twice as stiff as the sample soaked in the binder, which exhibits non-negligible viscoelastic properties in the creep test.

INTRODUCTION

It has been found that aggregates used in paving asphalt mixtures absorb the asphalt binder into the porous structure of the aggregates (Lee et al. 1990; Curtis et al. 1993; Roberts et al. 1996). National standard test procedures are also available to measure aggregate absorption (AASHTO 2010; ASTM 2007). These research observations and measurements on aggregate absorption are limited to the accessible voids at the aggregate surface. Little literature has reported any finding on the distribution of the molecules in the asphalt binder into the inside of the aggregates in an asphalt mixture.

This tech memo reports very recent findings on molecules in the asphalt binder traveling into the inside of aggregates in an asphalt mixture, which has non-negligible effects on the physical properties of the aggregates. Since the typical asphalt binders for paving purposes have complex chemical compositions, molecules are found to travel different distances into the aggregates. Specifically, a typical asphalt binder has four broad component groups, including asphaltenes, resins, aromatics, and saturates (Read and Whiteoak 2003). Molecules in these component groups have various molecular weights and chemical characteristics, which determine their traveling speed and distance inside the aggregate particles. With selective absorption, the aggregate particle changes from a homogeneous material to a heterogeneous material with asphalt molecules scattered inside the aggregate particle. The selective absorption not only changes the composition of the aggregate particle but also its physical properties, such as the modulus.

This chapter is organized in five sections. The next section presents the visualization of asphalt components in aggregate particles from both lab-mixed-lab-compacted (LMLC) mixtures and field cores. The following section details the verification of asphalt components inside aggregates using the Laser Desorption Ionization – Ion Mobility – Mass Spectrometer. The subsequent section describes the creep tests that are conducted on fresh limestone samples and

limestone soaked in an asphalt binder for a period of time in order to quantify the variation in mechanical properties of the aggregate particles. The last section summarizes the major findings.

VISUALIZATION OF AGGREGATES IN ASPHALT MIXTURES

In order to investigate the selective absorption of the asphalt binder by aggregates, asphalt mixtures are firstly examined visually under natural light and ultraviolet (UV) light (black light), respectively. The selected asphalt mixtures include both hot asphalt mixtures (HMA) and warm asphalt mixtures (WMA). These mixtures are either LMLC mixtures or field cores taken from asphalt pavements. In every selected asphalt mixture, the aggregate is a common Texas limestone which is considered to be porous.

Lab-Mixed-Lab-Compacted Mixtures

When investigating the LMLC HMA, the limestone aggregates are firstly sieved into a Type C dense aggregate gradation specified by Texas DOT (2004). The aggregate matrix is then mixed with an unmodified asphalt binder labeled as "AAD" in the Strategic Highway Research Program (SHRP) Material Reference Library (MRL) (Jones 1993). The AAD binder has a PG 58-28 grade. The mixing temperature is 135°C according to the Texas DOT Specification for HMA. Immediately after mixing, a coarse aggregate coated with the binder is picked up and then is sawed into halves, one half of which under natural light is shown in Figure 89 (a). This figure clearly demonstrates a distinctive difference between the outer layer and the inner part of the aggregate particle. Because of the absorption of the asphalt binder, the outer layer of the aggregate has a black color, while the inner part remains the white color of the original limestone rock. When the same aggregate particle is placed under UV light, as illustrated in Figure 89(b), a black layer with a thickness of approximately 2 mm is shown on the periphery of the cross-sectional area of the aggregate. A white (fluorescence) layer is shown next to the black layer and inwards to the center of the particle. Within the white layer, little fluorescence is shown in the picture.

(a) Under Natural Light

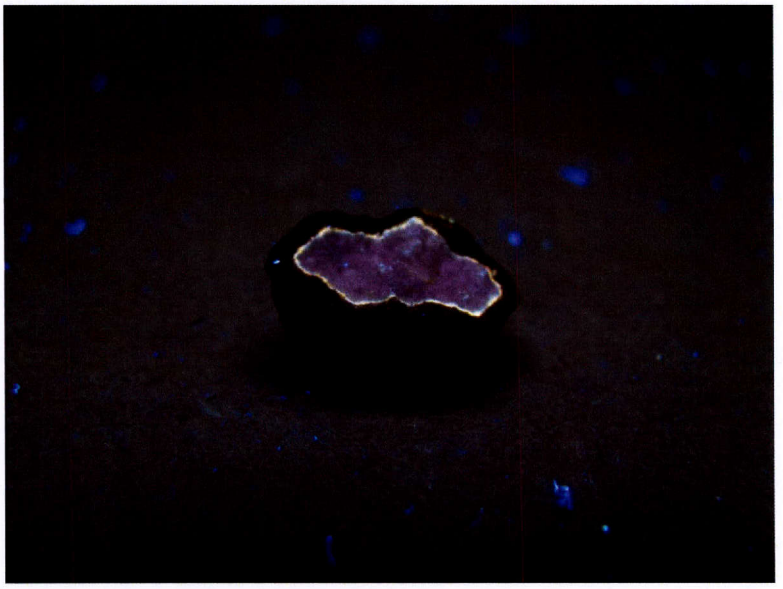

(b) Under UV Light

Figure 89. Limestone Aggregate Particle after Laboratory Mixing.

After examining the individual aggregate particle after mixing, the asphalt mixtures are compacted using the Superpave gyratory compactor at a compaction temperature of 121°C to produce a cylindrical specimen 6 in. in diameter and 7 in. in height. The specimen is cored and cut to 4 in. in diameter by 4 in. in height to achieve approximately uniform air void distribution. When visualizing the cross section of this specimen under natural light, similar observations are made on the aggregates in the HMA specimen. As shown in Figure 90(a), the outer layers of most aggregate particles in the specimen have a black or brown color while the center of most aggregates remains the while color. A good example is the aggregate particle in the red ellipse shown in Figure 90(a). This particle has a dark brown outer layer with a thickness of

approximately 2 mm, and its center part has the white color close to that of the original limestone rock. Subsequently, the same HMA specimen is examined under UV light, as presented in Figure 90(b). Fluorescence is identified in most aggregate particles under UV light. Particularly, the particle in the red ellipse in Figure 90(b) has a dark outer layer, an inner fluorescence layer, and the center part with little fluorescence. These observations match what is identified on the individual aggregate immediately after mixing.

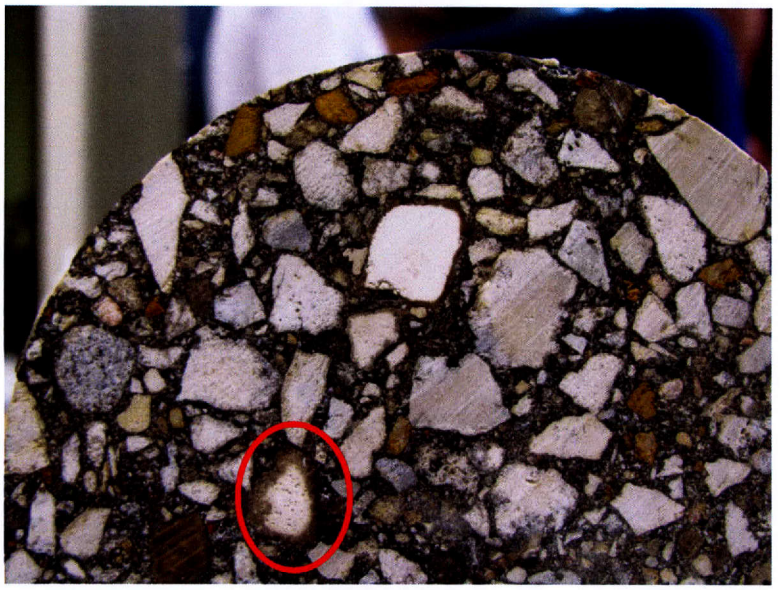

(a) Under Natural Light

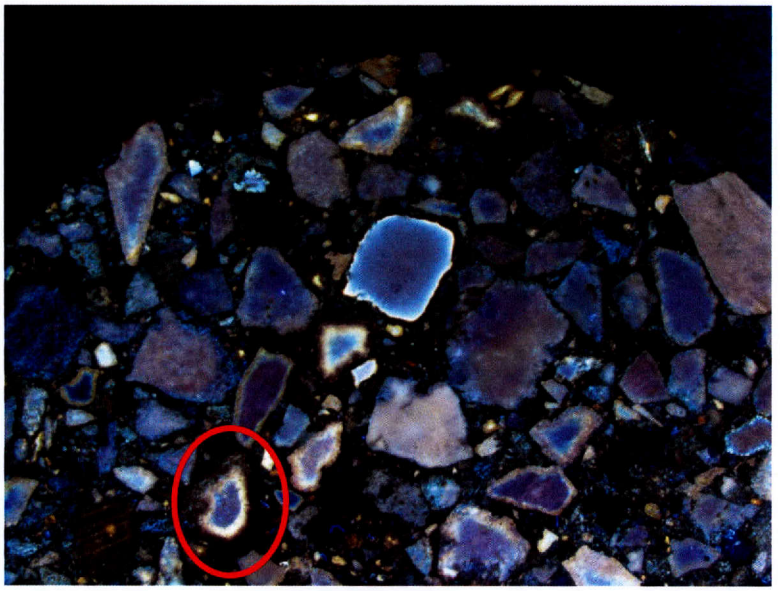

(b) Under UV Light

Figure 90. LMLC HMA Specimen with AAD Binder and Limestone Aggregates.

Figure 89 and Figure 90 indicate that the asphalt binder not only is absorbed into the accessible pores at the aggregate surface but also travels into the interior of the limestone aggregate. The layers with different levels of fluorescence shown on the aggregates under UV light demonstrate that different asphalt components travel different distances in the aggregates. The travel distance of a specific asphalt component may depend on its molecular weight and chemical properties as well as the mixing and compaction temperature. With different asphalt components at different locations in the cross section of an aggregate particle, the cross section shows a number of rings with different colors.

Because of the polar nature of the minerals in the aggregates, the non-polar asphalt components with lighter weights may penetrate into the center of the aggregates, and the polar components with heavy weights may stay in the outer layer of the aggregate particles showing the black color. The white (fluorescent) layer on the aggregates under UV light is a good indication of aromatic hydrocarbons since they strongly fluoresce under UV light.

Field Cores of Asphalt Pavements

In addition to LMLC asphalt mixtures, field cores of asphalt pavements are also investigated to evaluate the absorption of binder by aggregates in the field. The field cores selected in this study were taken from an HMA section and a WMA section, respectively, of Loop 368 in San Antonio, Texas. Both cores were taken when the sections had been in service for one year. The asphalt binder for the HMA section is a Valero PG 76-22; the base asphalt binder for the WMA section was a Valero PG 64-22 prior to modification, which was then modified using a warm mix additive Evotherm to meet the specifications of PG 76-22 (Button et al. 2007). The aggregates of both HMA and WMA sections are typical Texas limestone and field sand. Both HMA and WMA sections have the same aggregate gradation that meets the requirement of a TxDOT Type C dense-graded HMA. The HMA section was compacted at a temperature of 149°C; the WMA section was compacted at a temperature of 116°C.

Figure 91(a) and (b) present the HMA field core under natural light and UV light, respectively. A black or brown outer layer is easily identified on most aggregate particles under natural light, such as the one in the red solid ellipse and the one in the yellow dashed ellipse. When the same HMA field core is placed under UV light, the aggregate in the red solid ellipse clearly shows a black outer layer, a fluorescence layer, and little fluorescence in its center portion. This finding agrees with what is observed on the LMLC mixtures. In contrast, the aggregate particle in the yellow dashed ellipse has a dark brown outer layer and strong fluorescence in its entire center portion when it is under UV light. This observation indicates that the aromatic hydrocarbons may have already penetrated into the center of some aggregates in the HMA layer of an asphalt pavement in the field. A longer contacting period between the asphalt binder and the aggregates leads to more absorption of asphalt components by limestone aggregates.

(a) Under Natural Light

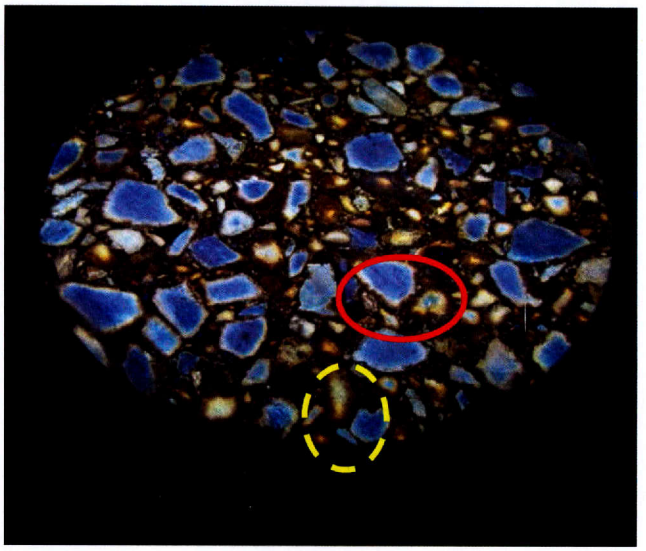

(b) Under UV Light

Figure 91. HMA Field Core Taken from Loop 368, San Antonio, Texas.

Compared to the aggregates in the HMA field core, the aggregate particles in the WMA field core do not have clear black or brown outer layers when it is under natural light, as shown in Figure 92(a). When the WMA field core is placed under UV light, most aggregates have a clearly fluorescent outer layer at the periphery of the aggregate particles, while a black/brown outer layer cannot be identified on the aggregate images, as illustrated in Figure 92(b). Figure 92 indicates that the polar components with heavy molecular weight may not be absorbed by the aggregate due to the significantly lower compaction temperature. In contrast, the limestone aggregates still absorb the aromatic hydrocarbons, which strongly fluoresce under UV light.

(a) Under Natural Light

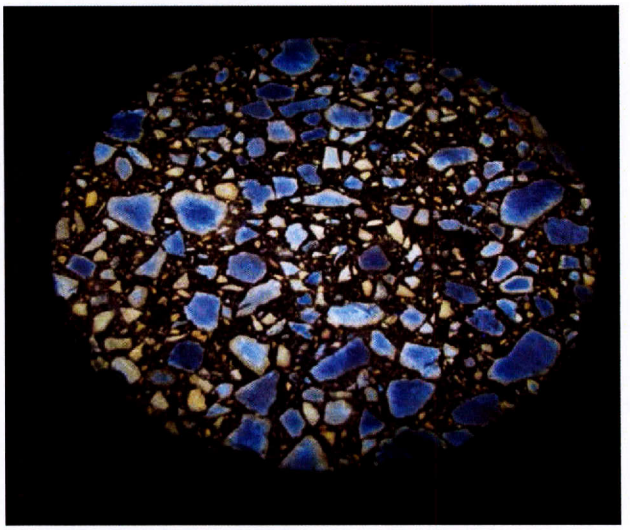

(b) Under UV Light

Figure 92. WMA Field Core Taken from Loop 368, San Antonio, Texas.

The comparison between the HMA and WMA field cores show that the selective absorption of asphalt binder depend on the compaction temperature. The limestone aggregates in an asphalt mixture compacted at a higher temperature tend to absorb more asphalt components. In other words, a higher temperature facilitates the absorption of asphalt components.

VERIFICATION OF AGGREGATE ABSORPTION USING MASS SPECTROMETER

Sample Preparation

The visual observation of the selective absorption of binder by aggregates is verified using the Laser Desorption Ionization – Ion Mobility – Mass Spectrometer (LDI-IM-MS). This equipment is used to identify possible asphalt components at different locations within a limestone specimen that is soaked in an asphalt binder for a period of time. Instead of a regular

aggregate particle in an asphalt mixture, a thin circular slice of limestone is preferred for the convenience of the LDI-IM-MS test. This section will present the details of the limestone collection, sample preparation, and LDI-IM-MS testing.

Limestone rocks are firstly collected from a quarry in San Marcos, Texas, which is the same quarry as the one from which the limestone aggregates are obtained to make the LMLC HMA specimens presented in last section. Each limestone rock is placed in a cylindrical plastic container, as shown in Figure 93(a). Cement mortar is then cast in the container in order to firmly position the limestone rock, as illustrated Figure 93(b). Every limestone rock is cored into a cylindrical limestone specimen approximately 2 in. in diameter and 3 in. in height. The actual height depends on the size of the individual rock. A couple of cylindrical fresh limestone specimens are shown in Figure 94(a).

(a) Limestone Rocks in Cylindrical Plastic

(b) Limestone Rock with Cast Cement Concrete Containers

Figure 93. Limestone Rocks Collected from San Marcos, Texas.

(a) Fresh Cylindrical Limestone Specimens Cored from Limestone Rocks

(b) Limestone Specimen Soaked in AAD Asphalt Binder for 32 Hours

Figure 94. Cylindrical Limestone Specimens.

Subsequently, a number of cylindrical limestone specimens are soaked in the AAD binder at the compaction temperature 121°C for 32 hours. Figure 94(b) shows an example of the limestone specimen after soaking in the asphalt binder for 32 hours. The soaking period (32 hours) is calculated based on the following algorithm. Suppose that a round aggregate particle has a diameter of D, and that the radial distance between the aggregate surface and the wetting front is C, as shown in Figure 95.

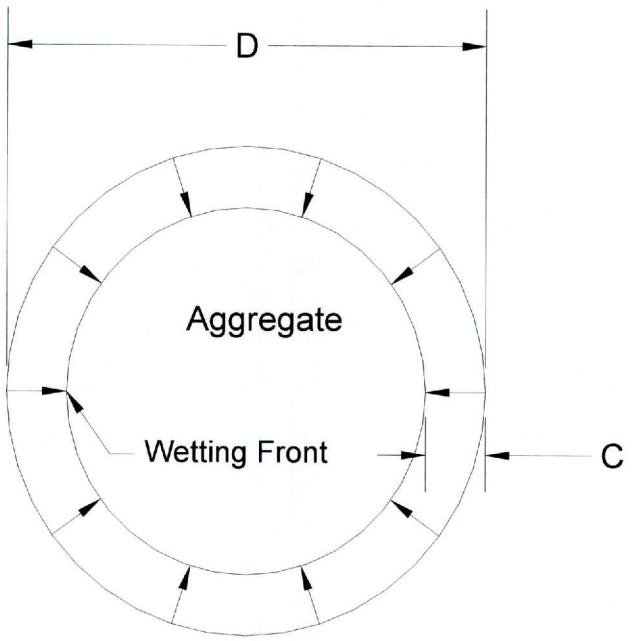

Figure 95. Round Aggregate with Absorbed Asphalt Binder.

Then the percentage of the completed absorption is:

$$u = \frac{C}{D} \tag{12-1}$$

It is assumed that u is proportional to the square root of the soaking time t, as shown in Equation 12-2:

$$u \propto \sqrt{t} \tag{12-2}$$

Equations 12-1 and 12-2 indicate that:

$$u \cdot D = C \propto \sqrt{t} \tag{12-3}$$

Equations 12-4 and 12-5 are then inferred for aggregates with different diameters:

$$u_1 \cdot D_1 \propto \sqrt{t_1} \tag{12-4}$$

$$u_2 \cdot D_2 \propto \sqrt{t_2} \tag{12-5}$$

When $u_1 = u_2$, the following equations are derived as follows:

$$\frac{D_2}{D_1} = \sqrt{\frac{t_2}{t_1}} \tag{12-6}$$

$$t_2 = t_1 \left(\frac{D_2}{D_1}\right)^2 \tag{12-7}$$

Equations 12-6 and 12-7 indicate the relationship between the soaking periods of two aggregate particles with different sizes when the same percentage of binder absorption is completed. When an asphalt pavement is constructed, it takes approximately 2 hours to produce the asphalt mixture and to ship the mixture to the construction site. Therefore, the soaking period of the aggregates in the asphalt binder approximates to 2 hours. If taking an aggregate with 0.5 in. in diameter in the mixture as an example, then $D_1 = 0.5$ and $t_1 = 2$. Therefore, t_2 can be calculated for the limestone rock specimen with 2 in. in diameter using Equation 7, provided that the aggregate with 0.5 in. in diameter has the same percentage of binder absorption completed as the limestone specimen with 2 in. in diameter. The value of t_2 is computed to be 32 hours. In summary, the binder absorption in the limestone specimen with 2 in. in diameter after soaking for 32 hours is equivalent to that in the aggregate particle with 0.5 in. in diameter after 2 hours of mixing and shipping to the construction site.

After soaking the limestone specimens in the AAD binder for 32 hours, a specimen is cut into halves. Figure 96 presents two pictures of the cross section of one half of this specimen, one of which is the specimen under natural light, and the other is the specimen under UV light. Layers with different colors are easily identified on the cross section of the specimen. This fact once again confirms the observations on the LMLC specimens and field cores that are presented in the previous section. Subsequently, the specimen is cut into thin slices with a thickness of approximately 2 mm for the LDI-IM-MS testing.

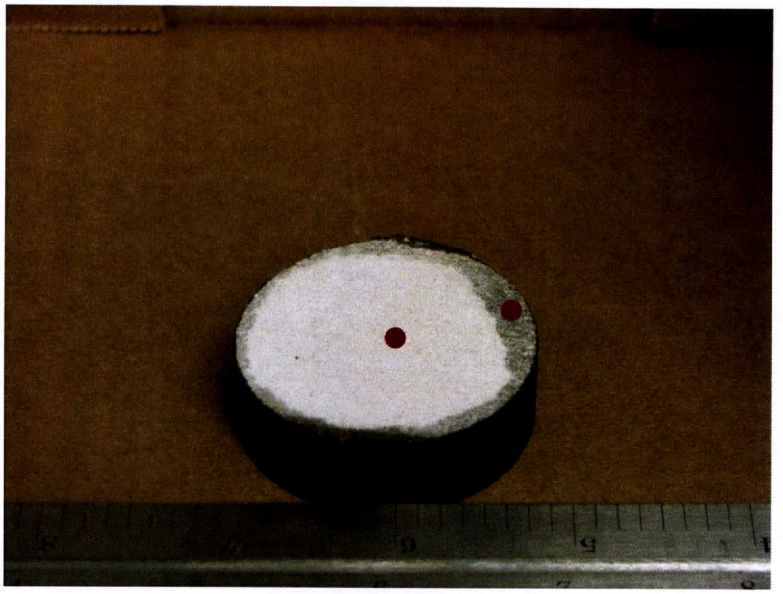

(a) Under Natural Light

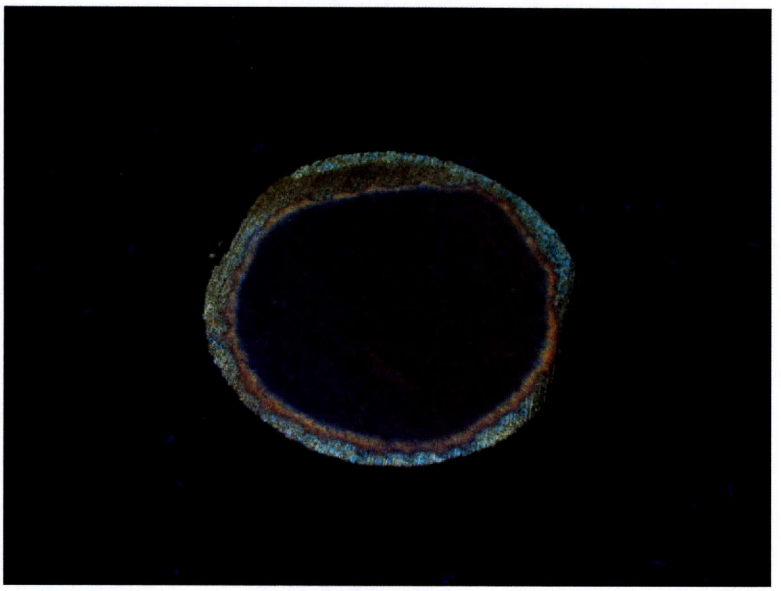

(a) Under UV Light

Figure 96. Cross Section of Limestone Specimen after Soaking in AAD Binder for 32 Hours.

LDI-IM-MS Testing

The circular limestone slice is tested using the LDI-IM-MS. Figure 97 is a schematic illustration of the LDI-IM-MS. The limestone slice sample is placed on a stainless steel plate inside the LDI-IM-MS. A laser beam is then focused on a specific point on the specimen to desorb and ionize that point on the specimen. This process is defined as Laser Desorption Ionization (LDI). After the LDI process, the ions from the specific point on the sample enter the

drift cell with a length of 5.9 in. and filled with an inert gas. In the drift cell, there is a periodic electrical voltage gradient field that separates the ions according to their mass-to-charge ratio (m/z). Once the IMS separation process is finished, ions are focused in the ion optics and are mass analyzed using a reflection time-of-flight (TOF) mass spectrometer (Becker et al., 2009).

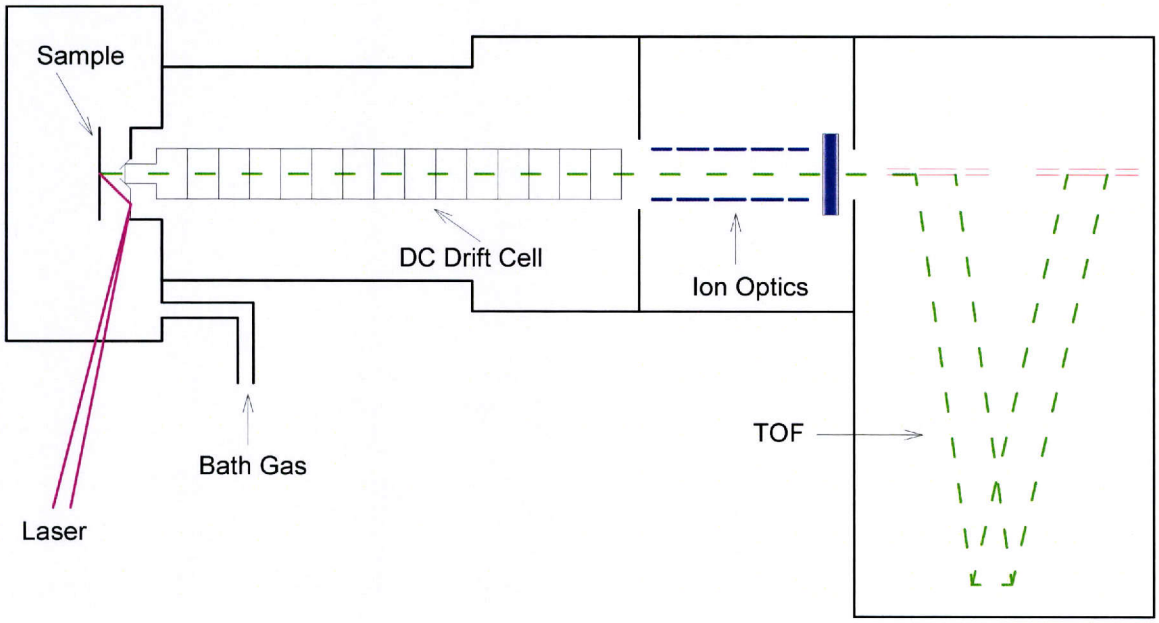

Figure 97. Schematic Illustration of LDI-IM-MS.

This testing process is applied to two specific points on the limestone sample, Point A and Point B as shown in Figure 96(a). The reason for selecting an edge spot and a center spot is to compare the chemical components at the two points so as to verify the selective absorption of the limestone rocks visualized in previous sections. Figure 98 shows the IM-MS spectrums of the edge spot and the center spot. Significant difference in asphalt component concentration is identified between the edge spot and the center spot when comparing Figure 98(a) to Figure 98(b). Specifically, the heteroatom hydrocarbons correspond to a nominal ion mass level of approximately 310 on the IM-MS spectrum. The edge spot has a considerably higher density in heteroatom hydrocarbons than the center spot. When magnifying the spectrum in the m/z range between 300 and 320, more than one peak at a nominal ion mass level are identified on the spectrum, as presented in Figure 99. This fact indicates that the complexity of the sample is significant, which is commonly observed in crude oils and asphaltene samples. In summary, the IM-MS spectrums plotted based on the LDI-IM-MS test results verify the visual observations on the nonuniform selective absorption of asphalt binders by limestone rocks.

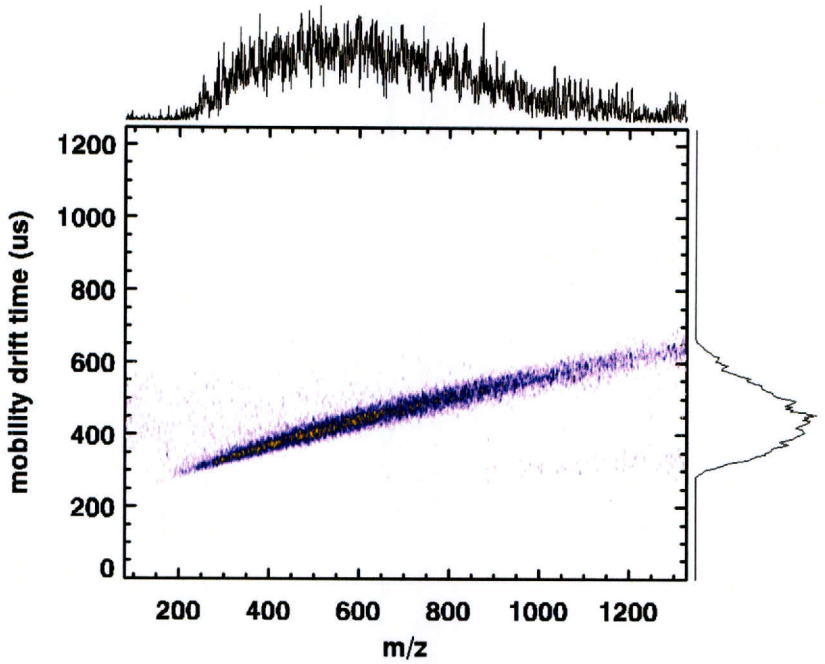

(a) IM-MS Spectrum of Point A (Edge Spot)

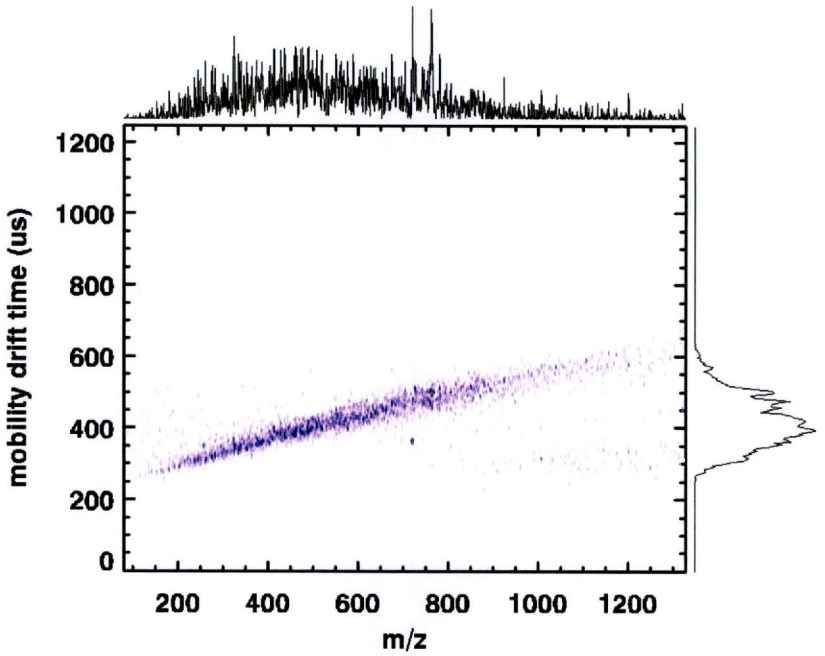

(b) IM-MS Spectrum of Point B (Center Spot)

Figure 98. IM-MS Spectrums of Selected Points on Limestone Sample.

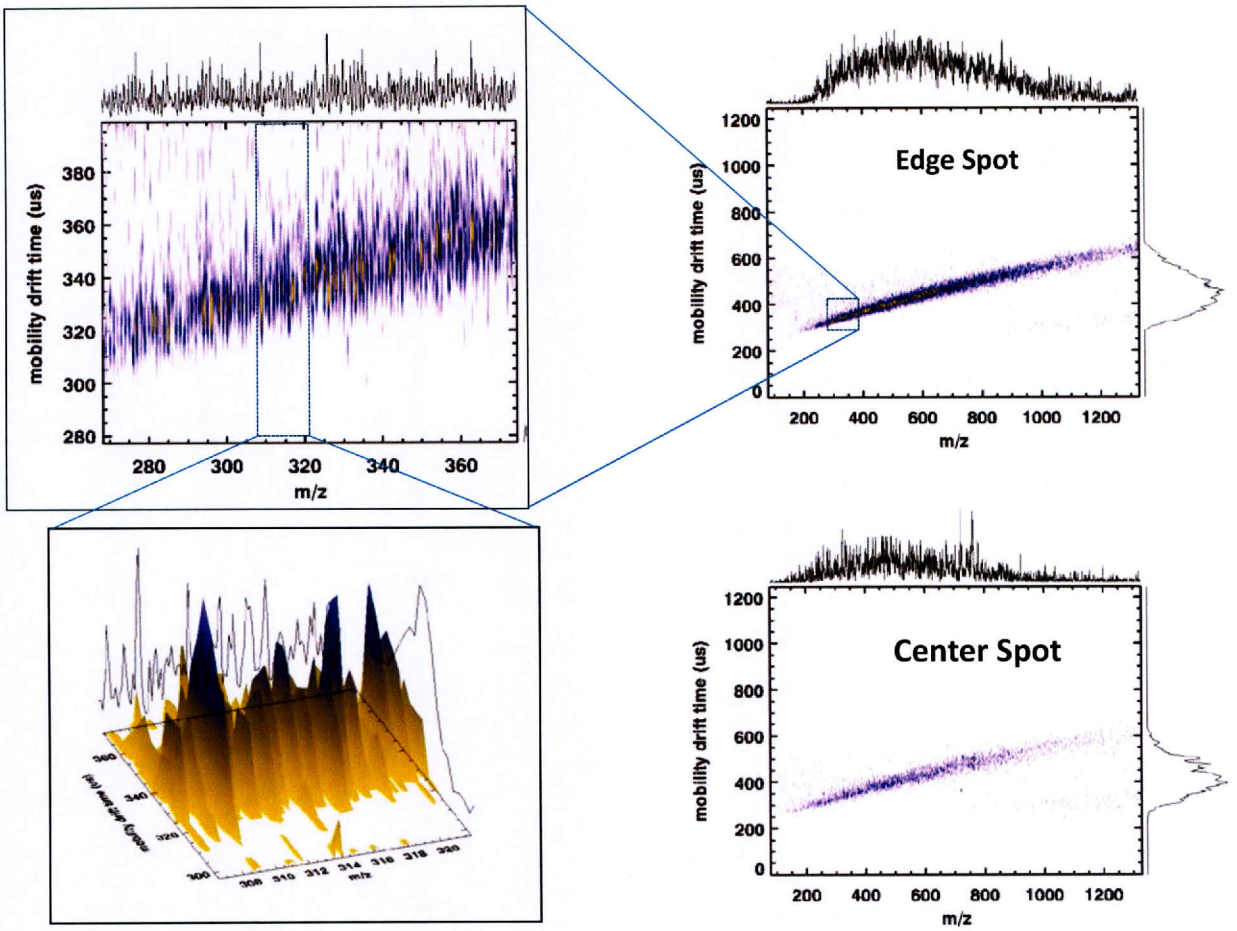

Figure 99. Detailed IM-MS Spectrums.

Quantification of Absorption Effect

It is commonly understood that a limestone rock can be taken as an elastic material while an asphalt binder is viscoelastic. The selective absorption of asphalt binder by the limestone rock definitely changes the physical properties of the limestone rock with absorbed asphalt binder. In order to quantify the absorption effect in terms of the change of physical properties of the limestone rock, creep tests are conducted at the room temperature on both fresh limestone rocks and limestone samples soaked in the AAD binder for 32 hours.

The Material Test System (MTS) is used to conduct the creep tests at a constant temperature of 20°C. As shown in Figure 100, three pairs of linear variable differential transformer (LVDT) holders are firstly glued to each test sample. Then three vertical LVDTs are mounted on the surface of the sample when it is set up in the environmental chamber of the MTS. The three vertical LVDTs are placed at 120° apart from each other around the sample surface to measure the vertical deformation of the test sample. The average value of the measured deformations from the three LVDTs is used in this study. After setting up the sample in the MTS, a static loading of 4,000 lb is applied to the test sample for 2 hours (7,200 sec).

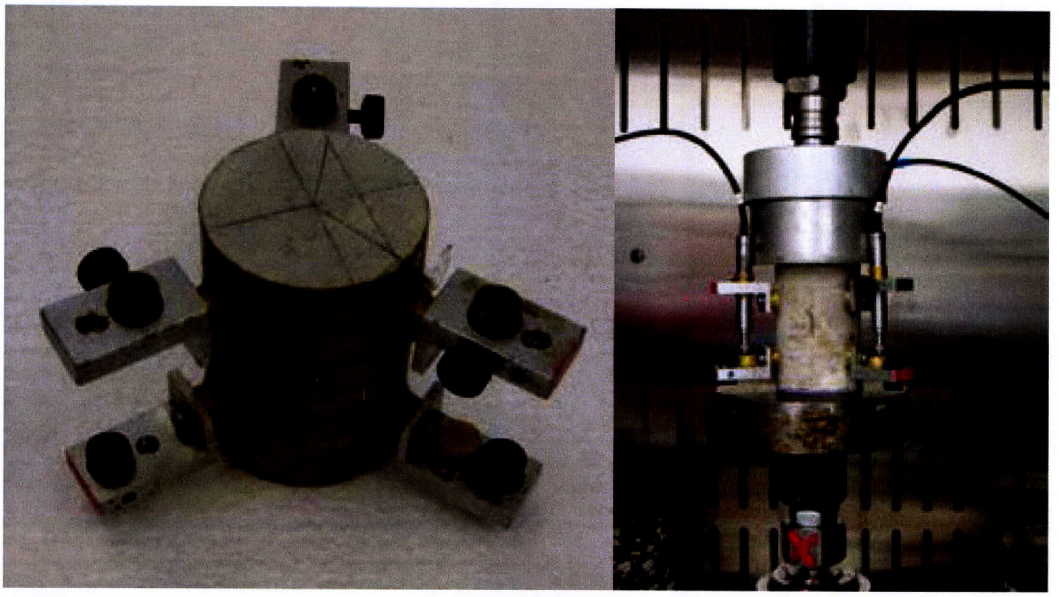

(a) Fresh Limestone Sample

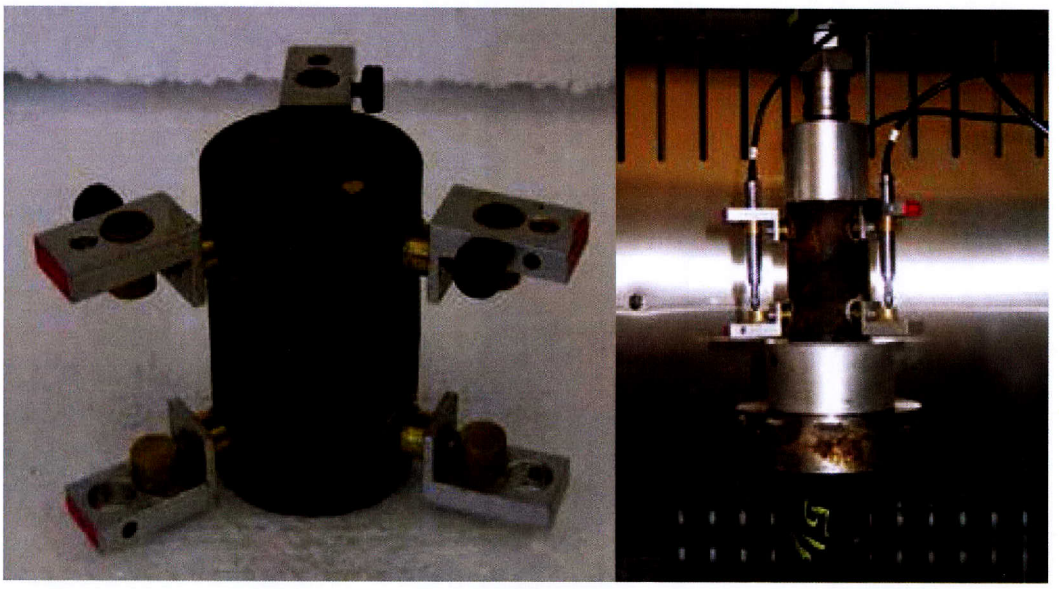

(b) Limestone Sample Soaked in AAD Binder for 32 Hours

Figure 100. Configuration of Creep Test on Limestone Samples.

The vertical strains of the test samples are calculated using the vertical deformations measured by the LVDTs. Figure 13 presents the vertical creep strains of a fresh limestone sample and a limestone sample soaked in the AAD binder for 32 hours. The vertical strain of the fresh limestone sample stays approximately constant with the elapse of time. In contrast, the vertical strain of the limestone sample soaked in the binder has an increasing absolute value of the strain as the testing time increases. Specifically, this limestone sample has a slow continuous deformation under constant load. The time-dependent behavior of this limestone sample indicates its nonnegligible viscoelastic characteristics introduced by the absorbed asphalt binder.

As a result, the selective absorption of the asphalt binder by limestone aggregates is shown to change the physical properties of the limestone aggregates, which turn into viscoelastic materials from elastic materials. This finding verifies the theoretical modeling results of the self-consistent micromechanics models that were developed for asphalt mixtures (Luo and Lytton, 2011). In addition, the magnitude of the compressive strain of the fresh limestone is approximately half of that of the limestone soaked in the AAD binder when they are subjected to the same compressive load. This fact indicates that the fresh limestone sample is approximately twice as stiff as the limestone sample soaked in the binder. In other words, the selective absorption of the asphalt binder by the aggregates makes the aggregate particles significantly more compliant.

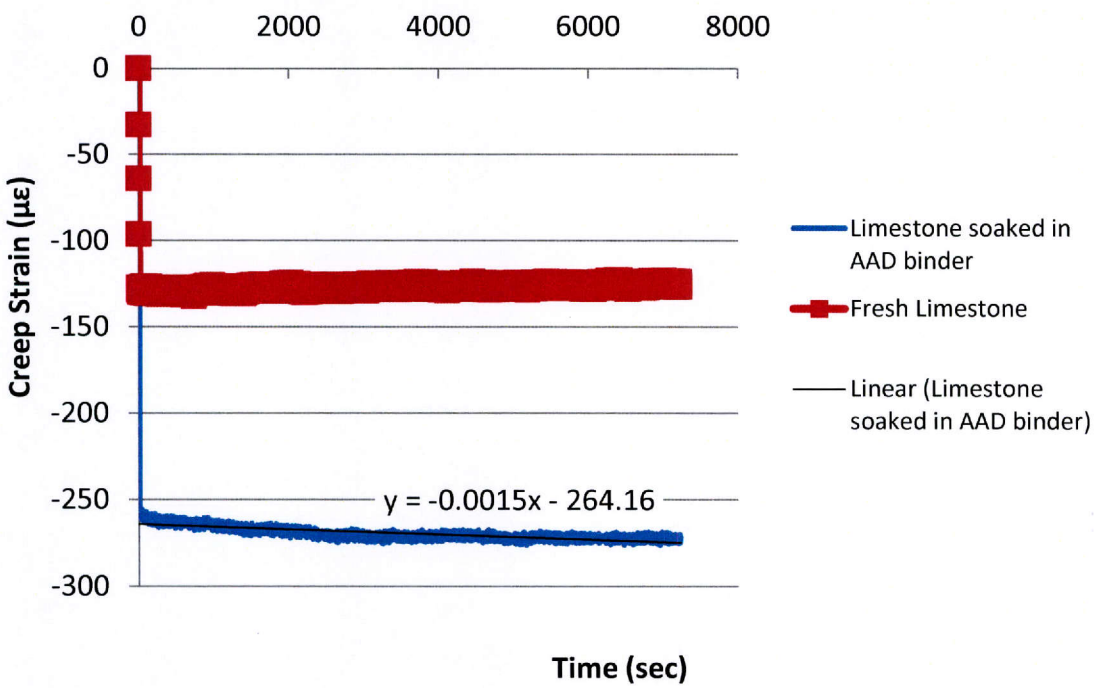

Figure 101. Measured Axial Strain of Limestone Samples in Creep Tests.

CONCLUSIONS

This paper presents the findings on the selective absorption of asphalt binder by aggregate particles in asphalt mixtures. The selective absorption of the binder is visualized on the aggregate surface under natural light and UV light. Rings with different colors are identified on the cross-sections of the aggregates in both HMA and WMA, which indicates different asphalt components at different radial distances from the center of the aggregates. The asphalt components penetrating into aggregates are verified using the Laser Desorption Ionization – Ion Mobility – Mass Spectrometer. Significantly higher concentration of asphalt components is identified at the edge of the limestone sample than in its center after it is soaked in the AAD asphalt binder for 32 hours. Creep tests are also conducted on fresh limestone samples and limestone samples soaked in the AAD binder. The fresh limestone sample behaves elastically

and is approximately twice as stiff as the sample soaked in the binder, which exhibits non-negligible viscoelastic properties in the creep test.

The findings of this study have significant impact on the fatigue and moisture damage of asphalt mixtures in terms of the bonding strength between the asphalt binder and aggregates. Because of the selective absorption of binder by aggregates, the bonding strength between the binder and the aggregates are in fact the bonding strength between specific asphalt components remaining on the aggregate surface and the aggregates with absorbed asphalt components. Therefore, the adhesive bond energy between the asphalt binder and the aggregates should be calculated using the surface energies of the asphalt components remaining on the aggregate surface (instead of the entire asphalt binder) and the aggregates with absorbed asphalt components (instead of the original limestone aggregates). In addition, when using micromechanics models to study an asphalt mixture as a composite material, aggregates in the asphalt mixture may have to be considered as viscoelastic materials due to the selective absorption of the asphalt binder.

Identification and quantification of the asphalt components left on the aggregate surface are the authors' ongoing work in order to more accurately estimate the adhesive bond energy between the asphalt binder and the aggregates.

CHAPTER 13. DYNAMIC MECHANICAL ANALYZER TESTS ON FINE AGGREGATE MIXTURES

In this subtask, a new test and data analysis protocol based on the pseudo strain energy equivalence theory to characterize the fatigue crack growth of FAM specimens conditioned at different aging period and RH levels. Compared to the previous torsional test, the newly proposed RDT test protocol greatly reduces the stress state complexity within the specimens by evenly distributing stress over the cross-section area of the cylindrical specimen.

EXPERIMENTAL TESTING PLAN

The experiments were designed to evaluate the effect of moisture, aging, and different additives on the asphalt mixture fatigue resistance. Materials, specimen fabrication, specimen aging, moisture conditioning, and laboratory testing for each experiment are discussed in this section.

Materials and Mix Design

The material selection, material properties, and corresponding mix designs are introduced in this section.

Asphalt Binder and Aggregate

The binder with PG64-22 and a non-absorptive quartzite are used for specimens' fabrication.

Gradation and Binder Content

A Superpave D mixture was selected from TxDOT, and the full mixture gradation is shown in Table 45. The corresponding aggregate gradation for Fine Aggregate Mix (FAM) is presented in Table 46.

Table 45. Aggregate Gradation for Lab Mix.

Sieve Size	Cum. Passing %
3/4"	100.0
1/2"	100.0
3/8"	93.1
No. 4	64.6
No. 8	40.7
No. 16	26.2
No. 30	14.6
No. 50	8.5
No. 200	3.5

Table 46. Corresponding Gradation for FAM Specimens.

Sieve Size	Individual Retaining %
No. 16	0
No. 30	44.23
No. 50	23.46
No. 200	18.85
Pan	13.46

The binder content of FAM specimens was determined using the aggregate surface area method based on the optimum binder content of the corresponding full mixture, which was determined to be 5.5 percent by the weight of the mixture according to the 2004 Texas Department of Transportation (TxDOT) specification. The aggregate surface area method assumes that the asphalt binder is proportionally distributed on the aggregate surface area. The specific surface area of perfectly spherical aggregates can be determined using the equation shown:

$$CR_i = 3K\left(\frac{1}{r_i D_i} + \frac{1}{r_i D_{i-1}}\right) \tag{13-1}$$

where CR_i = the specific surface area of the particle with diameters in the range between sieve sizes D_i and D_{i-1}; and r_i = effective density of aggregate, kg/m^3. K is a volume factor to adjust the assumption that the aggregate is in a perfect spherical shape. The optimum binder content for both fine aggregate mixtures was determined according to TxDOT test procedures and specifications. The optimum binder content was 9.7 percent by weight of the mixture.

Specimen Fabrication

The basic FAM specimen fabrication procedure involved aggregate batching, binder-aggregate mixing, short-term oven aging, compaction, sawing and coring, and volumetric analysis to determine the specimen air void content. These processes were conducted according to the 2004 TxDOT specification. The first step in the preparation of the specimens consisted of mixing and compacting, using the Superpave gyratory compactor (SGC), as shown in Figure 102, to obtain a 150-mm diameter cylindrical sample with an approximate height of 90 mm, as shown in Figure 102. This procedure was similar to the one used to prepare regular HMA specimens. The upper and lower parts of the cylinders were sawed in order to produce a new cylinder 150 mm in diameter and 50 mm in height. This compacted sample was cored into small DMA cylindrical specimens 12 mm in diameter and 50 mm in height. Each specimen was properly labeled and prepared for testing.

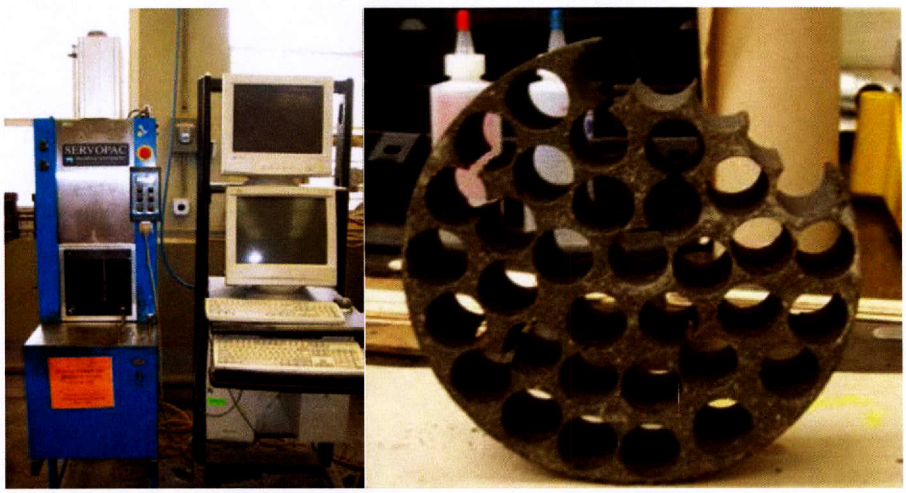

Figure 102. SGC Compactor and DMA Cylindrical Specimen.

Then, the FAM specimens for the DMA were tested to determine their air void contents. Since the DMA specimens were cored from samples with a 6-inch diameter made by the SGC, the DMA specimens cored from the outer circle of the 6-inch diameter specimen had a larger air void content than those cored from the inner circle, which was consistent with what was observed in the pilot testing. This indicates that the closer to the center of the 6-inch diameter gyratory specimen, the lower the air void content.

LABORATORY AGING AND MOISTURE CONDITIONING

For all of the mixtures, two laboratory aging periods of 0 and 6 weeks at 60°C were used for future testing. Heated air at 60°C circulated freely around the specimens in an environmentally temperature-controlled room and accelerated oxidation of the binder in the mixtures. Figure 103 illustrates the apparatus used for aging specimens. Basically, the FAM specimens were placed on the desiccators, which were open to the air in the environmentally controlled room.

Figure 103. Moisture-Conditioned DMA Specimens in Desiccators.

According to the RH profiles in asphalt pavements that were predicted by the suction model, two RH levels, 0 percent and 100 percent, were selected in this study to condition FAM specimens. A constant RH level can be achieved in the vacuum desiccator using a chemical solution whose affinity for water regulates the water vapor pressure in the closed system with little temperature fluctuation. The RH level in the vacuum desiccator corresponds to the specific solution that is chosen to use in the vacuum desiccator. Therefore, desiccant was used to achieve 0 percent RH level, and distilled water was used to achieve 100 percent RH level. Then the FAM specimens were placed in the vacuum desiccators with the specific RH, as shown in Figure 104.

Figure 104. DMA Specimens Conditioning in Desiccators.

TEST PROCEDURE

A controlled-stress RDT test method was developed to characterize the fatigue crack growth of the FAM specimens. As illustrated in Figure 105, each FAM specimen was glued to a pair of end caps and was then mounted using clamps in the environmental chamber of the DMA equipment for testing. During the test, the DMA applied a tensile force to the FAM specimen through the top loading cell while recording the stress and strain data of the test specimen. Two stress levels, one undamaged stress level at around 20 kPa and one damaged level at around 160 kPa, were applied to the specimens, respectively. To reduce data noise, the Fast Fourier Transform (FFT) was performed on the measured stress and strain data. Figure 106 shows examples of the measured and fitted stress and strain data. The test data with reduced noise were then analyzed to determine the fatigue properties of the FAM specimens, which are detailed in the following section.

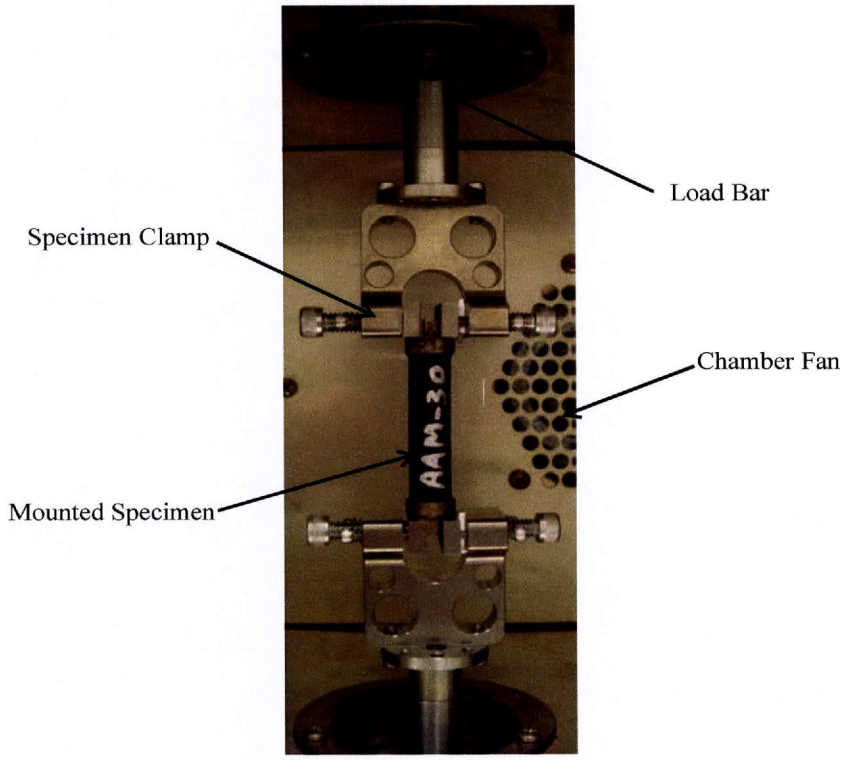

Figure 105. DMA Test Configuration.

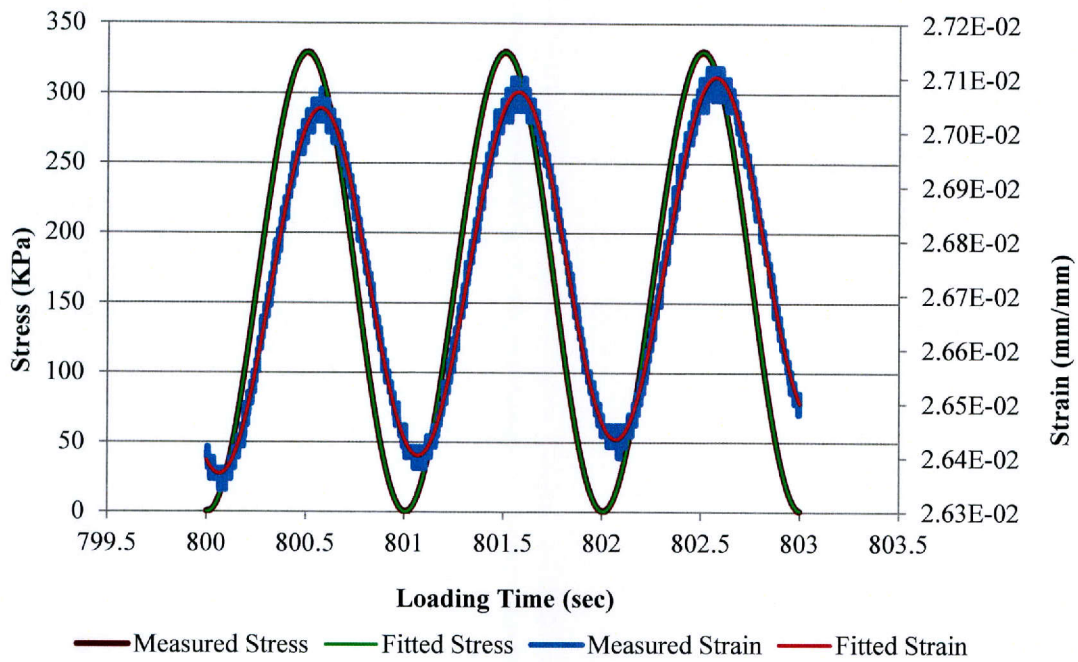

Figure 106. Stress And Strain Curve Measured From Controlled-Stress RDT Test.

MODELING AND ANALYSIS

The fatigue crack of asphalt mixture is governed by a modified form of Paris' Law, which is:

$$\frac{d\emptyset}{dN} = A'[\Delta J_R]^{n'} \tag{13-2}$$

where ϕ is the damage density; N is the number of load cycles; ΔJ_R is the pseudo-J integral; and A' and n' are the modified Paris' Law parameters.

The damage density of the FAM, as shown in Figure 107, was fitted to the form using the Equation 13-3:

$$\emptyset = \emptyset_0 + aN^b \tag{13-3}$$

By modeling the damage density increase using the modified Paris' law, the fracture parameter was also obtained from the formulation using the Equation 13-4:

$$\varphi = \varphi_0 + A^{\frac{1}{n+1}} \left(\frac{1}{2A_F}\right)^{\frac{n}{n+1}} (cd)^{\frac{n}{n+1}} \frac{n+1}{dn+1} N^{\frac{dn+1}{n+1}} \tag{13-4}$$

Comparing 13-3 to 13-4, the modified Paris' law fracture parameters n′ and A′ were obtained.

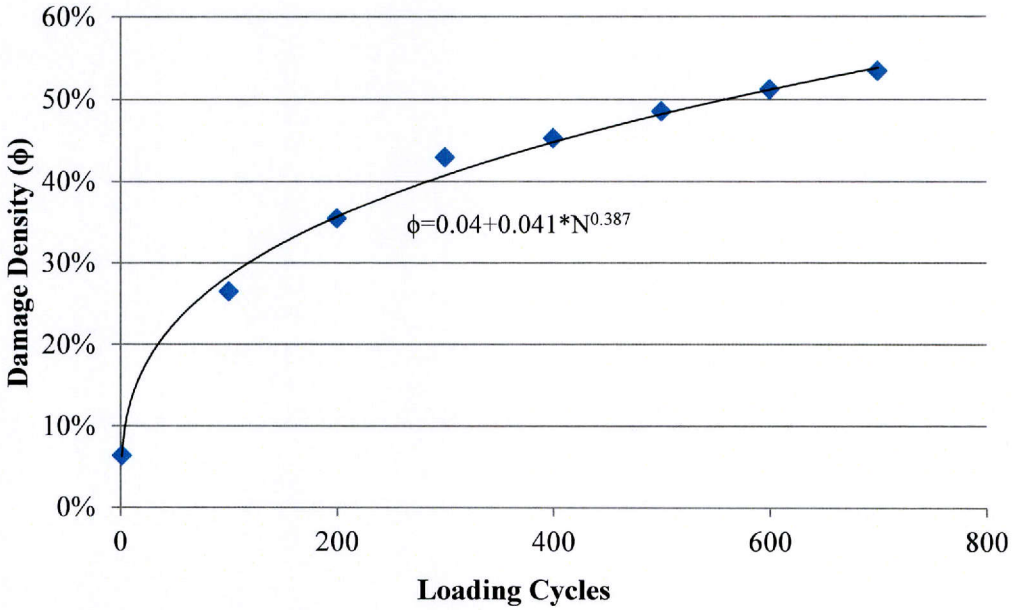

Figure 107. Damage Density vs. Loading Cycles.

Figure 108 illustrates some of the test results for both hot asphalt mix and warm asphalt mix with Evotherm DAT additives.

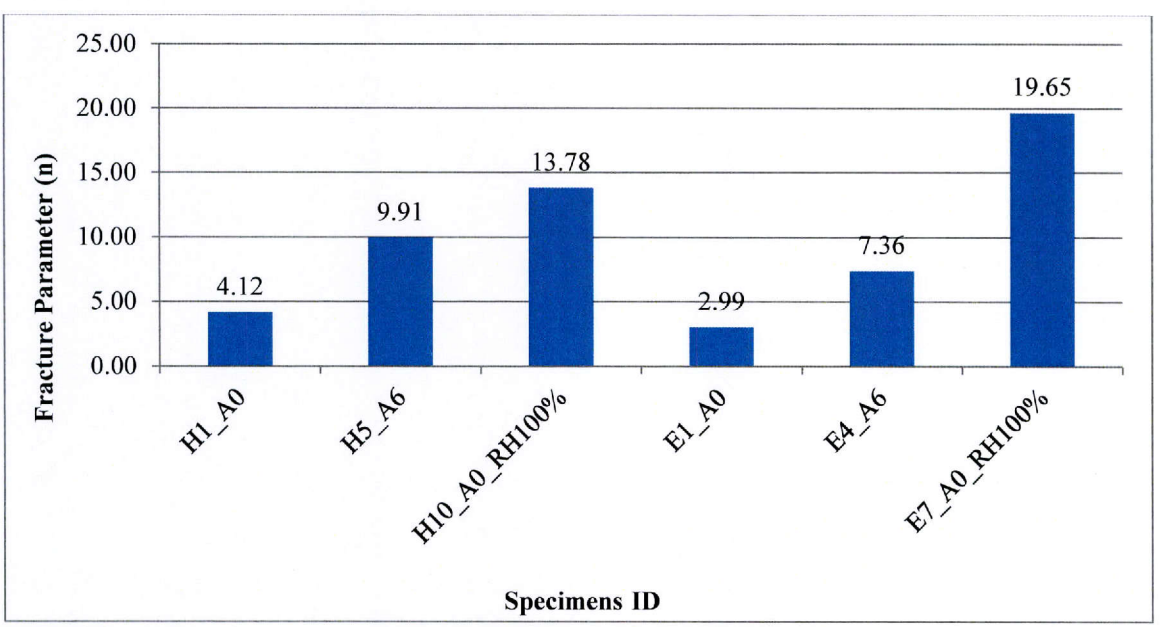

Figure 108. Test Results for HMA and WMA.

As is observed in Figure 108, as the conditioning relative humidity increased to 100 percent, the fracture parameter n tended to increase for both hot asphalt and warm mix specimens, which indicates that the saturated vapor pressure in the specimens significantly

increased the fatigue potential of the asphalt mix material. The modified Paris' law parameter A' tended to decrease as the relative humidity condition increased and this decrease is not adequate to offset the increase in n'. Therefore, it is concluded that the moisture presence in the asphalt due to vapor diffusion increases the rate of fatigue cracking of the asphalt mix significantly. It is also concluded that the aging increases the rate of asphalt fatigue cracking of both warm asphalt mix and hot asphalt mix. Another finding is that the n' is higher for the moisture conditioned specimens than that for aged specimens, which demonstrates that the water presence induces more damage than aging. These findings demonstrate that cracks grow faster in specimens with a higher RH level in both warm and hot asphalt mix. This fact indicates that the diffusion of subsurface water vapor into the asphalt layer accelerates the deterioration of the asphalt layer of flexible pavement faster than the aging. As a result, the RH level must be taken into consideration when predicting the fatigue life of any asphalt mixture and when designing asphalt pavements.

CONCLUSION

This RDT test protocol is more efficient than the torsional test in terms of characterizing the fatigue crack growth of FAM. The results show that 1): RH gradients existing in pavement layers are important in driving the diffusion of water vapor through the connected air voids into the surface asphalt layers and eventually degrading the integrity of the asphalt material; 2) as aging time increases, the asphalt mixture is more susceptible to fatigue cracking; 3) the water presence in the asphalt mix pavement induces more damage than aging does.

CHAPTER 14. SUMMARY AND RECOMMENDATIONS

SUMMARY OF SIGNIFICANT FINDINGS

Absorption

Asphalt absorption by aggregate has been extensively studied and it has been found that absorption is directly related to aggregate void fraction. The use of a density gradient column ("DGC") to study absorption allowed for measurement of absorption on single aggregate pieces. A few key findings are listed here.

- There is some effect of binder grade (viscosity).
- WMA absorption is somewhat less than HMA absorption.
- The DGC provides a reliable and relatively easy measure of absorption for an aggregate/binder pair.
- Standard (ASTM) methods for measuring absorption can be problematic, depending on the level of absorption.

Oxidation Kinetics

Binders modified using warm mix technologies were found to have similar oxidation kinetics to the unmodified binder.

Mixture Fatigue

The overlay tester and VEC measurements were successfully used to characterize mixture fatigue. A few key findings are listed here:

- Mixture fatigue resistance declines with binder oxidation.
- The VEC modulus varies over 1.5 inches of pavement depth due to the difference between the aging rate at the surface and the aging rate at 1.5 inches below the pavement surface. The magnitude of the difference depends largely on average annual daily solar radiation (MJ/m^2).
- Unaged binder properties, together with binder oxidation kinetics and climate data (primarily solar radiation) can be used to predict pavement durability (fatigue resistance).
- From the overlay tester results it can be shown that there is an aging function that relates the Paris' law exponent to aging, a result that is omitted entirely from typical pavement design guides (e.g., the MEPDG).

WMA Curing at Early Pavement Lives

Significant curing occurs in warm mix asphalt during the first summer of its service life. During the first summer oxidative aging, curing, and absorption have a significant beneficial effect on the performance of the mixture. In particular, at early times warm mixes are more susceptible to moisture damage than hot mixes.

RECOMMENDATION FOR A NEW BINDER SPECIFICATION FOR WMA PAVEMENT DURABILITY

WMA binder durability specifications incorporate project results on binder absorption, mixture fatigue, and WMA curing/aging in the field and are presented below. These are draft recommendations and are subject to modification and will appear in more detail in the project final report. Using the results on warm mix oxidation and mixture durability, and together with the results of the absorptions studies, two new approaches to binder specification for WMA pavement durability are proposed. Additionally, guidelines on binder absorption are presented. The new approaches include consideration of the following issues:

- The aging potential of the binder with warm mix additives.
- The moisture damage potential of the binder with warm mix additives. Moisture damage assessment was not mentioned explicitly as an objective of this project, yet the presence of surfactants and other additives almost certainly make it an issue in WMA durability and WMA versus HMA durability comparisons.
- Absorption of asphalt materials, including of binders in warm mix applications.

TWO APPROACHES TO A BINDER DURABILITY SPECIFICATION

We have developed two procedures for addressing a durability specification for warm mix binders that also apply to conventional hot mix binders.

Procedure 1

One of these procedures addresses the oxidation of binders, the hardening that occurs because of the oxidation, and the impact of this hardening on pavement durability. It is based on the oxidation and hardening fundamentals that are specific to each binder. As such, it requires characterizing the oxidation kinetics and hardening susceptibility of the specific binder along with the climate for the specific pavement location of interest. The approach then uses this information in a pavement oxidation model to predict pavement durability over time, according to the specific binder, mixture response to oxidative hardening, climate, and traffic loading. Not included directly in the pavement oxidation model is moisture damage, although adjustments can be made to model parameters that would indirectly account for both fatigue and moisture damage. This approach follows a three-step procedure:

1. **Estimate binder kinetics parameters at 1 atm** using 20.7 atm PAV aging, according to the procedure developed in TxDOT project 0-6009 (Glover et al., 2013):

    a. Age binders in the PAV apparatus at 90°C and 100°C for several aging times, sufficient to establish a constant-rate aging period at both temperatures (e.g., 20, 30, 40, 50 hours).
    b. Measure FTIR CA for each of the aged binder samples.
    c. From these measurements, calculate CA aging rates and from rate as a function of 1/RT determine an activation energy.
    d. Using the activation energy correlation that relates PAV to POV aging (TxDOT final report project 0-6009), convert the PAV aging constant-rate activation energy to a POV constant-rate activation energy, E_{ac}.

e. Using the pre-exponential factor–activation-energy correlation and E_{ac} (TxDOT final report project 0-6009), estimate the pre-exponential factor, A_c.
f. Using the fast-rate–constant-rate activation energy correlation (TxDOT final report project 0-6009), estimate the fast-rate activation energy, E_{af}.
g. Using the pre-exponential factor–activation energy correlation for the fast-rate reaction (TxDOT final report project 0-6009), estimate fast-rate pre-exponential factor, A_f.

2. Determine the CA initial jump and the Viscosity and DSR Fn Hardening Susceptibilities at 1 atm:
   a. Age binders in an oven at 100°C for several aging times at atmospheric pressure, sufficiently long to establish a constant-rate aging period (less than 7 days).
   b. Measure the low shear-rate limiting viscosity at 60°C, the DSR Fn and CA for each of the aged binder samples of Step 2 (a).
   c. From the CA versus time relationship, estimate (in a parameter optimization sense) CA_0, and an initial tank (unaged) CA value, CA_{tank}, and estimate (in a parameter estimation sense) the initial jump M ($M = CA_0 - CA_{tank}$), which is the ultimate or total contribution of the fast-rate reaction to increases in CA.
   d. From the log (low shear rate limiting viscosity) growth versus CA relationship, estimate (in a parameter estimation sense) the viscosity hardening susceptibility (HS).
   e. From the log (DSR Fn) growth versus CA relationship, estimate (in a parameter estimation sense) the DSR Fn hardening susceptibility (DSR Fn HS).

3. **Calculate pavement durability** for the candidate binder by using the parameters from steps (1) and (2), together with pavement temperature profiles calculated from the climatic weather data and the pavement temperature model of TxDOT project 0-6009, and mixture fatigue decline results from this project. Pavement durability will be in the form of projected fatigue life, in years.

With estimates for all of the binder parameters (E_{ac}, A_c, E_{af}, A_f, M, HS), use the pavement oxidation model to predict binder pavement oxidation for comparing the various binders of interest.

Procedure 2

The second procedure incorporates the same factors mentioned above, but is somewhat less specific to each binder, instead allowing for a more general characterization of binder type and climate but also including moisture susceptibility. Such a specification procedure would use a table that specifies the maximum allowable DSR Function value, according to mixture type, climate zone, and pavement target fatigue life as in Table 47.

Table 47. Relation between the DSR Function and Pavement Fatigue Life.

			WET-FR	WET-NOF	DRY-FR	DRY-NOF
Maximum Allowable DSR Functions (Neat Binder) MPa/sec	D_0	HMA	2.04E-05	8.27E-05	1.20E-04	4.84E-05
	D_0	WMA(EVO)	2.65E-05	1.03E-04	1.48E-04	6.15E-05
	D_0	WMA (Foaming)	2.98E-05	1.08E-04	1.53E-04	6.58E-05
	$Log_{10}(D_0)$	HMA	-4.69032	-4.08241	-3.9208	-4.31495
	$Log_{10}(D_0)$	WMA(EVO)	-4.57647	-3.98528	-3.82903	-4.21109
	$Log_{10}(D_0)$	WMA (Foaming)	-4.52569	-3.96617	-3.81666	-4.18205

- **Note: Target Fatigue Life=15 Years**

This table shows hot mix, warm mix (Evotherm), and warm mix (foaming). The DSR function is the rheological function G'/(n'/G') and has been shown to serve as a surrogate for binder ductility which, in turn, has been shown to correlate to pavement long-term fatigue/aging failure. The four climate zones for Texas are shown in Figure 109.

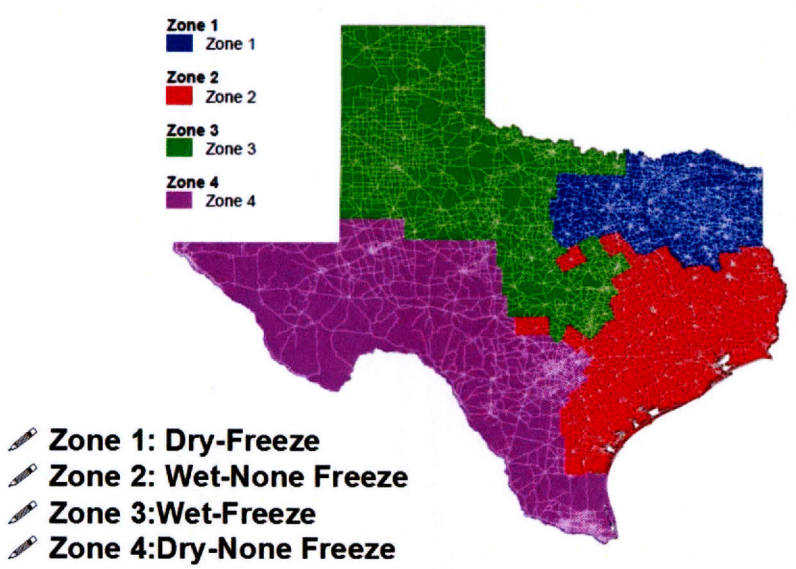

Figure 109. Climate/Soils Zones in Texas.

RECOMMENDATION FOR DETERMINING BINDER ABSORPTION

Data obtained from the work of this project have shown repeatedly that binder absorption is surprisingly consistent at approximately 40 percent of the volume of water absorption. Absorption for warm mix processes was found to be somewhat less, ranging from 30 to 40 percent of the volume of water absorption. Specifically, values measured for loose mix samples obtained at the time of placement at the Lufkin field site were: Advera: 27 percent, Evotherm and Rediset: 32 percent, and Sasobit: 39 percent.

SUGGESTED IMPLEMENTATION

The following actions are suggested:

1. Use the pavement durability prediction software developed in project 0-6009 to make predictions about WMA materials.
2. Collect refinery products over time and characterize them with respect to binder oxidation kinetics and rheology so as to build a database of materials used by TxDOT (with the caveat that there can be considerable variability in products caused by varying crude sources over time).
3. Validate models and performance prediction with additional field data.
4. Consider the use of RAP and RAS in WMA (and HMA), especially with respect to the problematic effectiveness of blending of RAP and RAS with new materials (issues: blending, mixture air voids, high aging levels of RAP and RAS binders that make them highly brittle).
5. Incorporate the interactions of binder, mixture, climate, traffic loading, and pavement structural properties in mixture design and performance prediction. Apply life-cycle cost analysis to determine potential value to TxDOT.
6. Develop a comprehensive and fundamentals based mixture design and pavement performance prediction methodology.

SUGGESTION FOR FUTURE WORK

A specification needs to be developed that addresses the use of RAP and RAS. This development should take into account the oxidation/hardening state of the RAP or RAS binder. Additionally, the effectiveness of the blending of the RAP or RAS with new material should be evaluated.

REFERENCES

AASHTO. (2010) AASHTO Designation: T 85 Standard Method of Test for Specific Gravity and Absorption of Coarse Aggregate. *AASHTO Provisional Standards*, Washington, D.C., June Ed.

ASTM C 127. (2007) Standard Test Method for Density, Relative Density (Specific Gravity), and Absorption of Coarse Aggregates. 2007 Annual Book of ASTM Standards, 04.03, ASTM, Easton, MD.

ASTM D 4123. (1995) Standard Test Method for Indirect Tension Test for Resilient Modulus of Bituminous Mixtures. 1995 Annual Book of ASTM Standards, 04.03, ASTM, Easton, MD.

Arnaut, L. R. (2008). Measurement Uncertainty in Reverberation Chambers - I. Sample Statistics. NPL Technical Report TQE 2, 2nd. ed., sec. 4.1.2.2 (National Physical Laboratory) TQE (2): 52.

Becker, C., Fernandez-Lima, F. A., and Russell, D. H. (2009) Ion Mobility-Mass Spectrometry: A Tool for Characterizing the Petroleome. *Spectroscopy*, Vol. 24, No. 4, pp. 38-42.

Burr B.L., R.R. Davison, C.J. Glover, and J.A. Bullin. (1990) Solvent Removal from Asphalt. *Transportation Research Record*, No. 1269, pp. 1–8.

Burr B.L., R.R. Davison, C.J. Glover, and J.A. Bullin. (1994) Softening of Asphalts in Dilute Solutions at Primary Distillation Conditions. Transportation Research Record, No. 1436, pp. 47–53.

Burr B.L., C.J. Glover, R.R. Davison, J.A. Bullin. (1993) New Apparatus and Procedure for the Extraction and Recovery of Asphalt Binder from Pavement Mixtures. *Transportation Research Record*, No. 1391, pp. 20–29.

Burr, B. L., R. R. Davison, H. B. Jemison, C. J. Glover, and J. A. Bullin. (1991) Asphalt Hardening in Extraction Solvents. *Transportation Research Record*, 1323, pp. 70-76.

Button, J.W., C.K. Estakhri, A.J. Wimsatt. (2007) A Synthesis of Warm-Mix Asphalt. FHWA/TX-07/0-5597-1. Texas Transportation Institute, College Station, TX.

Clifford, A. A. (1973) Multivariate Error Analysis: A Handbook of Error Propagation and Calculation in Many-Parameter Systems. John Wiley & Sons.

Coombs, S.H. (1981). A Density Gradient Column for Determining the Specific Gravity of Fish Eggs, with Particular Reference to Eggs of the Mackerel Scomber. *Marine Biology*, Vol 63, No. 1, pp. 101-106.

Cox D.R., Hinkley D.V. (1974) Theoretical Statistics. Chapman & Hall, pp. 49, pp. 209.

Curtis, C. W., Ensley, K., and Epps, J. (1993) Fundamental Properties of Asphalt-Aggregate Interactions Including Adhesion and Absorption. Strategic Highway Research Program (SHRP) Report No. SHRP-A-341, National Research Council, Washington, D.C.

Dave, E., Buttlar, W., Paulino, G., and Hilton, H. (2006) Graded Viscoelastic Approach For Modeling Asphalt Concrete Pavements. *Proc., Multiscale and Functionally Graded Materials 2006,* 736-741.

Domke, C.H., R.R. Davison, and C.J. Glover. (1999) Effect of Oxidation Pressure on Asphalt Hardening Susceptibility. *Transp. Res. Rec.*, Vol. 1661, pp. 114-121.

Doyle, J.D, and I.L. Howard. (2012). Factors Affecting the Measurment of Effective Specific Gravity for Reclaimed Asphalt Pavement. *International Journal of Pavement Research & Technology*. Vol. 5, No. 2, pp. 128-131.

Estakhri, C.K., J.W. Button, A.Alvarez Lugo. (2010) Evaluation of Warm Mix Asphalt in Texas: Technical Report FHWA/TX-10/0-5597-2, Texas Transportation Institute, College Station, TX.

Fortuin, J.M. H. (1960) Theory and Application of Two Supplementary Methods of Constructing Density Gradient Columns. *Journal of Polymer Science*, Vol. 44, No. 144, pp. 505-515.

Glover, C. J., Prapaitrakul, N., Han, R., Jin,X., Cui, Y., Rose, A., Lawrence, J.J., Padigala, M., Park, E.S., Arambula, E., and Epps Martin, A. (2013) Evaluation of Binder Aging and its Influence in Aging of Hot Mix Asphalt Concrete: Technical Report. FHWA/TX-13/0-6009-2. Texas Transportation Institute, College Station, TX.

Guin, J.A., H.S. Chang, and S.C. Yen. (1990). Absorption of Asphalt into Porous Aggregate. *Abstracts of Papers of the American Chemical Society*, Vol. 200, pp. 29.

Han, R., Jin, X., and Glover, C.J. (2011) Modeling of Pavement Temperature History for Use in Binder Oxidation Models and Pavement Performance Prediction. *J. Mater. Civ. Eng.* 23:351-359.

Jin, X., R. Han, Y. Cui, and C.J. Glover. (2011) Fast-Rate-Constant-Rate Oxidation Kinetics Model for Asphalt Binders. *Industrial & Engineering Chemistry Research*, Vol. 50, No. 23, pp. 13,373–13,379.

Jones, D. R. (1993) SHRP Materials Reference Library: Asphalt Cements: A Concise Data Compilation. Strategic Highway Research Program Report No.SHRP-A-645, National Research Council, Washington, D.C.

Kendall, M.G. and Stuart, D.G. (1973) The Advanced Theory of Statistics. Vol 2: Inference and Relationship, Griffin, London. Section 20.4.

Koohi, Y., Lawrence, J., Luo, R., and Lytton, R. (2012a) Complex Stiffness Gradient Estimation Of Field-Aged Asphalt Concrete Layers Using The Direct Tension Test. *Journal of Materials in Civil Engineering,* Vol. 24, 832-841.

Kandhal, P.S., and M.A. Khatri. (1991) Evaluation of Asphalt Absorption by Mineral Aggregates. *National Center for Asphalt Technology*, Issue 91, Part 4 of NCAT report.

Kandhal, P.S. and M.A. Khatri. (1992) Relating Asphalt Absorption to Properties of Asphalt Cement and Aggregate, *NCAT Report 92-02*.

Kandhal, P.S. and D. Lee. (1972). Asphalt Absorption as Related to Pore Characteristics of Aggregates. *Highway Research Record*, Vol. 404, pp. 97-11.

Koohi, Y., Luo, R., Lytton, R. and Scullion, T. (2012b) New Methodology To Find The Healing And Fracture Properties Of Asphalt Mixes Using Overlay Tester. *Journal of Materials in Civil Engineering,* Vol. 25, 1386-1393.

Ku, H. H. (1966). Notes on the Use of Propagation Of Error Formulas. *Journal of Research of the National Bureau of Standards* (National Bureau of Standards) 70C (4): 262.

Lee, D.Y. (1969) The Relationship Between Physical and Chemical Properties of Aggregates and Their Asphalt Absorption. *Proc. AAPT*, Vol. 38, pp. 242-275.

Lee, D. Y., Guinn, J. A., Khandhal, P. S., and Dunning, R. L. (1990). Absorption of Asphalt into Porous Aggregates. Strategic Highway Research Program (SHRP) Report No. SHRP-A/UIR-90-009, National Research Council, Washington, D.C.

Lee, D.Y., J.A. Guin, P.S. Kandhal, and R.L. Dunning. (1993). A Review on Absorption of Asphalt into Porous Aggregates 1. Physicochemical Mechanisms and Variables Affecting Absorption. *Fuel Science and Technology International*, Vol. 11, No. 3-4, pp. 585-608.

Lee, D.Y., J.A. Guin, P.S. Kandhal, and R.L. Dunning. (1993). A Review on Absorption of Asphalt into Porous Aggregates 2. Methods for Determinination and Minimization of Absorption. *Fuel Science and Technology International*, Vol. 11, No. 5-6, pp. 611-637.

Lettier, L.A., D.F. Fink, N.B. Wilson, and F.F. Fraley. (1949). Mechanism of Absorption of Bituminous Materials by Aggregate. *Proc. AAPT*, Vol. 18, pp. 278-300.

Levenberg, E And J. Uzan. (2004) Triaxial Small-Strain Viscoelastic-Viscoplastic

Modeling of Asphalt Aggregate Mixes. *Mechanics of Time-Dependent Materials*, Vol. 8, pp. 365–384.

Liu, M. J.M. Chaffin, R.R. Davison, C.J. Glover, and J.A. Bullin. (1996) The Kinetics of Carbonyl Formation in Asphalt. *AICHE J.*, Vol. 42, No. 4, pp. 1069-1076.

Luo, R., and Lytton, R. L. (2011) Self-Consistent Micromechanics Models of an Asphalt Mixture. *Journal of Materials in Civil Engineering*, Vol. 23, No.1, pp. 49-55.

NCHRP 1 -37A. (2002) Guide for Mechanistic-Empirical Design of New and Rehabilitated Pavement Structures. National Cooperative Highway Research Program Transportation Research Board National Research Council.

Neyman, J. (1937). Outline of a Theory of Statistical Estimation Based on the Classical Theory of Probability. Philosophical Transactions of the Royal Society A 236: 333–380.

Read, J., and Whiteoak, D. (2003). The Shell Bitumen Handbook. Thomas Telford Ltd, London, UK.

Roberts, F. L., Kandhal, P. S., Brown E. R., Lee, D. Y., and Kennedy, T. W. (1996) Hot Mix Asphalt Materials, Mixture Design, and Construction. NAPA Research and Education Foundation, Lanham, Maryland.

Rice. J.M. (1953) New Test Method for Direct Measurement of Maximum Density of Bituminous Mixtures. *Crushed Stone Journal.*

Rice, J.M. (1956) Maximum Specific Gravity of Bituminous Mixtures by Vacuum Saturation Procedure. *ASTM Special Technical Publication*, Vol 191.

Ruan, Y., R.R. Davison, and C.J. Glover. (2003) Oxidation and Viscosity Hardening of Polymer-Modified Asphalts. *Energy & Fuel*, Vol. 17. pp. 991-998.

Texas DOT. (2004) Standard Specifications for Construction and Maintenance of Highways, Streets, and Bridges, ftp://ftp.dot.state.tx.us/pub/txdot-info/des/specs/specbook.pdf.

Zar, J.H. (1984) Biostatistical Analysis. Prentice Hall International, New Jersey. pp. 43–45.

Zhang, Yuqing, Rong Luo, and Robert L. Lytton. (2011) Characterizing Permanent Deformation and Fracture of Asphalt Mixtures by Using Compressive Dynamic Modulus Tests. *Journal of Materials in Civil Engineering*, Vol. 24, No. 7, pp. 898-906.

Zhang, Y., Luo, R., and Lytton, R. (2013). "Mechanistic Modeling of Fracture in Asphalt Mixtures under Compressive Loading." *Journal of Materials in Civil Engineering*, Vol., 25, No. 9, pp. 1189–1197.

APPENDIX A: FM 973 FIELD CORE AIR VOID DATA

Table A1. RICE Density for Field Cores.

Section ID	G_{mm} (g/cm3)
1 (HMA)	2.420
7 (Foaming)	2.400
8 (Evotherm)	2.408

Table A2. Percent Air Voids by SSD Method (ASTM D2726).

Sample ID	Mass of sample in air (g)	Mass of SSD sample in air (g)	Mass of sample in water (g)	Bulk Specific Gravity (g/cm^3)	Air Voids (%)
S7-16	604.5	612.5	332.4	2.158	10.1
1-26-1	384.9	390.1	213.4	2.178	10.0
S1-24	390.4	393.1	213	2.168	10.4
1-24-1	381.5	383.8	203.8	2.119	12.4
S1-13	362.6	366.9	200.2	2.175	10.1
1-27-1	406.2	407.8	224.1	2.211	8.6
1-28-1	397.5	399.3	219.9	2.216	8.4
S1-20-1	589.1	596.4	322.6	2.152	11.1
S1-2	635.8	638.2	356.8	2.259	6.6
1-20-1	613.3	616.5	342.8	2.241	7.4
1-13-1	395.4	397.5	217.4	2.195	9.3
7-21-1	623.4	626	350.7	2.264	5.6
7-5-1	567.8	572.3	307.7	2.146	10.6
7-16-1	622.8	625	351.8	2.280	5.0
7-12-1	390.9	392.5	211.7	2.162	9.9
S7-15	382.3	384.6	209.5	2.183	9.0
7-24-1	614.1	616.9	342.1	2.235	6.9
S7-12	627.2	629.4	348.4	2.232	7.0
7-15-1	621.4	624.2	345.5	2.230	7.1
S7-5	618.5	622.3	344.2	2.224	7.3
8-4-1	584.3	587	317.1	2.165	10.1
S8-8	379.3	380.8	207.6	2.190	9.1
8-8-1	386	388.4	210.8	2.173	9.7
8-20-1	365.4	367.4	199.8	2.180	9.5
S8-4	390.4	392.3	213.7	2.186	9.2
8-12-1	601.1	603.7	327.6	2.177	9.6
8-18-1	578.7	585.2	318.1	2.167	10.0
S8-18	613.2	620.5	342.7	2.207	8.3
S8-12	591.2	593.2	327.1	2.222	7.7
8-24-1	593.5	588.8	320.3	2.210	8.2

APPENDIX B: ASPHALT CHARACTERIZATION TESTS

We selected more than 12 asphalts to determine the following characteristics: surface energy components, both wetting and de-wetting. The symbol "D" stands for De-wetting and is the fracture bond energy. The symbol "W" stands for Wetting and is the healing bond energy. Aging diminishes the size of the binder total surface energy.

Free Energy Symbols and Definitions

Γ: Total Surface Free Energy

Γ^{LW}: Non-polar Component of Surface Free Energy

Γ^{AB}: Polar Component of Surface Free Energy

Γ^{+}: Monopolar Acidic Component of Polar Component

Γ^{-}: Monopolar Basic Component of Polar Component

Table B1. Surface-Free Energy ("SFE") Characteristics (ergs/cm^2).

Material	Wetting or De-Wetting	Γ	Γ^{LW}	Γ^{AB}	Γ^{+}	Γ^{-}
Wright 64-22 B - Unaged	W	20.87	20.16	0.7	0.03	3.75
	D	48.15	43.74	4.42	0.59	8.27
Wright 70-22 S - Unaged	W	22.66	22.5	0.17	0	6.79
	D	47.26	44.82	2.44	0.12	12.2
Wright 76-22 TRS - Unaged	W	22.23	18.75	3.48	0.66	4.57
	D	48.42	45.2	3.22	0.27	9.62
Wright 76-22 S-A - Unaged	W	24.27	23.69	0.58	0.02	4.15
	D	48.2	43.21	4.99	0.55	11.4
Wright 76-22 S-B - Unaged	W	22.96	22.67	0.29	0	7.86
	D	48.79	46.96	1.84	0.06	13.71
Lion Oil 64-22 B - Unaged	W	29.79	29.79	0	0	1.42
	D	49.68	41.83	7.85	1	15.37
Lion Oil 70-22 S - Unaged	W	27.34	27.34	0	0	2.77
	D	51.37	41.95	9.42	1.15	19.32
Lion Oil 76-22 S - Unaged	W	33.22	33.22	0	0	2.3
	D	51.83	49.51	2.32	0.05	28.1
Alon 58-28 B - Unaged	W	18.96	18.96	0	0	3.26
	D	39.57	39.57	0	0	10.14
Alon 70-28 S - Unaged	W	23.01	23.01	0	0	5.44
	D	50.01	45.05	4.96	0.35	17.34
Alon 64-22 B - Unaged	W	32.17	32.17	0	0	0.92
	D	45.54	38.73	6.81	0.42	27.54

Table B1. Surface-Free Energy ("SFE") Characteristics (ergs/cm^2).

Material	Wetting or De-Wetting	Γ	Γ^{LW}	Γ^{AB}	Γ^{+}	Γ^{-}
Alon 70-22 S - Unaged	W	35.78	35.78	0	0	0.44
	D	49.12	44.89	4.23	0.12	38.05
Alon 76-22 TRS - Unaged	W	34.55	34.55	0	0	1.85
	D	47.71	42.4	5.31	0.19	36.69
Koch 64-22 B - Unaged	W	22.26	22.26	0	0	2.79
	D	45.84	41.48	4.36	0.22	21.19
Koch 70-22 S - Unaged	W	25.75	25.75	0	0	3.12
	D	48.4	39.19	9.21	1.69	12.55
Koch 76-22 S - Unaged	W	17.95	12.61	5.34	1.26	5.68
	D	48.04	44.37	3.67	0.23	14.8
Koch 70-28 S - Unaged	W	23.74	23.74	0	0	2.86
	D	49.05	45.5	3.55	0.14	22.62
Koch 76-28 S - Unaged	W	20.92	16.64	4.29	0.73	6.26
	D	53.85	47.78	6.07	0.36	25.27
MnRoad 120-150 AC Grade Unaged	W	26.86	26.86	0	0	0.02
	D	43.99	39.5	4.49	0.24	20.68
MnRoad 58-28 B - Unaged	W	25.79	25.79	0	0	0.26
	D	47.61	39.34	8.27	0.7	24.34
MnRoad 58-34 S - Unaged	W	16.86	16.86	0	0	2.85
	D	45.88	40.87	5.01	0.45	14.04
MnRoad 58-40 S - Unaged	W	19.28	19.28	0	0	2
	D	49.12	41.66	7.46	0.37	37.25
Valero-H 64-22 B - Unaged	W	17.35	15.3	2.05	0.32	3.31
	D	42.47	40.11	2.37	0.12	11.41
Valero-H 70-22 S - Unaged	W	18.83	17.27	1.56	0.13	4.82
	D	41.21	41.21	0	0	13.22
Valero-H 76-22 S - Unaged	W	19.27	16.82	2.45	0.28	5.31
	D	43.55	43.55	0	0	13.17
Valero-C 64-22 B - Unaged	W	20.28	19.72	0.56	0.03	2.7
	D	42.29	41.68	0.61	0.01	10.69
Valero-C 70-22 S - Unaged	W	18.7	16.9	1.8	0.28	2.87
	D	44.03	44.03	0	0	11.61

Table B1. Surface-Free Energy ("SFE") Characteristics (ergs/cm^2).

Material	Wetting or De-Wetting	Γ	Γ^{LW}	Γ^{AB}	Γ^{+}	Γ^{-}
Valero-C 76-22 S - Unaged	W	18.11	16.23	1.89	0.26	3.46
	D	41.37	41.37	0	0	12.02
Valero-O 64-22 B-S - Unaged	W	22.86	22.4	0.45	0.02	2.71
	D	43.29	39.82	3.47	0.18	17.02
Valero-O 70-22 S - Unaged	W	22.64	22.21	0.43	0.01	7.18
	D	46.87	43.13	3.73	0.13	26.88
Valero-O 76-22 S - Unaged	W	25.98	25.88	0.11	0	5.7
	D	45.05	39.71	5.34	0.25	28.58
Valero-O 64-22 B-SR (US 281) - Unaged	W	19.85	18.63	1.22	0.1	3.7
	D	42.56	42.02	0.54	0	17.01
Valero-O 76-22 SR (US 281 SBR) - Unaged	W	32.74	32.74	0	0	3.67
	D	47.13	45.35	1.78	0.04	20.86
Wright 64-22 B - SAFT	W	18.48	16.91	1.57	0.14	4.51
	D	42.6	42.34	0.26	0	11.26
Wright 70-22 S - SAFT	W	22.45	21.72	0.73	0.04	3.74
	D	45.6	45.6	0	0	12.52
Wright 76-22 TRS - SAFT	W	22.67	21.4	1.26	0.1	4.8
	D	45.4	45.1	0.3	0	13.6
Wright 76-22 S-A - SAFT	W	23.06	22.95	0.11	0	5.97
	D	41.09	41.09	0	0	15.94
Wright 76-22 S-B - SAFT	W	22.06	21.72	0.34	0.01	5.35
	D	44.01	44.01	0	0	13.28
Alon 58-28 B (70-28) - SAFT	W	21.28	21.3	0	0	2.9
	D	38.64	38.6	0	0	2.8
Alon 70-28 S - SAFT	W	20.26	20.3	0	0	2.9
	D	36.36	36.4	0	0	12.9

Table B1. Surface-Free Energy ("SFE") Characteristics (ergs/cm^2).

Material	Wetting or De-Wetting	Γ	Γ^{LW}	Γ^{AB}	Γ^{+}	Γ^{-}
Alon 64-22 B (*-22) - SAFT	W	28.12	28.1	0	0	1.4
	D	48.71	42.4	6.33	0.5	21
Alon 70-22 S - SAFT	W	28.8	28.6	0.2	0	2.5
	D	49.31	42.9	6.37	0.4	23
Alon 76-22 TRS – SAFT	W	26.98	27	0	0	4.6
	D	48.9	44.3	4.57	0.2	28.3
Wright 64-22 B – PAV	W	26.23	26.2	0	0	3.2
	D	43.21	43.2	0	0	11.6
Wright 70-22 S - PAV	W	21.29	21.3	0	0	4.1
	D	44.83	44.5	0.31	0.003	8.3
Wright 76-22 TRS - PAV	W	19.73	17.8	1.97	0.219	4.4
	D	33.87	24.9	8.92	1.632	12.2
Wright 76-22 S-A - PAV	W	26.91	26.9	0	0	5.4
	D	45.92	45.9	0	0	10.7
Wright 76-22 S-B – PAV	W	24.1	24.1	0	0	6.4
	D	43.69	43.7	0	0	12.5
Alon 58-28 B (70-28) – PAV	W	24.62	24.6	0	0	3.3
	D	43.26	39.9	3.36	0.233	12.1
Alon 70-28 S – PAV	W	20.57	17.7	2.89	0.441	4.7
	D	43.71	43.1	0.62	0.009	11.1
Alon 64-22 B (*-22) – PAV	W	25.97	26	0	0	5.1
	D	44.69	42.6	2.09	0.068	16
Alon 70-22 S - PAV	W	22.25	20.5	1.72	0.137	5.4
	D	43.69	41.3	2.44	0.106	14
Alon 76-22 TRS - PAV	W	25.78	24.8	0.95	0.027	8.5
	D	47.52	38.7	8.78	0.827	23.3
Lion Oil 64-22 B	W	29.79	29.79	0	0	1.42
	D	49.68	41.82	7.85	1	15.37

Table B1. Surface-Free Energy ("SFE") Characteristics (ergs/cm^2).

Material	Wetting or De-Wetting	Γ	Γ^{LW}	Γ^{AB}	Γ^{+}	Γ^{-}
Lion Oil 64-22 B UniChem 8162P	W	29.1	29.1	0	0	1.78
	D	44.53	38.66	5.87	0.4	21.3
Lion Oil 64-22 B ADhere HP Plus	W	29.75	29.72	0.03	0	5.12
	D	47.42	40.38	7.04	0.52	23.8
Lion Oil 64-22 B Lime	W	27.14	27.14	0	0	0.26
	D	47.02	40.13	6.89	0.65	18.26
Lion Oil 70-22 S	W	27.34	27.34	0	0	2.77
	D	51.37	41.95	9.42	1.15	19.32
Lion Oil 70-22 S UniChem 8162P	W	19.8	18.89	0.92	0.05	3.81
	D	39.76	38.63	1.13	0.02	17.09
Lion Oil 70-22 S Adhere HP Plus	W	24.79	24.79	0	0	1.67
	D	45.52	39.26	6.26	0.59	16.57
Lion Oil 70-22 S Lime	W	27.1	27.1	0	0	2.09
	D	48.34	41.55	6.79	0.62	18.46
Lion Oil 76-22 S	W	33.22	33.22	0	0	2.3
	D	51.83	49.51	2.32	0.05	28.1
Lion Oil 76-22 S UniChem 8162P	W	22.66	22.66	0	0	2.49
	D	48.15	40.64	7.51	0.58	24.26
Lion Oil 76-22 S ADhere HP Plus	W	26	25.91	0.09	0	2.91
	D	50.87	42.35	8.52	1.21	14.95
Lion Oil 76-22 S Lime	W	27.13	27.13	0	0	3.47
	D	50.65	44.38	6.27	0.45	21.94
TxDOT Asphalt A	W	22.77	22.68	0.09	0	0.88
	D	43.31	38.75	4.56	0.2	25.56

Table B1. Surface-Free Energy ("SFE") Characteristics (ergs/cm^2).

Material	Wetting or De-Wetting	Γ	Γ^{LW}	Γ^{AB}	Γ^{+}	Γ^{-}
TxDOT Asphalt P	W	19.24	19.24	0	0	0.07
	D	42.87	41.25	1.62	0.05	12.49
YRK A	W	18.16	17.83	0.33	0.01	2.64
	D	41.5	37.79	3.71	0.19	18.05
YRK B	W	18.95	18.85	0.1	0	1.81
	D	42.29	37.86	4.42	0.21	23.32
AAA	W	14.26	11.52	2.74	1.02	1.84
	D	54.44	15.98	38.46	8.87	41.69
AAD	W	14.73	14.73	0	0	2.57
	D	27.17	8.59	18.58	5.96	14.48
AAK	W	15.21	9.39	5.82	0.63	13.45
	D	25.86	21.13	4.73	0.48	11.66
AAM	W	10.04	4	6.04	6.57	1.39
	D	48.35	9.33	39.02	17.79	21.4
PG64-22 Lufkin Control	W	12.84	8.71	4.13	1.77	2.41
	D	41.2	21.67	19.53	5.62	16.96
PG64-22 Valero Control	W	17.86	17.38	0.48	0.03	1.93
	D	32	20.05	11.95	1.99	17.94
Wright (2007) 64-22 B	W	22.48	22.29	0.19	0.01	1.32
	D	42.51	42.51	0	0	13.33
Wright (2007) 70-22 SBS	W	18.29	16.42	1.87	0.4	2.2
	D	43.75	42.25	1.49	0.04	13.19
Wright (2007) 76-22 SBS	W	19.79	19.06	0.73	0.06	2.39
	D	42.33	42.33	0	0	11.16
Wright (2007) 76-22 TRS	W	18.39	17.55	0.83	0.04	4.09
	D	43.28	43.28	0	0	6.33
Lion Oil (2007) 64-22 B	W	19.65	18.51	1.14	0.28	1.17
	D	42.13	41.47	0.66	0	23.87

Table B1. Surface-Free Energy ("SFE") Characteristics (ergs/cm^2).

Material	Wetting or De-Wetting	Γ	Γ^{LW}	Γ^{AB}	Γ^{+}	Γ^{-}
Lion Oil (2007) 70-22 SBS	W	22.87	22.34	0.54	0.06	1.3
	D	43.94	40.72	3.22	0.1	26.38
Lion Oil (2007) 76-22 SBS	W	23.53	22.95	0.58	0.07	1.14
	D	44.45	40.21	4.24	0.19	23.2
Koch (2007) 64-22 B	W	25.64	25.6	0.04	0	1.36
	D	46.48	40.49	5.98	0.35	25.69
Koch (2007) 70-22 SBS	W	22.83	22.09	0.74	0.06	2.28
	D	47.32	41.56	5.76	0.31	27.17
Koch (2007) 76-22 SBS	W	20.61	18.51	2.1	0.47	2.35
	D	47.81	42.63	5.18	0.28	24.09
Koch (2007) 70-28 SBS	W	20.57	19.76	0.81	0.06	2.57
	D	46.45	40	6.45	0.37	28.18
Koch (2007) 76-28 SBS	W	19.22	17.14	2.08	0.35	3.08
	D	48.15	40.76	7.39	0.63	21.61
Valero - H (2007) 64-22 B	W	21.06	20.91	0.15	0	1.44
	D	35.98	35.98	0	0	15.49
Valero - H (2007) 70-22 SBS	W	19.45	17.99	1.46	0.27	1.95
	D	43.02	41.38	1.64	0.05	13.56
Valero - H (2007) 76-22 SBS	W	21.07	21.07	0	0	2.98
	D	42.75	42.75	0	0	14.31
Valero - C (2007) 64-22 B	W	20.44	19.8	0.64	0.06	1.78
	D	39.95	39.95	0	0	13.84
Valero - C (2007) 70-22 SBS	W	20.42	20.42	0	0	2.39
	D	41.84	41.84	0	0	11.98
Valero - C (2007) 76-22 SBS	W	22.03	21.36	0.67	0.05	2.12
	D	43.56	43.56	0	0	13.11

Table B1. Surface-Free Energy ("SFE") Characteristics (ergs/cm^2).

Material	Wetting or De-Wetting	Γ	Γ^{LW}	Γ^{AB}	Γ^{+}	Γ^{-}
Valero - O (2007) 64-22 B	W	22.57	22.23	0.35	0.02	1.77
	D	45.05	41.49	3.55	0.13	24.96
Valero - O (2007) 70-22 SBS	W	20.82	19.55	1.28	0.28	1.44
	D	45.71	41.09	4.62	0.24	22.59
Valero - O (2007) 76-22 SBS	W	18.77	16.58	2.19	0.43	2.81
	D	44.9	41.67	3.23	0.11	24.74
Control 64-22 B	W	21.06	20.95	0.11	0	2.08
	D	41.27	38.91	2.36	0.1	14.48
Sasobit 64-22 Sasobit	W	17.58	15.65	1.93	0.42	2.24
	D	39.06	35.67	3.39	0.17	16.94
Advera 64-22 Advera	W	16.16	14.26	1.89	0.32	2.81
	D	42.12	38.13	3.99	0.26	15.07
Ad-RAP 64-22 RAP	W	17.07	15.85	1.23	0.08	4.81
	D	40.68	37.75	2.92	0.15	14.06
Evotherm 64-22 Evotherm	W	20.14	17.58	2.57	0.38	4.33
	D	40.17	37.18	2.99	0.08	29.27

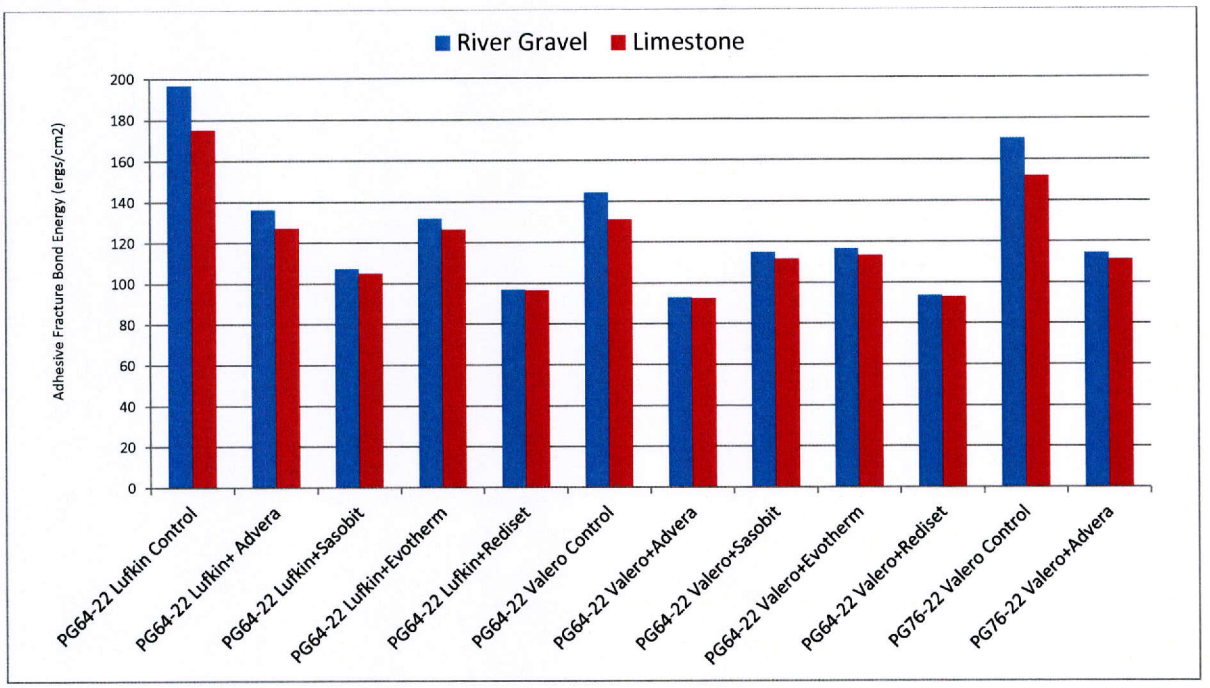

Figure B1. Adhesive Fracture Bond Energy without Water.

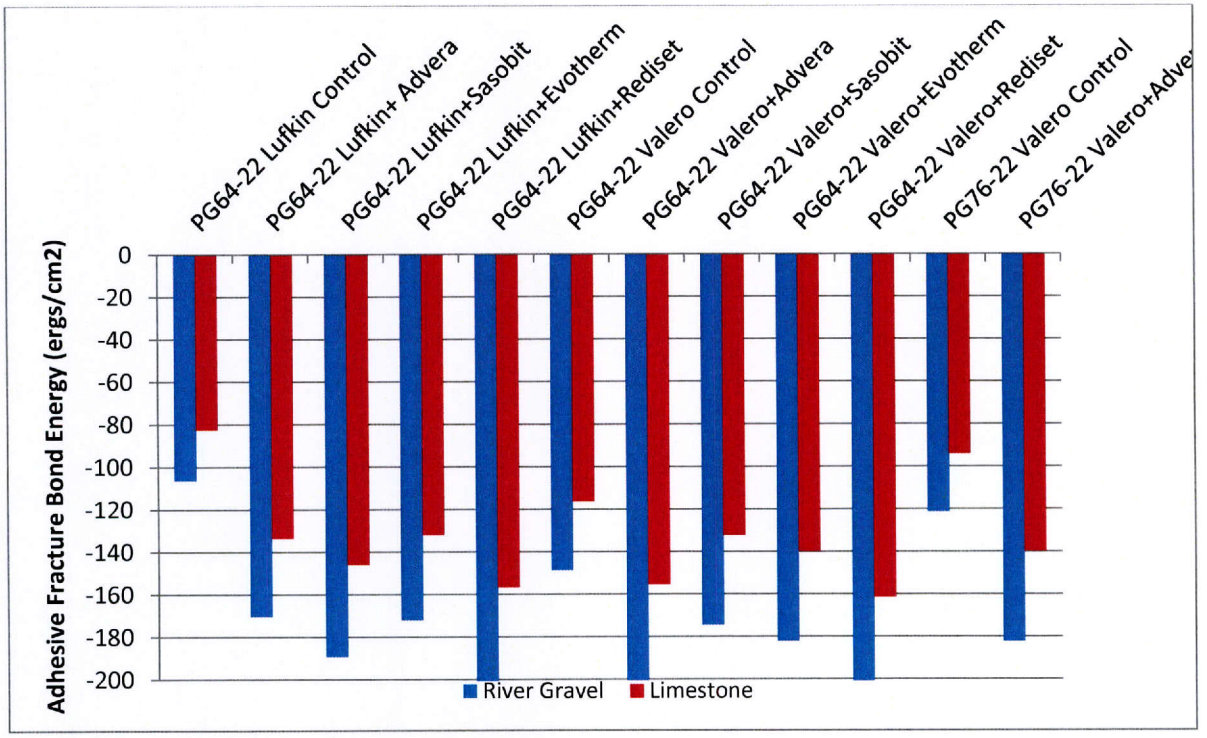

Figure B2. Adhesive Fracture Bond Energy with Water.

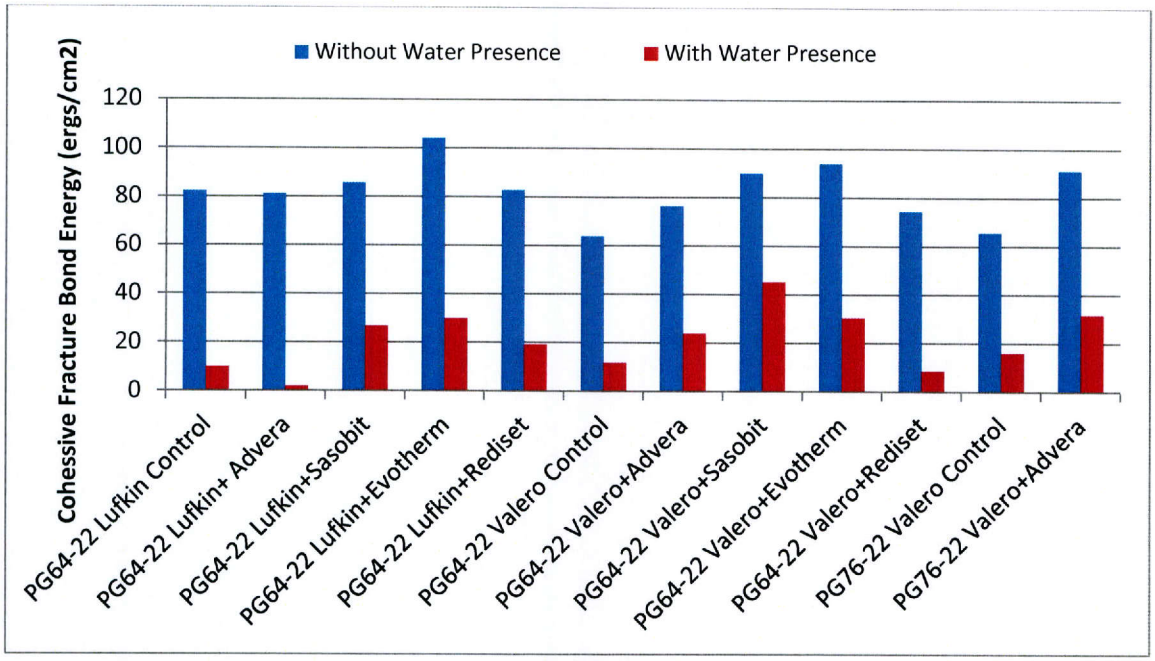

Figure B3. Cohesive Fracture Bond Energy without Water and without Water.

Texas A&M Transportation Institute
College Station, TX 77843-3135
979-845-1734
http://tti.tamu.edu